Hydraulic fracturing in hard rock

Numerical studies from laboratory to reservoir scale

Márton Pál Farkas

Cumulative dissertation

to obtain the academic degree "doctor rerum naturalium" (Dr. rer. nat.)

in the scientific discipline Geophysics

Submitted to the

Faculty of Science

University of Potsdam, Germany

Prepared at

Section 2.6 Seismic Hazard and Risk Dynamics

Section 4.8 Geoenergy

GFZ – Geman Research Centre for Geosciences

and

Institute of Geosciences, University of Potsdam, Germany

Place and date of defense:

Potsdam, 02.05.2022

Academic advisor: apl. Prof. Dr. Arno Zang, University of Potsdam, Germany
Second advisor: Prof. Dr. Günter Zimmermann, Technical University of Berlin, Germany

Reviewers:
1. apl. Prof. Dr. Arno Zang, University of Potsdam, Germany
2. Prof. Dr. Günter Zimmermann, Technical University of Berlin, Germany
3. Prof. Dr. Heinz Konietzky, TU Bergakademie Freiberg, Germany

Examination committee:
1. apl. Prof. Dr. Arno Zang, University of Potsdam, Germany
2. Prof. Dr. Günter Zimmermann, Technical University of Berlin, Germany
3. Prof. Dr. Heinz Konietzky, TU Bergakademie Freiberg, Germany
4. Chairperson: Prof. Dr. Max Wilke, University of Potsdam, Germany
5. Prof. Dr. Jens Tronicke, University of Potsdam, Germany
6. apl. Prof. Dr. Martin H. Trauth, University of Potsdam, Germany

Published online on the
Publication Server of the University of Potsdam:
https://doi.org/10.25932/publishup-54934
https://nbn-resolving.org/urn:nbn:de:kobv:517-opus4-549343

Statement of Originality

I hereby declare that this thesis is the product of my own work. All the assistance received in preparing this thesis and the sources used have been acknowledged. The work contained in this thesis has not been previously submitted for a PhD degree at any other higher education institution.

Potsdam, _____

_____

Márton Pál Farkas

Table of Contents

Abstract

Hydraulic-driven fractures play a key role in subsurface energy technologies across several scales. By injecting fluid at high hydraulic pressure into rock with intrinsic low permeability, in-situ stress field and fracture development pattern can be characterised as well as rock permeability can be enhanced. Hydraulic fracturing is a commercial standard procedure for enhanced oil and gas production of rock reservoirs with low permeability in petroleum industry. However, in EGS utilization, a major geological concern is the unsolicited generation of earthquakes due to fault reactivation, referred to as induced seismicity, with a magnitude large enough to be felt on the surface or to damage facilities and buildings. Furthermore, reliable interpretation of hydraulic fracturing tests for stress measurement is a great challenge for the energy technologies. Therefore, in this cumulative doctoral thesis the following research questions are investigated. (1): How do hydraulic fractures grow in hard rock at various scales?; (2): Which parameters control hydraulic fracturing and hydro-mechanical coupling?; and (3): How can hydraulic fracturing in hard rock be modelled?

In the laboratory scale study, several laboratory hydraulic fracturing experiments are investigated numerically using Irazu2D that were performed on intact cubic Pocheon granite samples from South Korea applying different injection protocols. The goal of the laboratory experiments is to test the concept of cyclic soft stimulation which may enable sustainable permeability enhancement (Publication 1).

In the borehole scale study, hydraulic fracturing tests are reported that were performed in boreholes located in central Hungary to determine the in-situ stress for a geological site investigation. At depth of about 540 m, the recorded pressure versus time curves in mica schist with low dip angle foliation show atypical evolution. In order to provide explanation for this observation, a series of discrete element computations using Particle Flow Code 2D are performed (Publication 2).

In the reservoir scale study, the hydro-mechanical behaviour of fractured crystalline rock due to one of the five hydraulic stimulations at the Pohang Enhanced Geothermal site in South Korea is studied. Fluid pressure perturbation at faults of several hundred-meter lengths during hydraulic stimulation is simulated using FracMan (Publication 3).

The doctoral research shows that the resulting hydraulic fracturing geometry will depend “locally”, i.e. at the length scale of representative elementary volume (REV) and below that (sub-REV), on the geometry and strength of natural fractures, and “globally”, i.e. at super-REV domain volume, on far-field stresses. Regarding hydro-mechanical coupling, it is suggested to define separate coupling relationship for intact rock mass and natural fractures. Furthermore, the relative importance of parameters affecting the magnitude of formation breakdown pressure, a parameter characterising hydro-mechanical coupling, is defined. It can be also concluded that there is a clear gap between the capacity of the simulation software and the complexity of the studied problems. Therefore, the computational time of the simulation of complex hydraulic fracture geometries must be reduced while maintaining high fidelity simulation results. This can be achieved either by extending the computational resources via

parallelization techniques or using time scaling techniques. The ongoing development of used numerical models focuses on tackling these methodological challenges.

Zusammenfassung

Hydraulische Risserzeugung (aus dem Englischen „Hydraulic Fracturing“; auch hydraulische Stimulation genannt) spielt eine Schlüsselrolle in unterirdischen Energietechnologien auf verschiedenen Skalen. Durch Injektion von Flüssigkeit mit hohem hydraulischem Druck im Gestein mit geringer Permeabilität können das Spannungsfeld und das Bruchentwicklungsmuster in-situ charakterisiert sowie die Gesteinspermeabilität erhöht werden. Hydraulic Fracturing ist ein kommerzielles Standardverfahren zur verbesserten Öl- und Gasförderung aus geringpermeablen Gesteinsformationen in der Erdölindustrie. Ein großes geologisches Problem bei der geothermischen Nutzung ist die ungewollte Erzeugung von Erdbeben aufgrund einer Verwerfungsreaktivierung, die als induzierte Seismizität bezeichnet wird und eine Größenordnung hat, die groß genug ist, dass sie an der Oberfläche zu spüren ist und sogar Gebäude beschädigen kann. Darüber hinaus ist die zuverlässige Interpretation von Hydraulic-Fracturing-Tests zur Spannungsmessung eine große Herausforderung für die Energietechnologien. Daher werden in dieser kumulativen Dissertation folgende Forschungsfragen untersucht: (1): Wie wachsen hydraulische Risse in Hartgestein in verschiedenen Skalen? (2): Welche Parameter steuern das hydraulische Versagen und die hydromechanische Kopplung? und (3): Wie kann hydraulische Risserzeugung in Hartgestein modelliert werden?

In der Studie im Labormaßstab werden mehrere Hydrofracturing-Laborexperimente numerisch mit Irazu2D untersucht, die an intakten kubischen Pocheon-Granitproben aus Südkorea unter Anwendung verschiedener Injektionsprotokolle durchgeführt wurden. Das Ziel der Laborexperimente ist es, das Konzept der zyklischen sanften Stimulation zu testen, die eine nachhaltige Permeabilitätserhöhung ermöglichen kann (Veröffentlichung 1).

Die Studie im Bohrlochmaßstab untersucht Hydraulic Fracturing Tests, die in Bohrlöchern in Mittel-Ungarn durchgeführt wurden, um das in-situ Spannungsfeld für eine geologische Standortuntersuchung zu bestimmen. In einer Tiefe von etwa 540 m zeigen die aufgezeichneten Druck-Zeit-Kurven im Glimmerschiefer mit einer Schieferung mit geringem Neigungswinkel eine atypische Entwicklung. Um diese Beobachtung zu erklären, wird eine Reihe von diskreten Elementberechnungen unter Verwendung von Particle Flow Code 2D durchgeführt (Veröffentlichung 2).

In der Studie im Reservoirmaßstab wird das hydromechanische Verhalten des aufgebrochenen kristallinen Gesteins an einer der fünf hydraulischen Stimulationen am Pohang Enhanced Geothermal System (EGS) Standort in Südkorea untersucht. Mit FracMan wird die Fluiddruckstörung an Verwerfungen von mehreren hundert Metern Länge während der hydraulischen Stimulation simuliert (Veröffentlichung 3).

Die Ergebnisse dieser Dissertation zeigen, dass die resultierende hydraulische Bruchgeometrie „lokal“, d. h. auf der Längenskala des repräsentativen Elementarvolumens (REV) und darunter (sub-REV) von der Geometrie und Stärke natürlicher Risse und „global“, d.h. bei Super-REV-Domänenvolumen, vom Spannungsfeld abhängt. In Bezug auf die hydromechanische Kopplung wird vorgeschlagen, separate

Kopplungsbeziehungen für intakte Gesteinsmassen und natürliche Risse zu definieren. Darüber hinaus wird die relative Bedeutung von Parametern definiert, die die Größe des Formationsbruchdrucks beeinflussen, ein Parameter, der die hydromechanische Kopplung charakterisiert. Es kann auch festgestellt werden, dass es eine klare Lücke zwischen der Leistungsfähigkeit der Simulationssoftware und der Komplexität der untersuchten Probleme gibt. Daher muss die Rechenzeit der Simulation komplexer hydraulischer Rissgeometrien reduziert werden, währenddessen die Simulationsergebnisse mit hoher Genauigkeit beibehalten werden. Dies kann entweder durch Erweiterung der Rechenressourcen über Parallelisierungstechniken oder durch Verwendung von Zeitskalierungstechniken erreicht werden. Die Weiterentwicklung der verwendeten numerischen Modelle konzentriert sich auf die Bewältigung dieser methodischen Herausforderungen.

List of Symbols

C	Elastic tensor
e	Hydraulic aperture
E	Young's modulus
E'	Plane strain modulus
FBP	Formation breakdown pressure
K'	Mode I toughness for scaling
K_{IC}	Mode I fracture toughness
K_{IIC}	Mode II fracture toughness
K_{IIIC}	Mode III fracture toughness
K_p	Bulk modulus of the rock with pores
K_s	Bulk modulus of the rock without pores
$\mathcal{K}$	Dimensionless parameter characterising the effect of rock toughness
L	Fracture path
$\mathcal{M}$	Dimensionless parameter characterising the effect of fluid viscosity
O	Regime characterising large fluid lag
P	Fluid pressure
P_p	Pore pressure
q	Two-dimensional flow rate
Q_0	Constant injection rate
S_H	Maximum horizontal stress
S_h	Minimum horizontal stress
T_0	Rock tensile strength
t_{exp}	Experimental time
t_{mk}	Characteristic time for the transition between M and K regimes
t_{om}	Characteristic time for the transition between O and M regimes
v_l	Leak-off flow velocity
$\mathcal{Z}$	Dimensionless parameter characterising the effect of minimum principal stress
α	Biot's coefficient
ε	Linear strain tensor
μ	Fluid viscosity
μ'	Fluid viscosity for scaling
ν	Poisson's ratio
σ	Cauchy stress tensor
σ_0	Minimum principal stress
σ_{eff}	Effective stress tensor
φ	Trajectory parameter

Chapter 1 Introduction and numerical approaches

This chapter gives first a brief introduction to the underlying processes and scales of hydraulic fracturing, and the related mathematical-physical principles in general. This is followed by giving an overview on the available numerical models for the simulation of hydraulic fracturing. Based on the overview, the evaluation and selection of numerical codes are presented. At the end of the chapter, structure of the thesis is presented.

1.1 Problem statement

Hydraulic-driven fractures play a key role in subsurface energy technologies across several scales (Figure 1). The target of these is often the same. In hydraulic fracturing, by injecting fluid at high hydraulic pressure into rock with intrinsic low permeability in several cycles (Figure 2), in-situ stress field and fracture development pattern can be characterised (Zang and Stephansson, 2010; Zoback, 2007). Hydraulic fracturing as a stress measurement method involves minimum stress and fracture characterization via shut-in pressure analysis and the determination of maximum horizontal stress direction based on the analysis of impression packer record or borehole televiewer logs (Haimson and Cornet, 2003).

At reservoir scale, in the case of unconventional oil and shale gas as well as deep geothermal reservoirs, hydraulic fracturing is an efficient way to increase the hydraulic permeability of rock and to create a fracture network for transport paths in tight rock (Economides and Nolte, 2000). In the geothermal application, the hydraulic stimulation of unconventional reservoirs located at a depth of two to five thousand meters are referred to as hot dry rock (HDR) systems, or enhanced geothermal systems, EGS, depending on the presence of high enthalpy fluid in the rock formation (Huenges, 2010). Furthermore, at tunnel scale, geotechnical and mining engineering, e.g. the construction of underground nuclear waste repository, requires the safety assessment of geological risks with highest confidence. These are often related to fracture opening due to the percolation of groundwater from degraded underground man-made structures and subsequent seepage through interconnected fractures or seismic events in deep crustal rock (Ahusborde et al., 2021). In order to get a better understanding of micromechanical processes during hydraulic fracture growth, laboratory experiments can be conducted (Zhuang and Zang, 2021).

Hydraulic fracturing is a commercial standard procedure for enhanced oil and gas production of tight rock reservoirs in petroleum industry. However, in EGS utilization, a major geological concern is the unsolicited generation of earthquakes due to fault reactivation, referred to as induced seismicity, with a magnitude large enough to be felt on the surface or to damage facilities and buildings (Grünthal, 2014; Zang et al., 2014). Thus, large induced seismic events may result in project suspension or closure (Tester, 2006). Furthermore, the generation of fracture network with insufficient permeability and, in particular, insufficient flow rate, may make an EGS project uneconomic (Breede et al., 2013; Lu, 2017).

Therefore, recent geoscientific research projects, such as DESTRESS and GEMEX projects focus on designing hydraulic stimulation treatments that enable safer and more economic production (Bruhn et al., 2021; Huenges et al., 2021). Apart from that, reliable interpretation of hydraulic fracturing tests for stress measurement is of great importance for all rock engineering problems presented above (Amadei and Stephansson, 1997). There is an increasing need for tools that can gain in-depth insights into the process of hydraulic fracture growth that can be linked with the recorded pressure history for joint interpretation (Lavrov et al., 2016).

The process of hydraulic fracturing or hydraulic stimulation composes of three main processes: fracture initiation, fracture propagation and shut-in or flow-back (Chen et al., 2021). The three main processes can be extended by fracture coalescence and crack arrest-stopping phases between fracture propagation and shut-in (Zang and Stephansson, 2010). The complexity of predicting the resulting fracture network is controlled by several factors:

1. Fluid flow within the fracture is coupled with rock deformation and vice versa. This is referred to as hydro-mechanical coupling (Jaeger et al., 2007).
2. Several multiphysics processes are included, such as interaction between natural and hydraulic fractures and leak-off. The interplay and the competition between these processes lead to multiple length scales (Figure 1) and time scales (Detournay, 2016; Hyman et al., 2016).
3. Geological and operational conditions are challenging to model accurately due to the variable availability of validating data and often high associated costs (Chen et al., 2021).

Although numerical modelling can be an effective tool to analyse and predict coupled hydro-mechanical processes during hydraulic fracturing at various scales, however, several aspects of the problem must be simplified. This has resulted in the development of various analytical solutions and numerical models with their suggested applicability and limitations (Shen et al., 2020).

In the following chapters, brief overview is given on the relevant physical processes and mathematical models on hydraulic fracturing as well as on numerical models relevant for the doctoral thesis.

Microscale	Mesoscale	Macroscale
1 mm – 1 cm fracture length	1 m – 10 m fracture length	100 m – 1000 m fracture length
Laboratory scale	Tunnel/borehole scale	Reservoir scale
Research projects	Geotechnical and mining engineering	Petroleum and geothermal engineering

Figure 1: The process of hydraulic fracturing is a multiscale process ranging from fracture length of mm to km. Typical fracture lengths, application scale as well as relevant energy technologies are summarised. Microscale: computed tomography (CT) scan of laboratory hydraulic fracture in Pocheon granite from South Korea. Mesoscale: granodiorite tunnel in the Äspö Hard Rock Laboratory in Sweden. Macroscale: Outcrop of the granodiorite basement rock near Pohang, South Korea.

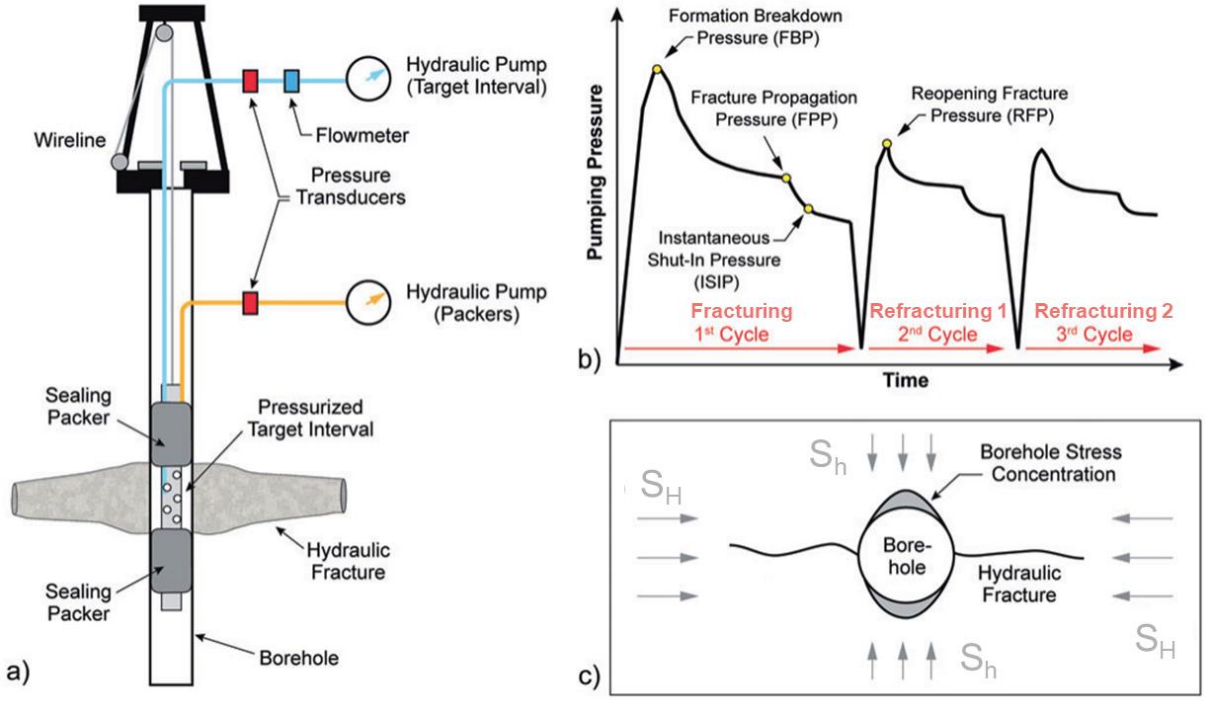

Figure 2: (a): Schematic illustration of hydraulic fracturing setup. (b): typical hydraulic fracture treatment record of pumping pressure versus time with distinct pressure in each pumping cycle. (c): geometry of the induced hydraulic fracture with respect to the maximum (S_H) and minimum horizontal (S_h) in-situ stresses for a horizontal plane through a vertical borehole (modified from Eberhardt and Amini, 2018).

1.2 Main physical processes and mathematical models

1.2.1 Rock deformation

Rock deformation is controlled by rock properties and boundary conditions such as fluid pressure and in-situ stresses. Due to the intrinsic complexity, one of the most widely adopted constitutive relationship between stress and strain is linear elasticity based on Hooke's law formulated as:

$$\sigma = C\varepsilon \tag{1}$$

where σ is the Cauchy stress tensor, C is the elastic tensor determined by Poisson's ratio (ν) and Youngs's modulus (E), and ε is the linear strain tensor (Goodman, 1989).

1.2.2 Fluid flow in the fracture

Fluid flow in the fracture during hydraulic fracturing is generally modelled based on the lubrication theory, which assumes that the aperture of a hydraulic fracture is much smaller than its height and length (Bear and Verruijt, 1987). This is expressed by the cubic law (Poiseuille's law or Darcy's law) where flow rate is related with the pressure gradient along the fracture:

$$q = \frac{-e^3}{12\mu}\frac{dP}{dL} \tag{2}$$

where q is the two-dimensional flow rate, e is the hydraulic aperture (non-linearly related to permeability), μ is the fluid viscosity, P is the fluid pressure, and L is the fracture path.

Furthermore, the continuity equation is considered, which is generally expressed as:

$$\frac{de}{dt} + \frac{dq}{dL} + v_l = 0 \tag{3}$$

where v_l is the leak-off flow velocity.

1.2.3 Fracture growth

In fracture mechanics, fracture growth is determined by rock failure criteria. The most widely adopted failure criteria are those based on phenomenological observation, mechanistic theory, linear elastic fracture mechanics (LEFM) criteria that are based on critical stress intensity factor (fracture toughness) as well as non-linear fracture mechanics (NFM) criteria that are based on rock (cohesive) process zone (Zang and Stephansson, 2010). The phenomenological failure criteria include Mohr-Coulomb criterion for compact rock without appreciable open cracks and the empirical Hoek-Brown criterion. The most widely used general mechanistic failure criterion is the Griffith criterion for quasi-static single tensile crack growth based on specific surface fracture energy. As for LEFM criteria, fracture toughness for mode I (tensile, Figure 3a), K_{IC}, mode II (sliding-, Figure 3b), K_{IIC}, and mode III (tearing shear, Figure 3c) fractures, K_{IIIC}, are generally assumed. In NFM approach, process zone ahead of the fracture with given radius is assumed to reduce stress singularity to finite strength value (Figure 3d-f). In rock

mechanics, the process zone is seen as volume of fresh created microcracks ahead of the tip of a propagating macroscopic fracture.

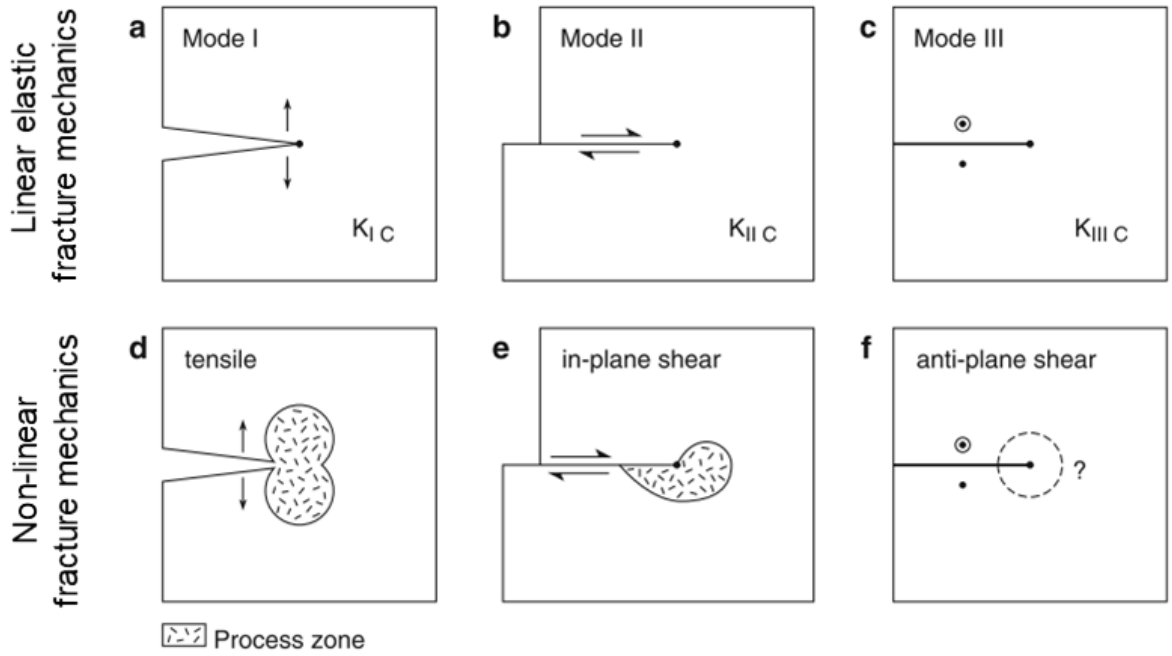

*Figure 3: Synoptic illustration of mode I, II and III fracture propagation in linear elastic fracture mechanics (LEFM, top) and non-linear fracture mechanics (NFLM, bottom). An idealised, sharp cut in elastic, homogeneous, isotropic material represents mode I tensile crack (**a**), mode II in-plane shear crack (**b**) and mode III anti-plane shear crack (**c**) growth in LEFM. The idealised shape of the process zone of a tensile fracture (**d**), sliding mode shear fracture (**e**) and tearing mode shear fracture (**f**) is contoured by approximate solutions in NFM. The actual geometry of the process zone of an anti-plane shear rupture is not yet known (modified from Zang and Stephanson, 2010).*

Regarding hydraulic fracture models, the most widely adopted fracture criterion is the Haimson-Fairhurst or the poroelastic hydraulic fracture criterion (Haimson and Fairhurst, 1967), which defines the formation breakdown pressure, *FBP*, required for mode I fracture initiation due to hydraulic pressurization:

$$FBP = \frac{3S_h - S_H + T_0}{2 - \alpha\left(\frac{1-2\nu}{1-\nu}\right)} \tag{4}$$

where α is Biot's coefficient, T_0 is the rock tensile strength as well as S_h and S_H are the minimum and maximum horizontal stress in the Earth's crust, respectively.

1.2.4 Further physical properties and processes

Apart from the noted three main hydraulic fracturing processes, further physical properties and processes can be considered, such as poroelasticity, leak-off, interaction of hydraulic and natural fractures, rock heterogeneity and anisotropy as well as fluid lag and proppant transport.

Poroelasticity, i.e. the coupled effect of porosity and pore pressure in rock deformation has been also adopted in linear elastic constitutive models (Jaeger et al., 2007). Using Biot's consolidation theory

(Biot, 1941; Nur and Byerlee, 1971), Biot's coefficient, α, is introduced to relate pore pressure in pores and rock deformation where pore pressure, P_p, and effective stress tensor, σ_{eff}, are related as follows:

$$\alpha = \left(1 - \frac{K_p}{K_s}\right); \quad \sigma_{eff} = \sigma - \alpha P_p \tag{5}$$

where K_s is the bulk modulus of the rock without pores and K_p is the bulk modulus of the rock with pores, also called the modulus of the frame. Since $\alpha < 1$ by definition, the pore pressure cannot completely counteract the effect of the confining pressure in changing the bulk volume. Thus, the Biot's coefficient is also known as the effective stress coefficient. In the case of granitic hard rock, the effect of pore pressure on shear strength of intact formation is often demonstrated by combining the Mohr-Coulomb failure criterion with the concept of effective stress.

The effect of leak-off on hydraulic fracturing treatments can be twofold (Ahmed and Meehan, 2016). It may retard fracture propagation, and thus change the geometry of induced fracture network. Secondly, if additive particles (proppants) are added to the fracturing fluid, final proppant distribution is highly affected by leak-off. Carter's leak-off model is widely used (Economides and Nolte, 2000), where q_l depends on fluid viscosity, formation permeability and filtrate cake formation. The model is derived from the one-dimensional Darcy's law; thus, it is only valid for leak-off during the propagation of a single planar hydraulic fracture.

Natural fractures influence hydraulic fracturing treatments in various ways including leak-off and proppant transport. Due to interaction between them, natural fractures may be reactivated or crossed during the treatment resulting in a complex fracture network instead of a planar fracture. According to Kolawole and Ispas (2020) and Shahid et al. (2016), the fracture geometry resulting from the interaction between hydraulic and natural fractures depends on various geological and operational parameters, such as the in-situ stress field, the shear strength of natural fractures, the intersection angle as well as the injection flow rate.

Shale rock and several metamorphic hard rock types, e.g. mica schist, are recognised to show not only heterogeneity, but anisotropy at different scales as well (Jaeger et al., 2007). Their significance is associated with their effect on the breakdown pressure and the geometry of the generated fracture network. Due to limited available geological information, the geometry of natural anisotropic structures are commonly characterised via statistical distributions, e.g. power-law type relationships or uniform distributions.

Fracturing fluid may fill the fracture partially. The difference between fluid front and fracture tip is referred to as fluid lag. When fracture toughness is small, the effect of fluid lag is significant (Garagash, 2006). At reservoir scale, due to high confining stresses, fluid lag effects can be often neglected (Detournay, 2016).

The incorporation of proppants makes fluid flow a mass transport process. Their influence on hydraulic fracturing are manifold (Barboza et al., 2021). First, they change the rheological properties of the fracturing fluid. Second, proppant settling and convection as well as proppant build up must be considered. Third, after flow back, proppant distribution affects the final fracture network. Although, the application of proppant for hydraulic fracturing in deep geothermal reservoirs has been tested (Blöcher et al., 2016; Moska et al., 2021; Zimmermann and Reinicke, 2010), these are not used in the experiments presented in this thesis. Thus, their effect is not discussed.

The interaction of the processes mentioned in Chapters 1.2.1 and 1.2.2 are captured via various coupling approaches discussed in Chapter 1.4. A generalised summary of various two-way interacting mechanisms between mechanical, hydraulic, thermal and chemical processes is given in Figure 4. Although the focus is on coupled hydro-mechanical processes during hydraulic fracturing in this thesis, Ahusborde et al. (2021) and Gaucher et al. (2015) pointed out that thermal and chemical processes may also play an important role in energy technologies.

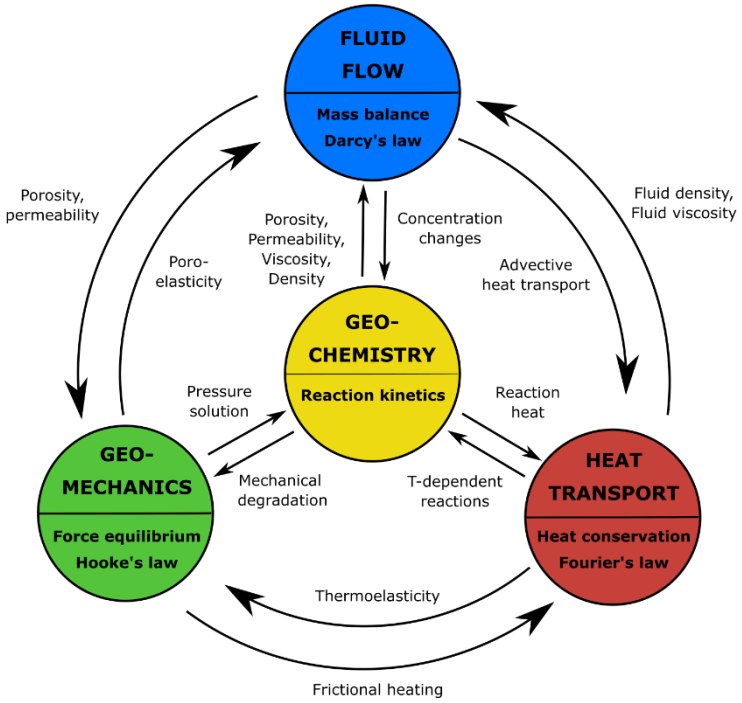

Figure 4: Illustration of generalised coupled thermal-hydro-mechanical-chemical processes relevant to hydraulic fracturing in hard rock (modified from Gaucher et al., 2015 and Ahusborde et al., 2021).

1.3 The multiple length and time scales of hydraulic fracturing

1.3.1 Length scale effects

The length scale effects are associated with heterogeneity and anisotropy of rock mass. It is often observed that the measured value of any geomechanical property, e.g. porosity, permeability, stress, always depends on how pre-existing defects are considered (Figure 5; Wong, 2018; Zang and

Stephansson, 2010). Thus, representative elementary volume (REV) can be defined for any given body (Bear and Verruijt, 1987; Hudson and Harrison, 2000). For a given REV, the size of the sample tested contains a sufficient number of defects for the "average" value of the investigated property to be consistent with repeated testing. Jing (2003) points out that scale effects have the following implications on rock properties:

- Properties measured in the lab may have to be "upscaled" (also referred to as homogenised) at a larger scale;
- Properties at larger scale cannot be measured directly;
- Properties may have to be determined by empirical methods; and
- Uncertainty of property cannot be quantified unambiguously.

As a result, it is always suggested to test parameters at the given scale *in-situ* to minimise scale effects.

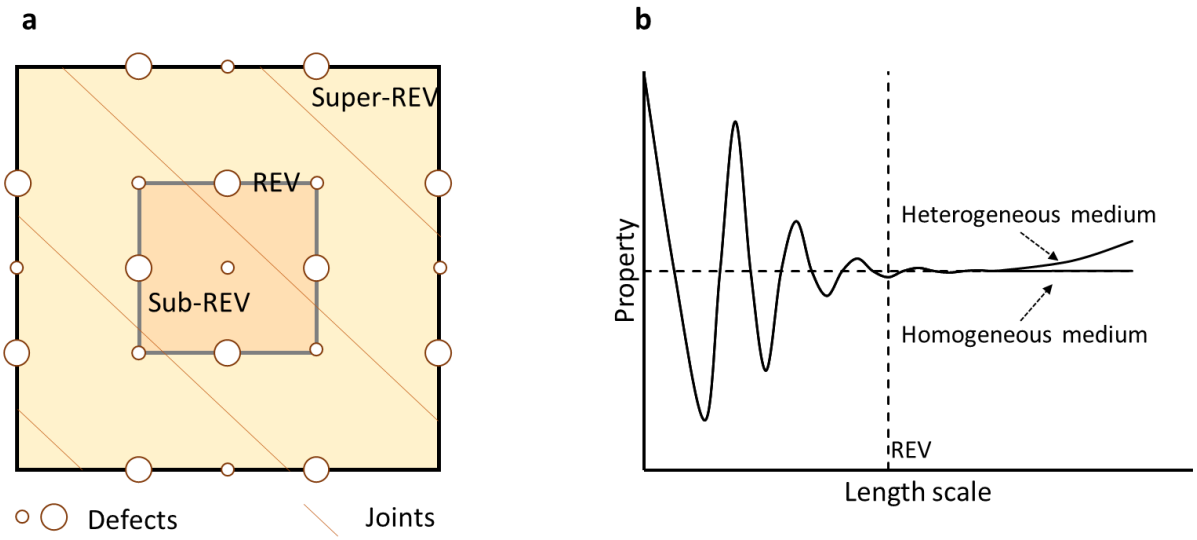

Figure 5: Concept of the representative elementary volume (REV). **a**: REV describing the rock mass by capturing different defects and set of joints (discontinuities); **b**: variability of a rock property (e.g. porosity, stress, permeability, etc.) in the function of length scale (modified from Zang and Stephansson (2010)).

1.3.2 Time scale effects

Based on Detournay (2016), there are several time scales during a hydraulic fracturing experiment that characterise the growth of hydraulic fractures referred to as limiting fracture behaviours, regimes or asymptotic solutions. These limiting regimes are associated with concurring energy dissipation mechanisms, that is, toughness and viscosity, as well as competing fluid volume conservation processes, i.e. storage and leak-off. In order to generalise the solutions for each limiting regime, referred to as vertices, dimensionless groups are introduced by Detournay (2016). Dimensionless parameters characterising various physical processes are derived and the solutions are expressed in terms of those. Three combinations of material parameters are introduced to these equations:

$$E' = \frac{E}{1-\nu^2}; \quad \mu' = 12\mu; \quad K' = 4\left(\frac{2}{\pi}\right)^{1/2} K_{IC} \tag{6}$$

where *E'* is the plane strain modulus, μ' is fluid viscosity for scaling as well as *K'* is mode I toughness for scaling. Detournay (2004) introduces two dimensionless groups, $\mathcal{M}$ and $\mathcal{K}$, characterising the effect of fluid viscosity and rock toughness, respectively:

$$\mathcal{M} = \mu' \left(\frac{Q_0^3 E'^{13}}{K'^{18} t^2}\right)^{1/5} \sim t^{-2/5} \tag{7}$$

$$\mathcal{K} = \mathrm{K}' \left(\frac{t^2}{\mu'^5 Q_0^3 E'^{13}}\right)^{\frac{1}{18}} \sim t^{1/9} \tag{8}$$

where Q_0 is the constant injection rate as well as $\mathcal{M}$ and $\mathcal{K}$ are dependent ($\mathcal{M} = \mathcal{K}^{-18/5}$). The time-dependence of $\mathcal{M}$ and $\mathcal{K}$ implies that the hydraulic fracture evolution may show transition from an early viscosity-dominated state to toughness-dominated propagation given sufficient amount of time. The transition between the two regimes, t_{mk}, can defined as

$$t_{mk} = \left(\frac{E'^{13} \mu'^5 Q_0^3}{K'^{18}}\right)^{1/2} \tag{9}$$

Eq. (9) shows that if characteristic experimental time, $t=t_{exp}<<t_{mk}$, the hydraulic fracture propagation is viscosity-dominated. If fluid lag is considered, a transitional regime characterising the vanishing fluid lag effect, t_{om}, can be defined (Savitski and Detournay, 2002):

$$t_{om} = \frac{E'^2 \mu'}{\sigma_0^3} \tag{10}$$

where σ_0 is the minimum principal stress or confining pressure.

Figure 6 illustrates the evolution of a penny-shape hydraulic fracture propagating in an impermeable elastic medium assuming zero leak-off. According to that, the triangular space *OMK* can be introduced with the dimensionless parameter $\mathcal{Z}$:

$$\mathcal{Z} = \left(\frac{t}{t_{om}}\right)^{1/3} \sim \sigma_0 \; ; \; \mathcal{K} = \left(\frac{t}{t_{mk}}\right)^{1/9} \sim K' \tag{11}$$

where $\mathcal{Z}$ characterises the effect of minimum principal stress and $\mathcal{K}$ the effect of toughness on vanishing fluid lag. The triangle illustrates the evolution of a penny-shape hydraulic fracture based on Detournay (2016) where the propagation regimes evolve from the small-time *O*-vertex (large fluid lag, $\mathcal{Z} = \mathcal{K}=0$)

over intermediate-time *M*-vertex (vanishing fluid lag in viscosity regime, $\mathcal{Z} > 0$ and $\mathcal{K} \to 0$) to large-time *K*-vertex (zero fluid lag in toughness regime, $\mathcal{Z} \to \infty$ and $\mathcal{K} \to \infty$). The transition between the vertices is determined by the trajectory parameter, $\varphi = t_{om}/t_{mk}$. If fluid lag can be neglected, i.e., $t >> t_{om}$, the triangle reduces to *MK*-edge only, and the regimes evolve from viscosity-dominated (*M*-vertex) to toughness-dominated (*K*-vertex) fracture propagation with the time scale t_{mk} only.

Here several notes must be made. First, if both storage and leak-off effects must be additionally considered in the hydraulic fracture growth, the parametric spaces *OMK* including storage and $\tilde{O}\tilde{M}\tilde{K}$ including leak-off can be introduced. A detailed overview over the solutions for all parametric spaces is given by Detournay (2016). Second, besides these parametric spaces, another time scale can be also applied for early time processes associated with fluid and pumping system compressibility and phenomena involving interaction of the crack with the wellbore. Furthermore, at laboratory scale, an additional time scale is associated with the finite lengths of rock specimens meaning that at some point in time the fracture has no space to extend (Bunger et al., 2005).

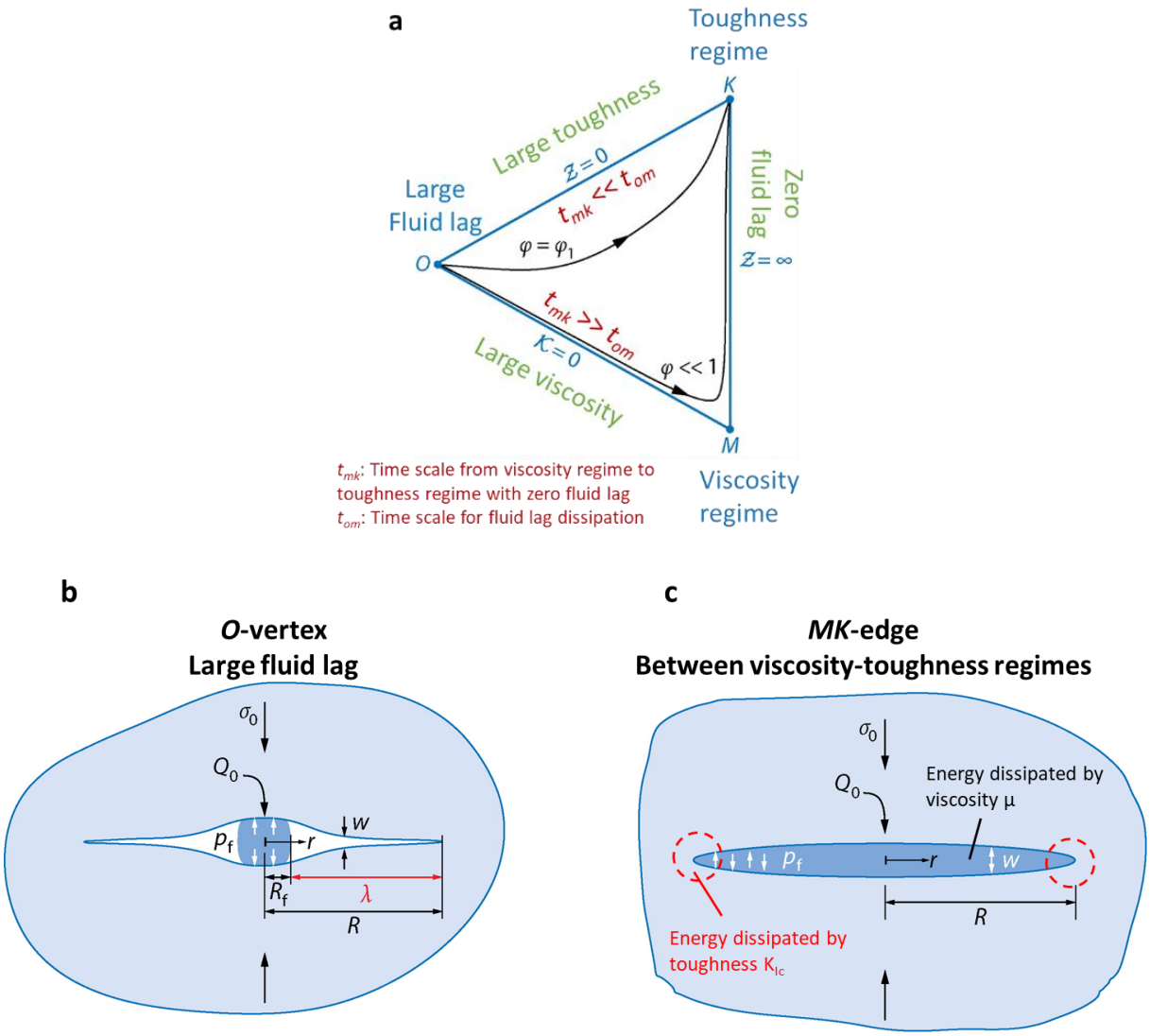

Figure 6: Generalised temporal evolution of a hydraulic fracture. ***a****: The parametric space OMK with the three vertices represent the small-time (O), intermediate-time (M), and large-time (K) similarity solutions for a penny-shaped hydraulic fracture propagating in an impermeable elastic medium. The evolution of the fracture from the O- to the K-vertex depends on the trajectory parameter $\varphi=t_{om}/t_{mk}$. The two sketches illustrate a hydraulic fracture near the O-vertex with large fluid lag (****b****) and along the MK-edge with zero fluid lag (****c****). Q_0: constant injection rate, σ_0: minimum principal stress, P_f, fluid pressure, w: fracture opening, R_f: fluid-front radius, R: fracture radius, $\lambda=R-R_f$, fluid lag, r: radial coordinate, $\mathcal{K}$: dimensionless toughness, $\mathcal{Z}$: dimensionless far-field stress. Modified from Detournay (2016) and Wong (2018).*

1.4 Hydraulic fracturing models and numerical simulators

Between the 1950s and 1980s, the classic models have been designed to predict the geometry of the induced hydraulic fracture, such as the Kristianovich-Geertsma-de Klerk (KGD) model (Geertsma and De Klerk, 1969), the Perkins-Kern-Nordgren (PKN) model (Nordgren, 1972), radial or penny crack model (Savitski and Detournay, 2002) as well as the pseudo 3D model (P3D, Cleary, 1980) and planar 3D model (PL3D, Siebrits and Peirce, 2002). Table 1 summarises the key assumptions and the fracture shape cross section of the classical hydraulic fracturing models and its features.

An important common feature of these models is that rock deformation is calculated directly by solving the elastic equation relating the fracture width to fluid pressure instead of time discretization

techniques (Chen et al., 2021). This reduces the complexity of numerical computation, and the computational costs as well. However, the main limitation of these classical models is that the hydraulic fracture is restricted to propagate along a planar plane. Furthermore, the incorporation of natural fractures is limited. Therefore, the need for simulating more realistic and more complex hydraulic fracturing treatments lead to the development of various advanced numerical methods, referred to as modern models.

Table 1: Overview of classic hydraulic fracturing models based on Chen et al. (2021) and Cottrell et al. (2013).

Model	**Major limiting assumptions on geometry**	**Fracture shape cross section**	**Features**	**References**
Penny or radial crack	Propagation in a given plane; symmetrical to the wellbore	Circular	3D fracture geometry and 1D fluid flow	Bunger and Detournay (2005); Geertsma and de Klerk (1969); Savitski and Detournay (2002)
KGD	Fixed fracture height; plane strain in horizontal direction	Rectangular	2D fracture geometry and 1D fluid flow	Carbonell et al. (1999); Geertsma and De Klerk (1969); Khristianovic and Zheltov (1955); Lecampion and Detournay (2007)
PKN	Fixed fracture height; plane strain in vertical direction	Elliptical	3D fracture geometry and 1D fluid flow	Detournay et al. (1990); Nordgren (1972); Perkins and Kern (1961)
Cell-based or lumped P3D	Plane strain in vertical direction	Elliptical	3D fracture geometry and 1D fluid flow	Cleary (1980); Cleary et al. (1983); Cleary and Fonseca (1992); Meyer (1989)
PL3D	Fix meshing of hydraulic fracture	Rectangular	3D fracture geometry and 2D fluid flow	Clifton and Abou-Sayed (1979); Clifton and Abou-Sayed (1981); Ouyang et al. (1997); Siebrits and Peirce (2002)

In the past several decades, modern hydraulic fracturing models have been developed. These simulate the complex propagation of hydraulic fractures with rigorous governing equations and numerical methods. These are commonly categorised as continuum-based models including finite element (FEM), finite difference (FDM) and phase field models (PFM), discontinuum-based methods including discrete element method (DEM) as well as hybrid continuum/discontinuum-based methods including finite-discrete element method (FDEM). Although these models capture the complexity of hydraulic fracture growth, two important aspects are commonly ignored in these. First, hydraulic fracturing models are practically limited to a given length scale. Second, the rigorous and complex 3D models are computationally expensive, which limits usability for treatment design (Chen et al., 2021). A comparison of numerical models is provided in Table 2.

Table 2: Overview of selected modern hydraulic fracturing models based on Chen et al. (2021).

Numerical method	Numerical solver	Advantages	Disadvantages	References
Continuum-based methods	FEM	Relatively easy implementation of heterogeneous formation properties and complex constitutive model	Equivalent fracture width; difficulties in remeshing when fracture intersection happens in 3D space	Wangen (2011); Wangen (2013)
	FDM	Easy implementation of formation heterogeneities and complex constitutive model; Remeshing is not essential	Equivalent fracture width; difficulties in remeshing when fracture intersection happens in 3D space	Zhou and Hou (2013)
	PFM	Easy implementation of formation heterogeneities; Remeshing is not essential when dealing with complex intersection of fractures even in 3D space	Smeared fracture path; High computational cost; Extremely fine mesh and small-time step are requested when validated with analytical solutions; Equivalent fracture width	Lepillier et al. (2020); Miehe and Mauthe (2016)
Discontinuum-based methods	Particle-based DEM	Easy implementation of the programme; Easy implementation of formation heterogeneities and DFN; Fracture initiation and propagation are a spontaneous process without additional criterion; Suitable for microscale analysis when the realistic rock grains are represented by particles	Alignment of fracture paths on body boundaries; Difficulty in determining reasonable particle size and parameters	Potyondy and Cundall (2004)
	Block-based DEM	Sharp fracture surfaces and paths; Easy implementation of DFN; Suitable for microscale analysis when the realistic rock grains are represented by blocks; Fracture initiation and propagation are a spontaneous process without additional criterion	Determination of reasonable block size and parameters; Alignment of fracture paths on block boundaries	Damjanac and Cundall (2016)
	RBSN	Easy implementation of DFN; Fracture initiation and propagation are a spontaneous process without additional criterion	Alignment of fracture paths on body boundaries	Asahina et al. (2014)
Hybrid continuum/discontinuum-based methods	FDEM	Sharp fracture surfaces and paths; Relatively easy implementation of heterogeneous formation properties	High computational cost for simulation lasting for a long time period; Alignment of fracture paths on element boundaries; Reduction of material stiffness due to the finite stiffness of the joint elements	Lisjak et al. (2017)
		Best presentation of sharp fracture surfaces and paths with remeshing; Relatively easy implementation of heterogeneous formation properties	High computational cost for simulation lasting for a long time period; Difficulties in remeshing	Profit et al. (2016)

Apart from the classic and modern hydraulic fracturing simulators discussed above, several numerical tools have been developed by the petroleum industry in the past decades. Chen et al. (2021) provide a review of available commercial software for hydraulic fracturing design. They point out that these are based on classic hydraulic fracturing models. This is explained by the time of release when PKN, KGD and PL3D models were developed, and the reasonable trade-off between the accuracy of fracture geometry and computational costs. Furthermore, these can provide real-time analysis of fracture growth and leak-off. The effect of natural fractures, if available, is simulated using the discrete fracture network (DFN) approach with significant simplifications on geometry and/or interaction mechanism. Furthermore, these tools have straightforward calibration workflow against injection pressure record and microseismic events. We note that numerous commercial hydraulic fracturing simulators are available, however, in this thesis, the focus lies on the most widely used tools and on those relevant for the thesis. These include Elfen, FracMan, FracPro, GOHFER and XSite. Their features are compared in Table 3 including numerical model, incorporation of multiple hydraulic fractures, leak-off, natural fractures as well as handling of microseismic event input and providing synthetic microseismic output.

Table 3: Overview of capabilities of selected commercial software for hydraulic fracturing treatment design. Note that HF represents hydraulic fracture and MS represents microseismic events (modified from Chen et al. (2021)).

Software	**Numerical Method**	**Multiple HFs**	**Leak-off**	**Natural fractures**	**MS Input**	**Synthetic MS Output**
Elfen	FDEM	+	+	+	+	+
FracMan	FEM+DFN	+	+	+	+	+
FracPro	P3D and PL3D	+	+	-	+	-
GOHFER	PL3D	+	+	-	+	-
XSite	FDEM	+	+	+	-	+

1.5 Evaluation and selection of numerical approach

In the previous chapter, several numerical methods are reviewed that are capable of solving coupled hydrogeological and geomechanical processes, and have been widely applied to numerous reservoir engineering problems. Based on that, an evaluation was undertaken to explore which methods would be the most suitable for simulating deep fluid injection into hard rock with pre-existing fractures.

In Table 4, several commercial software is evaluated based on the availability of two- or three-dimensional simulation, numerical method and solver, fracture growth (failure criterion, failure mode and fracture geometry), available coupling as well as hydraulic aperture versus normal stress relationship. According to this table, discontinuum or hybrid continuum/discontinuum-based methods are best suitable for simulating hydraulic fracture propagation in hard rock mass. Therefore, the primary methods for the micro- and mesoscale simulations are Irazu 2D and Particle Flow Code 2D, respectively. For the reservoir scale modelling study, the commercial software for hydraulic fracturing FracMan is

chosen which combines FEM with DFN method. Thus, it can be used for treatment design, incorporation of pre-existing fractures using DFNs, rapid simulation of hydraulic stimulation and can easily handle microseismic data as well.

Table 4: Evaluation of numerical code capable of simulating deep fluid injection into hard rock.

Numerical Code	2D/3D availability	Numerical method and solver	Failure criterion	Failure mode	Fracture path and geometry	Coupling	Hydraulic aperture vs normal stress relationship	Comments	Reference study
FLAC	2D/3D	Continuum-based FDM	Mohr-Coulomb and sliding/opening of natural fractures	Intact rock and fracture may fail in mode I or mode II	Determined by topology of connected elements	H-M	Hyperbolic	Example for fluid injection into porous reservoir is published by Konietzky et al. (2017)	Konietzky et al. (2017)
FracMan	3D	Continuum-based FEM	Mohr-Coulomb	Intact rock may fail in mode I, or natural fracture may fail in mode II	Determined by volume balance and location of pre-existing fractures	H-M	Hyperbolic based on Barton-Bandis law (Barton et al., 1985)	Only induced hydraulic fracture propagation is simulated explicitly. Natural fractures can be either jacked or hydro-sheared	Cottrell et al. (2016)
IRAZU	2D/3D	Hybrid continuum-/discontinuum-based FDEM	LEFM: fracture toughness	Intact rock and fracture may fail in mode I or mode II	Determined by topology of connected elements	(T-)H-M	Linear	Workflow for verifying fluid injection into porous reservoir is published by Lisjak et al. (2017). 3D T-H-M coupling has been recently reported by Geomechanica (2020)	Bai et al. (2021)
Particle Flow Code	2D/3D	Discontinuum -and particle-based DEM	Mohr-Coulomb and sliding/opening of natural fractures	Intact rock and fracture may fail in mode I or mode II	Determined by topology of connected elements	H-M	User-defined for rock mass and natural fractures; most widely exponential relationship used	2D H-M coupling is under continuous development	Yoon et al. (2014)
TOUGH-FLAC	3D	Continuum-based FDM	Mohr-Coulomb and sliding/opening of natural fractures	Intact rock and fracture may fail in mode I or mode II	Determined by topology of connected elements	(T-)H-M where temperature-dependent hydraulics is simulated in TOUGH and mechanical deformation is simulated using FLAC3D	Exponential	Workflow for verifying fluid injection into granitic rock has been recently published by Yoo et al. (2021). No explicit simulation of hydraulic fracture propagation	Yoo et al. (2021)
UDEC/3DEC	2D/3D	Discontinuum- and block-based DEM	Mohr-Coulomb and sliding/opening of natural fractures	Intact rock and fracture may fail in mode I or mode II	Determined by topology of connected elements	H-M	Linear	Polygonal block models are computationally more expensive than particle-based ones (Lisjak and Grasselli, 2014)	Damjanac and Cundall (2016)

1.6 Structure of the thesis

1.6.1 Overview of publications included as chapters of this thesis

The cumulative thesis is based on three main publications. All these publications investigate hydraulic fracture growth in hard rock at various scales using different numerical tools depending on the studied problem. For each study, numerical models are verified against existing data, i.e. laboratory and field records. It must be noted that the studies presented in this thesis are organised according to the length scale investigated therein, i.e. from laboratory to reservoir scale, and not to their publication date.

In the first publication (Farkas et al., 2022), several laboratory hydraulic fracturing experiments are investigated numerically that were performed on intact cubic Pocheon granite samples from South Korea applying different injection protocols. The goal of the laboratory experiments is to test the concept of cyclic soft stimulation which may enable sustainable permeability enhancement. The Irazu 2D FDEM numerical code, which combines the advantages of finite-element and discrete element methods, is used to verify the experiments via simulation of explicitly coupled hydraulic diffusion and fracturing processes under bi-axial stress conditions. The novelty of this study is the development of a workflow for verifying and investigating *microscale* hydro-mechanically coupled processes, i.e. mimicking hydraulic fractures with lengths of millimetres to centimetres within a mineral assembly.

In the second publication (Farkas et al., 2019), hydraulic fracturing tests are reported that were performed in boreholes located in central Hungary to determine the in-situ stress for a geological site investigation. At depth of about 540 m, the recorded pressure versus time curves in mica schist with low dip angle foliation (anisotropic rock) show atypical evolution. In order to provide explanation for this observation, a series of discrete element computations using the commercial software Particle Flow Code 2D are performed. The uniqueness of the investigation is twofold: it summarises the approach to verify the field experiments, and it proposes the likely phenomenon of viscous blocking effect acting at the area around the borehole. The studied hydraulic fractures have a length of several decimetres, i.e. referred to as *mesoscale*. The workflow presented therein is the improvement of the method reported by Yoon et al. (2014). Borehole is defined as a fluid line source and separate hydraulic aperture versus normal stress relationship are defined for smooth joints and intact rock mass.

In the third publication (Farkas et al., 2021), the hydro-mechanical behaviour of fractured crystalline rock due to one of the five hydraulic stimulations at the Pohang Enhanced Geothermal site in South Korea is studied. The software FracMan is used to simulate fluid pressure perturbation at faults of several hundred to kilometre lengths during hydraulic stimulation. In this study, the evolution of hydraulic aperture and the extent of overpressure zone are studied. The method is based on the hybrid FEM+DFN approach reported by Cottrell et al. (2016), which is extended by transient hydro-mechanical coupling mechanism based on Barton et al. (1985). In this *macroscale* study, workflow for verification

against recorded dataset using FracMan is demonstrated for the first time. The length of the studied fracture planes are several kilometres long.

The three main publications of the doctoral thesis with my contributions are summarised below.

Main publication 1: **Farkas, M. P.**, Hofmann, H., Zimmermann, G., Zang, A., Zhuang, L., Kim, K. Y., 2022. Numerical investigation of laboratory hydraulic fracturing tests in Pocheon granite. Under review at Acta Geotechnica.

Contribution of Márton Pál Farkas: Model conceptualization, laboratory data curation, methodology design, numerical formal analysis, visualization, writing original draft.

Main publication 2: **Farkas, M. P.**, Yoon, J., Zang, A., Zimmermann, G., Stephansson, O., Lemon, M., Dankó, G., 2019. Effect of foliation and fluid viscosity on hydraulic fracturing tests in mica schists investigated using distinct element modeling and field data. Rock Mechanics and Rock Engineering, 52(2), 555–574.

Contribution of Márton Pál Farkas: Model conceptualization, field data acquisition and curation, methodology design, numerical formal analysis, visualization, writing original draft, revised draft and editing.

Main publication 3: **Farkas, M. P.**, Hofmann, H., Zimmermann, G., Zang, A., Bethmann, F., Meier, P., Cottrell, M., Josephson, N., 2021. Hydromechanical analysis of second hydraulic stimulation at well PX-1 in Pohang fractured geothermal reservoir, South Korea, Geothermics 89, 101990.

Contribution of Márton Pál Farkas: Model conceptualization, field data curation, methodology design, numerical formal analysis, visualization, writing original draft, revised draft and editing.

1.6.2 Additional relevant publication

The third main publication of the thesis (Farkas et al., 2021) is based on the large dataset associated with the field application of the cyclic soft stimulation concept at the Pohang EGS site reported by Hofmann et al. (2019). The stimulation design was based on available structural geology, geomechanical, logging, seismological data as well as previous injection tests. During the field experiments, a seismic real-time monitoring and traffic light system were introduced. The hydraulic and seismological field observations, including pressure history, microseismic location and magnitude data are used for the verification of the numerical model presented in Farkas et al. (2021). Thus, this publication complements the numerical modelling study of Farkas et al. 2021. The field operations reported by Hofmann et al. 2019 are not

included as a chapter of this thesis, but the hydraulic and seismological field observations of the field experiment are discussed in Chapter 3.

Additional publication: Hofmann, H., Zimmermann, G., **Farkas, M.**, Huenges, E., Zang, A., Leonhardt, M., Kwiatek, G., Martinez-Garzon, P., Bohnhoff, M., Min, K-B., Fokker, P., Westaway, R., Bethmann, F., Meier, P., Yoon, K-S., Choi, J-W., Lee, T-J., Kim, K.Y., 2019. First field application of cyclic soft stimulation at the Pohang Enhanced Geothermal System site in Korea. Geophysical Journal International, 217(2), 926-949.

Contribution of Márton Pál Farkas: providing assistance in the following tasks: injection experiment conceptualization, hydraulic well test methodology design, field hydraulic data curation; visualization: preparation of Figure 1: Map showing Pohang EGS project location, surface geology and inferred surface faults.

Chapter 2 Objectives and research questions

In this chapter, the overarching research questions (RQ) are outlined that form the structure of the cumulative doctoral thesis. The first two questions address fundamental coupled fracturing processes: RQ1 focuses on fracture initiation and propagation due to fluid injection, and RQ2 covers phenomena related to coupling between mechanical and hydraulic processes as well as scale-dependencies. RQ3 focuses on the methodological and technical challenges of the numerical modelling of hydraulic fracturing in hard rock. A joint interpretation of the findings by the research questions are discussed in Chapter 6.

Research question 1

How do hydraulic fractures grow in hard rock at various scales?

In the first two main publications of the doctoral thesis, hydraulic fracture initiation, propagation and interaction with natural fractures in hard rock at various scales are studied. In microscale publication 1, hydraulic fractures of mm-cm length are induced in granite rock samples, and in mesoscale publication 2, hydraulic fractures at the scale of dm-m are induced during minifrac tests in mica schist. In these modelling studies, the REVs are sufficiently small for capturing fracture initiation phenomena and the modelling domain (super-REV) is large enough to capture fracture propagation and interaction with pre-existing fractures. Hydraulic fracture growth is modelled via the spatio-temporal evolution of microcracks that eventually form a chain which can be considered macroscopic fractures.

The main difference between the two studies is that in publication 1, hydraulic fractures are investigated in quasi-isotropic granitic rock, and in publication 2, the fracturing process is analysed in highly anisotropic mica schist. Thus, the detailed understanding of hydraulic fracturing is of great importance to control fracture growth in various hard rock types for energy technologies.

Research question 2

Which parameters control hydraulic fracturing and hydro-mechanical coupling?

Fracturing processes are directly and indirectly linked to the response of stimulated rock. These are described by various hydro-mechanical coupling formulations which are tested in all main publications. The main publications investigate the effect of various rock and hydraulic parameters on the fracturing (deformation) and fluid flow responses of the loaded rock via hydraulic aperture versus normal stress relationship. Regarding fracturing and deformation processes, at micro- and meso scale (publications 1 and 2), these are directly studied. At reservoir scale (publication 3), rock deformation is simulated indirectly, i.e. without explicit fracture propagation. The integrated discussion of the individual

publications can contribute to the reduction of length scale effects (Chapter 1.3.1) by understanding parameters controlling hydro-mechanically coupled processes at given scale, such as minimum horizontal stress and injection rate. Furthermore, time scale analysis of the experiments can be used for comparing the simulation results regarding the key mechanisms governing hydraulic fracture propagation.

Research question 3

How can hydraulic fracturing in hard rock be modelled?

Since the beginning of hydraulic fracturing modelling, the main challenge of the simulations lies in the prediction of hydraulic fracture growth and related hydraulic processes more realistically. For this reason, a verification workflow for calibrating hydro-mechanical models is presented in each main publication. This not only enables identifying methodological challenges, but may enable overcoming limitations of past hydraulic fracturing models as well.

Chapter 3 Microscale publication 1: Grain scale laboratory study

Numerical investigation of laboratory hydraulic fracturing tests in Pocheon granite

Farkas, M. P., Hofmann, H., Zimmermann, G., Zang, A., Zhuang, L., Kim, K. Y. (2022)

Manuscript is under review at Acta Geotechnica.

Numerical investigation of laboratory hydraulic fracturing tests in Pocheon granite

Márton Pál Farkas[a,c], Hannes Hofmann[a], Günter Zimmermann[a], Arno Zang[b,c], Li Zhuang[d], Kwang Yeom Kim[e]

[a] Section 4.8 Geoenergy, Helmholtz Centre Potsdam GFZ German Research Centre for Geosciences, Potsdam, Germany

[b] Section 2.6 Seismic Hazard and Risk Dynamics, Helmholtz Centre Potsdam GFZ German Research Centre for Geosciences, Potsdam, Germany

[c] Institute of Geosciences, University of Potsdam, Potsdam, Germany

[d] Korea Institute of Civil Engineering and Building Technology, Goyang, Republic of Korea

[e] Department of Energy & Resources Engineering, Korea Maritime & Ocean University, Busan, Republic of Korea

Abstract

This study investigates numerically several hydraulic fracturing experiments that were performed on intact cubic Pocheon granite samples applying different injection protocols. The goal of the laboratory experiments is to test the concept of cyclic soft stimulation which aims to increase permeability sustainably among others. The Irazu 2D numerical code is used to simulate explicitly coupled hydraulic diffusion and fracturing processes under bi-axial stress conditions. Using the hybrid finite-discrete element modelling approach, we test two injection schemes, constant-rate continuous injection and cyclic progressive injection on homogeneous and heterogeneous samples. Our study focuses on the connection between the geometry of hydraulic fractures, fracturing mechanisms and the permeability increase after injection. The models capture several characteristics of the hydraulic fracturing tests using a time-scaling approach. The numerical simulation results show good agreement with the laboratory experiments in terms of pressure evolution characteristics and fracture pattern. Based on the simulation results, the constant-rate continuous and cyclic progressive injection schemes applied to heterogeneous rock sample with pre-existing fractures show the highest hydraulic aperture increase, and thus permeability enhancement.

Keywords: Irazu software, fluid injection experiment, laboratory scale simulation, hydro-mechanical processes

Highlights:

- Application of time-scaling approach to FDEM simulation of hydro-mechanical processes during fluid injection experiments in crystalline rock sample in the laboratory.
- Constant-rate continuous injection and cyclic progressive injection schemes are studied in intact and fractured rock samples.

- Fracturing process during fluid injection is quantified in terms of fracture pattern, failure mechanisms, stress field deviation as well as hydraulic aperture.
- Constant-rate continuous and cyclic progressive injection schemes in heterogeneous rock sample with pre-existing fractures show the highest hydraulic aperture fold of increase. Cyclic progressive injection in intact samples results in the lowest hydraulic aperture increase.

3.1 Introduction

Hydraulic fracturing is used in several engineering applications, such as increasing production in unconventional oil and gas reservoirs, enhancing the permeability of geothermal systems by hydraulic stimulation as well as injecting large amounts of waste water (Zang and Stephansson, 2010). Although the method is applied routinely, the quantitative characterization of the underlying process is still subject of research due to its physical complexity and uncertainties. These include non-linear, complex hydro-mechanical processes at different spatio-temporal scales (Detournay, 2016).

One major technological challenge associated with productivity enhancement in geothermal reservoirs is the unsolicited induced seismicity. Thus, in the framework of the European Union's Horizon 2020 project DESTRESS, i.e. Demonstration of Soft Stimulation Treatments of Geothermal Reservoirs, optimal stimulation techniques were investigated which allow increasing reservoir transmissivity, maintaining the productivity while mitigating environmental impacts (Huenges et al., 2021).

Zang et al., 2013 introduced the concept of cyclic injection which may allow enhancing permeability and reducing the magnitude of seismic events. The concept has been demonstrated experimentally at different scales in crystalline rock in the recent years. At field (km) scale, demonstration at the Pohang enhanced geothermal system (EGS) site in South Korea is presented by Hofmann et al. (2019). At mine (dm) scale, progressive cyclic and pulse stimulation underground tests in crystalline rock mass are reported by Zang et al. (2017). The concept has been tested at laboratory (cm) scale in South Korean Pocheon granite samples in several studies (e.g. Zhuang et al., 2019; Zhuang et al., 2020; Zhuang and Zang, 2021). These studies focus on testing various injection schemes, the resulting hydraulic and acoustic emission (AE) responses as well as fracturing characteristics. The investigations were conducted on intact samples at constant room temperature and exhibited tensile dominated fracturing.

In order to extend and optimize the testing of the concept, one should gain a better understanding of the underlying processes during hydraulic fracturing. For optimization processes, numerical tools are used since these allow systematic investigations at relatively low costs compared to laboratory or field experiments. However, the modelling of these phenomena, especially at laboratory scale has been challenging (Lisjak et al., 2017). Concepts not implemented in the respective code can play a key role in the natural hydraulic fracturing process like cohesive crack tip zones as compared with stress singularity at crack tips modelled in linear elastic fracture mechanics (LEFM). Deviations from LEFM predictions have been reported at the laboratory and field scales in some cases, notably a larger fluid pressure and a shorter fracture length (Detournay, 2016). Liu (2021) contributes the additional energy dissipation compared with LEFM to the impact of the rough fracture process zone on viscous fluid flow. Second, these challenges include extensive computational requirements to reproduce the hydro-mechanical characteristics during pressurization and fracture propagation at the same time. One

promising tool to model fluid pressure-induced fracturing processes in porous brittle rocks at laboratory scale is the hybrid finite-discrete element method (FDEM) code Irazu 2D (Geomechanica, 2020).

The goal of this study is to develop a numerical model that enables studying the processes that may lead to the observations of the laboratory tests reported in Zhuang et al. (2020). We characterize the injection pressure history, the failure mechanisms, the fracture pattern including hydraulic apertures. The numerical model can be used to study the effect of different injection schemes on the fracturing processes and hydraulic aperture enhancement. Results can be used to make implications for the best injection strategy and selecting optimal rock fabric to induce a wide hydraulic fracture network with the possible highest hydraulic apertures, referred to as aperture fold of increase, suggested by Hofmann et al. (2016).

The paper is structured as follows. First, we give an overview of the laboratory tests. Second, we present the numerical model and the computational implementation of the fluid injection experiments. After that, we summarize the results for homogeneous and heterogeneous materials as well as for two injection schemes, the conventional constant-rate continuous injection and the novel cyclic progressive injection scheme. In the discussion section, we compare the simulation results between the modelling cases and against the laboratory experiments. Finally, we make implications for field injection strategies and point out the limitations of the numerical model.

3.2 Overview of laboratory tests

In this section we briefly summarize the concept, methodology and the key results of the laboratory hydraulic fracturing (HF) experiments including the testing conditions, the tested samples as well as pre- and post-test measures as reported by Zhuang et al. (2020).

The laboratory test conditions are summarized in Figure 1. For the experiments a true triaxial hydraulic fracturing test setup with cubic specimens is used. The testing apparatus allows a maximum applied stress of 10 MPa. The maximum injection pressure allowed by the servo-control hydraulic pump is 35 MPa. Possible AE events during the hydraulic fracturing tests are monitored using eight Nano30 sensors that are directly installed on the corners of the specimens. Two sensors were attached close to the corners of each lateral face of the sample, and none on the top or bottom.

The tested Pocheon granite is prepared as cubic specimen with an edge length of 100 mm. A concentric, cylindrical vertical borehole is drilled at the top of the specimen with a diameter of 5 mm and length of 70 mm. For details on the mechanical properties of the granite, we refer to Table 1 and Zhuang et al. (2019).

The cubic specimens are subjected to three principal stresses (Figure 1): 6 MPa representing the maximum horizontal stress (S_x), 4 MPa in vertical direction as intermediate principal stress (S_z) and 3 MPa as the minimum horizontal stress (S_y). Consequently, hydraulic fractures open up in the direction of minimum horizontal stress, and propagate in the plane spanned out by maximum horizontal stress and intermediate vertical stress.

In order to test the concept of cyclic soft stimulation, several different injection schemes were used in Zhuang et al. (2020). Among these tests, hydraulic fracturing tests denoted as "CCI1" and "CPI3" are the subject of this paper as these experiments are used for creating the reference numerical model. In the "CCI1" experiment (Figure 2a), water is injected at 100 mm^3/s (10^{-7} m^3/s) flow rate for 65 seconds until shut-in. Due to injection, pressure in the borehole increases until a peak level is reached known as the formation breakdown pressure (FBP). At this point a hydraulic fracture is induced which is followed by a pressure drop. The injection pressure decreased from the peak value of approx. 15 MPa to 10 MPa, interpreted as the pressure required for propagating the HF, the fracture propagation pressure (FPP). As the pumping is stopped, the pressure decreases from the FPP to the initial, static level of 0 MPa. AE time clusters were first detected before and after observing the FBP. The maximum AE amplitude of 84 dB was detected about 5 seconds after reaching the peak pressure (not shown in Figure 2a). More AE clusters were observed during the shut-in period. The recorded injection pressure and cumulative number of acoustic emission events are shown in Figure 2a.

For the cyclic progressive injection case "CPI3" (Figure 2b), injection rates are increased stepwise from 20 to 100 mm^3/s ("high" rate) with fixed injection rate of 10 mm^3/s ("low rate") between these steps. Based on the AE activity and pressure evolution, a hydraulic fracture is generated between the injection steps of 70 and 80 mm^3/s. However, the maximum AE amplitude of 74 dB was observed ahead of these steps, at the 50 mm^3/s step, before the failure inferred from the injection pressure curve (not shown in Figure 2b).

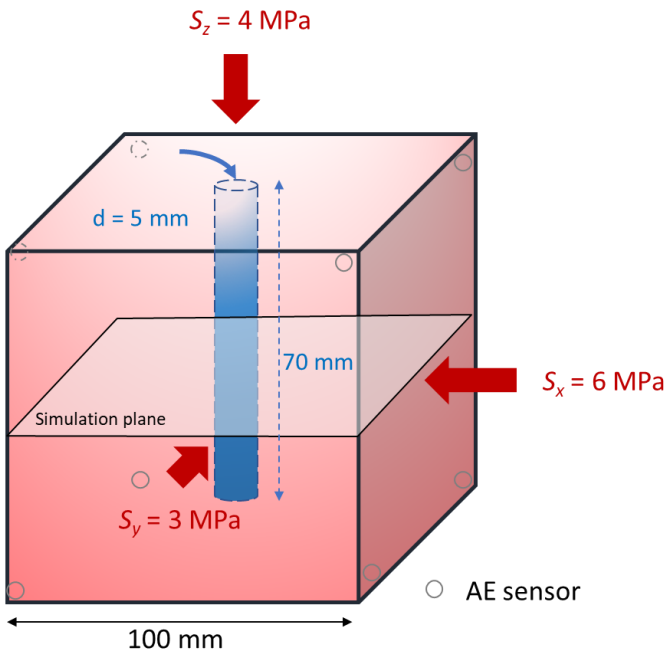

Figure 1: Schematic illustration of the laboratory hydraulic fracturing test and the horizontal cross-section representing the 2D numerical modelling domain where hydraulic fracture (HF) propagates (modified from Zhuang et al., 2020).

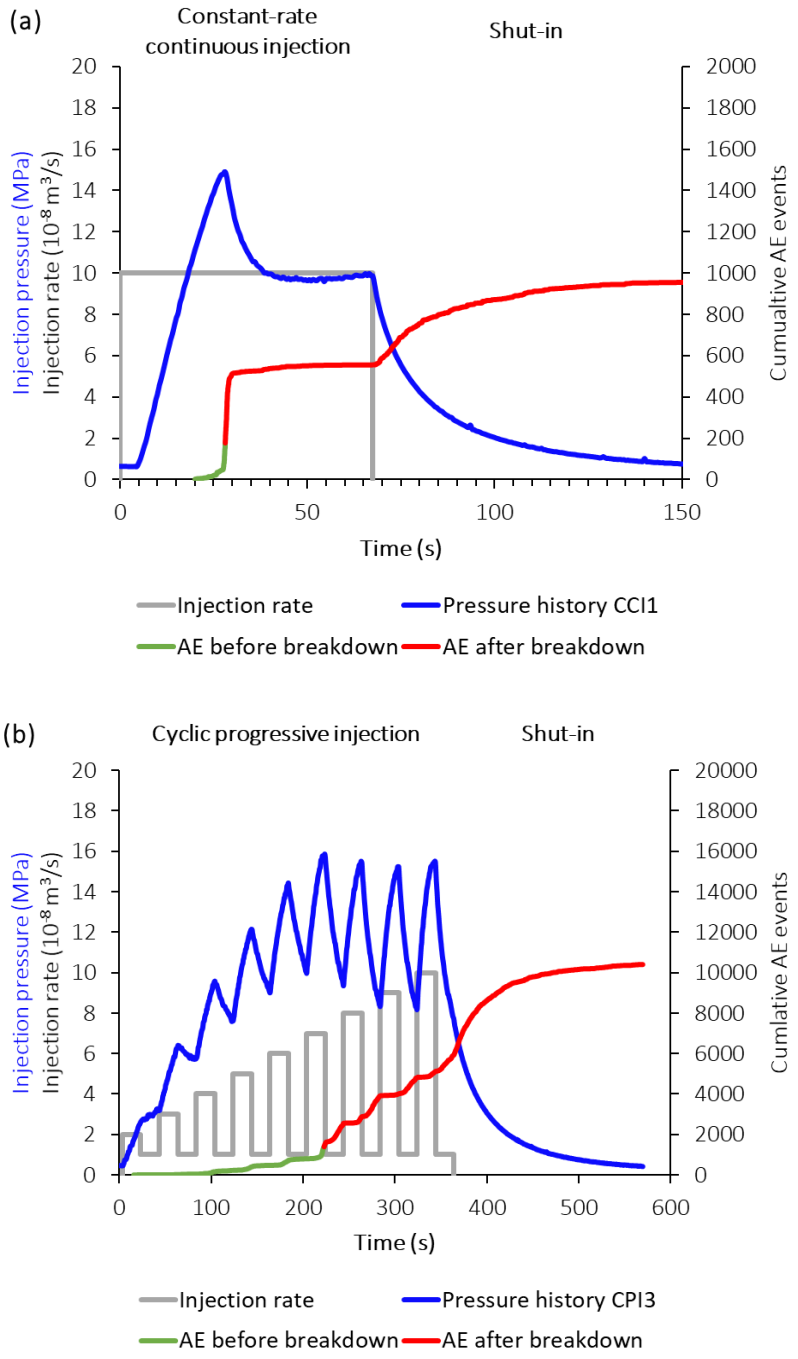

Figure 2: Injection pressure record (blue) with flow rate (grey) and cumulative number of acoustic emission events before (green) and after (red) breakdown during (a) constant injection rate test "CCI1" and (b) cyclic progressive injection rate test "CPI3" (modified from Zhuang et al., 2020)

3.3 Numerical Model

3.3.1 Irazu 2D Code

In this study, we use Irazu 2D version 4.0 (Geomechanica, 2020) that allows simulating hydro-mechanically coupled processes in low-porosity rock samples using discrete, triangular elements. In this section, the principles of the numerical code are briefly presented based on Geomechanica (2020) and

Lisjak et al. (2017). Since laboratory experiments were conducted at constant room temperature, thermal effects are not considered and solely hydro-mechanically coupled processes are simulated.

As for the mechanical part of the simulation, the discrete bodies can deform elastically, translate, rotate, interact, and fracture upon satisfying a given fracture criterion, hence producing new discrete bodies. The newly generated elements can further move, interact, deform, and crack. The code uses a combination of Finite Element Method (FEM) to calculate the deformation and to assess the failure criterion for fracturing and Discrete Element Method (DEM) for detecting new contacts and realizing translation, rotation, and interaction of discrete bodies. The method is referred to as Finite-Discrete Element Method (FDEM).

In the simulation loop, first connected triangular elements are identified for the mechanical calculations. Then, the nodal forces associated with interaction, deformation, and fracturing, due to internal or external loading are calculated. Using these forces, the equation of motion is integrated to update the new nodal coordinates. This loop is repeated until a pre-defined number of mechanical time integration steps.

The generation and propagation of explicit fractures are simulated in Irazu using the theory of nonlinear fracture mechanics (NLFM) (Barenblatt, 1962; Dugdale, 1960). According to this concept, at the tip of a crack, an area characterized by non-linear behaviour, called the fracture process zone (FPZ), begins to form (Zang et al., 2000). In brittle rock materials, the FPZ is affected by interlocking and microcracking. In Irazu, an analogous FPZ behaviour is simulated ahead of crack tips subjected to loading. The load carrying capacity of the FPZ is approximated by triangular cohesive crack elements. Whether process zone cracks are mode I, mode II or mixed mode, depends on the boundary conditions of fracture growth (Lisjak et al., 2017).

The constitutive behaviour of a crack element is defined in terms of the evolution of the bonding stresses. The relative displacement in the normal direction, o, depends on the effective normal stress, σ, and that in the tangential direction, s, is the function of shear stress, τ (Figure 3).

Under Mode I loading (Figure 3a), the failure of a crack element is a function of its tensile strength, f_t, and the Mode I fracture energy, G_I. The dependence of f_t on G_I is implemented as a heuristic function defined below. At Mode I loading, the accumulating stress is calculated as:

$$\sigma = \left[\frac{2o}{o_p} - \left(\frac{o}{o_p}\right)^2\right] f_t \tag{1}$$

$$o_p = \frac{2hf_t}{p_f} \tag{2}$$

where, o_p is the peak crack element opening, h is the edge length of the triangular element and p_f is the fracture penalty. Under Mode II loading (Figure 3b), the constitutive response is governed by the shear strength, f_s, and the Mode II fracture energy, G_{II}. The dependence of f_s on G_{II} is implemented as a heuristic function defined below. At Mode II loading, the accumulating stress is calculated as:

$$\tau = \left[\frac{2s}{s_p} - \left(\frac{s}{s_p}\right)^2\right] f_s \tag{3}$$

$$s_p = \frac{2hf_s}{p_f} \tag{4}$$

where, s_p is the peak crack element slip. The shear strength, f_s, is defined in terms of the Mohr-Coulomb failure criterion:

$$f_s = C + \sigma_n \tan\varphi \tag{5}$$

where, C is the cohesion, σ_n is the normal stress acting across the crack element and φ is the internal friction angle.

The softening behavior, i.e. post-peak gradual reduction of σ and τ, acting on crack elements are governed by the general form proposed by Munjiza et al. (1999):

$$\sigma = f(D) f_t \tag{6}$$

$$\tau = f(D) f_s \tag{7}$$

where $f(D)$ is a heuristic function approximating the shape of the experimental stress-displacement curves of Evans and Marathe (1968):

$$f(D) = \left[1 - \frac{a+b-1}{a+b} e^{D\frac{a+cb}{(a+b)(1-a-b)}}\right][a(1-D) + b(1-D)^c] \tag{8}$$

where, a=0.63, b=1.8 and c=6.0 are empirical curve fitting parameters, and D is the damage coefficient with a value between 0 for intact and 1 for damaged crack element. The value of D for a given crack element is defined as depending on the mode of displacement. For mode I displacement, D is calculated as

$$\text{Mode I: } D = \frac{o - o_p}{o_r - o_p} \tag{9}$$

$$o_r = o_p + \frac{3G_I}{f_t} \tag{10}$$

where, o_r is the residual crack element opening.

For mode II displacement, D is defined as

$$\text{Mode II: } D = \frac{s - s_p}{s_r - s_p} \tag{11}$$

$$s_r = s_p + \frac{3G_{II}}{f_s} \tag{12}$$

where, s_r is the residual crack element slip. Based on this analogy, the residual shear strength of a crack element, f_r, is calculated as

$$f_r = \sigma_n \tan\varphi_r \tag{13}$$

where, φ_r is the residual friction angle.

For mixed Mode I-II fracturing (Figure 3c), an elliptical coupling relationship is employed between crack opening and slip:

$$\text{Mode I-II: } D = \sqrt{\left(\frac{o - o_p}{o_r - o_p}\right)^2 + \left(\frac{s - s_p}{s_r - s_p}\right)^2} \tag{14}$$

There are two rate-dependent phenomena implemented in Irazu. The first one is related to the viscous damping formulation: viscous damping tensor is computed based on the strain rate tensor of an element. Since quasi-static process with critical viscous damping is modelled (viscous damping factor is equal to one in Table 1), thus its effect can be neglected. The second one is the strain-rate dependency that emerges from fracturing simulations. Even though the fracture model itself does not have any rate dependency, it can be shown that in general the emergent strength of the rock increases with higher loading/strain rate (Tatone and Grasselli, 2015).

For more details on the implementation of the mechanical processes, the reader is referred to Geomechanica (2020).

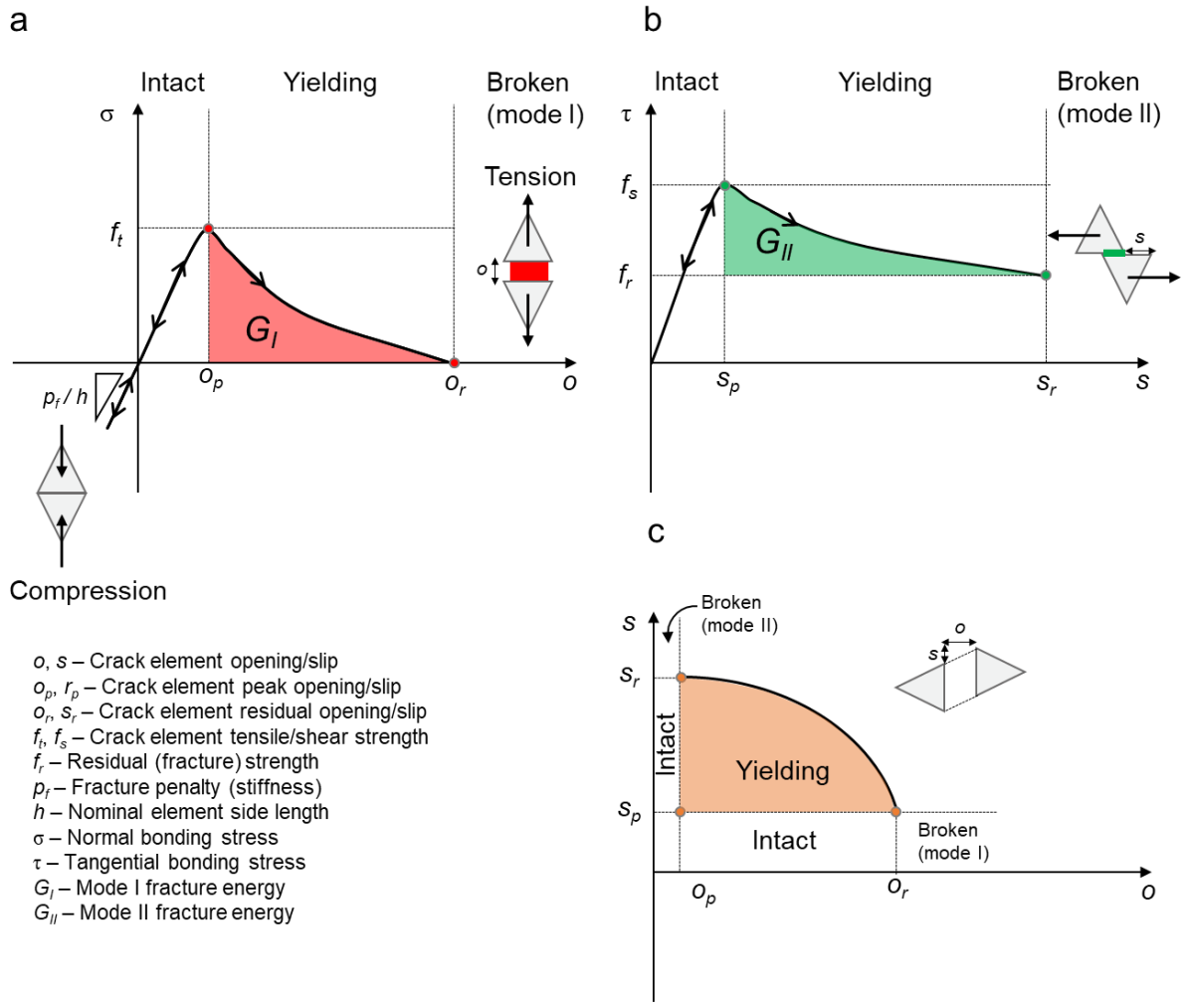

Figure 3: Numerical constitutive behaviour of the crack elements. (a) Normal bonding stress versus crack opening for pure compressive/tensile loading and failure (Mode I); (b) shear bonding stress versus crack slip for pure shear loading and failure (Mode II); (c) elliptical coupling relationship between fracture opening and slip for mixed-Mode fracturing. Arrows denote loading, unloading, and reloading paths. The area under the curves in (a) and (b) is defined by G_I and G_{II}, respectively (modified from Lisjak et al., 2017).

The hydraulic part of the simulation employs a hydraulic solver which assumes that fluid flows through a channel network generated from the same triangular mesh used for the mechanical calculations (Figure 4a). The channels are defined at the interfaces of connected triangular finite elements. These flow channels connect virtual cavities or pores corresponding to the nodes of the original triangular

mesh (blue dots in Figure 4a). Each cavity behaves as a fluid reservoir with uniform pressure and volume.

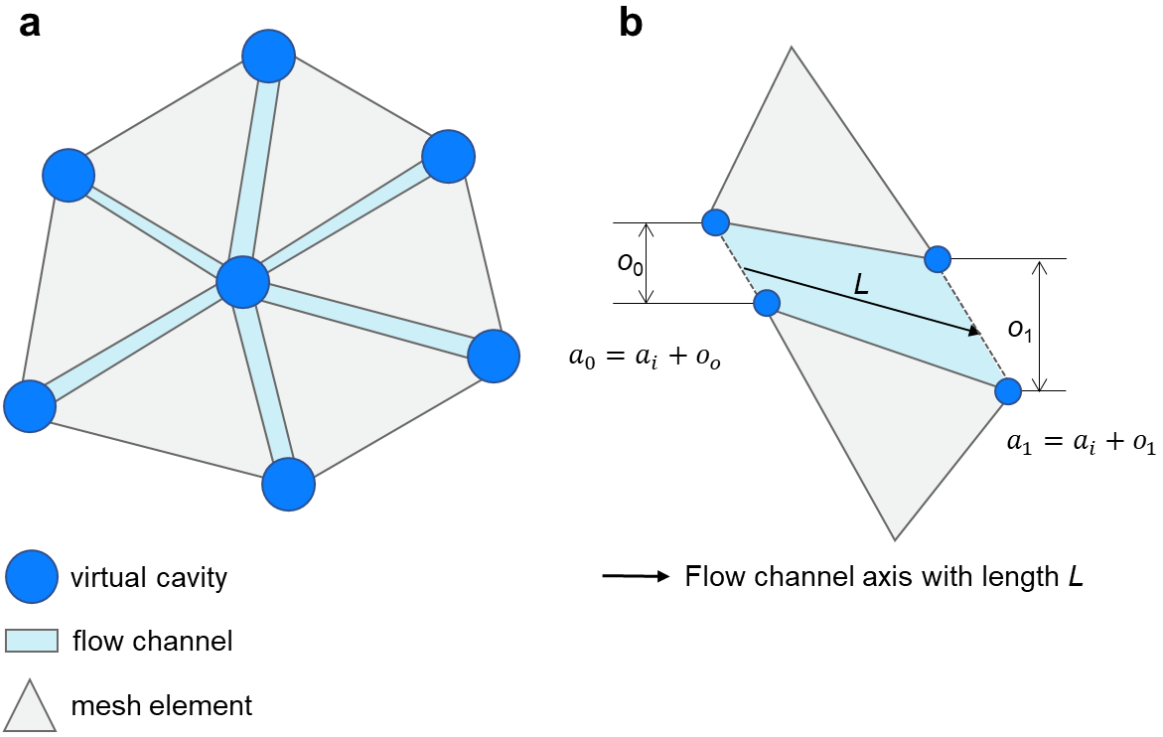

Figure 47: Computational framework adopted in the fluid flow solver using finite element mesh. Initial hydraulic aperture, a_i, are assigned to virtual cavities. (a): network of rectangular flow channels connecting two virtual cavities before rock deformation. (b): illustration of hydro-mechanical coupling in terms of linearly-varying hydraulic aperture at two end-points of the flow channel, a_0 and a_1 due to mechanical deformation, o_0 and o_1 (modified from Geomechanica, 2020).

The volume of the *j*th flow channel is defined as

$$V_j = L_j \frac{a_0 + a_1}{2} \tag{15}$$

where L_j is the length of the flow channel, and a_0, and a_1 are the hydraulic apertures at two end-points of the channel (Figure 4b).

Fluid volume is stored at cavity, V_c, that is derived from the volume of the surrounding flow channels as

$$V_c = \sum_j \frac{V_j}{2} \tag{16}$$

The explicit formulation of fluid flow allows straightforward coupling with the mechanical solver and parallelization. During each hydraulic time step, the following main steps are sequentially performed:

1. Channel hydraulic aperture and cavity volume are computed;
2. Darcy's law and parallel-plate flow model at each channel are applied;
3. The hydraulic continuity equation at each cavity is applied; and
4. Fluid pressure field is calculated.

During the last step, the fluid pressure in a cavity is determined by considering the change in pressure using a linear fluid compressibility model:

$$P_t = P_{t-1} + K_f \frac{\Delta m}{\rho_f V_t} \quad (17)$$

where P_t and P_{t-1} are the fluid pressure at time step t and $t-1$, respectively, V_t is the cavity volume at time step t, Δm is the change in fluid mass, K_f is the fluid bulk modulus and ρ_f is the fluid density.

The hydro-mechanical coupling is realized via a two-way explicit coupling approach, i.e. alternation between the mechanical and the hydraulic solvers while stepping forward in time (Figure 5a). Consequently, the mechanical calculations are affected by inter-element fluid pressure; and the flow calculations are affected by the variation of hydraulic aperture between finite elements due to the rock deformation and fracturing process.

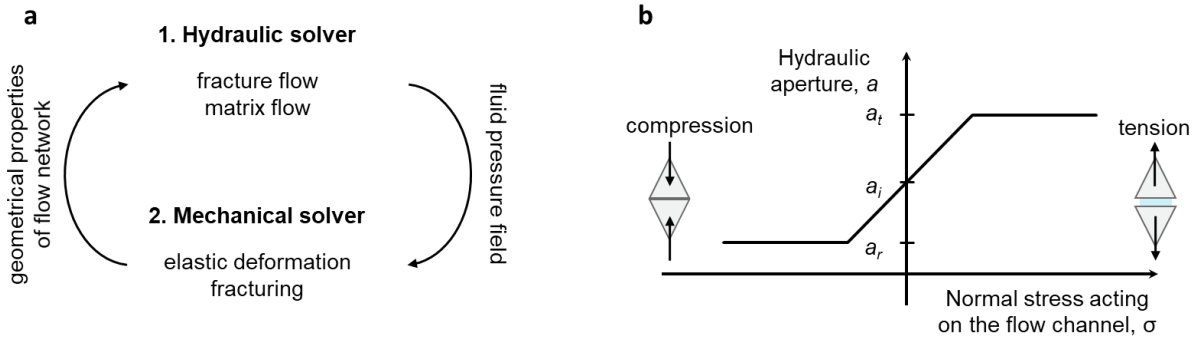

Figure 5: (a) Explicit two-way hydro-mechanical coupling in the Irazu 2D model. (b) Relationship between hydraulic aperture and normal stress acting across the flow channel. Hydraulic aperture parameters are threshold (a_t), initial (a_i) and residual aperture (a_r) (modified from Geomechanica, 2020).

Figure 5b illustrates the hydraulic aperture as a function of effective normal stress acting on the flow channel. The hydraulic aperture is assumed to have lower (residual) and upper bounds (threshold), a_r and a_t, beyond which additional mechanical closing (compression) and opening (tension) have no effect. A linear relationship between aperture and normal stress is implemented. These definitions are applied for the sake of calculation simplicity. The initial hydraulic aperture, a_i, represents the aperture before any mechanical deformation (Geomechanica, 2020).

Two time-discretization schemes are defined in the Irazu 2D code to maintain numerical stability during mechanical and hydraulic time-stepping. The coupling frequencies are defined in terms of the number of mechanical and hydraulic time steps for which each solver is run before switching to the other one.

Stability of the mechanical solver is controlled by the mechanical time step size for the integration of equations of motion of the discretized system. We refer to Lisjak et al., 2017 for more details on the time marching approach of the explicit time integration scheme. The stability of the hydraulic solver is secured by controlling the size of the hydraulic time step (Δt_h) as (Geomechanica, 2020),

$$\Delta t_h \leq min_c \left(\frac{V_c}{\frac{K_f}{\rho_f} \sum_j \left(\frac{(a_0 a_1)^2}{6 \nu_f (a_0 + a_1) L_j} \right)} \right) = min_c \left(\frac{V_c}{\frac{K_f}{\rho_f} \sum_j \left(\frac{1}{R_j} \right)} \right) \quad (18)$$

with *c* and *j* indexing over all the cavities and flow channels, respectively. K_f is the fluid bulk modulus, ρ_f is fluid density. υ_f is fluid kinematic viscosity and *R* is the flow resistance. Since mechanical time step is generally smaller than the hydraulic time step (nanoseconds versus milliseconds), thus, computational time is governed by the mechanical time step size. For the same reason, 15 mechanical cycles are calculated for each hydraulic step.

3.3.2 Numerical simulation of constant-rate injection test in Pocheon granite sample

Geometry and boundary conditions

Pocheon granite rock samples are represented as a set of discrete triangular mesh elements in a horizontal cross-section spanned by the minimum and maximum principal stress with a side length of 100 mm. The distinct bodies are generated using the Delaunay triangulation method in the open-source mesh generation software, Gmsh version 4.4.1. Two mesh generation areas are defined at the center of the rectangular modelling domain, where the inner one has an edge length of 60 mm parallel to the y-axis. (Figure 6a). In the inner mesh generation domain, the average mesh edge length is 0.75 mm; in the outer one, that length is 1.5 mm. The inner, finer mesh aims at capturing hydraulic fracture initiation and fluid flow at the center of the model (Figure 6b). The outer, coarse mesh network serves as gradual size transition from finer to coarse mesh to maintain calculation times within practical limits. The numerical model contains 35614 elements with 17981 nodes.

Two types of mechanical boundary conditions are defined in the numerical model. First, the maximum and minimum principal stresses act perpendicular to the sample boundaries, i.e. $S_x=S_H=6$ MPa, and $S_y=S_h=3$ MPa. The stresses are acting upon the boundary elements in the respective directions. The second, mechanical boundary condition pins the boundary nodes, i.e. no displacement of those is allowed. The combination of the two boundary conditions mimics the 2D section of the true-triaxial stress loading conditions and thus allows simplification of the numerical model.

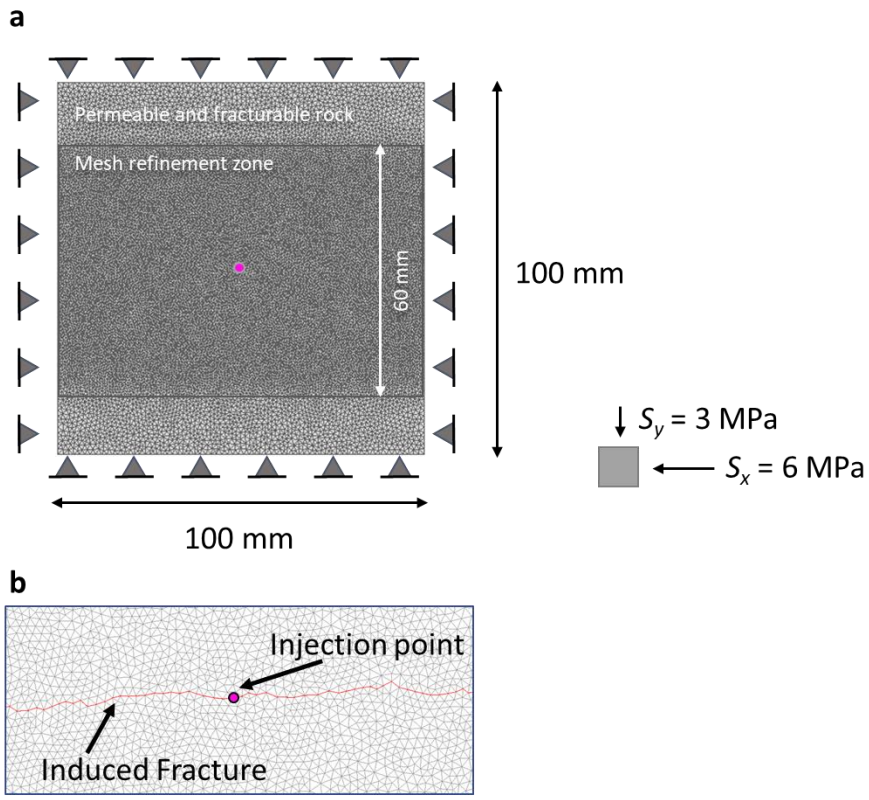

Figure 6: (a) Geometry and boundary conditions of the laboratory-scale hydraulic fracturing numerical model. The average mesh element size in the refined zone is 0.75 mm, in the outer zone that equals 1.5 mm. (b): illustration of the hydraulic fracture along the edges of the triangular mesh elements.

Material parameters and injection schemes

Two types of mechanical models and injection schemes are defined resulting in four modelling cases in total (Figure 7). The model A is a homogeneous model from a mechanical point of view, and in model B a discrete fracture network (DFN) is added. In model B, the DFN is defined as a set of pre-existing joints with a length of 2.80 mm, fracture spacing of 1.85 mm as well as orientation of -39°, -11° and 86° measured counter-clockwise from the horizontal axis based on measured parameters reported by Park (2015). In this paper, joints share the same initial hydraulic properties as the rock mass and zero tensile strength is assigned to them. Thus, these joints can only sustain shear stresses characterized by residual friction. Consequently, joints are defined to explore shear-slip induced failure in the rock sample. It must be noted that no joints are generated in an area of 10 x 10 mm2 around the injection point to enable distinction between pure hydraulic fracturing and shear-slip induced failure of pre-existing joints at the beginning of the injection.

As for the injection schemes, in case 1, pumping water at constant flow rate of 100 mm3/s is simulated as fluid injection into a single cavity (point) located at the center of the model based on the laboratory test "CCI1" reported by Zhuang et al. (2020). The second hydraulic injection scheme is based on the concept of cyclic soft stimulation (CSS). A cyclic progressive injection (CPI) scheme is applied with an injection rate increased by a given flow rate in each step until a target value of 100 mm3/s is

reached based on the laboratory test "CPI3" reported by Zhuang et al. (2020). The duration of each step is determined using the approach described below.

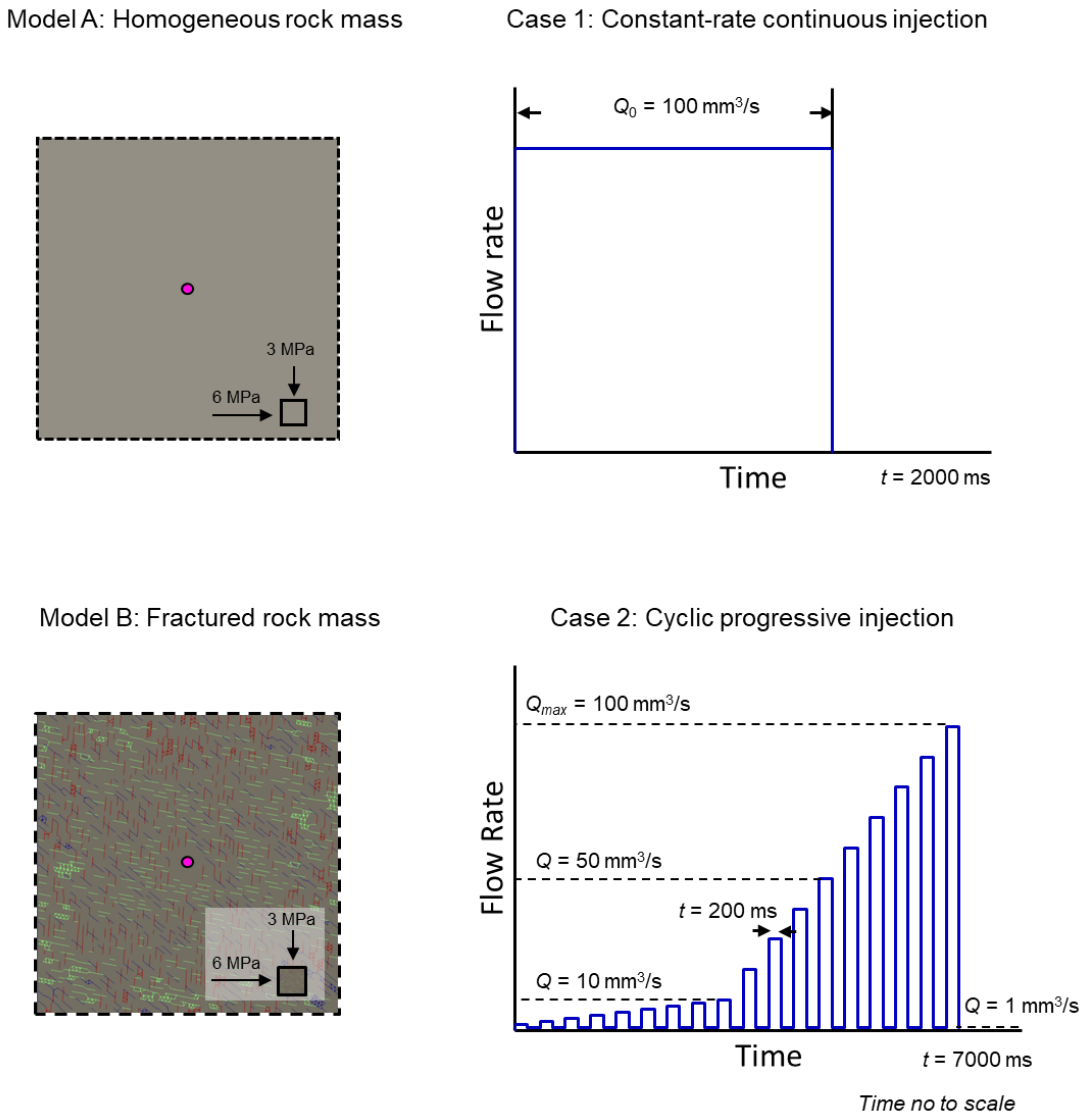

Figure 7: Mechanical models (left column) and injection cases (right column) tested in the numerical study. Injection point is represented by solid purple circle.

Table 1: Material and hydraulic parameters of the numerical model and the Pocheon granite samples. Discrete fracture network properties are based on Zhuang et al. (2019) and Park (2015), respectively. The number of laboratory tests are indicated as N.

Type	**Parameter**	**Model Value**	**Laboratory Average**
Elastic properties	Density, ρ (kg/m^3)	2609	2609
	Young's modulus, E (Pa)	5.75×10^{10}	5.75×10^{10} (N = 5)
	Poisson's ratio, ν (-)	0.26	0.26 (N = 5)
Strength properties	Coefficient of internal friction, φ (-)	0.6	-
	Cohesion, C (Pa)	2.5×10^7	-
	Tensile strength, f_t (Pa)	10.5×10^6	7.5×10^6 (BTS, N=10)
	Mode I fracture energy, G_{Ic} (N/m)	0.9	-
	Mode II fracture energy, G_{IIc} (N/m)	9	-
	Mode I fracture toughness, K_{Ic} (MPa× m$^{1/2}$)	-	1.048 (N = 5)
Discrete fracture network properties	Fracture number, N_f	80	80
	Fracture length, l_f (mm)	2.80	2.80 (N = 37)
	Fracture spacing, s_f (mm)	1.85	1.85 (N = 104)
	Fracture orientation, θ_f (°, measured counter-clockwise from horizontal axis)	-39, -11, 86	-
	Tensile strength, f_{tr}	0 (broken)	-
	Residual coefficient of internal friction, φ_r	0.5	0.5±0.01 (N = 2)
Numerical properties	Viscous damping factor (-)	1	-
	Fracture penalty, p_f (Pa)	5.7×10^{11}	-
	Normal penalty, p_n (Pa × mm)	5.7×10^{11}	-
	Tangential penalty, p_t (Pa/mm)	5.7×10^{11}	-
Hydraulic properties	Fluid kinematic viscosity, υ_f (m^2/s)	10^{-6}	10^{-6}
	Bulk modulus, K_f (Pa)	2.2×10^9	2.2×10^9
	Fluid density, ρ_f (kg/m^3)	1000	1000
	Permeability (m^2)	10^{-17}	10^{-17} (N = 1)
	Porosity (%)	0.66	0.66 (N = 1)
	Residual channel aperture, a_r (m)	3.3×10^{-6}	-
	Initial channel aperture, a_i (m)	3.3×10^{-6}	-
	Threshold channel aperture, a_t (m)	3.3×10^{-5}	-

The modelling time scale of the base case numerical model, A1, is determined via the laboratory scaling approach proposed by Bunger et al. (2005) in order to ensure comparison of numerical models against experimental results at reasonable computational costs. According to them, there are several time scales during a laboratory hydraulic fracturing experiment that characterize the induction and propagation of hydraulic fractures referred to as limiting fracture behaviors (Detournay, 2016). These limiting regimes are associated with concurring energy dissipation mechanisms, that is, toughness and viscosity, as well as fluid volume conservation, i.e. storage and leak-off. Another time scale can be also applied for early time processes associated with fluid and pumping system compressibility and phenomena involving interaction of the crack with the wellbore. An additional timescale is associated with the finite lengths of experimental specimens meaning that at some point in time the fracture has no space to extend.

Due to practical reasons, we neglect the period linked with early wellbore compressibility and fracturing effects. Thus, we focus on the time scale that approximates the duration of the fracturing experiment. The estimated maximum time expected for the hydraulic fracturing test, t_e, can be defined using the plain strain modulus, E', and stress intensity factor, K' (Bunger et al., 2005):

$$t_e = \frac{H^{\frac{5}{2}} K'}{Q_0 E'} \tag{19}$$

$$K' = 4\left(\frac{2}{\pi}\right)^{\frac{1}{2}} K_{Ic} \tag{20}$$

$$E' = \frac{E}{1-\upsilon^2} \tag{21}$$

where H is the distance to the critical specimen boundary, i.e. where interaction between the induced fracture and the specimen is expected, Q_0 is the (constant) injection rate, K_{Ic} is the mode I (tensional) fracture toughness, E is the Young's modulus, and υ is the Poisson's ratio. Note that H here equals to the sample length since a bi-wing hydraulic fracture is simulated in the numerical model.

Using the boundary conditions presented above, for injection rate Q_0 = 100 mm^3/s and mechanical parameters listed in Table 1, t_e gives approx. 1500 ms. This agrees with the recorded characteristics of the lab test "CCI1", where instantaneous pressure drop and associated increased acoustic emission activity are observed within few seconds (Figure 2a). Thus, in the homogeneous model and heterogeneous model cases with constant-rate continuous injection (CCI), cases A1 and B1, respectively, fluid is injected at 100 mm^3/s for 2000 ms.

Based on Detournay (2016), one can calculate the characteristic time scale for given limiting regimes, i.e. for toughness- and viscosity-dominated fracture propagation, here referred to as MK- and OM-transitions, respectively. For this, we use the parameters listed in Table 1 and t_e ~ 1500 ms. The timescale for the MK-transition is t_{mk}<1 ms and that for OM-transition is t_{om}~1500 ms for this set of parameters. Thus, the hydraulic fracture should propagate in the toughness-dominated regime.

Consequently, we assume toughness-dominated hydraulic fracture propagation with neglectable leak-off due to the very low intrinsic permeability of the granite samples.

The simulated duration of the CPI tests is determined based on the characteristic fracturing time of the "CCI" lab test and the step-wise manner of increasing the injection flow rate from lower levels to the desired flow rate of 100 mm^3/s. The low steps, as base loading steps, are kept at 1 mm^3/s, while the high steps are first increased from 2 to 10 in 1 mm^3/s incremental steps, then from 10 to 100 mm^3/s in 10 mm^3/s increments. Each step lasts for 200 ms. Such scheme ensures keeping the injection pressure below the formation breakdown pressure in the initial injection steps. Consequently, modelling cases A2 and B2 last for 7000 ms.

Prior to simulating fluid-injection into the rock sample, the mechanical and hydraulic microscopic properties of the numerical model are calibrated following the procedures described in Tatone and Grasselli (2015) and Lisjak et al. (2017), respectively. The mechanical calibration is a trial-and-error approach where a combination of uniaxial compression and Brazilian tensile strength tests are conducted to match the mesh tensile and shear fracture penalty, energy as well as toughness parameters against the laboratory elastic and strength parameters. The desired macroscopic permeability is obtained by assigning an initial hydraulic aperture to the flow channels (a_i) and calibrating it via simple permeability test simulations. The calibrated rock material parameters, including elastic, strength and hydraulic properties are summarized in Table 1. The cavities are initially saturated to mimic laboratory conditions. The treatment begins at the onset of injection and the computation ends at the time of injection stop.

The numerical model parameters give a mechanical time step of 1.7×10^{-9} s. First, 200,000 mechanical time steps are repeated to initialize the anisotropic stress field. Since the time scale between mechanical and hydraulic processes are different, e.g. nanoseconds versus milliseconds, respectively, 20 mechanical steps are performed for each hydraulic step in the simulation. Model runtime lasts approx. three weeks on a workstation equipped with Intel Xeon CPU E5 processor unit, 128 GB of RAM and Nvidia Quadro P4000 GPU using parallel computation.

We must point out that no fluid-induced microseismicity is modelled. Instead, we directly analyse the failure mechanism and the spatial distribution of the microcracks.

3.4 Results

3.4.1 Summary of main simulation results

The four modelling cases and the respective results are summarized in Table 2. In each simulation case, the effects of fluid injection on hydro-mechanical fracturing processes is investigated. These processes are characterized via the formation breakdown pressure (FBP), the average pressure during fracture propagation (fracture propagation pressure, FPP), the maximum hydraulic aperture and the respective aperture fold of increase as well as the macroscopic total crack length. The aperture fold of increase is the ratio of maximum hydraulic aperture of the microcracks versus the initial crack aperture. Based on

the hydraulic calibration procedure described in Lisjak et al. 2017, this corresponds to the permeability increase of the rock sample. The effect of injected volume is investigated as well. This is an advantage compared to the laboratory experiments, where the injected fluid did not accumulate in the saturated sample due to drainage along the sample boundary surfaces (Zhuang et al., 2020). The total crack length is defined as the temporal sum of microcrack lengths in the sample.

The presentation of the simulation results is structured in the following way. The points of interest are discussed separately for homogeneous and heterogeneous rock samples. For each sample, the effect of injection schemes is investigated. First, the evolution of fluid injection pressure and the cumulative injected volume at the injection point as well as the cumulative crack length of the rock sample are discussed. This is followed by the characterization of the hydraulic fracture initiation and propagation as well as its interaction with pre-existing fractures in the case of heterogeneous samples. Lastly, elastic stress transfer effects due to direct pore pressure effect and stress transfer across the triangular elements are analysed in two ways. In one way, the principal stress trajectories (orientations) are compared against the hydraulic fracture pattern and fluid pressure distribution across the sample at the end of the simulation. In another way, the principal stress magnitudes and fluid pressure profiles are analysed in two directions: in the direction of anticipated hydraulic fracture propagation, i.e. parallel to maximum principal stress, denoted as X-axis and perpendicular to that, termed as Y-axis. The two profiles intersect at the injection point, and they are studied shortly after hydraulic fracture initiation and at the end of simulation. We note that fluid pressure has positive value, while tensional and compressional stresses are positive and negative, respectively.

Table 2: Summary of modelling cases, injection parameters and test results and their comparison against laboratory experimental results reported by Zhuang et al. (2020) and Zhuang et al. (2021).

Simulation results							
Case	**Injection rates (mm^3/s)***	**Injected volume (mm^3); Duration (s)****	**FBP (MPa)**	**Average FPP (MPa)**	**Max hydraulic aperture (μm)*****	**Aperture increase (FOI)********	**Total crack length (mm)**
Homogeneous, CCI (A1)	100	200; 2	14.9	5.5	8	2.4	70
Homogeneous, CPI (A2)	Part 1): High steps: 2 to 9, Low steps: 1 Part 2): High steps: 10 to 100, Low steps: 1	120; 7	15.4	5.6	7.2	2.1	75
Heterogeneous, CCI (B1)	100	200; 2	14.5	5.8	20	6	162
Heterogeneous, CPI (B2)	Part 1): High steps: 2 to 9, Low steps: 1 Part 2): High steps: 10 to 100, Low steps: 1	120; 7	15.5	5.8	20	6	96
Laboratory experiment results							
Lab CCI1	100	6300; 65	14.91	10	18.1	2.3	-
Lab CPI3	High steps: 20 to 100, Low steps: 10	12600; 365	15.86	-	8.6	1.3	-

* High steps: temporary maximum level of injection rate, low steps: base flow rate between high steps

**Duration of tests until shut-in

*** Laboratory max hydraulic aperture is determined from mechanical aperture measured on CT-scans after injection treatment reported by Zhuang et al. 2021

**** Laboratory aperture fold of increase is based on post-fracturing injectivity measurement

3.4.2 Investigation of injection schemes on homogeneous samples

The evolution of fluid injection pressure at the injection point, the cumulative injected volume as well as cumulative crack length due to constant-rate continuous injection in homogeneous rock sample are shown in Figure 8. In this modelling case A1, the fluid pressure reaches the fracture breakdown pressure (FBP) of approx. 15 MPa within milliseconds during the initial pressurization phase. The pressurization phase is followed by a pressure drop to 5 MPa after 150 ms (shortly after state "a" in Figure 8). This pressure level corresponds to the fracture propagation pressure (FPP) around which the pressure undulates until the injection stops at 2000 ms (state "b" in Figure 8).

The cumulative crack length, here the macroscopic length of the hydraulic fracture evolves initially at the same rate as the cumulative injected volume until approx. 800 ms. This is associated with the symmetrical propagation of the hydraulic fracture. Due to intrinsic mesh directional effect, asymmetric fracture propagation is sustained from this point until 1650 ms. Moreover, the injection pressure and the number of cracks remain constant from 1300 ms for 350 ms. This can be explained by fluid pressure accumulation within the hydrofrac until fluid pressure is high enough for extension in the shorter fracture direction.

At the end of the simulation, a symmetrical hydraulic fracture of 70 mm is generated after injection of 200 mm^3 fluid (Figure 8, Figure 9 and Table 2). The aperture fold of increase is 2.4 with a maximum hydraulic aperture of 8 µm.

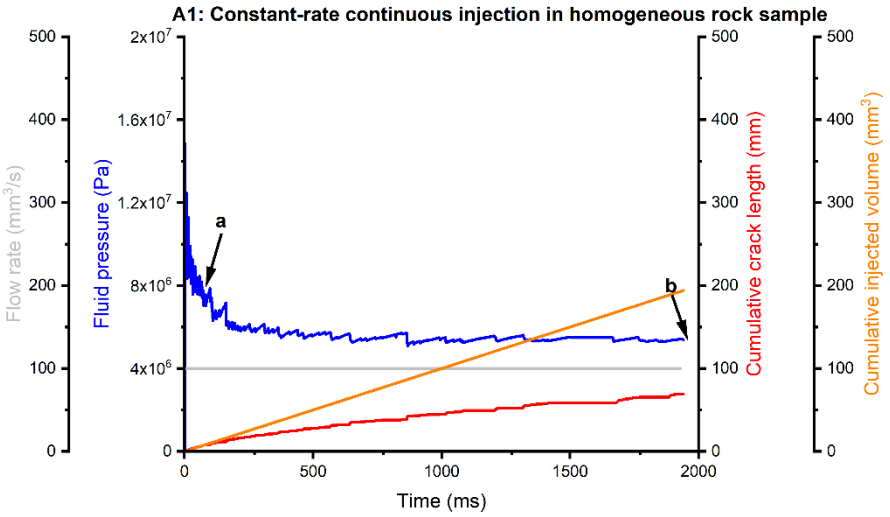

Figure 8: Evolution of fluid pressure, cumulative crack length and injected volume at the injection point due to constant-rate continuous fluid injection in homogeneous rock sample. Pointers a and b refer to distinct states of the simulation shown in Figure 9 and Figure 10.

The generated fracture pattern, fluid pressure distribution and principal stress directions are shown in Figure 9. Due to the homogeneous nature of the rock sample, only microcracks with mode I are induced that are oriented parallel to the direction of the maximum principal stress. According to Figure 9, the fluid pressure accumulates only in the hydraulic fracture. This is associated with the low

permeability of the rock mass which limits leak-off into intact rock. As for the principal stress trajectories, the orientation of the maximum principal stress is deviated by 25° around the fracture tips. The deviation angle decreases with increasing distance from the hydraulic fracture towards sample boundaries in the direction of the minimum principal stress. Around the injection point, the principal stress trajectories are rotated back to the directions acting at the sample boundaries.

The relationship between fracture pattern, fluid pressure distribution and principal stress magnitudes for the base case model A1 at two stages of the simulated injection experiment is illustrated in Figure 10. Shortly after reaching the FBP, the principal stress magnitudes and fluid pressure distribution reveal the extent of newly induced hydraulic fracture (Figure 10a). The minimum and maximum principal stresses are both compressive within the hydraulic fracture with a length of 10 mm along the X-axis, parallel to the direction of maximum principal stress. At both fracture tips, concentration of tensional minimum principal stress is observed preceding the generation of new microcracks and so the extension of the hydraulic fracture. Few millimeters away from the fracture tips, the magnitudes of the principal stresses agree with the boundary conditions, i.e. i.e. S_x=S_H=6 MPa, and S_y=S_h=3 MPa. Consequently, both the direct pore pressure effect and the elastic stress transfer are limited in this direction. In the Y-axis, parallel to the acting minimum principal stress, elevation of principal stresses in compression due to fluid pressure increase is observed. The stress alteration effect continuously diminishes with increasing distance from the injection point over 20 mm, which corresponds to the double distance of the hydraulic fracture length. Elevated fluid pressure dissipates a few mm away from the injection point due to lack of leak-off into the intact rock mass.

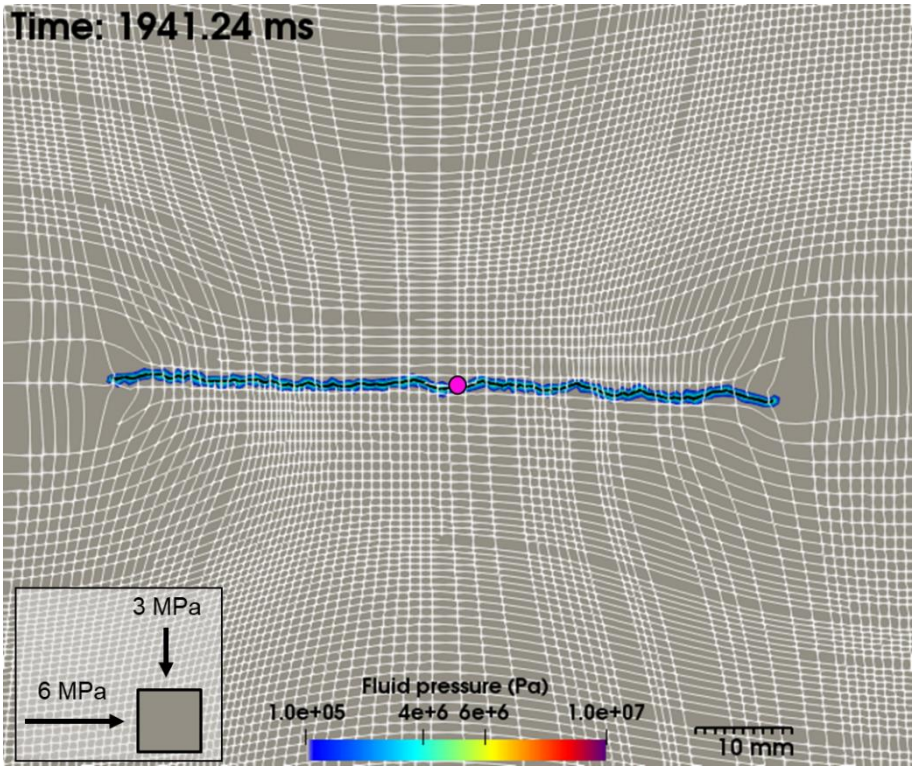

Figure 9: Hydraulic fracture pattern (black line), fluid pressure distribution (colour bar) and principal stress trajectories (white lines) in the granitic rock sample at the end of constant-rate continuous fluid injection in the homogeneous rock sample (Base case model A1).

At the end of the fluid injection experiment (Figure 10b), the fluid pressure along the hydraulic fracture shows a perturbation around 5 MPa which can be explained by the random orientation of the triangular element edges. However, the principal stress magnitudes as well as the minimum principal stress concentrations show the symmetrical location of the hydraulic fracture tips. Although the hydraulic fracture tips are relatively close to the sample boundaries, the maximum principal stress magnitudes are slightly affected there. In the perpendicular direction, however, both principal stress magnitudes are elevated along the profile. This is an indication for elastic stress transfer through the sample perpendicular to the hydraulic fracture caused by hydraulic fracture opening.

A1: Constant-rate continuous injection in homogeneous rock sample

a: Shortly after induction of hydraulic fracture

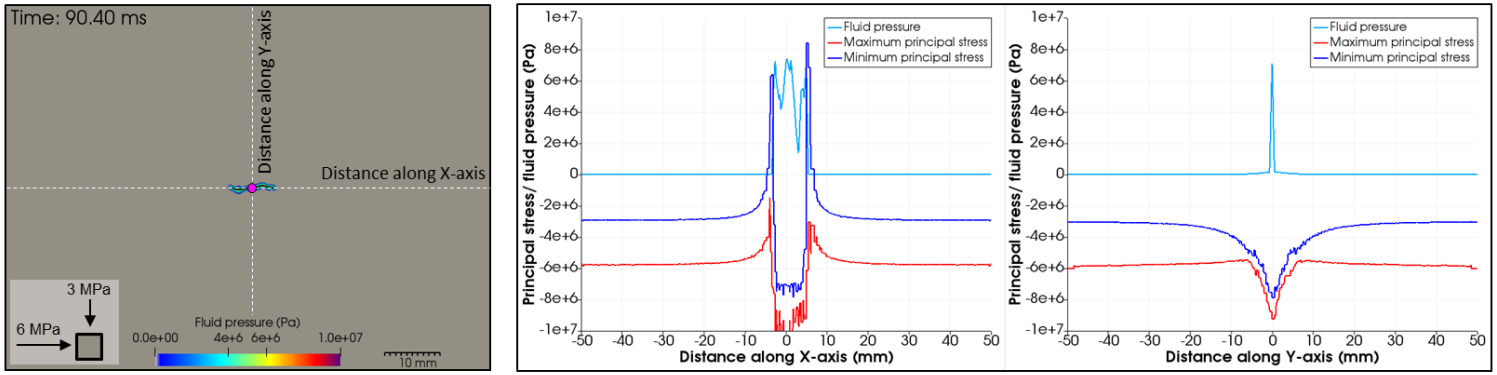

b: End of fluid injection experiment

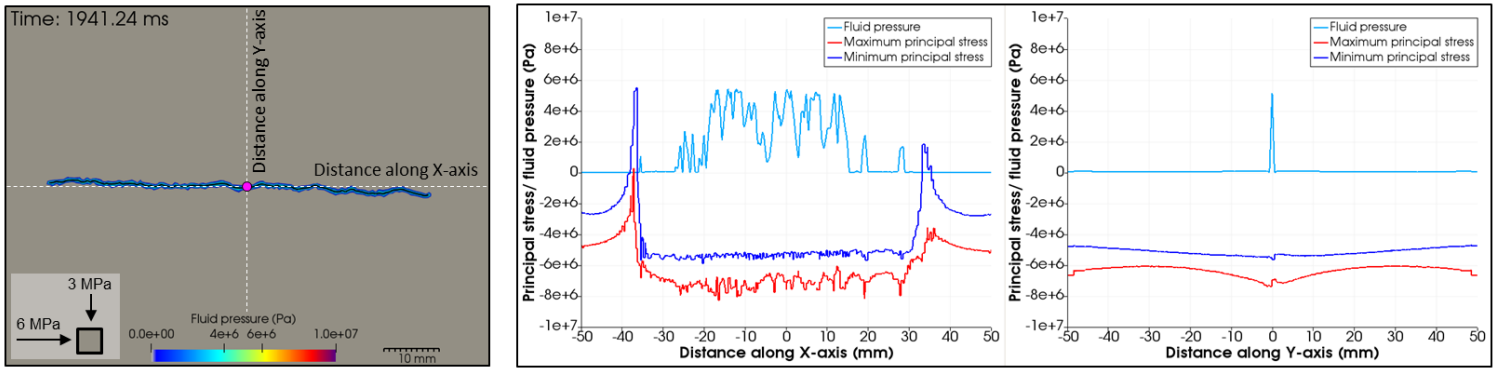

Figure 10: Hydro-mechanical characterization of induced hydraulic fracture propagation due to constant-rate continuous injection into homogeneous rock sample at its center (magenta dot) at early phase (a) and end of the experiment (b). Left panel: fluid pressure distribution and hydraulic fracture evolution. Right panel: fluid pressure and principal stress profiles across the hydraulic fracture (X-axis) and perpendicular to that (Y-axis). Note that fluid pressure is only positive, while tensional and compressional stresses have positive and negative values, respectively.

Figure 11 shows the evolution of fluid injection pressure at the injection point, the cumulative injected volume as well as cumulative crack length due to cyclic progressive injection in the same rock sample (simulation case A2). The initial pressurization phase is characterized by linear pressure increase in the first "low" and "high" injection steps. At the end of first "high" injection step with 2 mm^3/s injection rate, first crack is initiated at FBP equal to 15.4 MPa. This is followed by moderate pressure drop and further pressure increase, which is associated with stress singularity due to loading and unloading cycles with low flow-rates and without any significant leak-off into the microcrack and rock mass. Thus, the apparent peak pressure is interpreted as unsolicited artefact. Subsequently, pressure drops, undulates and sequentially reaches an average FPP of 5.6 MPa at decreasing amplitudes. Comparing the fluid pressure evolution against cumulative crack length, it is evident that it takes several injection steps to increase the fluid pressure so that new microcracks can be generated (state "a" in Figure 11a). The total length of the hydraulic fracture equals 75 mm as a result of fluid injection of 120 mm^3 (state "b" in Figure 11). The resulting aperture fold of increase is 2.1 (Table 2).

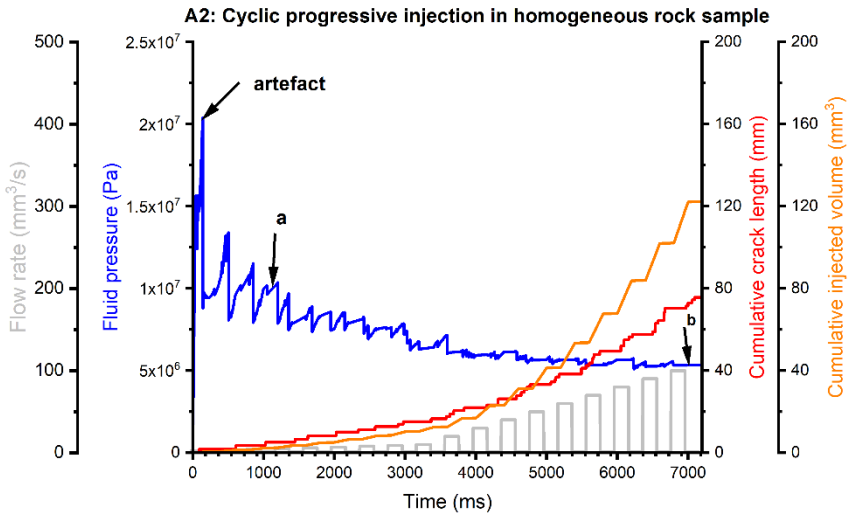

Figure 11: Evolution of fluid pressure, cumulative crack length and injected volume at the injection point due to cyclic progressive fluid injection in homogeneous rock sample. Pointers a and b refer to distinct states of the simulation shown in Figure 12 and Figure 13.

In Figure 12, the fracture pattern, fluid pressure distribution and principal stress directions at the end of simulation case A2 are illustrated. The figure shows that the fluid pressure is limited in the asymmetric hydraulic fracture composed of mode I microcracks. The asymmetric nature of the hydraulic fracture is associated with the random orientation of the mesh edges. Furthermore, around the fracture tips, the orientation of maximum principal stress trajectories is deviated by 25° from that defined at the boundaries. As in modelling case A1, the deviation angle decreases with increasing distance from the hydraulic fracture tips towards sample boundaries in the direction of the minimum principal stress. Interestingly, in contrast to case A1, the minimum principal stress orientations are not altered at the end of simulation, which is a hint towards stress orientation redistribution after injection is stopped.

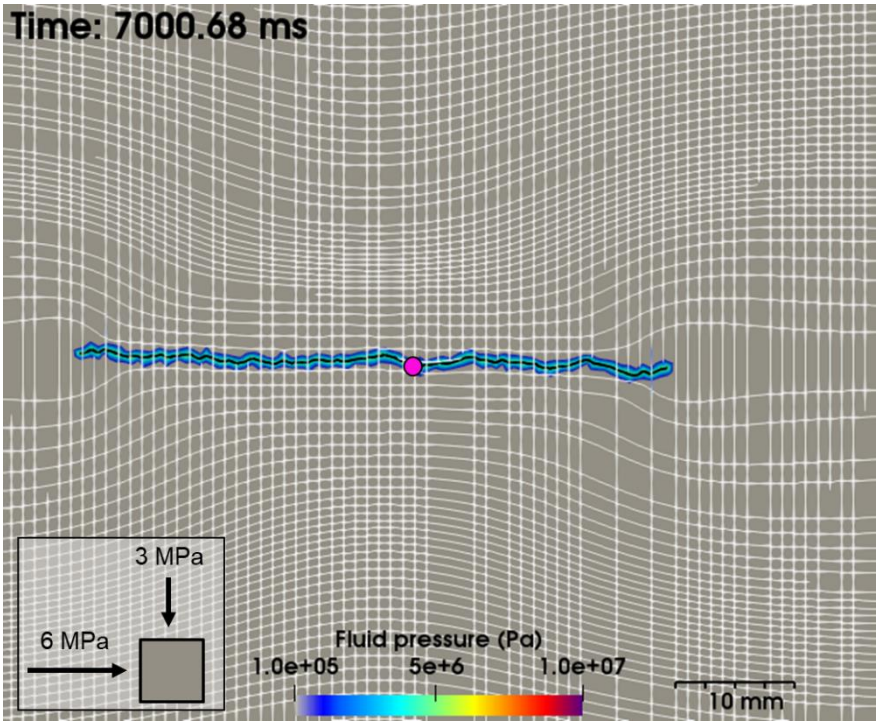

Figure 12: Asymmetric hydraulic fracture pattern (black line), fluid pressure distribution (colour bar) and principal stress trajectories in the granitic rock sample (white orthogonal lines) at the end of cyclic progressive fluid injection in homogeneous rock sample (model case A2).

As for the extent of elastic stress transfer (Figure 13), at the time of hydraulic fracture initiation (Figure 13a), both direct pore pressure and elastic stress effects are concentrated around the injection point. At the end of the fluid injection experiment (Figure 13b), the extent of the perturbation of the principal stress magnitudes due to elastic stress transfer, i.e. deviation from the magnitudes defined at the boundaries shows an asymmetric pattern which is linked to the macroscopic fracture geometry.

A2: Cyclic progressive injection in homogeneous rock sample

a: Shortly after induction of hydraulic fracture

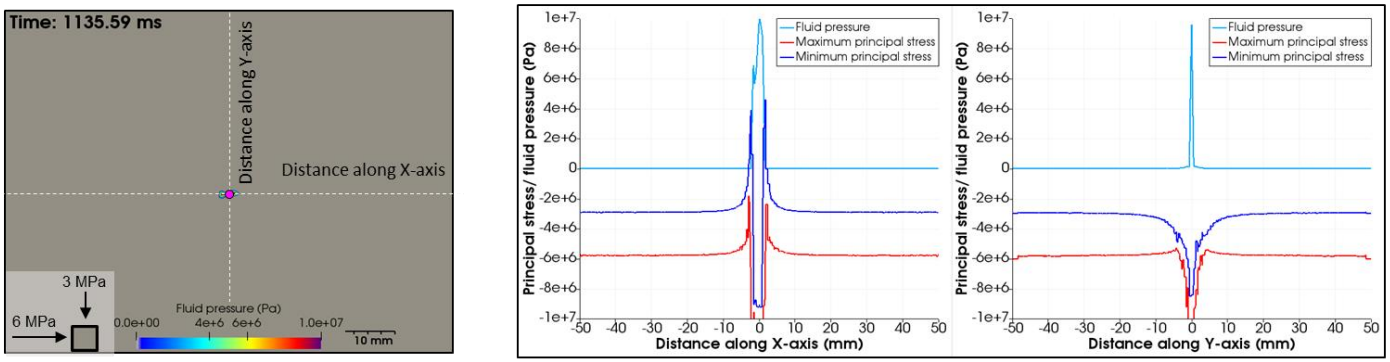

b: End of fluid injection experiment

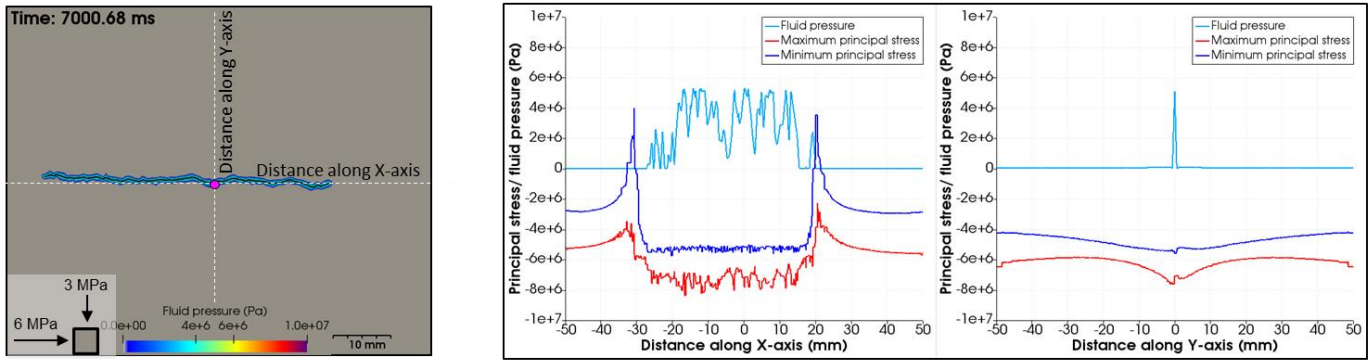

Figure 13: Hydro-mechanical characterization of induced hydraulic fracture propagation due to cyclic progressive injection into homogeneous rock sample at its center (magenta dot) at early phase (a) and end of the experiment (b). Left panel: fluid pressure distribution and hydraulic fracture evolution. Right panel: fluid pressure and principal stress profiles across the hydraulic fracture (X-axis) and perpendicular to that (Y-axis). Note that fluid pressure is only positive, while tensional and compressional stresses have positive and negative values, respectively.

3.4.3 Investigation of injection schemes on heterogeneous samples

The fluid injection pressure due to injection at a constant rate of 100 mm^3/s into a fractured rock sample and the resulting cumulative crack length and injected volume are summarized in Figure 14. In the modelling case B1, the FBP of 14.5 MPa is reached within few 10 ms. After that, pressure decreases rapidly within few 100 ms to an average FPP level of approx. 6 MPa (state "a" in Figure 14). Pressure fluctuates around FPP as the hydraulic fracture extends until the end of the treatment (state "b" in Figure 14). As for the crack length evolution during the experiment, it increases directly proportional to increasing injected volume from the onset of injection until fluctuation of the fluid pressure around average FPP begins (state "a" in Figure 14). From that point on, the extension of the growing hydraulic fracture requires more fluid, thus the fracture propagation holds sequentially.

At the end of the simulation, a complex hydraulic fracture composed of microcracks with a total length of 162 mm is generated after 200 mm^3 of fluid injection (Figure 15). The aperture fold of increase is equal to a factor of 6 with a maximum hydraulic aperture of 20 µm.

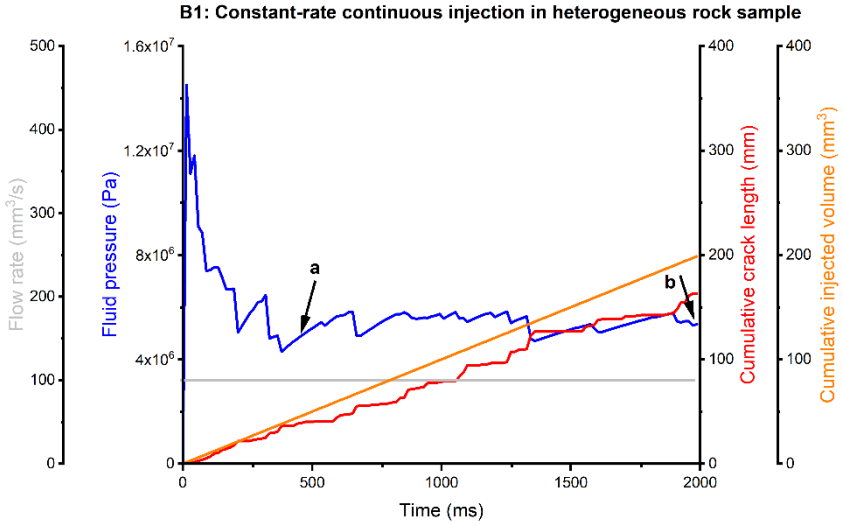

Figure 14: Evolution of fluid pressure, cumulative crack length and injected volume at the injection point due to constant-rate continuous fluid injection in a heterogeneous rock sample. Pointers a and b refer to distinct states of the simulation shown in Figure 15 and Figure 16.

In Figure 15, the principal stress trajectories, fluid pressure distribution and the microcrack pattern at the end of the injection experiment are shown. First, symmetrical mode I microcracks are induced in the intact rock mass around the injection point that are parallel to the direction of the maximum principal stress (black elements in Figure 15). As the propagating hydraulic fracture approaches the pre-existing joints, those encounter first softening, then failure in mode II, referred to as hydro-shearing (light pink and dark purple elements, respectively, in Figure 15). Due to hydraulic aperture increase associated with that, the joints are infiltrated and fluid pressure builds up due to ongoing injection. As pumping continues, new joints soften and fail as well as new mode I microcracks are generated that establish connection between two hydro-sheared joint elements. Mode I microcracks are only oriented parallel to the maximum principal stress. Interestingly, mode II fractures have various

failure angles, i.e. failure angles that are not associated with optimally oriented for hydro-shearing. This can be explained by the fluid pressure build up and the limited leak-off into the rock mass. Since pressure accumulation is restricted to the fractured elements, fracture propagation requires less energy towards a not optimally oriented pre-existing joint (e.g. parallel to the minimum principal stress) than to induce a new mode I microcrack.

Comparing the distribution of pressurized elements against the location of microcracks, it is evident that the generated fractures are not restricted to pressurized regions. Thus, mode II cracks and softened elements due to elastic stress transfer are observed. Mode II microcracks are up to 10 mm away from the tip of the hydraulic fracture, i.e. farthest pressurized element from the injection point. In the case of mode II softened elements these can be as far as several 10 millimeters.

The complex fracture network has a clear influence on the stress trajectories. At the tips of the hydraulic fracture, the minimum stress orientations are diverted by up to 30° and the maximum principal stress orientations are slightly deviated. With increasing distance away from the hydraulic fracture tips in the direction of the minimum stress, horizontal stress directions show increasing deviation from the principal direction as well. Interestingly, around the injection point, where no pre-existing fractures were present, both principal stress directions agree with the boundary conditions. Possible explanation for this observation is that the high pressurized fracture elements close to the injection point act as free surface with principal stresses parallel and perpendicular.

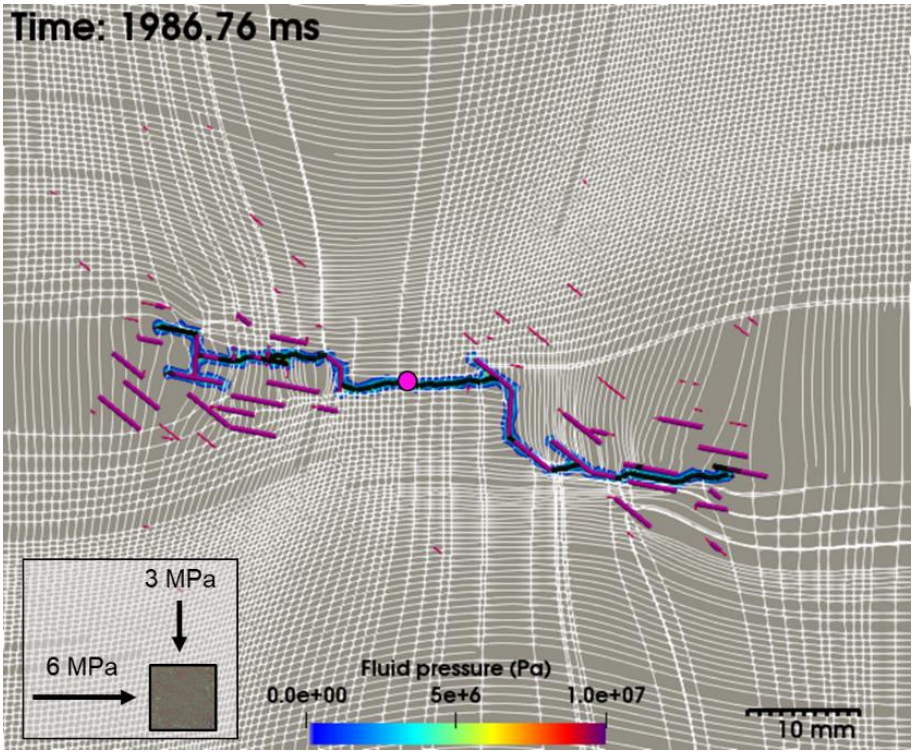

Figure 15: Principal stress trajectories and fluid pressure distribution in the induced hydraulic fracture at the end of constant-rate continuous fluid injection in heterogeneous rock sample. Microcracks induced in tension in rock matrix are shown as black elements; hydro-sheared pre-existing fractures are dark purple elements as well as softened pre-existing fractures are illustrated as light pink elements. Pre-existing discrete fracture network is not shown for enhanced visibility (model case B1).

Figure 16 summarizes the hydraulic fracture propagation as well as fluid pressure distribution and principal stress profiles due to constant-rate continuous injection into heterogeneous rock sample (model case B1) at early (a) and later stage of the experiment (b). At the early stage of the injection experiment, i.e. shortly after first mode II microcracks are generated during hydraulic fracture propagation, an approximately symmetrical fracture pattern is observed with a larger right wing due to interconnected joint elements. The symmetrical bi-wing fracture pattern is also apparent in both principal stress profiles where the minimum stress concentrations reveal a fracture half-length of 10 mm along the X-axis profile from the injection point. 10 mm away from the minimum stress concentrations, i.e. fracture tips in both profiles, the principal stresses agree with the magnitudes defined at the boundaries. This shows that the elastic stress transfer has a radius of ~20 mm which is about four times the hydraulic fracture half length. In contrast to the elastic effects, the direct pore pressure effect is limited to the extent of the hydraulic fracture and that is negligible perpendicular to the fracture as a result of lack of fluid leak-off into the intact rock mass.

At the end of the treatment (Figure 16b), the half-distance of the pressurized farthest fracture tips is located 25 mm from the injection point parallel to the maximum principal stress. Around the fracture tips, elevated minimum stresses are visible in the X-axis profile, which diminishes to the pressure level defined at the boundaries within few 10 mm. Perpendicular to the hydraulic fracture, around the injection point, the principal stresses are slightly more compressional. Towards the boundaries, the maximum principal stress reduces to the level defined at the boundaries, whereas the minimum stress remains slightly more compressional, i.e. 4 MPa, at the boundaries.

B1: Constant-rate continuous injection in heterogeneous rock sample

a: Shortly after induction of hydraulic fracture

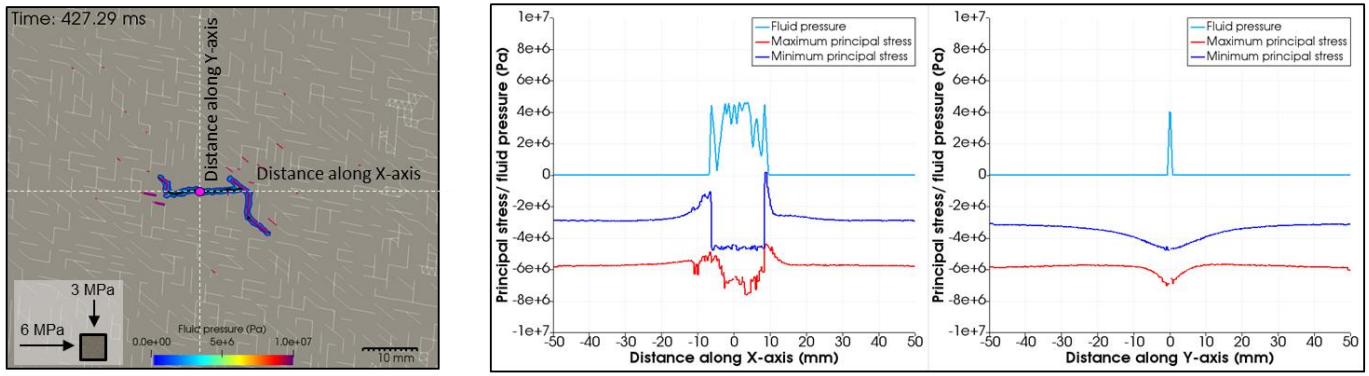

b: End of fluid injection experiment

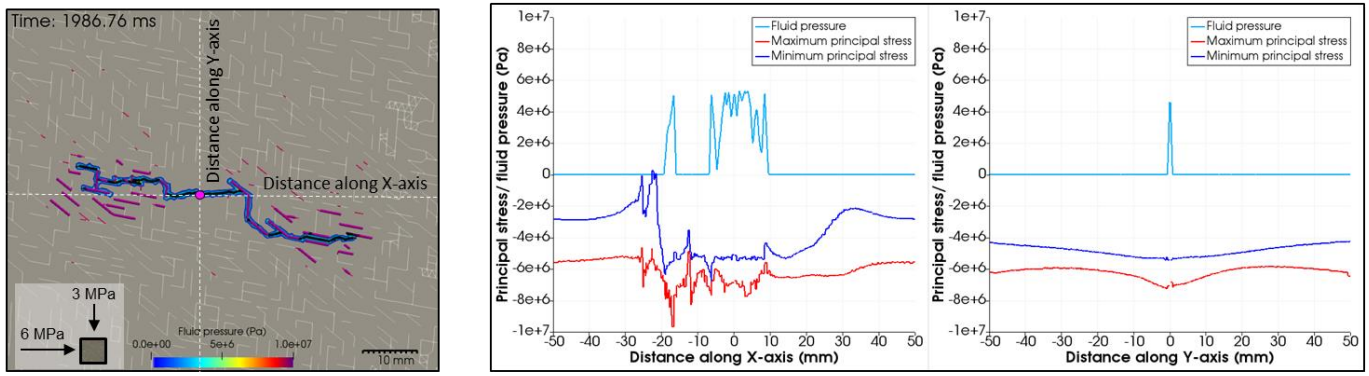

Figure 16: Hydro-mechanical characterization of induced bi-wing hydraulic fracture propagation due to constant-rate continuous injection into heterogeneous rock sample at its center (magenta dot) at early phase (a) and end of the experiment (b). Left panel: fluid pressure distribution and hydraulic fracture evolution. Right panel: fluid pressure and principal stress profiles across the hydraulic fracture (X-axis) and perpendicular to that (Y-axis). Note that fluid pressure is only positive, while tensional and compressional stresses have positive and negative values, respectively.

Figure 17 exhibits the fluid pressure evolution due to cyclic progressive injection and the resulting cumulative crack lengths and injected volume in fractured rock sample (model case B2). Fluid pressure shows steady increase until FBP at a value of 15.5 MPa is reached during "high" injection step with a flow rate of 4 mm^3/s where first crack is generated. Subsequently, pressure increases further until 22 MPa which is followed by large drop. The apparent peak pressure is associated with unsolicited numerical instability, as also observed for modelling case A2. Thus, the peak pressure is interpreted as numerical artefact. The pressure drop after reaching artefact is followed by pressure undulation with decreasing amplitudes as the propagating hydraulic fracture requires less pressure build up to extend. At this stage of the experiment, cumulative crack length and injected volume show similar evolution characteristics (state "a" in Figure 17). After the hydraulic fracture reaches pre-existing joints, i.e. from the "high" step of 40 mm^3/s, extension of the hydraulic fracture requires more fluid pressure due to the higher volume of the pressurized system. Thus, hydraulic fracture propagates at an average FPP of 5.8 MPa until the end of the treatment (state "b" in Figure 17).

At the end of the simulation, a complex hydraulic fracture composed of microcracks with a total length of 96 mm is generated after 120 mm^3 of fluid injection (Figure 18). The aperture fold of increase is equal to a factor of 6 with a maximum hydraulic aperture of 20 µm.

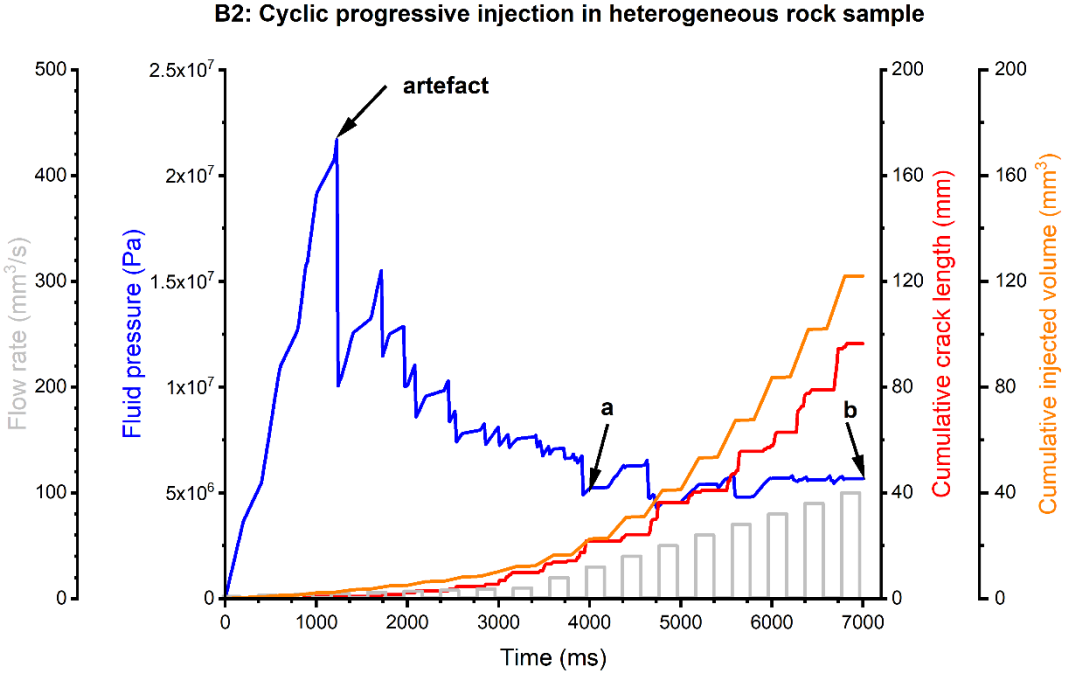

Figure 17: Evolution of fluid pressure, cumulative crack length and injected volume at the injection point due to cyclic progressive fluid injection in heterogeneous rock sample. Pointers a and b refer to distinct states of the simulation shown in Figure 18 and Figure 19.

In Figure 18, the principal stress trajectories, the fluid pressure distribution and the generated microcracks are illustrated at the end of the treatment. The complex fracture network is the result of the hydraulic fracture induced at the injection point that propagates away parallel to the maximum principal

stress and interferes with the pre-existing joints. It is evident in Figure 18 that microcracks are generated both due to direct pore pressure, i.e. characterized by pressurized newly induced mode I fractures and hydro-sheared pre-existing joints, and as a consequence of elastic stress transfer effect. Interestingly, the minimum principal stress orientations are not deviated, however, the maximum principal stress trajectories are distorted around the hydraulic fracture tips and away from that perpendicular to the hydraulic fracture. Around the injection point, the trajectories agree with the boundary conditions.

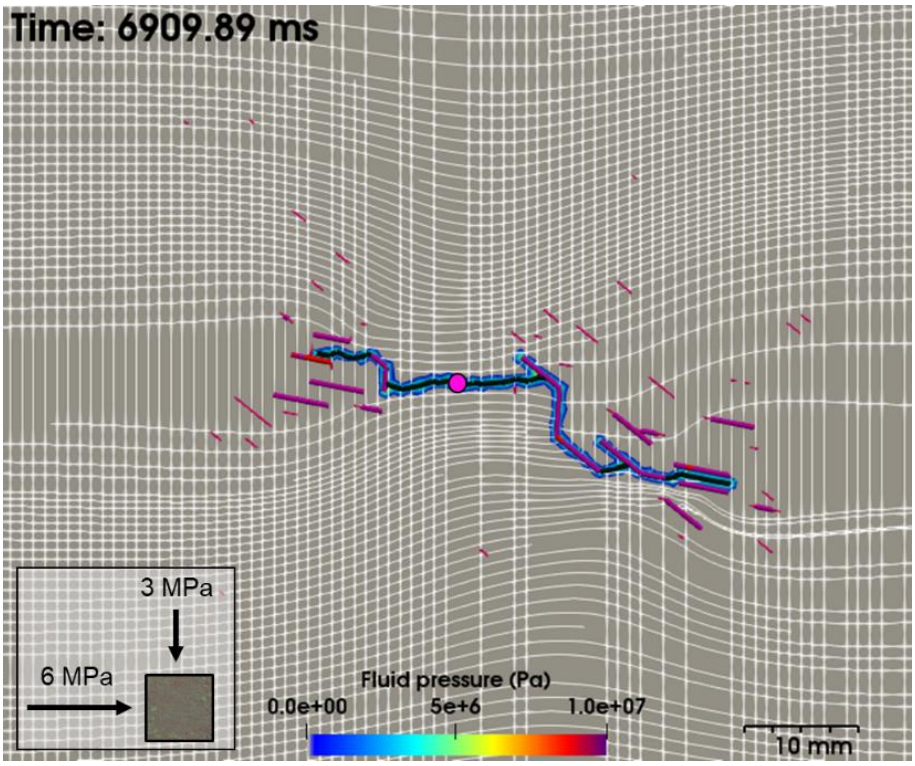

Figure 18: Principal stress trajectories and fluid pressure distribution in the induced hydraulic fracture at the end of cyclic progressive fluid injection in heterogeneous rock sample. Microcracks induced in tension in rock matrix are shown as black lines; hydro-sheared pre-existing fractures are dark purple elements as well as softened pre-existing fractures are illustrated as light pink elements. Pre-existing discrete fracture network is not shown for enhanced visibility (model case B2).

The main hydro-mechanical characteristics of the cyclic progressive injection treatment in heterogeneous rock are summarized in Figure 19. The characteristics, such as the extent of perturbed minimum and maximum principal stresses during hydraulic fracture propagation and at the end of injection are similar to model case B1.

B2: Cyclic progressive injection in heterogeneous rock sample

a: Shortly after induction of hydraulic fracture

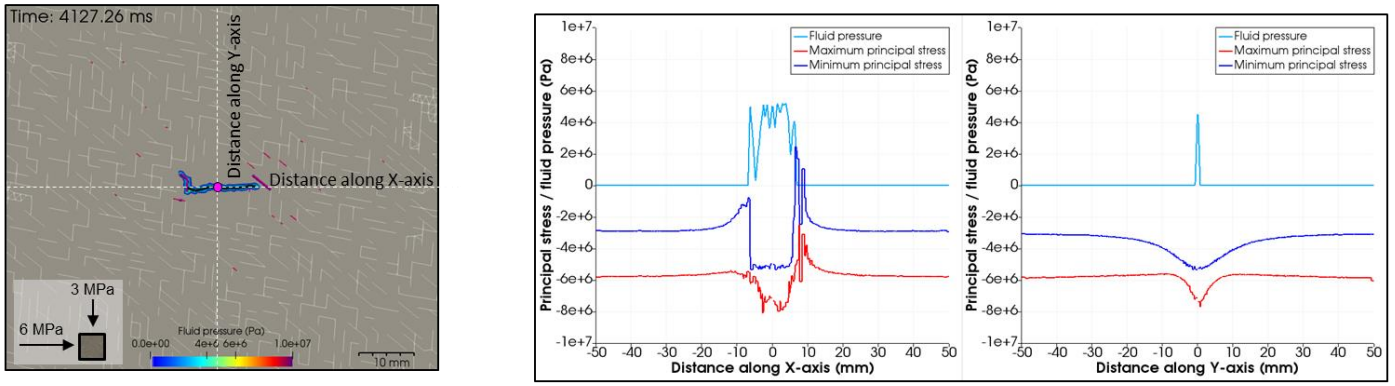

b: End of fluid injection experiment

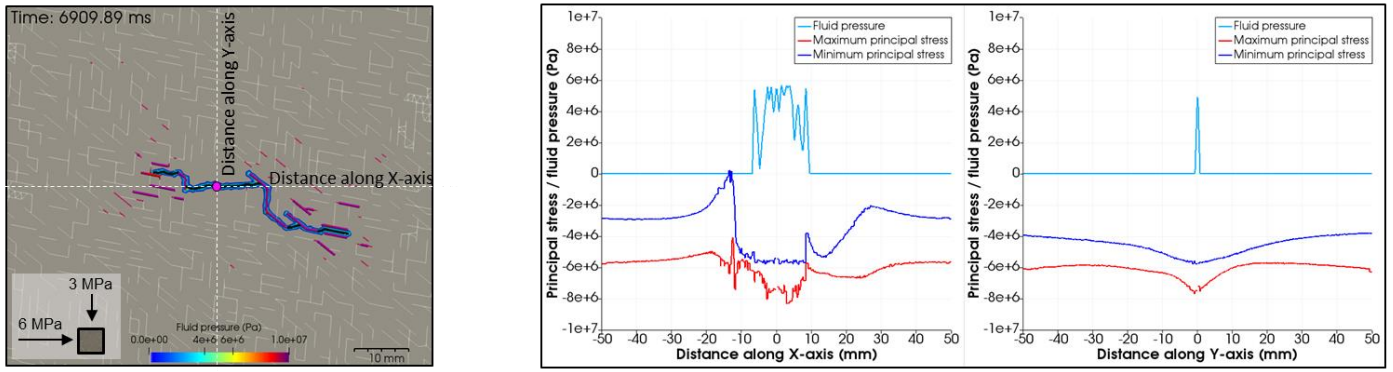

Figure 19: Hydro-mechanical characterization of induced hydraulic fracture propagation due to cyclic progressive injection into heterogeneous rock sample at its center (magenta dot) at early (a) and end of the experiment (b). Left panel: fluid pressure distribution and hydraulic fracture evolution. Right panel: fluid pressure and principal stress profiles across the hydraulic fracture (X-axis) and perpendicular to that (Y-axis). Note that fluid pressure is only positive, while tensional and compressional stresses have positive and negative values, respectively.

3.5 Discussion

3.5.1 Comparison of hydro-mechanical indicators due to different injection schemes

By comparing the hydraulic and mechanical results of the different injection schemes in Table 2, following points can be discussed.

First, the FBP is slightly higher using the CPI scheme, between 0.5 and 1 MPa, regardless of rock fabric. Although this agrees with the laboratory experiments of Zhuang et al. (2020), this is in contrast to laboratory studies such as Patel et al. (2017) and Kang et al. (2020) where FBP drops with number of injection cycles. Considering the laboratory tests of Zhuang et al. (2020), there are mainly two reasons for the variation of FBP. First, sample heterogeneity can cause 1-2 MPa variance in BTS; and second, limitation in the test equipment that is likely to cause 1-2 MPa error. In the numerical model, the discrepancy can be explained by the limited leak-off into rock mass, random properties of pre-existing fractures, how the fluid volume is injected in the modelled rock sample as well as numerical effects. Considering numerical effects, cyclic loading would require more mechanical time steps for a given hydraulic time step to enable more effective relaxation, and hence unsolicited stress concentration leading to higher FBP and unsolicited apparent peak pressures. However, this would result in impractical lengthy computational times. Thus, it can be hypothesized that an improved numerical definition of the calculation scheme would result in reduced FBP for both schemes.

Second, the FPP is interestingly approx. the same in all modelling cases. Thus, that is neither influenced by the injection scheme nor the rock fabric. This is even more striking given that the pressurized joints have a larger aperture than the intact rock mass and the induced mode I microcracks. This is associated with the presence of only mode I microcracks around the injection point that control initial FBP and subsequent pressure drop during the injection experiment.

The comparison of the microcrack patterns, stress magnitude profiles and trajectories merits further discussion.

The fracture patterns in the homogeneous modelling cases (A1 in Figure 10 and A2 in Figure 13) show that the hydraulic fracture propagation is driven by classical fracture tip lubrication. Thus, at the end of the simulation, fluid pressure and the principal stresses are uniform parallel to the direction of propagation. Slight variations in fluid pressure are attributed to the irregular orientations of the mesh edges that connect virtual pores storing injected fluid. No microcrack is generated ahead of the fracture tip or away from the hydraulic fracture, i.e. no fracture process zone (FPZ) develops. The principal stress trajectories at the end of the homogeneous modelling cases (A1 in Figure 9 and A2 in Figure 12) show that the perturbation area, where the trajectories are oriented from the boundary condition, is around the fracture tip injection points (case A2) which propagates as the hydraulic fracture extends (case A1). Thus, at the time scale of the experiment, stress orientation redistribution can be observed around the injection point.

In contrast to the homogeneous modelling cases, more complex fracture patterns are generated in the heterogeneous modelling cases (B1 in Figure 15 and Figure 16 as well as B2 in Figure 18 and Figure 19). Initially, hydraulic fracture propagation is analogous to the homogeneous modelling cases, A1 and A2, as only mode I microcracks are generated in the intact portion of the heterogeneous rock sample. As soon as the propagating hydraulic fracture reaches the jointed rock mass, the main driving mechanism becomes the hydraulic pressurization of the jointed elements. These hydro-sheared pre-existing elements have various orientations regardless of optimal orientation for hydro-shearing. Only few mode I microcracks are generated in intact rock that connect two jointed elements. Moreover, joints soften and fail as mode II elements away from the tips of the hydraulic fracture. This is an indication that a mode II fracture process zone develops instead of mode I FPZ. The most distant softened or sheared elements are located 10-15 mm away from the tips with orientation of -39° measured counter-clockwise from the direction of maximum principal stress. Furthermore, more indirect microcracks are generated around the pressurized fracture elements in the CCI scheme than in the CPI scheme. The complex fracture pattern including microcracks away from the hydraulic fracture is therefore the result of both fracturing due to direct pore effects and indirect elastic stress transfer. Thus, we demonstrate that locally the fracture follows the rock fabric (pre-existing fractures) and on a larger scale it follows overall the stress field directions.

The stress magnitude profiles in the heterogeneous cases exhibit asymmetric variation at the profile parallel to the fracture propagation, since that propagates rather through the hydro-sheared joints with different orientations. In both injection schemes, the stress magnitude profiles show asymmetric stress concentrations. This observation agrees with in-plane shear mechanism described in classical theory of linear elastic fracture mechanics (Zang and Stephansson, 2010, their Chapter 3). As for the principal stress trajectories, those at the end of the heterogeneous modelling cases (B1 in Figure 15 and B2 in Figure 17) show that the perturbation area, where the trajectories are oriented from the boundary condition, is not only around the fracture tips but around the indirectly hydro-sheared microcracks as well. However, analogously to the homogeneous modelling cases, at the time scale of the experiment, stress orientation redistribution can be observed around the injection point.

3.5.2 Comparison of simulation treatments against laboratory experiments

The simulation cases allow comparing the results with observations from laboratory experiments reported by Zhuang et al. (2020).

First of all, test duration as well as time required for complete fracturing of the sample in the lab and the numerical simulation can be compared. As for the laboratory experiments, this can be determined indirectly via the evolution of the cumulative recorded AE curves while in the numerical model, this is simulated directly. Similarly, the permeability (aperture) fold of increase of the injection experiments due to the lab experiments are determined directly from the pressure curves and post-

fracturing permeability test, whereas, in the numerical model, this is inferred from increase in hydraulic apertures.

In the case of CCI injection scheme with 100 mm^3/s injection rate (Figure 2a), the cumulative AE evolution indicates fracturing within few seconds, i.e. hydraulic fracture is induced instantaneously compared to the time of shut-in at approx. 65 s. Thus, the simulated duration of approx. two seconds for cross fracturing of the rock sample agrees with the proposed duration in eq. 19 and in the lab (simulation cases A1 in Figure 8 and case B1 in Figure 14).

For the CPI injection scheme from 20 to 100 mm^3/s in 10 mm^3/s steps (Figure 2b), the time required for complete fracturing of the sample cannot be determined unambiguously. Based on model cases A2 and B2, the fracturing of the sample using the CPI injection scheme requires at least seven seconds. This is much shorter, and thus, computationally beneficial compared to the laboratory experiment, where fracturing of the sample with the same injection scheme requires 250 seconds after initial pressurization and before shut-in.

Second, several hydro-mechanical process indicators can serve as comparison between the simulated and laboratory experiments. These include the FBP, the FPP, the comparison of characteristics of cumulative AE with simulated crack length curves as well as permeability increase (aperture fold of increase).

The reported FBP for CCI injection scheme with injection rates of 100 mm^3/s is approx. 15 MPa which agrees with the simulated one. The reported FPP, however, is higher than the simulated one, i.e. 10 MPa versus 5.6 MPa (average FBPs of cases A1 and B1 in Table 2). Another possible explanation can be the lack of installed packers in the borehole, resulting in a hydraulic fracture with a height smaller than the length of the open hole section. Since the fluid-filled hydraulic fracture in the laboratory sample cross-cuts the sample as FBP is recorded, the higher FPP is likely associated with boundary effects in the laboratory. Similar observation is reported by Parisio (2020), where fluid is injected at cubic granitic rock samples and such experiment is modelled using numerical code OpenGeoSys.

The simulated FBP for the CPI injection scheme shows good agreement with that reported in Zhuang et al. (2020). Considering the heterogeneity of the laboratory samples, and mesh sensitivity, the difference is insignificant. Thus, the larger FBP for the CPI injection scheme compared to CCI shows good agreement with the laboratory experiments and the simulation results. The FPP cannot be unambiguously determined for the laboratory experiments. Thus, no direct comparison is possible.

As for the characteristics of the AE curves, in the case of CCI injection scheme, the instantaneous rise of the cumulative AE curve stops and remains flat until shut-in as shown in Figure 2a. As discussed above, this is a hint towards rapid hydraulic fracture generation that reaches sample boundaries. Therefore, this evolution agrees with that of the cumulative crack length of numerical model cases A1 and B1 as shown in Figure 8 and Figure 14, respectively.

The simulated permeability increment of the injection tests show that higher aperture fold of increase can be reached via using the CPI injection scheme compared to CCI, i.e. approx. 6 versus 2.

However, in the lab, the injectivity increase for the CPI scheme and the maximum hydraulic aperture are lower than that for CCI. We can explain this discrepancy in that fracture aperture measured after cyclic injection in the lab is smaller compared with the maximum value during fracture propagation, i.e. during injection. This is due to fracture closure after injection is stopped.

3.5.3 Implications for EGS field injection strategies

The simulation results allow making implications for field injection strategies regarding natural and engineering factors for developing an optimal fracture network for EGS utilization. The natural factors considered here are the fracture pattern, stress field, and driving mechanisms of crack generation. Regarding the driving failure mechanisms, here we discuss the proposed phenomena underlying field-scale seismicity which is referred to either as induced or triggered (Ellsworth et al., 2019). Although the analysis of microseismicity is not the subject of this study, the hydraulic and mechanical controlling factors on the spatial extent of microcrack generation from the injection point can be discussed. The discussed engineering factor is the injection scheme.

A complex fracture network is a prerequisite for potential good hydraulic and thermal performance of an EGS system. Hofmann et al. (2016) demonstrate that this is more favorable compared to the presence of a dominant single fracture path. Apart from that, hard and brittle rock with low permeability, a complex pre-existing fracture network with at least two intersecting natural fracture sets and with sets characterized by favorable orientation to the in-situ stress field are favorable. Our numerical results confirm that heterogeneous models (model cases B1 and B2) not only show agreement with these properties of hard and brittle rock but these models also exhibit higher maximum hydraulic apertures. Therefore, heterogeneous models imply potentially better hydraulic conductivity, compared to the homogeneous modelling cases (model cases A1 and A2) where single hydraulic fracture path with lower hydraulic aperture dominates the failure mechanism. Moreover, the heterogeneous models can be used in a future study to test their thermal performance as well. For field scale application, it is inferred that pre-fractured and heterogeneous formations lead to more complex fracture growth.

Considering the changes in stress field discussed in Section 3.5.1, the magnitude changes observed in the principal stress profiles show that the shearing of pre-existing fractures exerts additional compressive stress in the direction normal to the fracture as proposed by Warpinski and Branagan (1989). Thus, the numerical models demonstrate stress shadow effect as a result of both propagation of newly induced fracture and hydro-shearing of discrete fracture elements. This changes the local stress magnitudes and orientations around the injection point and the stimulated area. Consequently, if in one well a frac is generated which alters the stress field at a relatively close location, hydraulic fracture can propagate irrespective of local S_{Hmax} direction. Similar behavior has been demonstrated in laboratory and numerical experiments recently by Abe et al. (2021) and Abe and Horne (2021).

Regarding direct pore pressure effect and elastic stress transfer, the numerical model can be used for making implications towards hydro-mechanical controlling mechanisms during injection. The

modelling results reveal that the microcrack generation is dominated by direct pore pressure effect. Fracturing due to elastic stressing occurs only in the heterogeneous model cases and those fractures are generated close to the directly pressurized fractures. However, such indirectly induced cracks are observed ahead of directly pressurized pre-existing microcracks. This demonstrates that a rupture front propagates faster than the fluid pressure front as shown by Bhattacharya and Viesca (2019). The directly reactivated fractures are mainly aligned close to the direction of the maximum principal stress direction, i.e. -11° measured counter-clockwise from the horizontal axis, whereas the indirectly reactivated ones are oriented at an angle of -39° from the same direction. The various orientations of the reactivated fractures are the consequence of an interplay of stress alteration and rotation effects. As a result, the factors controlling critical stress for hydro-shearing of pre-existing fractures are modified locally.

Injection scheme, i.e. flow rate, duration as well as injected volume are significant engineering factors of stimulation strategies, apart from rock mass properties. Our numerical investigations show that with the right strategy permeability can be increased by more than factor five if naturally fractured rock is stimulated instead of intact rock. However, this self-propping mechanism is not maintained if the injection is stopped. This leads to apparently lower maximum hydraulic aperture and aperture fold of increase in the CPI case as reported in the post-fracturing laboratory injectivity experiments (Table 2).

Lastly, it must be noted that, although thermal effects are not considered in this study, they may influence the hydro-mechanical properties of rock, especially rock strength properties and permeability (Jiang et al., 2018; Li et al., 2021), and are worth future experimental research.

3.5.4 Numerical limitations

The limitations of the numerical experiments are the consequence of the algorithmic solutions used to simulate the hydro-mechanical processes described in this paper. The explicit temporal integration scheme solving the motion and flow equations in the mechanical and hydraulic solver, respectively, are well suited for non-linear, dynamic problems. However, in order to avoid numerical instabilities, sufficiently small integration time steps for both solvers must be defined. That requires setting a trade-off between the number of mesh elements, mesh size as well as upper limit of hydraulic aperture according to eq. 18. Therefore, a sub-mm scale simulation of the hydro-mechanical processes underlying laboratory fluid-injection experiments can only be conducted using the time scaling approach of the fracturing processes proposed by Bunger et al. (2005). Otherwise, the attempt to match the injection time in simulation with that of an experiment is practically impossible. The same limitation has been reported in numerical studies where explicit time-integration scheme is adopted for hydro-mechanically coupled simulations, e.g. Bai et al. (2020) and Kong et al. (2021).

Another deficiency of the approach is that the induced hydraulic fracture does not fully reach the draining sample boundaries for the sake of numerical stability. Hence, the injected fluid volume accumulates within the interconnected fracture elements. Since the rock matrix elements have very low

permeability, the fluid is trapped in the fractured elements. Consequently, fluid cannot leak into the rock matrix or out of the sample along the boundaries, therefore, no pressure drop is observed during shut-in or reduced injection rate periods in the numerical model as compared to the laboratory experiments.

Moreover, microcracks can only propagate along the mesh edges mimicking intergranular fracturing, i.e. cracking along mineral grain boundaries. In the laboratory, both intragranular, where mineral grains are cut through, and intergranular fracturing occur during fluid injection into granitic rock samples (Zhuang et al., 2020; Zhuang and Zang, 2021). Furthermore, this unintentionally leads to asymmetric hydraulic fracture propagation in the case of CPI injection schemes regardless of rock fabric (Figure 13 and Figure 18). These may be solved by introducing a set of closed-loop polygons. The loop segments can be defined as joint elements that encompass several intact mesh elements representing the inner part of distinct mineral grains. An example for application of this approach is demonstrated by Yoon et al. (2018), where blocky structures are simulated using discrete element modelling technique.

3.6 Conclusions

In this paper, we report on numerical simulation of laboratory fluid-injection experiments of Pocheon granite under two injection schemes and rock sample representations. The hydro-mechanical processes during the experiments are investigated. The research outcomes are summarized as follows:

1. The hybrid finite-discrete element simulation of pressurization and fracturing periods of laboratory fluid injection experiments can provide insights into hydro-mechanically coupled fracturing processes at reasonable computational costs using a time-scaling approach.
2. Stress rotation effect and elevated compressional stresses are observed around the fracture tips where elements are not infiltrated. This indirect elastic stress transfer leads to microcrack generation around the propagating tips of the macroscopic hydraulic fracture in heterogeneous samples. In these samples, the microcracks are located in an “off-fault” damage zone approximately perpendicular to the direction of hydraulic fracture propagation.
3. Constant-rate continuous injection and cyclic progressive injection schemes in heterogeneous rock sample with pre-existing fractures shows the highest hydraulic aperture increase compared to intact samples. Our numerical investigations show that hydraulic aperture can be increased by more than factor five if naturally fractured rock is stimulated instead of intact rock until shut-in. However, laboratory experiments show higher aperture fold of increase, consequently permeability enhancement after constant-rate injection. This shows that the self-proppant mechanism of cyclic progressive injection is not sustained if injection is stopped.
4. The least aperture fold of increase is produced by the same cyclic progressive injection scheme into homogeneous rock sample where the aperture increase is approx. factor two. This observation highlights the need and the potential for adjusted injection schemes for different geological conditions in order to optimize hydraulic stimulation treatments.

5. The numerical simulation results show good agreement with the laboratory experiments in terms of pressure evolution characteristics and fracture pattern. Furthermore, rock fabric has a significant on the simulated aperture fold of increase, and consequently on permeability increase. On the other hand, hydraulic fracture geometry is influenced by mineral grains in the laboratory experiments. Therefore, future numerical model should incorporate grain strength for improved simulations. Furthermore, the lack of explicit wellbore model and limited leak-off into the intact rock mass hinders simulation of coupled hydro-mechanical processes during early pressurization and shut-in periods, respectively.

Acknowledgements

The DESTRESS project has received funding from the European Union's Horizon 2020 research and innovation program under grant agreement No 691728. First and second author are funded by this project. This work was also supported by the Helmholtz Association's Initiative and Networking Fund for the Helmholtz Young Investigator Group ARES (contract number VH-NG-1516). We are extremely grateful to the developers of the Irazu simulation software, Dr. Andrea Lisjak and Dr. Omid Mahabadi, who actively supported suiting the code for the purposes of this study.

References

Abe, A., Horne, R.N., 2021. Investigating stress shadowing effects and fracture propagation patterns: Implications for enhanced geothermal reservoirs. International Journal of Rock Mechanics and Mining Sciences. 142: 104761.

Abe, A., Kim, T.W., Horne, R.N., 2021. Laboratory hydraulic stimulation experiments to investigate the interaction between newly formed and preexisting fractures. International Journal of Rock Mechanics and Mining Sciences. 141: 104665.

Bai, Q., Liu, Z., Zhang, C., Wang, F., 2020. Geometry nature of hydraulic fracture propagation from oriented perforations and implications for directional hydraulic fracturing. Computers and Geotechnics, 125: 103682.

Barenblatt, G. I., 1962. The Mathematical Theory of Equilibrium Cracks in Brittle Fracture, in: Dryden, H.L., von Kármán, T., Kuerti, G., van den Dungen, F.H., Howarth, L. (Eds.). Advances in Applied Mechanics. Elsevier, pp. 55-129.

Bhattacharya, P., Viesca, R.C., 2019. Fluid-induced aseismic fault slip outpaces pore-fluid migration. Science. 364(6439): 464-468.

Bunger, A. P., Jeffrey, R. G., Detournay, E., 2015. Application of Scaling Laws to Laboratory-Scale Hydraulic Fractures. Alaska Rocks 2005, The 40th U.S. Symposium on Rock Mechanics (USRMS), Anchorage, Alaska, June 2005. ARMA-05-818.

Detournay, E., 2016. Mechanics of Hydraulic Fractures. Annual Review of Fluid Mechanics. 48(1): 311-339.

Dugdale, D.S., 1960. Yielding of steel sheets containing slits. Journal of the Mechanics and Physics of Solids. 8(2): 100-104.

Ellsworth, W. L., Giardini, D., Townend, J., Ge, S., Shimamoto, T., 2019. Triggering of the Pohang, Korea, Earthquake (Mw 5.5) by Enhanced Geothermal System Stimulation, Seismological Research Letters 90(5): 1844-1858.

Evans, R., Marathe, M., 1968. Microcracking and stress-strain curves for concrete in tension. Materials and Structures 1: 61-64.

Geomechanica Inc., 2020. Irazu 2D Geomechanical Simulation Software version 4.0. Theory Manual.

Hofmann, H., Babadagli, T., Yoon, J.-S., Blöcher, G., Zimmermann, G., 2016. A hybrid discrete/finite element modeling study of complex hydraulic fracture development for enhanced geothermal systems (EGS) in granitic basements. Geothermics. 64: 362-381.

Hofmann, H., Zimmermann, G., Farkas, M., Huenges, E., Zang, A., Leonhardt, M., Kwiatek, G., Martinez-Garzon, P., Bohnhoff, M., Min, K.-B., Fokker, P., Westaway, R., Bethmann, F., Meier, P., Yoon, K. S., Choi, J.W., Lee, T. J., Kim, K. Y., 2019. First field application of cyclic soft stimulation at the Pohang Enhanced Geothermal System site in Korea. Geophysical Journal International. 217(2): 926-949.

Huenges, E., Ellis, J., Welter, S., Westaway, R., Min, K.-B., Genter, A., Meier, P., Wassing, B., Marti, M., 2021. Demonstration of Soft Stimulation Treatments in Geothermal Reservoirs. Proceedings of the World Geothermal Congress 2020+1, March-October, 2021.

Jiang, G., Zuo, J., Li, L., Ma, T., Wie, X., 2018. The Evolution of Cracks in Maluanshan Granite Subjected to Different Temperature Processing. Rock Mechanics and Rock Engineering. 51: 1683-1695.

Kang, H., Zhang, J., Fan, X., Huang, Z., 2020. Cyclic Injection to Enhance Hydraulic Fracturing Efficiency: Insights from Laboratory Experiments. Geofluids. ID: 8844293.

Kong, L., Ranjith, P.G., Li, B.Q., 2021. Fluid-driven micro-cracking behaviour of crystalline rock using a coupled hydro-grain-based discrete element method. International Journal of Rock Mechanics and Mining Sciences. 144: 104766.

Li, N., Zhang, S., Wang, H., Wu, S., Zou, Y., Ma, X., Zhou, T., 2021. Thermal Shock Effect on Acoustic Emission Response During Laboratory Hydraulic Fracturing in Laizhou Granite. Rock Mechanics and Rock Engineering. 54: 4793-4807.

Lisjak, A., P. Kaifosh, L. He, B. S. A. Tatone, O. K. Mahabadi, and G. Grasselli., 2017. A 2D, fully-coupled, hydro-mechanical, FDEM formulation for modelling fracturing processes in discontinuous, porous rock masses. Computers and Geotechnics. 81: 1-18.

Liu, D., 2021. Hydraulic fracture growth in quasi-brittle materials. PhD Thesis No. 8360 Ecole polytechnique federale de Lausanne. 220 pages.

Munjiza, A., Andrews, K.R.F., White, J.K., 1999. Combined single and smeared crack model in combined finite-discrete element analysis. International Journal for Numerical Methods in Engineering. 44: 41-57.

Parisio, F., 2020. Numerical simulation of the Hydraulic Fracturing experiments using different simulation codes. In: The robust stimulation model for the EGS-reservoir in the hot magmatic environment at Acoculco and its verification against the laboratory fracking experiment (Ed. by Deb, P.). Deliverable 6.5 for the GEMex project, 34-42.

Park, D.-W., 2015. Characteristics of the Rock Cleavage in Jurassic Granite, Geochang. The Journal of the Petrological Society of Korea. 24(3): 153-164.

Patel, S.M., Sondergeld, C.H., Rai, C.S., 2017. Laboratory studies of hydraulic fracturing by cyclic injection. International Journal of Rock Mechanics and Mining Sciences. 95: 8-15.

Tatone, B.S.A., Grasselli, G., 2015. A calibration procedure for two-dimensional laboratory-scale hybrid finite–discrete element simulations. International Journal of Rock Mechanics and Mining Sciences. 75: 56-72.

Warpinski, N.R., Branagan, P.T., 1989. Altered-Stress Fracturing. Journal of Petroleum Technology. 41(9): 990–997.

Yoon, J-S., Zang, A., Stephansson, O., Hofmann, H., Zimmermann, G., 2018. Discrete Element Modelling of Fluid Injection and Induced Seismicity in a Blocky Structured Rock Mass. 2nd U.S. Rock Mechanics/Geomechanics Symposium, Seattle, Washington, June 2018. ARMA-2018-787.

Zang, A., Wagner, F. C., Stanchits, S., Janssen, C., Dresen, G., 2000. Fracture process zone in granite, J. Geophys. Res. 105(B10): 23651-23661.

Zang, A., Stephansson, O., 2010. Stress Field of the Earth's Crust. Springer.

Zang, A., Yoon, J.S., Stephansson, O., Heidbach, O., 2013. Fatigue hydraulic fracturing by cyclic reservoir treatment enhances permeability and reduces induced seismicity. Geophysical Journal International. 195(2): 1282-1287.

Zang, A., Stephansson, O., Stenberg, L., Plenkers, K., Specht, S., Milkereit, C., Schill, E., Kwiatek, G., Dresen, G., Zimmermann, G., Dahm, T., Weber, M., 2017. Hydraulic fracture monitoring in hard rock at 410 m depth with an advanced fluid-injection protocol and extensive sensor array. Geophysical Journal International. 208(2): 790-813.

Zhuang, L., Jung, S.G., Diaz, M., Kim, K.Y., Hofmann, H., Min, K.-B, Zang, A., Stephansson, O., Zimmermann, G., Yoon, J.-S., 2020. Laboratory true triaxial hydraulic fracturing of granite under six fluid injection schemes and grain-scale fracture observations. Rock Mechanics and Rock Engineering. 53: 4329-4344.

Zhuang, L., Kim, K.Y., Jung, S.G., Diaz, M., Min, K.-B., 2019. Effect of water infiltration, injection rate and anisotropy on hydraulic fracturing behavior of granite. Rock Mechanics and Rock Engineering. 52(2): 575-589.

Zhuang, L., Zang, A., 2021. Laboratory hydraulic fracturing experiments on crystalline rock for geothermal purposes. Earth-Science Reviews. 216: 103580.

Chapter 4 Mesoscale publication 2: Borehole scale study

Effect of foliation and fluid viscosity on hydraulic fracturing tests in mica schists investigated using distinct element modeling and field data

Farkas, M. P., Yoon, J., Zang, A., Zimmermann, G., Stephansson, O., Lemon, M., Dankó, G. (2019)

Published in Rock Mechanics and Rock Engineering, 52 (2): 555-574.
http://doi.org/10.1007/s00603-018-1598-7.

Effect of foliation and fluid viscosity on hydraulic fracturing tests in mica schists investigated using distinct element modeling and field data

Márton Pál Farkas[a,b,c], Jeoung Seok Yoon[d], Arno Zang[d,c], Günter Zimmermann[a], Ove Stephansson[d], Michael Lemon[e] and Gyula Dankó[b]

[a] Section 6.2 Geothermal Energy Systems, GFZ - German Research Centre for Geosciences, Telegrafenberg, Potsdam 14473, Germany

[b] Golder Associates Hungary, Hűvösvölgyi út 54, Budapest 1021, Hungary

[c] Institute of Earth and Environmental Science, University of Potsdam, Karl-Liebknecht-Straße 24/25, Potsdam 14476, Germany

[d] Section 2.6 Seismic Hazard and Risk Dynamics, GFZ - German Research Centre for Geosciences, Telegrafenberg, Potsdam 14473, Germany

[e] Golder Associates Ltd., 6925 Century Avenue, Suite 100, Missisouga, Ontario L5N 7K2, Canada

Abstract

Several hydraulic fracturing tests were performed in boreholes located in central Hungary in order to determine the in-situ stress for a geological site investigation. At a depth of about 540 meters, the observed pressure versus time curves in mica schist with low dip angle foliation show atypical pressure versus time results. After each pressurization cycle, the fracture breakdown pressure in the first fracturing cycle is lower than the refracturing or reopening pressure in the subsequent pressurizations. It is assumed that the viscosity of the drilling mud and observed foliation of the mica schist have a significant influence on the pressure values. In order to study this problem, numerical modelling was performed using the distinct element code PFC (Particle Flow Code), which has been proven to be a valuable tool to investigate rock engineering problems such as hydraulic fracturing. The two-dimensional version of the code applied in this study can simulate hydro-mechanically coupled fluid flow in crystalline rock with low porosity and pre-existing fractures. In this study, the effect of foliation angle and fluid viscosity on the peak pressure is tested. The atypical characteristics of the pressure behavior are interpreted so that mud with higher viscosity penetrates the sub-horizontal foliation plane, blocks the plane of weakness and makes the partly opened fracture tight and increase the pore pressure which decreases slowly with time. We see this viscous blocking effect as one explanation for the observed increase in fracture reopening pressure in subsequent pressurization cycles.

Keywords

Hydraulic fracturing; Stress measurement; Particle Flow Code; Hydro-mechanical coupling; Micro cracking; Viscous blocking

4.1 Introduction

The knowledge of the current stress state is essential for underground construction and stability. To determine the in situ state of stress at a given site is a challenging task (Stephansson and Zang, 2012). In particular, stress magnitudes play a key role in calibration of geomechanical models for the safety assessment of underground or surface site such as nuclear waste repository or nuclear power plant (*NPP*). The measured in-situ stress field contributes to the assessment of tectonic evolution and any potential fault slip. A fault slip may jeopardize the long term stability of the facilities. Therefore, such assessments must consider the ranges of stress magnitudes and orientation at different depths to determine tectonic regimes and their stability.

Hydraulic fracturing (*HF*) is the most widely used in-situ stress measurement technique that enables estimating stress magnitudes and orientation at various depths over relatively large rock volume, i.e. 0.5 to 50 m^3 (Amadei and Stephansson, 1997). The suggested *HF* test procedure by Haimson and Cornet (2003) and Zang and Stephansson (2010) is summarized as follows.

The suggested method assumes a borehole drilled parallel to a principal stress direction (typically vertical) and requires the identification of rock formations to be tested using extracted cores and/or borehole images. The selection of test intervals for *HF* aims at avoiding fractures or other structural features. The test interval is sealed off by inflating straddle packers at the selected depth, generally by pumping water.

The test interval is first pressurized to assess the performance of the packers and to confirm that open, conductive fractures are not present (formation integrity test). During the first, breakdown cycle, the interval pressure is raised by maintaining a constant, predetermined, flow rate to achieve the peak pressure at which the borehole wall fractures, termed as fracture breakdown pressure *FBP* (Zang and Stephansson 2010) within 3 to 5 minutes. Immediately after observing tensile breakdown, the interval pressure is shut-in to limit the extent of hydraulic fracture propagation. Interval pressure will decay, initially at a higher rate while the newly created hydraulic fracture is still open, and then much slower, after the fracture has closed. The pressure decay is monitored for approximately 5 minutes, then released to initial, static pressure (termed as venting or flow back). The pressure at which the fracture closes is termed shut-in pressure (*SIP*). The pressure measured immediately after the shut-in operation started is referred to as instantaneous shut-in pressure (*ISIP*).

Once the interval pressure returns to the static pressure, the interval is pressurized at the same flow rate as breakdown cycle to observe the reopening or refracturing pressure of the newly created hydraulic fracture (*RFP*). The flow is maintained for several minutes to observe the fracture propagation pressure, followed by shut-in. The pressure decay is monitored to identify the shut-in pressure. Reopening cycles can be conducted two or three times in order to establish consistent fracture reopening and shut-in pressure.

After the reopening cycle(s), a step-rate or jacking pressurization cycle can be conducted to confirm the RFP under controlled conditions. The pressure in the interval is first brought to a very low level and maintained constant while the flow rate is measured. Thereafter, the interval pressure is raised to a new higher value and again the flow rate is allowed to stabilize at a constant level. This is repeated several times, which results in constant pressure levels measured at different flow rates. Once the interval pressure exceeds the RFP, the newly created fracture opens, i.e. deviation from linear trend is observed on pressure versus flow rate plot. The injection is stopped and the test interval is shut-in for pressure decay monitoring. After completion of the test cycles, the packers are deflated and moved to the next test interval.

The fluid pressure required to generate, propagate, sustain and reopen fractures in rock is related to the magnitude of the existing stresses. The direction of the in-situ stresses is inferred by observing the orientation of the hydraulically induced fractures by comparison of the pre- and post-test (acoustic or resistivity) borehole images to determine the presence and orientation of a newly created hydraulic fracture.

Although it is relatively straightforward to measure stress magnitudes using *HF* (Zang and Stephansson 2010, Zoback 2010), pressures determined by this method still suffers from uncertainties due to the natural (intrinsic) anisotropy and heterogeneity of the rock mass. Furthermore, uncertainties in *HF* stress measurements are not only related to inherent rock properties but also to measurement technique and data analysis (Amadei and Stephansson, 1997).

It must be noted that methods commonly used for determining the minimum stress – apart from traditional hydraulic fracturing – are the leak-off tests (*LOT*) and extended leak-off tests (*xLOT*). The main difference between *HF* and *LOT*/*xLOT* is that *HF* is conducted in a section away from the well bottom while the latter is normally performed under the casing shoe, typically at the very bottom of the drill hole. The difference in geometry between *HF* and *LOT*/*xLOT* is likely to have an influence on the determination of the minimum stress (Zang et al., 2012).

Several field, laboratory and numerical studies have been reported on pressure-time records that are unusual and make the interpretation complicated. In the following, we give three examples for anomalous breakdown and peak pressure behavior during HF testing. First, early in-situ *HF* tests in deep intervals (up to 1000 m depth) as reported by Healy and Zoback (1988) and Hickman and Zoback (1983) show the peak pressure attained in crystalline rock on the first cycle is lower than that attained on subsequent cycles. The authors explain the unusual behavior by either fracture formation at the time of the packer inflation or low, and varying rock tensile strength. Second, recent HF stress measurements in granite and shale on laboratory scale reported by L. Zhou et al. (2016) and Lin et al. (2017), respectively, show similar, peak pressure features when increasing injection fluid density and viscosity. These observations from laboratory investigations are also supported by results from numerical modeling presented by Shimizu et al. (2011) and Zhou J et al. (2016a).

In this study, we use recent in-situ *HF* rock stress measurements in boreholes at depth up to 1500 m that were conducted by Golder Associates Hungary (Lemon et al., 2016) to assess the stress regime as part of a geotechnical and hydrogeological investigation for the Paks II Nuclear Power Plant (*NPP*) Extension Project (Paks II project) in Hungary (ÁKMI, 2016). At several test intervals, in-situ *HF* stress measurements were performed in which recorded pressure – time data exhibit higher *RFP*s than *FBP*.

The goal of this study is to better understand processes that can lead to larger reopening fracture pressure *(RFP)* than first breakdown pressure (*FBP)* as observed in stress measurement data obtained in the project. Thus, we performed numerical modelling using the distinct element method and the two-dimensional Particle Flow Code, PFC^{2D} (Itasca, 2008) to simulate several pumping cycles in three different PFC models.

The paper is structured as follows. In section 4.2, the most relevant characteristics of the Paks II *NPP* Extension Project and the *HF* rock stress field measurements are summarized. In section 4.3, the two-dimensional hydro-mechanically coupled discrete element code and the model geometry are reported. In section 4.4, the injection procedure and the breakdown and reopening pressure cycles are described. In sections 4.5 and 4.6, results of the PFC modeling are compared with field data, assessed and discussed. Finally, the viscous blocking idea is developed for anisotropic rock (mica schist) to explain the lowering of peak pressure in subsequent hydraulic testing cycles observed in the field.

4.2 Hydraulic Fracturing Stress Measurements and Data

4.2.1 The Paks II Project Testing Program

The Paks Nuclear Power Plant (*NPP*) is located south of the town of Paks in central Hungary (Figure 1). To comply with requirements of the Hungarian Atomic Energy Authority and the International Atomic Energy Agency for permitting construction of new power units, referred to as Paks II project, a geological investigation was conducted in 2015-2016 (ÁKMI, 2016). In the framework of this project, several Hydraulic Fracturing (*HF*) stress measurements were performed to create a geomechanical model of the site (Lemon et al., 2016). The measurements were conducted at 19 intervals in each of four boreholes, PAET-26, PAET-27, PAET-29 and PAET-34, drilled for geotechnical and hydrogeological investigations. Figure 1 shows the location of the four boreholes tested and Figure 2 summarizes the obtained stresses. The target depths of the test zones were selected to assess the in-situ stresses within the primary geologic units of the site. Variscan metamorphic basement rocks are intercepted by borehole PAET-26, Mesozoic carbonate basement rocks (Jurassic marl and limestone rocks) are intercepted by borehole PAET-27 and Miocene dacitic rocks (Mecsek Andesite Formation) intercepted by PAET-29 and PAET-34. The depth of test intervals varies between 500 and 1500 m.

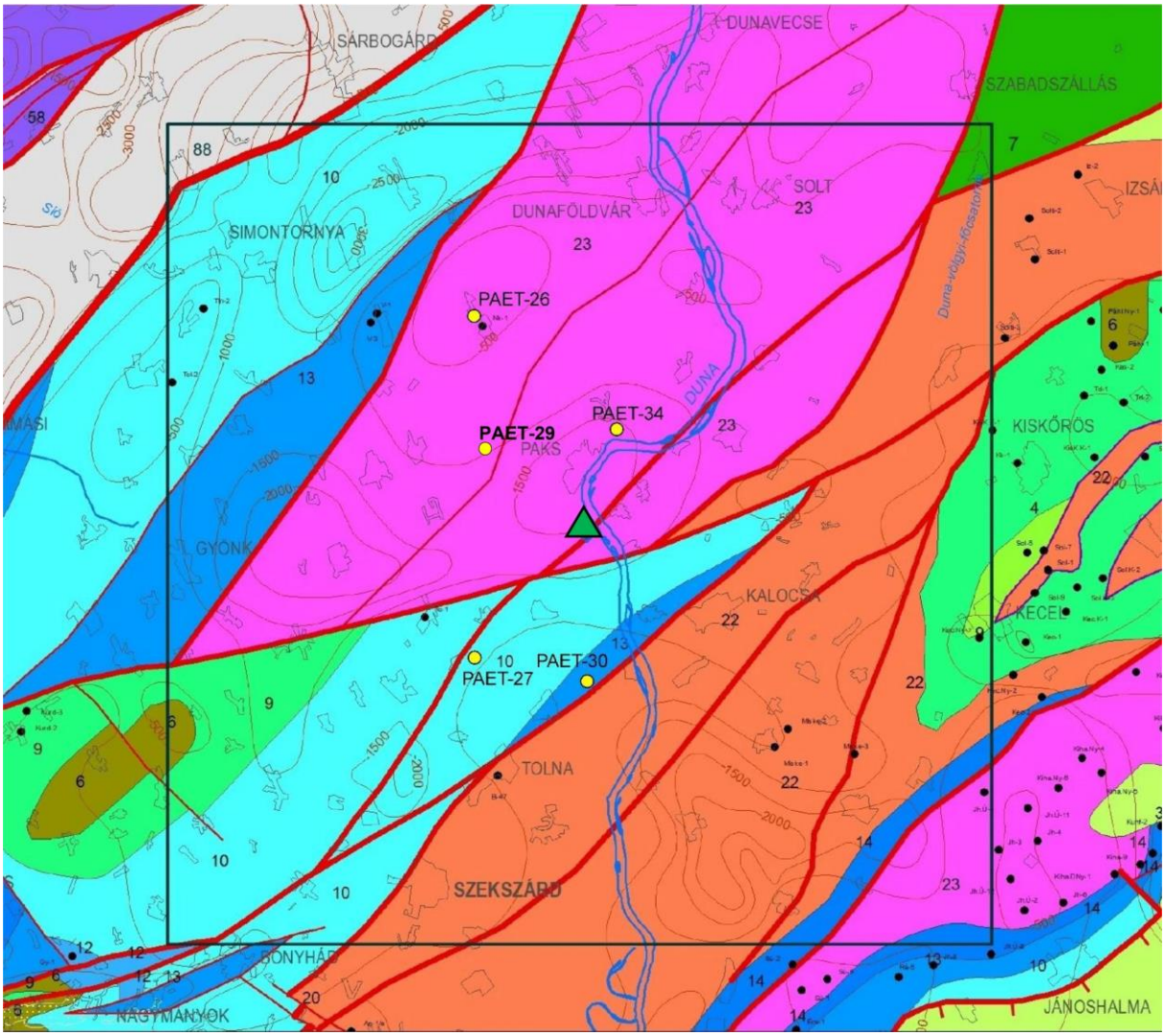

Figure 1: Map of Pre-Cenozoic basement rock in central Hungary, showing mapped faults. The boundary of the study area of Paks II project is indicated by black square (60 x 60 km). The map shows the location of boreholes tested excluding PAET-30 (yellow circles). The Paks Nuclear Power Plant is indicated by green triangle. Rock types: Cyan (color code 10): Lower-middle Jurassic pelagic, fine siliciclastic rock; pink (color code 23): Variscan metamorphic rock (after ÁKMI, 2016).

The testing equipment was provided by Golder Associates Hungary and included the following:

- Two inflatable packers, arranged for a test interval length of 1.33 meters;
- High pressure pump for inflating packers and injecting water into the test interval;
- Inflation line attached to the test tubing;
- Flow control board, located at surface for controlling water pressure and flow rate of test interval and packer pressure;
- Electronic instrumentation and data acquisition system for monitoring and recording injection pressures, flow rates and packer pressures; and
- Pressure gauge with internal memory, positioned inside the test interval.

Packer pressure, test interval pressure, and flow rate were continuously monitored and recorded during each test. Pre- and post-testing acoustic borehole images (BHTV) were used to determine the location and orientation of any newly created fracture.

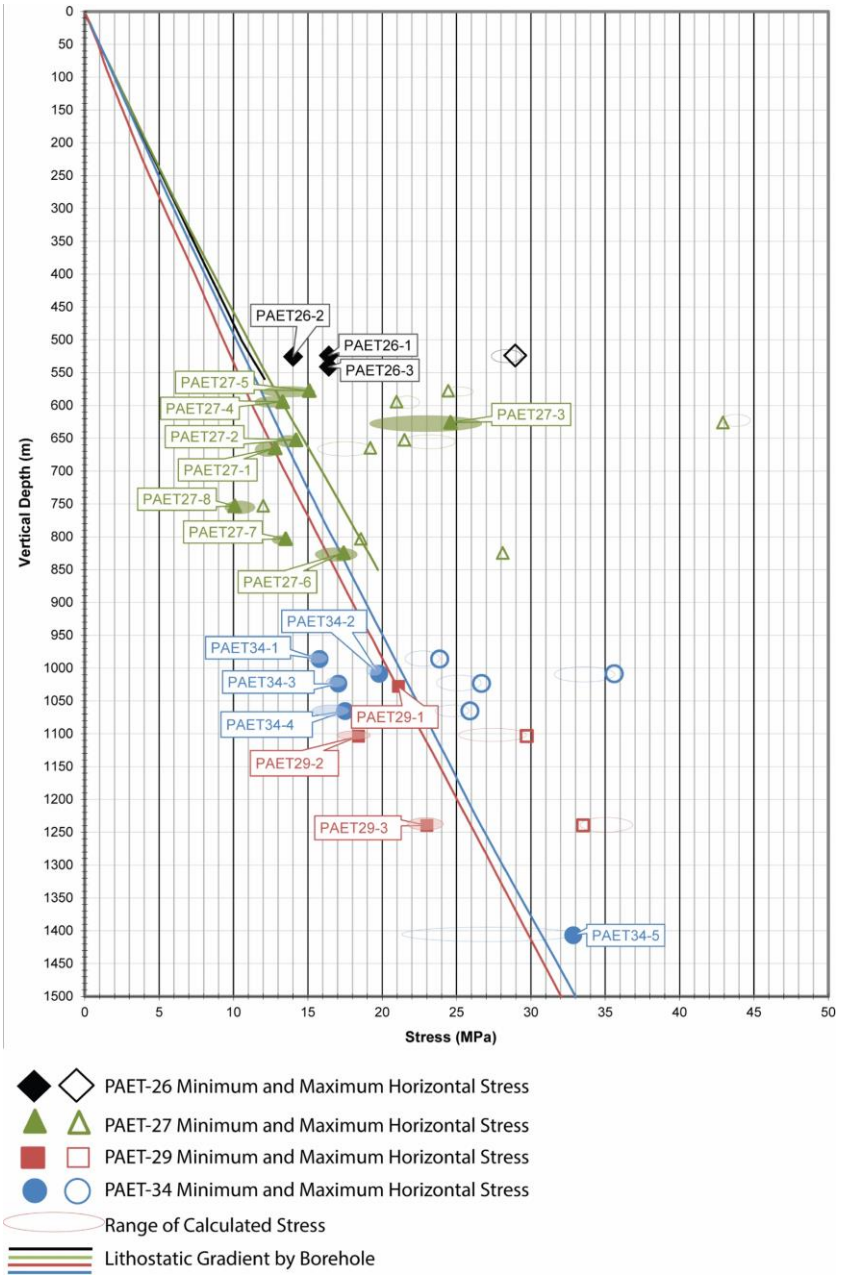

Figure. 2: Summary of in-situ stresses measured at 19 intervals in basement rock of boreholes PAET-26, PAET-27, PAET-29 and PAET-34 for the Geological Research Program for Paks II project in Hungary (after Lemon et al., 2016).

4.2.2 Results of Hydraulic Fracturing Tests in Borehole PAET-26

In this paper, we focus on the interpretation of the pressure versus time records of the test results from borehole PAET-26 as a representation of the test intervals showing ambiguities in the interpreted *FBP* and *RFP*. For other test interval results and analysis, the reader is referred to ÁKMI (2016) and Lemon et al. (2016).

Borehole PAET-26 was drilled vertically down to 560 m, with a 4 ¾" casing down to 502 m in 2015. The tested open hole section is approx. 60 m long with a diameter of 96 mm. The open hole section is located in Variscan metamorphic basement rock formation which lies beneath the poorly consolidated sedimentary sequence of Upper Pannonian Újfalu and Algyő Formations (Figure 3).

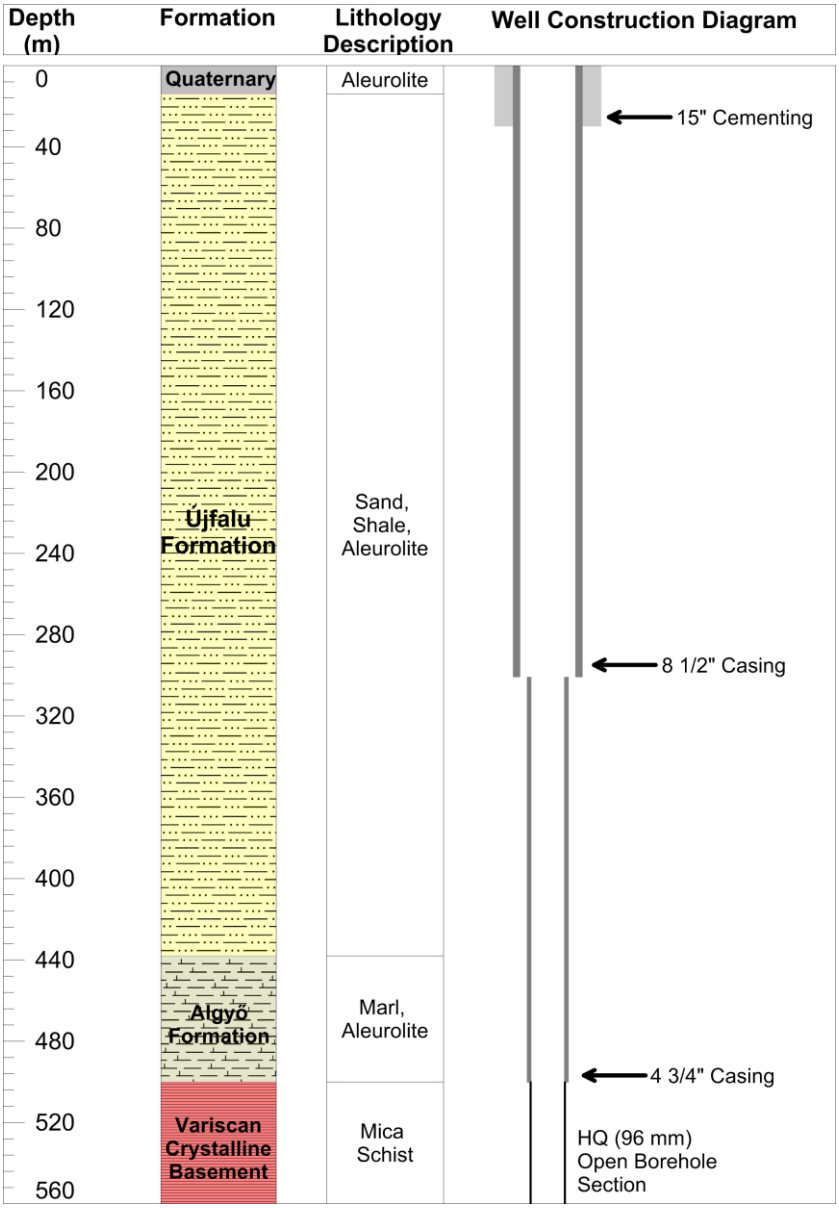

Figure 3: Stratigraphy and well construction diagram of borehole PAET-26.

In borehole PAET-26, the rock tested is fresh, strong, dark gray to light gray, mica schist which has a W-NW strike and mostly shallow dipping foliation of between 0° and 15° at depth between 500 to 550 m (Figure 4). Test intervals in crystalline basement rock were selected from sections free of natural fractures and relatively limited presence of planes of foliation planes. Prior to testing, the open borehole intervals were not flushed by water to prevent wellbore instabilities. Thus, hydraulic fracturing could only be performed using drilling mud with a density of 1060–1160 kg/m^3.

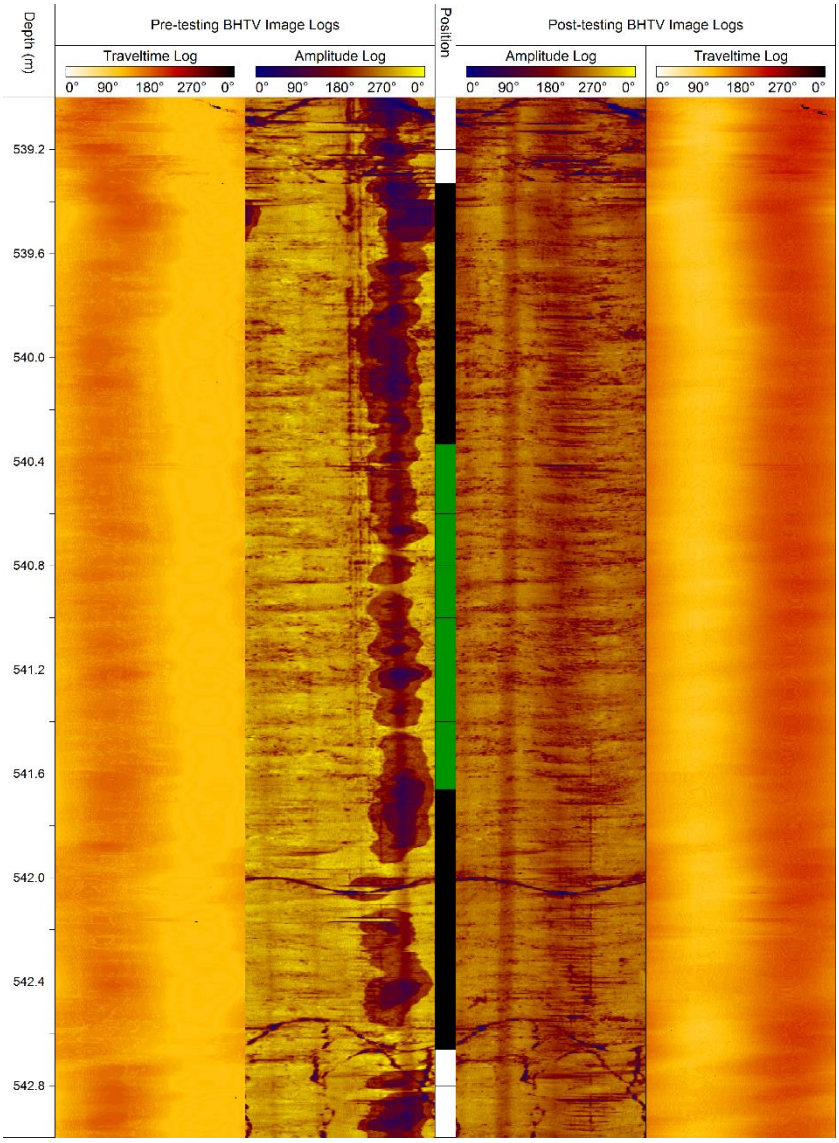

Figure 4: Pre- and post-testing acoustic borehole televiewer (BHTV) logs of the tested Mica Schist rock interval in borehole PAET-26 at approx. 540 m depth. Area highlighted in green in center shows the hydrofractured interval which does not show any fracture prior to testing. The areas in black below and above the interval show the location of the straddle packers. Continuous, blurry areas are results of device effects. No new features are visible in the post-testing images which indicates an induced fracture that closed after stimulation or hydraulic fracture propagation in horizontal plane.

The goal of the pressurization cycles is to provide sufficient data to obtain repeatable values of the following pressures from each test interval:

- Fracture breakdown pressure (*FBP*), determined from the peak pressure of Cycle 1;
- Reopening or refracturing pressure (*RFP*), identified as the variation in pressurization rate of Cycle 2 relative to Cycle 1;
- Derivative shut-in pressure (*DPDT*), determined by the intersection of tangents on the time derivative of pressure plot, which indicate a change in the interval conductivity caused by the fracture closure, from cycle 2 and subsequent cycles; and

- Jacking pressure (*JP*), determined by the deviation from linear or laminar flow on the plot of pressure against flow rate from a series of jacking or step-rate test steps based on Doe and Korbin (1987).

These pressure values are used to estimate the minimum stress (σ_3) exerted perpendicular to the fracture face that is opened. The maximum horizontal stress (S_{Hmax}) is calculated from the minimum horizontal stress (S_{hmin}), the *FBP*, the *RFP*s and the tensile strength of the rock (T) using the Hubbert-Willis equation in Zang and Stephansson (2010):

$$S_{Hmax} = 3S_{hmin} - FBP + T - P_p, \quad (1)$$

where P_p is the pore pressure. The vertical stress, the magnitude of overburden load or lithostatic stress (S_v) is accepted to act vertically, parallel to the well orientation, and is calculated from the cumulative neutron density profile.

Three successful *HF* tests were completed in PAET-26. The complete pressure-time records for one of the tested intervals in PAET-26 for depth at 540.33 to 541.66 m are presented in Figure 5a as a representation of all conducted measurements in this borehole. The breakdown, refracturing, shut-in and jacking pressures and the estimated stresses for this interval are calculated, and summarized in Table 1. These show that after an initial interval or formation integrity test (*FIT*), a breakdown cycle is followed by two refracturing cycles and a jacking cycle. The jacking cycle was invalid due to pump malfunction. A third refracturing cycle was conducted with an extended pumping period followed by a modified jacking cycle and a final, fourth refracturing cycle.

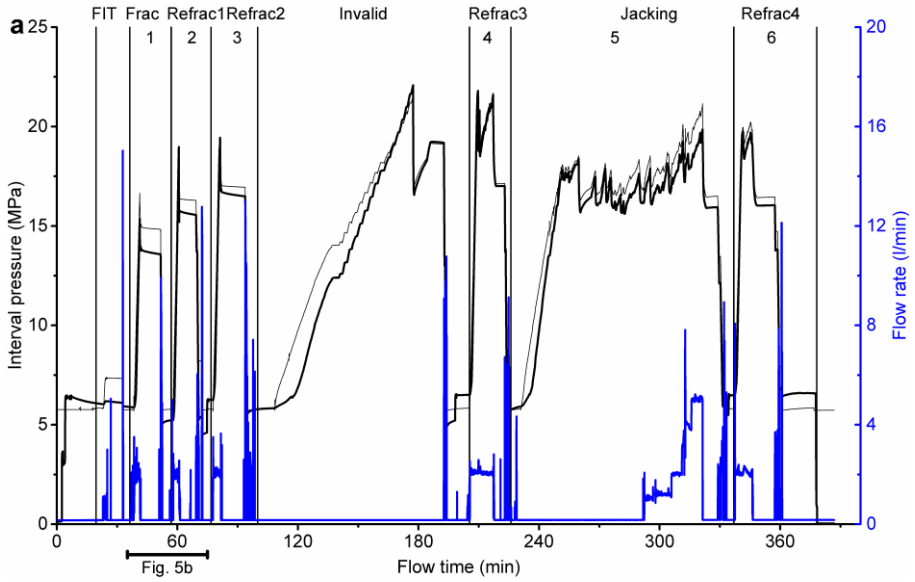

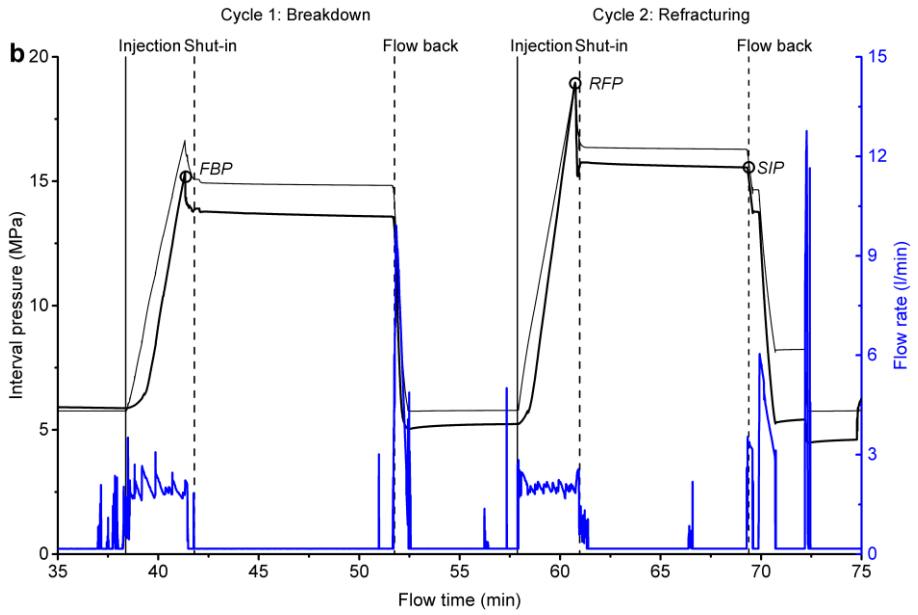

Figure 5: a: Summary plot of interval pressure and flow rate of pressurization cycles at a tested interval at approximately 540 m depth in borehole PAET-26. The cycles are indicated by numbers with respect to information in Table 1. Black thick and thin pressure curves show pressure recorded at the interval and within the packers, respectively. Vertical lines indicate the duration of each injection cycle. Flow rate (blue) during injection and flow back are plotted on same positive axis. For color interpretation of this figure, the reader is referred to electronic version of this paper (after Lemon et al. 2016). b: Summary plot of interval pressure and flow rate of pressurization cycle 1 (Breakdown) and cycle 2 (Refracturing) at a tested interval at approximately 540 m depth in borehole PAET-26. Black thick and thin pressure curves show pressure recorded at the interval and within the packers, respectively. Thick and dashed vertical lines indicate duration of each cycle and operations during testing, respectively. Flow rate (blue) during injection and flow back are plotted on same positive axis.

Table 1 Summary of HF tests in one tested intervals as a representation for all three in-situ stress measurements in borehole PAET-26. Pressures presented are measured at the test interval, which includes the pore pressure. The pressures in bold provide confidence in the selected minimum stress (S_{hmin}) value (after Lemon et al., 2016).

	Cycle number	Cycle type	Injected Fluid Volume (l)	Flow Back Volume (l)	Peak Pressure (MPa)**	Shut-in Pressure (MPa)	Jacking Pressure (MPa)
Test interval in borehole PAET-26 in Mica Schist* Depth: 540.33 - 541.66 m	1	Breakdown	6.7	4.9	16.5	-	-
	2	Refracturing	6.9	6.5	19.0	**16.4**	-
	3	Refracturing	8.8	8.3	19.3	17.0	-
	4	Refracturing	25.0	7.5	21.7	17.1	-
	5	Jacking	72.0	6.6	21.1	**16.4**	**16.5**
	6	Refracturing	18.6	6.6	20.2	**16.4**	-

* Drilling mud viscosity and density: 10 mPa s, 1060–1160 kg/m^3
** Fracture breakdown pressure (*FBP*), refracturing or reopening pressure (*RFP*) of respective cycles

The interval tested shows a tensile *FBP* in Cycle 1 with increasing peak pressures in subsequent refracturing cycles to a maximum of 19.3 MPa in Cycle 3 at a flowrate of approximately 4 l/min (Figure 5b). The shut-in pressure (*SIP*) of the refracturing cycles as well as the jacking cycle show similar fracture closure pressure of approximately 16.4 MPa. The determination of fracture closure pressure from cycle 2 using the pressure versus square root time and DPDT plots is illustrated in Figure 6a and Figure 6b, respectively.

Based on these consistent pressures, the minimum principal stress of 16.4 MPa is selected for the test interval. Using eq. (1), the estimated maximum principal stress (σ_1) equals 29 MPa. The vertical stress (S_v) is estimated as 11.6 MPa from neutron density logging. Figure 2 shows that the minimum

stresses measured for all three tests in this well are above lithostatic stress, which indicates either thrust faulting regime (S_v<S_{hmin}<S_{Hmax}) or the test results indicate an intermediate stress (Table 1 and Figure 2). Comparison of pre and post-testing acoustic televiewer logs for three tested intervals in PAET-26 does not show any newly induced hydraulic fracture (Figure 4), which prohibits assessment of the direction of the measured minimum stress.

The estimated stresses and the lack of presence of induced hydraulic fracture in the post-testing borehole image imply that either the fracture closed completely after *HF* or the newly induced or reactivated fracture propagated in the direction of the sub-horizontal foliation plane.

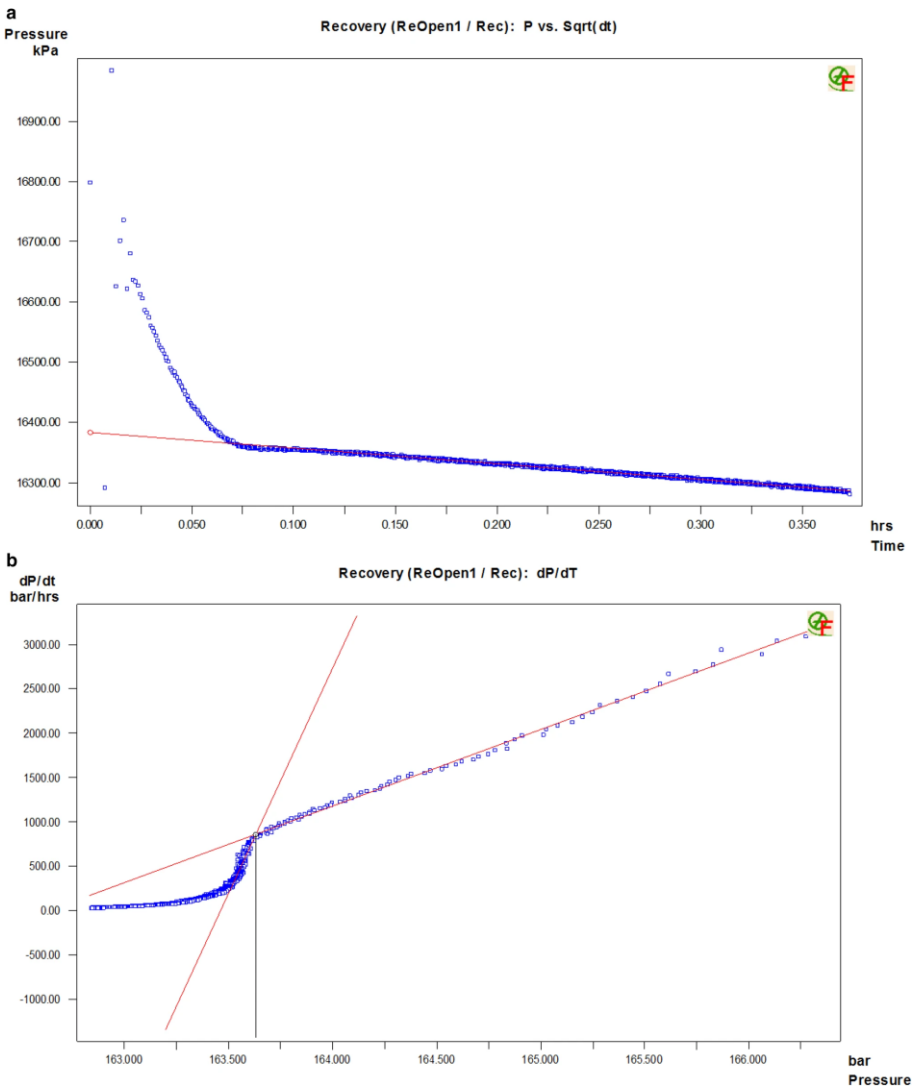

Figure 6: a: Plot of pressure versus square root time showing a SIP of 16.4 MPa for cycle 2 (Refracturing) at a tested interval at approximately 540 m depth in borehole PAET-26 (after Lemon et al. 2016). b: Time derivative of pressure (DPDT) versus square root time showing a SIP of 16.4 MPa for cycle 2 (Refracturing) at a tested interval at approximately 540 m depth in borehole PAET-26 (after Lemon et al., 2016).

4.3 Numerical Model

4.3.1 Two-dimensional Particle Flow Code and fluid flow algorithm

The ITASCA Particle Flow Code (PFC^{2D}) uses an explicit time integration scheme to solve the equations of motion for an aggregate of rigid discrete circular particles (Itasca 2008). PFC^{2D} is also referred to as the bonded-particle model (BPM) since the contacts between the circular particles are defined through so-called parallel bonds and enhanced by cementing material at the contacts with finite thickness (Figure 7). The integration scheme, that is, the mechanical calculation cycle in PFC2D is a time stepping algorithm that iterates between the law of motion applied to each particle and the linear force displacement law including fluid induced deformation applied to each contact (Figure 8). The geomechanical simulator defines strength at the contacts in terms of Mohr-Coulomb failure criterion (Itasca 2012; Labuz and Zang 2012). Due to mechanical loading and loading from fluid pressure, the bonds can break in tension (Mode I) or shear (Mode II). For more details, we refer to Potyondy and Cundall (2004).

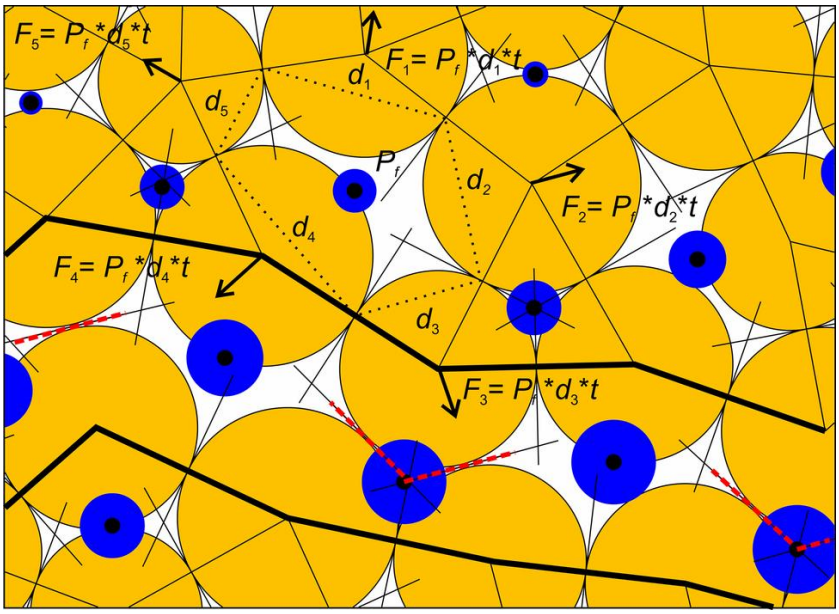

Figure 7: Close-up view of numerical model showing circular particles of different size (average particle radius is 1 mm) and pore network model. Flow channels (solid segments at contacts between two particles) are connecting to neighbouring domains (pore spaces) bounded by a solid polygon. Black dots at the polygon centres are virtual pores where fluid pressure (P_f) is stored. The blue circles around those are proportional to magnitude of stored fluid pressure. The dotted polygon shows contributing segments used for calculating domain volume. Arrows are resultant forces applied to the particles surrounding the pore spaces due to fluid pressure P_f. Micro cracking due to fluid injection is represented as broken parallel bond contacts (dashed line) either in mode I or mode II. A chain of micro cracks builds up a visible macrocrack which can be bounded (area between two bold lines).

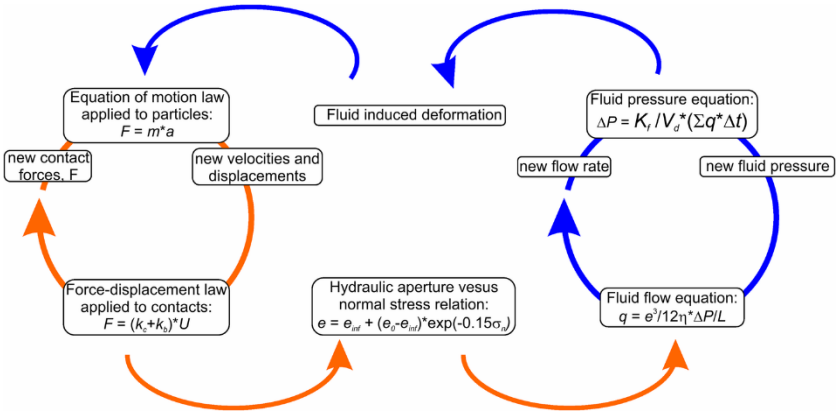

Figure 8: Hydro-mechanical coupling in PFC^{2D} (m: particle mass; a: acceleration; k_c: contact stiffness, k_b: bond stiffness; U: particle overlap).

The fluid flow algorithm of the hydraulic cycle provides a way to investigate hydraulic treatment from a borehole into the host rock. In this study we use the hydro-mechanically coupled code of PFC^{2D} developed by Hazzard (2002), Yoon et al. (2014) and Yoon et al. (2017). The algorithm assumes that each particle bonded contact corresponds to a flow channel which connects up pore spaces (so-called domains) that can store pressure and once a domain is pressurized, it becomes fully saturated (Figure 7). In this sense poroelasticity is explicitly considered in the applied version of PFC^{2D}.

We use the experimentally derived relation between hydraulic aperture and normal stress in crystalline rock based on Hökmark et al. (2010):

$$e = e_{inf} + (e_0 - e_{inf})exp(-\alpha\sigma_n), \quad (2)$$

where e_{inf} denotes the residual hydraulic aperture at infinite normal stress, e_0 is hydraulic aperture at zero normal stress, σ_n corresponds to effective normal stress on a flow channel and coefficient α controls the rate of aperture decrease with increasing normal stress. We assume that the foliation plane does not have asperities that may prevent surface closure. Based on developments by Yoon et al. (2017) the PFC^{2D} code uses two different hydraulic aperture (e) versus normal stress (σ_n) relations. These are assigned to particle contacts representing foliation (smooth joint introduced by Mas Ivars et al. 2008) and rock matrix (parallel bond). Figure 9 shows that initial hydraulic aperture (e_0) in rock matrix (orange) is approx. 0.6 µm and 6 µm in foliation (blue) and decreases to 0.1 µm and 1 µm (e_{inf}), respectively, with increasing normal stress. These values are in good agreement with aperture derived from field hydraulic tests (ÁKMI, 2016). Coefficient of decay (α) is set to 0.15 for both foliation and rock matrix based on Hökmark et al. (2010).

Permeability of rock matrix and foliation are defined by hydraulic aperture. The initial hydraulic aperture for a given permeability (k) is estimated using the derivation by Hazzard et al. (2002):

$$e_0 = \sqrt[3]{\frac{24k\pi\sum_{particles}R^2}{(1-n)\sum_{pipes}L}}, \quad (3)$$

where R is the particle radius, n is the mean porosity and L is the pipe (flow channel) length.

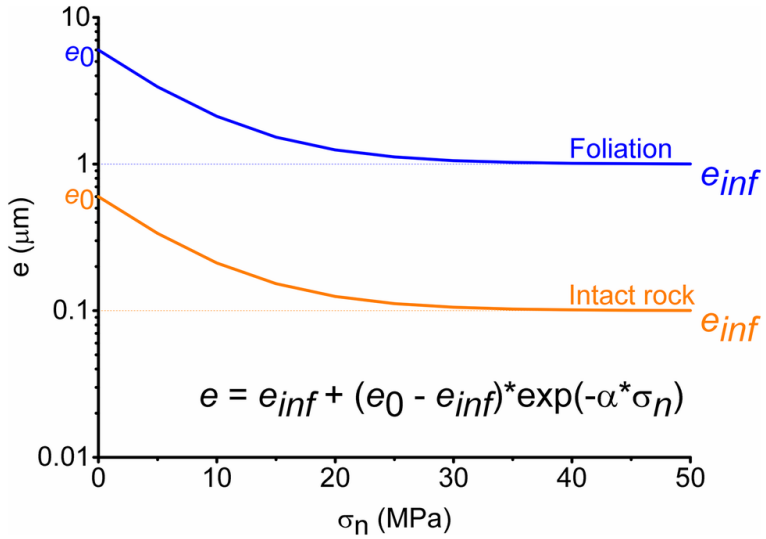

Figure 9: *Hydraulic aperture (e) versus normal stress (σ_n) of intact rock and foliation plane.*

4.3.2 Model description

The coupling between hydraulically induced fracture propagation, fluid flow and foliation is studied through three rock mass models. The first model contains no foliation, i.e. the material is considered homogeneous and isotropic as well as serves as base model (case A in Figure 10). In the second and third rock mass models (case B and C in Figure 10), smooth joint contacts are applied to simulate foliation. In model B smooth joints are parallel to S_H and in model C tilted by 15° clockwise with respect to S_H.

Field data presented in Section 4.2 suggest that the induced fracture propagated in the horizontal direction (parallel to sub-horizontal foliation) and therefore, 2D vertical sections of 2 m x 2 m are generated (Figure 10). The chosen size of the rock model to the volume involved in *HF* stress measurement is an isolated, approx. one-meter-long open hole section. About 15.000 particles are generated in the models with the parameters listed in Table 2. Average particle size is about 1 mm, and, in agreement with grain size of typical mica schist from the Paks site.

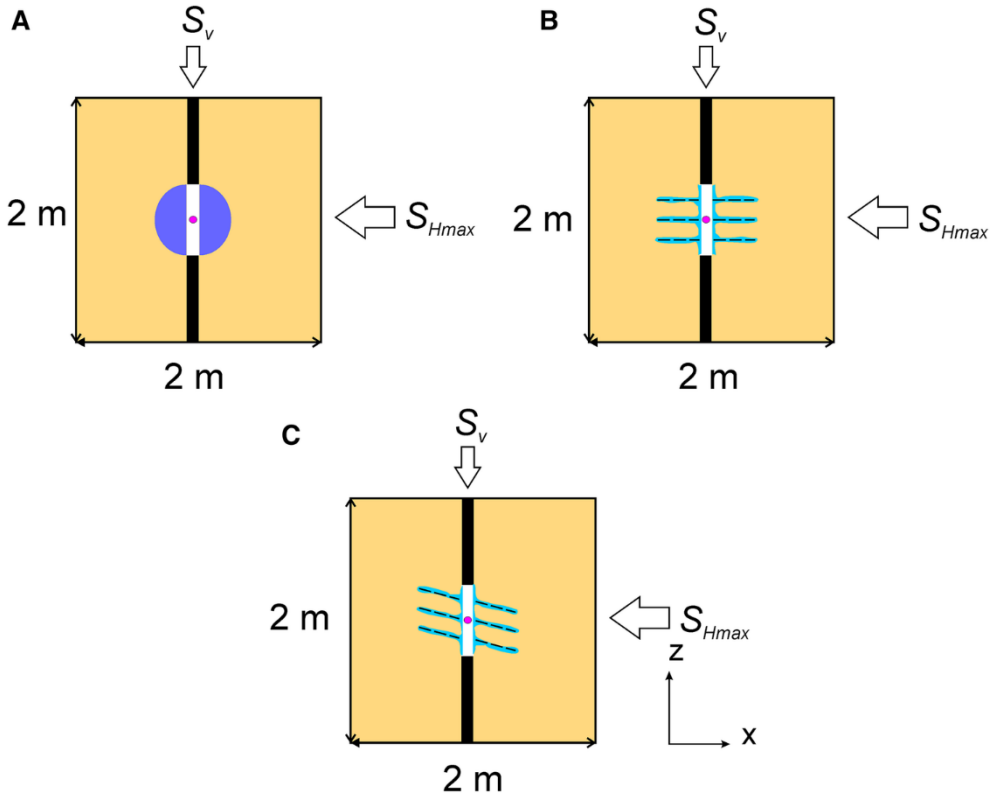

Figure 10: *Three 2D numerical rock models with the in-situ stress field and idealized fluid front distributions. A: rock model without foliation; B: rock model with foliation parallel to orientation of maximum horizontal stress; C: rock model with foliation tilted by 15° with respect to maximum horizontal stress (S_{Hmax}). Injection point is in open test section created by deleting particles between upper and lower packers in the borehole. Injection fluid has a viscosity of 1 mPa s in rock model A (blue), and that of 10 mPa s in rock models B and C (cyan).*

Table 2: Parameters used in the bonded-particle numerical modelling with PFC ^{2D}.

Particle parameters		Units	Parallel-bond parameters for rock matrix		Units
Particle number	15299	-	Radius multiplier	1	-
Young's modulus	40	GPa	Moment contribution factor	1	-
Normal/shear stiffness ratio	2.5	-	Young's modulus	40	GPa
Coefficient of friction	0.9	-	Normal/shear stiffness ratio	2.5	-
Minimum radius	0.7	mm	Tensile strength	11.5±-1.5	MPa
Max/min radius ratio	1.5	-	Cohesion	26±-2.6	MPa
Ball density	2630	kg/m^3	Angle of internal friction	45	°
Parallel-bond parameters for sealing packers		**Units**	**Parallel-bond parameters for smooth joints**		**Units**
Radius multiplier	1	-	Normal stiffness	300	GPa/m
Moment contribution factor	1	-	Shear stiffness	30	GPa/m
Young's modulus	40	GPa	Friction coefficient	0.9	-
Normal/shear stiffness ratio	2.5	-	Dilation angle	3	°
Tensile strength	20.5	MPa	Tensile strength	3	MPa
Cohesion	35	MPa	Cohesion	0.1	MPa
Angle of internal friction	45	°	Angle of internal friction	30	°

The mechanical properties of the host rock is calibrated through a trial-and-error process described in Potyondy and Cundall (2004). The rock mass model without foliation is calibrated against laboratory data using the rock model described above (Table 3). According to Table 3, the calibrated Young's modulus, Poisson's ratio and Uniaxial Compressive Strength (*UCS*) are between measured minimum and maximum values, however, the Brazilian Tensile Strength (*BTS*) is somewhat higher in

the rock mass model. This can be associated with the limited capability of PFC2D in complete matching of *UCS* to *BTS* ratio (Potyondy and Cundall, 2004). On the other hand, the high variability in BTS is typical for foliated metamorphic rock, such as gneiss or mica schist (Zang and Berckhemer, 1993).

Table 3: Geomechanical laboratory data from ÁKMI et al. 2016 and simulation data.

Parameter	Laboratory data (average, min, max)	Simulated data	Units
Young's modulus	36.3, 24.7, 59.7	52.9	GPa
Poisson's ratio	0.25, 0.18, 0.34	0.24	-
Uniaxial compressive strength	65.5, 51.5, 98.8	97.3	MPa
Brazilian tensile strength	4.9; 2.8, 6.4	9.8	MPa

Numerical microparameters in Table 2 are chosen to best resemble foliated mica schist and provide reasonable computation time as well. Foliations in this study are implemented as smooth-joints model which is a contact model that allows particles to slide past one another without over-riding one another (Mas Ivars et al., 2008). A joint is created by assigning this contact model to all contacts between particles that lie upon opposite sides of the joint surface. Length and number of joints are arbitrarily determined. The generated joint fabric is then overlaid on to the bonded particle assembly. Those particle contacts which were assigned with parallel bonds and located along the joint fabric are switched to smooth joint contacts and assigned with mechanical properties that are listed in Table 2. The length of each segment of joint set (0.2 m) is chosen arbitrarily in order to prevent model boundary effects. The rock mass model is pre-conditioned to have a bulk permeability of 10^{-18} m^2 that determines initial hydraulic aperture (e_0) in both rock matrix and foliation based on eq. (3).

The chosen parameter value enables maintaining numerical stability, provides reasonable time steps and also, hydraulic aperture that shows good agreement with data derived from hydraulic field tests (Lemon et al., 2016). The pressure at both pore spaces (domains) connected by this broken contact is set to the average of those pressures. Therefore, it is assumed that the two pore spaces that were separated before the bond break become one space (Figure 7).

Figure 10 shows rock mass models A, B and C, in which the open hole interval between the packers is created by deleting particles in the center area with a size of 50 cm x 5 cm. Straddle packers are modelled as material regions above and below the open hole area by defining lower hydraulic aperture (1 nm, that is, impermeable) to prevent leak-off into the packers during injection. Furthermore, the particle contacts in the packer are treated stiffer and stronger than those contacts in the rock part to prevent fracturing (Table 2).

The applied in-situ stress field of the rock mass models agrees with the measured in-situ data (Section 4.2): the vertical stress ($S_v = S_{zz}$) equals 15 MPa and the maximum horizontal stress ($S_{Hmax} = S_{xx}$) equals 30 MPa.

4.4 Simulation of injection procedure

Several injection cycles are performed to simulate injection phases and flow back. After injection, shut-in is simulated by stopping pumping and the interval pressure decreases as fluid leaks-off into stimulated rock mass. Since pressure relaxation always requires more time than to create or extend hydraulic fracture – especially for fluid with higher viscosity– the time for shut-in periods are set longer, i.e. double of that for injection in each model case. It must be noted that injected fluid cannot be removed from the borehole model, hence, interval pressure will not decay to zero after any stimulation cycle. The simulation ends after the refracturing cycle as the induced hydraulic fracture reaches model boundary.

Hydraulic fracturing of a given interval in a borehole is modelled as fluid being injected into an unpressurized hydraulic domain (Section 4.3.1). This is located at the center of the open borehole section as well as the rock mass model, which is represented by particles deleted between the sealing packers. Injected fluid may flow from the stimulated central domain to those which are directly connected.

Figure 10 illustrates how water - with viscosity of η = 1 mPa s - is injected into model A, in rock mass without foliation. In model B and model C, drilling mud with viscosity of η =10 mPa s, is used for stimulation into rock mass with pre-existing foliation. In all models the injection flow rate is set to 3.6 l/min according to the applied flow rate of the field tests (Table 4).

Hydro-mechanical processes during simulation of injection are studied through spatial-temporal monitoring of fluid pressure evolution and micro crack generation process. Micro crack generation due to failure at either parallel or smooth joint contacts are observed simultaneously. The chain of micro cracks is identified visually as a macrocrack. Micro cracks induced due to fluid injection may be origin of pure tension (Mode I) or shearing (Mode II) at either contact type.

4.5 Modelling results

Results of numerical simulation of *HF* into crystalline rock mass are presented as flow rate (Q), injected fluid volume (V_{inj}), interpreted pressures, like fracture breakdown pressure (*FBP*) and refracturing pressure (*RFP*), type and amount of generated micro cracks as well as field testing data are summarized in Table 4. The results are detailed for each rock mass model, i.e. homogeneous rock mass (A), rock mass with horizontal foliation (B) and sub-horizontal (C) foliation.

For each model, general observations based on monitored interval pressure and time-dependent number of generated micro cracks for the pressurization cycles are presented first. This is followed by analyzing the spatial distribution of micro and macro cracks for each of the models.

Table 4 Summary of simulation models and field data as well as generated type and ratio of micro cracks at the end of hydraulic fracturing. Q: injection flow rate, V_{inj}: total injected volume, FBP: fracture breakdown pressure, RFP: refracturing or fracture reopening pressure.

Simulation case	*Q* (l/min)	V_{inj} (l)	*FBP* (MPa)	*RFP* (MPa)	Generated microcrack failure type (%)*
A – homogeneous rock mass, stimulation by water injection	3.6	14.4	24	21.5	pb_n (100); pb_s (0)
B – horizontally foliated rock mass, stimulation by drilling mud injection	3.6	2.4	17	18.5	pb_n (71); pb_s (0); sj_n (18); sj_s (11)
C – sub-horizontally foliated rock, stimulation by drilling mud injection	3.6	4.8	30	27	pb_n (69); pb_s (0); sj_n (9); sj_s (22)
Field data	3.6–3.8	10^1–10^{2**}	16.5	19	-

* failure types: parallel bond, normal (pb_n), parallel bond, normal (pb_s), smooth joint, normal (sj_n) and smooth joint, shear (sj_s)

** injected volume: order of magnitude

4.5.1 Stimulation of homogeneous rock mass model A by water injection

Interval pressure, flow rate and cumulative number of generated micro crack records of model A are presented in Figure 11. The results show that minor fracturing occurs during the first injection cycle. This is reflected by relatively low increase in number of induced micro cracks versus time associated with two distinct pressure drops in the order of 1 to 2 MPa. Although pressure drops are observed during this stimulation cycle, no characteristic pressure signature of fracture breakdown and subsequent fracture propagation is visible in the pressure versus time record. Therefore, the first cycle is interpreted as a cycle in which tensile fracture initiates. After shut-in, micro crack generation stops.

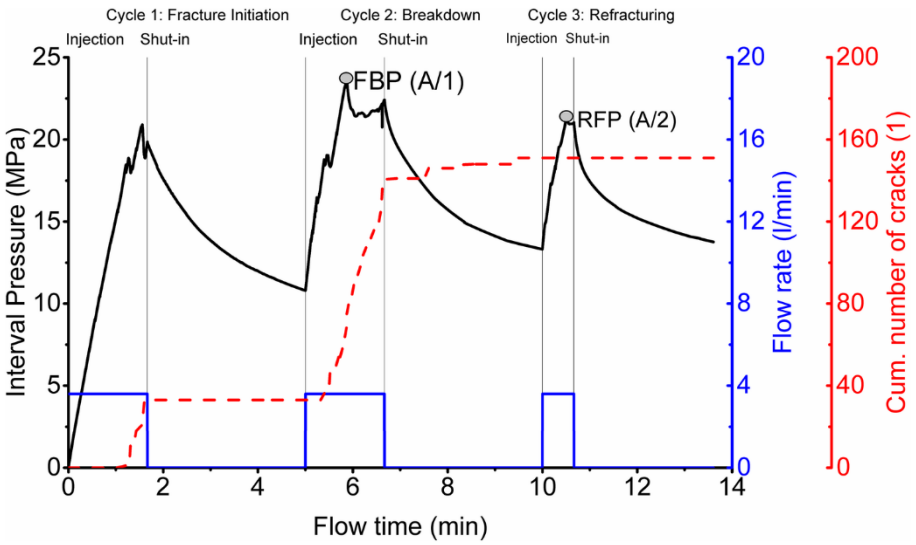

Figure 11: Interval pressure, flow rate and cumulative number of micro cracks versus time (dashed) of PFC ^{2D} simulation in model A (simulation of homogeneous rock mass by water injection) with identified fracture breakdown pressure FBP and reopening pressure RFP. Vertical lines show onset of injection and shut-in phases. Stages A/1 and A/2 show the occurrence of fracture breakdown and refracturing, respectively.

The second injection cycle shows a clear pressure drop and subsequent pressure undulation (Figure 11) during continuous flow. This is interpreted as fracture breakdown pressure (*FBP*) at a peak pressure of 24 MPa which is followed by fracture propagation until injection is stopped at 21.5 MPa.

After this injection phase, minor micro crack generation can be seen in Figure 11, in contrast to the shut-in phase of cycle 1.

The last injection cycle exhibits a peak pressure of 21.5 MPa and short pressure undulation at about 21 MPa, (Figure 11). The refracturing pressure (*RFP*), therefore, is considered to be 21.5 MPa which is lower than the *FBP* and similar to the fracture initiation pressure of the first cycle. The duration of the last cycle is shorter as the induced hydraulic fracture reaches model boundary. Few cracks are generated during reopening and no cracks are observed during shut-in.

Figure 12 provides information about the generation of microfractures during pressurization of model A with water at two stages, fracture breakdown (A/1) and refracturing (A/2). Stage A/1 in Figure 12 demonstrates that several micro cracks are induced in tension close to the boundary region between the sealing packers, open borehole area and the rock mass. Furthermore, a chain of microscopic tensile micro cracks on the right side of the model region builds a macroscopic hydraulic fracture. This is extended during the fracturing and refracturing cycles, approx. parallel to the direction of maximum principal stress, the maximum horizontal stress (S_{Hmax}). The undulation in the hydraulic fracture propagation reflects inherent variability in strength of the particles and parallel bond contacts representing the rock mass.

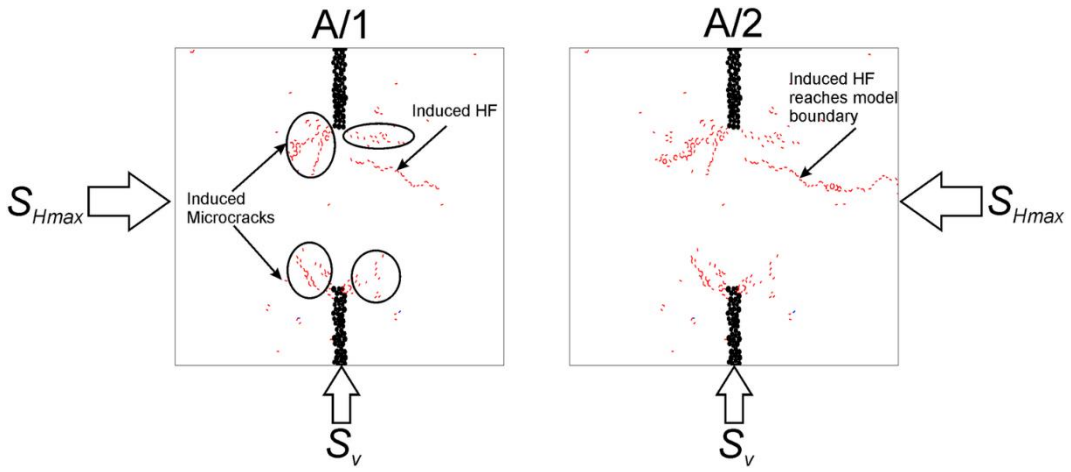

Figure 12: Snapshots of micro cracking process in model A (homogeneous rock mass) at time stages A/1 (fracture breakdown) and A/2 (refracturing) of the pressure versus time recording presented in Figure11. Stage A/1 shows micro cracks induced close to the packers (indicated by black circles) as well as initiation and propagation of hydraulic fracture at time stage. At stage A/2, the induced hydraulic fracture reaches model boundary. All particles except for those representing straddle packers above and below the open borehole interval (black) are removed for enhanced visibility. The vertical stress (S_v) equals 15 MPa and the maximum horizontal stress (S_{Hmax}) equals 30 MPa. Micro crack symbols, red: parallel bond normal failure, cyan and magenta: smooth joint normal and shear failure, respectively. Foliation planes (smooth joint contacts) are shown in grey.

4.5.2 Mud injection into model B with horizontal foliation

The interval pressure, flow rate and generated micro crack records for simulation of model B are presented in Figure 13. In this model horizontal foliation is parallel to direction of maximum horizontal stress and the rock mass is pressurized by drilling mud with a viscosity of 10 mPa s.

The first injection cycle in Figure 13 exhibits a first breakdown peak pressure *FBP* of 17 MPa, which is followed by a pressure reduction to 13.5 MPa. Shortly after this pressure drop, the flow is shut-in. Micro crack generation begins before reaching peak pressure and after shut-in the number of micro cracks increases steadily. Based on these observations, the first injection cycle can be interpreted as breakdown cycle with a *FBP* of 17 MPa.

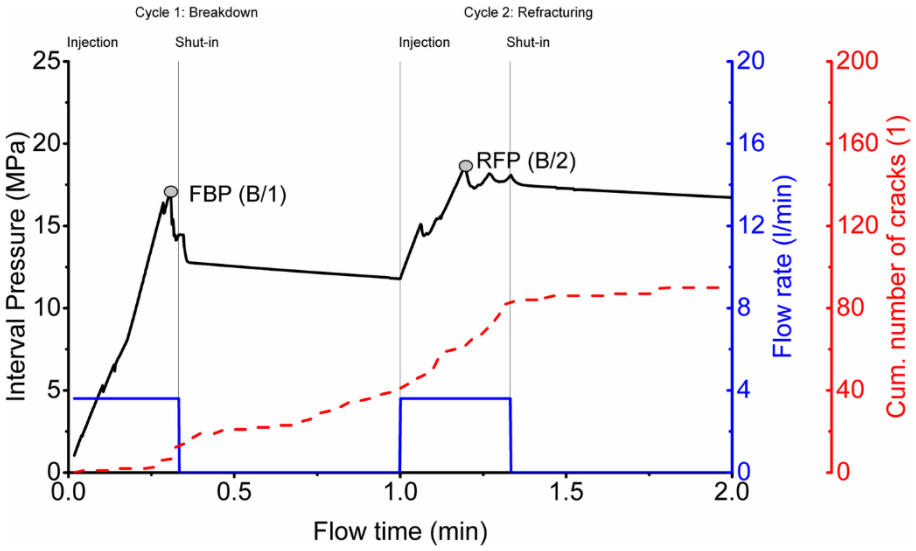

Figure 13: Interval pressure, flow rate and cumulative number of generated micro cracks versus time (dashed) for simulation of model B (injection of drilling mud in to rock mass with horizontal foliation) with identified fracture breakdown pressure, FBP (B/1) from the first cycle and slightly larger reopening or refracturing pressure RFP (B/2) from the second cycle. Vertical lines show onset of injection and shut-in phases.

The pressure versus time record of second stimulation cycle in Figure 13 exhibits a refracturing pressure *RFP* of 19 MPa. Small pressure drop before reaching *RFP* can be observed as well. Undulating pressure of approximately 17-18 MPa following *RFP* indicates hydraulic fracture propagation that can be caused by differences in strength and permeability of the foliation planes in the rock mass. Therefore, this cycle is interpreted as refracturing cycle with a *RFP* of 19 MPa, which is higher than the *FBP*. After shut-in of the refracturing cycle, only relatively small amount of micro cracks are generated.

Figure 14 gives insight into the generation of microfractures during pressurization of model B with mud at two stages, fracture breakdown (B/1) and refracturing (B/2). After the first, breakdown cycle, induced micro cracks are observed around the boundary of sealing packers, open borehole area and rock mass, as well as partly at the horizontal foliation planes (stage B/1 in Figure 14). The cracks are mostly induced in tension. An initiation of a newly induced hydraulic fracture is visible around the open borehole area between two foliation planes. After shut-in in refracturing cycle (stage B/2 in Figure 14), fractures are extended both in the rock mass and foliation planes, parallel to the maximum principal stress S_{Hmax}. The tensile hydraulic fracture in the rock mass propagates to a greater extent. The foliation planes are fractured mostly in tension, a fracturing mechanism which is expected for hydraulic

fracturing. Shear micro cracks are also generated, however, their relative smaller portion to tensile micro cracks may suggest that the foliation planes are not optimally oriented for hydro-shearing.

Comparison of interval pressures during cycle 1 and 2 (Figure 13) with micro crack distribution (Figure 14) shows that as soon as the mud penetrates the foliation planes, the interval pressure remains high. This implies that higher fluid pressure is required to pump the mud into the foliation and to the rock mass. This explains the higher *RFP* compared to the *FBP* of this stimulation with high viscous mud.

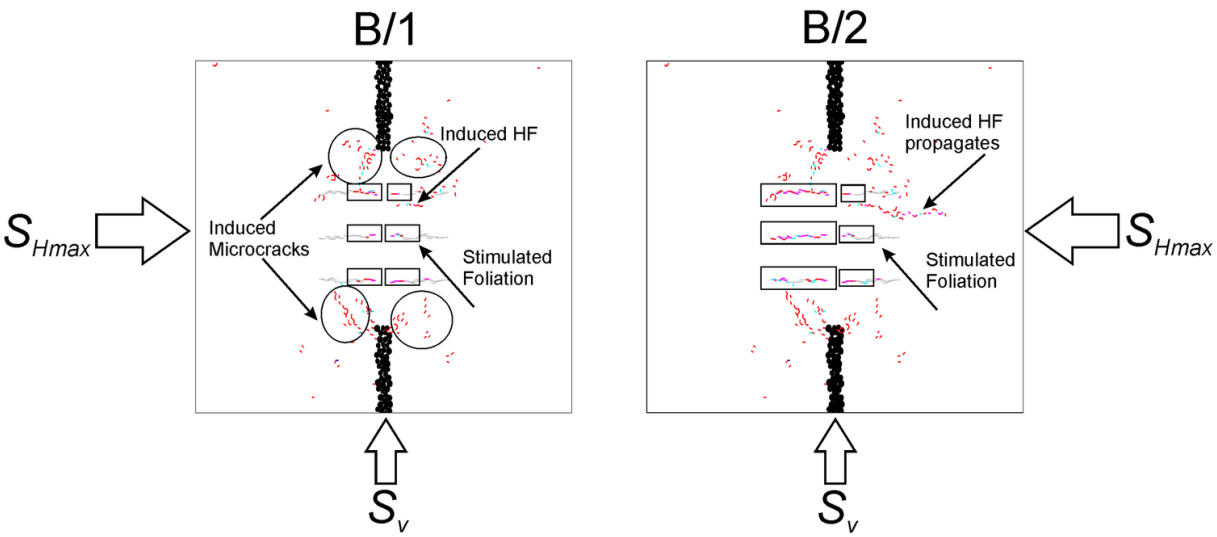

Figure 14: Snapshots of micro cracking process in simulation case B (stimulation of rock mass with horizontal foliation by drilling mud) at 2 points in time, occurrence of fracture breakdown and reopening, near borehole area (stages B/1 and B/2 in Figure 13). Stage B/1 shows micro cracks induced close to the packers (indicated by black circles), stimulated foliation (indicated by black rectangles) as well as induced hydraulic fracture. Stage B/2 illustrates propagation of hydraulic fracture. All particles except for those representing straddle packers above and below the open borehole interval (black) are removed for enhanced visibility. The vertical stress (S_v) equals 15 MPa and the maximum horizontal stress (S_{Hmax}) equals 30 MPa. Micro crack symbols, red: parallel bond normal failure, cyan and magenta: smooth joint normal and shear failure, respectively. Foliation planes (smooth joint contacts) are shown in grey.

4.5.3 Mud injection into model C with slightly inclined foliation

The interval pressure, flow rate and generated micro crack (dashed) records for model C are summarized in Figure 15. In this simulation case the rock mass contains foliation tilted by 15° with respect to direction of maximum horizontal stress. Drilling mud is represented as a fluid with viscosity of 10 mPa s.

Figure 15 shows the pressure increase during injection until shut-in and relatively slow pressure decay after that of the first injection cycle. The evolution of number of generated micro cracks suggests minor fracturing during injection starting at a pressure level of approx. 15 MPa. The crack generation process continues at a faster rate throughout the shut-in period of the first cycle. Consequently, the first cycle is interpreted as a phase in which tensile fracture initiates at a fracture initiation pressure (*FIP*) of 15 MPa that equals the minimum stress in the model which corresponds to the vertical stress, S_v in the field.

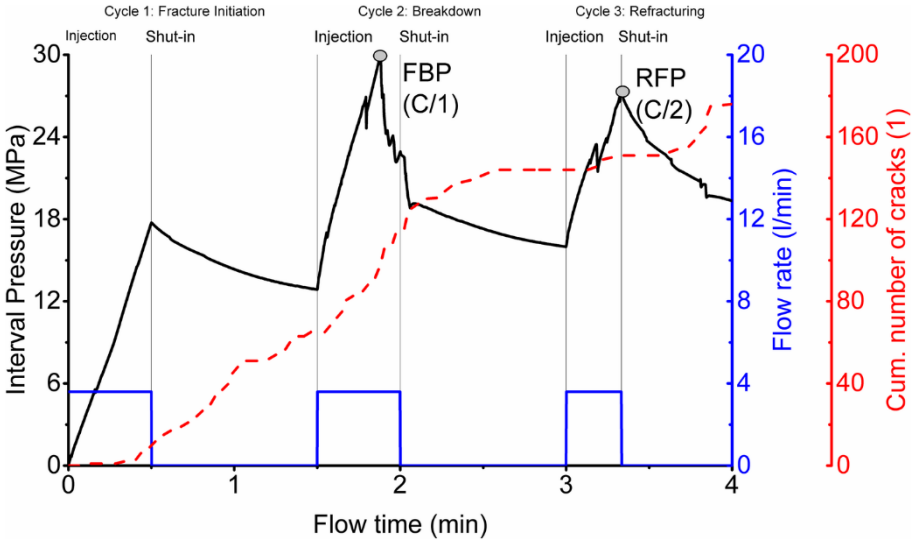

Figure 15: Interval pressure, flow rate and cumulative number of generated micro cracks versus time (dashed) records for simulation of model C (mud injection of rock mass with slightly inclined foliation by) with identified fracture breakdown pressure, FBP(C/1) and reopening or refracturing pressure RFP(C/2). Vertical lines show onset of injection and shut-in phases.

The second injection cycle initially shows a few minor pressure drops that are followed by breakdown *FBP* (C/1) at 30 MPa and characteristic pressure drop to 23 MPa at shut-in (Figure 15). The peak pressure is interpreted as the *FBP* which is followed by fracture propagation until injection is stopped. Therefore, this injection cycle can be considered as breakdown cycle. After the injection phase, micro crack generation continues during shut-in.

The third injection cycle shows a peak pressure at 27 MPa which is interpreted as the *RFP* (C/2) which is slightly lower than the *FBP* (C/1). Interestingly, more micro fractures are generated during the shut-in period than during injection. This can be an artefact due to fracturing close to the model boundary.

Figure 16 provides information about the generation of micro cracks during pressurization of model C with mud at two stages, fracture breakdown (C/1) and refracturing (C/2). Micro cracks at stage C/1 are induced around the boundary between the sealing packers, open borehole area and rock mass, as well as at the sub-horizontal foliation planes. Hence, an initiation of a newly induced, tensile hydraulic fracture in the rock mass and stimulated foliations are visible at fracture breakdown stage in Figure 16. The micro crack evolution during breakdown and refracturing cycles (stages C/1and C/2 in Figure 16) indicate that fractures are extended both in the rock mass and foliation planes, approximately parallel to the maximum principal stress S_{Hmax}. The tensile hydraulic fracture in the rock mass propagates to a greater extent. The foliation planes are fractured in tension as the main stimulation mechanism. Shear fracturing, therefore, is not the main fracturing mechanism, since the planes of weakness are not optimally oriented for hydro-shearing.

Comparing Figure 15 to Figure 16, the evolution of fluid pressure suggests that as the mud penetrates the foliation planes, the fluid pressure remains high. Higher fluid pressure is required to pump the mud into the foliation and, therefore, to reopen and extend the tensile hydraulic fracture at the tip of

the foliation. Although pressure build up is partitioned between the domains located at the smooth joint and parallel bond contacts, it requires less hydraulic energy to extend the initial tensile hydraulic fracture throughout the parallel bond contacts representing the rock mass. This explains the high *FBP* and *RFP* as well as the lower *RFP* compared to *FBP* of this stimulation with high viscous mud.

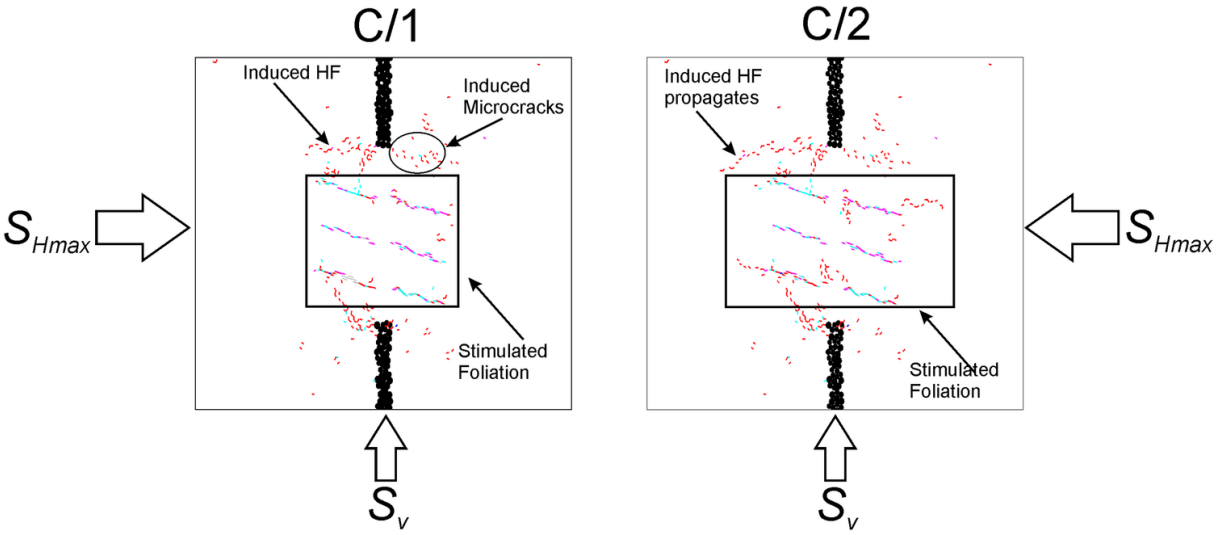

Figure 16: Snapshots of micro cracking process in simulation case C (stimulation of rock mass with sub-horizontal foliation by drilling mud) at 2 points in time, occurrence of fracture breakdown and reopening, near borehole area (stages C/1 and C/2 in Figure 15). Stage C/1 shows micro cracks induced close to the packers (indicated by black circle), stimulated foliation (indicated by black rectangles) as well as induced hydraulic fracture. Stage C/2 illustrates propagation of hydraulic fracture. All particles except for those representing straddle packers above and below the open borehole interval (black) are removed for enhanced visibility. The vertical stress (S_v) equals 15 MPa and the maximum horizontal stress (S_{Hmax}) equals 30 MPa. Micro crack symbols, red: parallel bond normal failure, cyan and magenta: smooth joint normal and shear failure, respectively. Foliation planes (smooth joint contacts) are shown in grey.

4.6 Discussion

4.6.1 Comparison of simulation results for the three models

Table 4 shows that the injected volume of fluids during numerical simulation of hydraulic fracturing (*HF*) in models with foliation (model B and C) is about one order of magnitude smaller than that on field testing. In case A (simulation of homogeneous rock mass by water injection) the pressure versus time record agrees with injected rate and volume recorded on field testing. The lower injected fluid volume in the rock models with foliation is the result of using 2D section for the interval in the borehole, i.e. the lack of fluid flow in the out-of-plane direction. Consequently, this is a clear limitation of the 2D version of the numerical code and should be subject of future development. We should note that field data include recorded flow back rate (Figure 5b), however, this is not simulated in present study. This is not required, since these data cannot be used for the numerical study as the flow back was interrupted to check the sealing condition of the packers. Hence, matching flow rate records from field tests and numerical simulation with the 2D version of codes is not relevant.

The peak pressures, i.e. measured fracture breakdown (*FBP*) and refracturing pressure (*RFP*) are different for each simulation case. In case A with homogeneous rock mass the *FBP* is higher than

the *RFP*, i.e. the model shows good agreement with the classical pressure-time record of hydraulic fracturing (Figure 11). On the other hand *FBP* and *RFP* are somewhat higher than those observed in field testing which implies that pre-existing fractures in the numerical rock mass models are required to reproduce these pressure values. This is supported by model case B for which the simulated *FBP* and *RFP* agree with field data (Table 4). Not only the magnitudes show good match, but also the numerical code is able to capture the higher *RFP* for a rock mass with horizontal foliation.

Interestingly, when simulating model case C with tilted plane of foliation, the *RFP* is lower than the *FBP*; and both values are higher than that recorded pressure from field testing (Table 4). The higher *FBP* can be explained in a way that the area of tilted foliation planes to be fractured is higher compared to the case in which the foliation planes are horizontal, consequently the tilted foliation has larger volume for fluid storage. The higher *FBP* with higher fracture inclination angle agrees with the modelling results presented by Lavrov et al. (2016). On the other hand, this might also be related to the limitation of the 2D version of the numerical code. Therefore, further investigations are required.

The peak pressure during the first injection cycle in homogeneous model A and in in model C with tilted foliation is not interpreted as *FBP* although a pressure drop of several MPa is observed, see Figure 11 and Figure 15. This is the case for which the fracture initiation around the borehole is affected by the strength contrast between the rock mass and the packers. Due to the pressure drop, the injection must be stopped to avoid numerical instability. This limitation is overcome by pressure relaxation after shut-in which is followed by injection at the same flow rate.

The results presented in Table 4 and Figure 12 show that only parallel bonds break in simulation of model A, which is expected for hydraulic fracturing of homogeneous rock mass. The portion of different failure types at parallel bonds and smooth joints for model case B and C suggest (Figure 14 and Figure 16) that the fracturing processes are different in these models. Although the dominant type of fracturing is tensional for a rock mass with foliation, shear micro cracks are also generated. The lower number of shear fractures suggest that the foliation planes are not optimally oriented for hydro-shearing. Our numerical modelling results show that fracture initiation develop from the stiffness and strength contrast between packers in the borehole and the surrounding rock mass. Furthermore, the low tensile strength of foliation planes in the rock mass may contribute to this. Consequently, our results confirm the results and interpretations of field tests described by Healy and Zoback (1988) and Hickman and Zoback (1983). Similar to our findings, they linked the anomalous breakdown pressure to lower tensile strength and anisotropy of the rock mass.

4.6.2 Hypothesis of viscous blocking

The results of coupled numerical modelling show that orientation of rock foliation with respect to direction of major principal stress affects hydraulic fracturing results. The fracture breakdown pressure and refracturing pressure seem to be inversely proportional to angle between foliation and maximum in-situ stress which agrees with the observation made by Lavrov et al. (2016).

Considering the results of all simulated models (A, B and C), and the discussion above, the rock mass with horizontal foliation (model B) injected by high viscosity mud shows best fit with field data. The atypical field observation with higher RFP in the second cycle of pressurization can be explained by the injection of high viscous fluid (mud) and existing foliation in the mica schist. First, injected mud flows into foliation plane, remains there and blocks the flow. Mud flows into the initial tensile fracture induced within a weaker area in the rock mass close to the packer and interval and propagates the initiated fracture during the fracturing cycle. Due to the presence of mud in the foliation planes, higher RFP is required to reopen the tight foliation planes and to create and to extend fractures in subsequent refracturing cycles. However, when the foliation is inclined (model C), the shearing does not provide large hydraulic aperture increase to let the viscous mud in, compared to the horizontal foliation. This may explain why simulation of injection into tilted foliation with high viscous mud does not explain the atypical field data.

4.7 Conclusions

In this study, an atypical behavior of hydraulic fracturing tests in low permeable mica schist is investigated. The field data from site investigations in Hungary show that the fracture breakdown pressure (*FBP*) is lower than the refracturing pressure (*RFP*) of the subsequent injection cycles for one and the same flow rate. This field observation motivated the application of the Particle Flow Code (PFC^{2D}) to study the atypical hydraulic fracturing behavior in a series of two-dimensional models subjected to several injection cycles. The effect of foliation and its orientation with respect to the direction of maximum horizontal stress and the viscosity of injected fluid (drilling mud) on breakdown and refracturing pressures is tested through different rock mass models.

The modelling results show that homogeneous rock mass that is stimulated by water pressure follows the classical principle of hydraulic fracturing with an induced hydraulic fracture that propagates parallel to the direction of maximum principal stress. However, the results of the models that are foliated parallel to maximum principal stress and stimulated by mud suggest that foliation and high viscosity fluid are required to match the field observations. We argue that the drilling mud penetrates the sub-horizontal foliation plane and makes the opened fracture tight by an effect which is referred to as viscous blocking. The process prevents leak-off from the opened hydrofracture that can explain the increased *RFP* in subsequent cycles. On the other hand when the rock mass has dipped foliation and is stimulated by mud, the RFP is lower than the FBP. This might be explained by hydroshearing with foliation that is not optimally oriented compared to the horizontal foliation.

The study shows that crack development and progression in cases where foliation is present reflects that in-situ stress measurements require further understanding. Therefore, sensitivity of orientation, length and strength (stiffness) of foliation as well as stress regime configuration, flow rate, fluid density and well orientation must be also tested in a future study. This may contribute to a more precise stress determination and analysis method.

Acknowledgements

The work was kindly supported by Golder Associates Hungary.

References

ÁKMI Ltd (2016) Conduction of Geological Research Program Required for Paks II Site Permit. Final report of the Geological Research Program. Document ID: MÁ/PA2-16-FT-14 V2 (Paks II Telephelyengedélyének Megszerzéséhez Szükséges Földtani Kutatás Végrehajtása. Földtani Kutatási Program Zárójelentése (in Hungarian), Pécs, Hungary

Amadei B, Stephansson O (1997) Rock stress and its measurement, Chapman & Hall, London

Doe TW, Korbin GE (1987) A Comparison of Hydraulic Fracturing and Hydraulic Jacking Stress Measurements, 28th US Symp on Rock Mech, Tuscon, 283–290

Haimson BC, Cornet FH (2003) ISRM Suggested Methods for rock stress estimation – Part 3: Hydraulic Fracturing (HF) and/or hydraulic testing of pre-existing fractures (HTPF), International Journal of Rock Mechanics and Mining Sciences, 40:1011-1020

Hazzard JF, Young RP, Oates SJ (2002) Numerical modeling of seismicity induced by fluid injection in a fractured reservoir, In Proceedings of the 5th North American Rock Mechanics Symposium Mining and Tunnel Innovation and Opportunity, Toronto, ON, Canada, 7–10 July 2002, 1023–1030

Healy JH, Zoback MD (1988) Hydraulic fracturing in–situ stress measurements to 2.1 km depth at Cajon Pass, California, Geophys Res Let, 15:1005–1008

Hickman SH, Zoback MD (1983) The interpretation of hydraulic fracturing pressure-time data for in-situ stress determination, in Hydraulic Fracturing Measurements (ed. by Zoback MD, Haimson BC), National Academy Press, Washington D.C., 44–54

Hökmark H, Lönnqvist M, Fälth B (2010) THM–issues in repository rock. Thermal, mechanical, thermo–mechanical and hydro–mechanical evolution of the rock at the Forsmark and Laxemar sites. Technical Report, TR–10–23, SKB Publications, 2010, Updated 2011-10

Itasca Consulting Group Inc (2008) PFC2D version 4.0 Manual (Particle Flow Code in 2 dimensions), Minneapolis, USA

Itasca Consulting Group Inc (2012) Technical Memorandum to PFC2D (Particle Flow Code in 2 dimensions) version 4.0 – 5.0 Parallel Bond Enhancement, Minneapolis, USA

Labuz J, Zang A (2012) ISRM suggested methods for rock failure. Mohr–Coulomb failure criteria, Rock Mech Rock Eng, 45:975–979

Lavrov A, Larsen I, Bauer A (2016) Numerical modelling of extended leak–off test with a pre-existing fracture, Rock Mech Rock Eng, 49:1359–1368

Lemon M, Farkas MP, Korpai F, Dankó G (2016) Technical report of hydraulic fracturing tests. Conduction of Geological Research Program Required for Paks II Site Permit, Golder Associates Hungary, Budapest, Hungary

Lin C, He J, Li X,, Wan X, Zheng B (2017) An experimental investigation into the effects of the anisotropy of shale on hydraulic fracture propagation, Rock Mech Rock Eng, 50:543–554

Mas Ivars D, Potyondy DO, Pierce M, Cundall, PA (2008) The smooth–joint contact model. Proceedings of the 8th World Congress on Computational Mechanics – 5th European Congress on Computation Mechanics and Applied Science and Engineering, Venice, Italy, 2008

Potyondy DO, Cundall PA (2004) A bonded–particle model for rock, Int J Rock Mech Min Sci, 41:1329–1364

Shimizu H, Murata S, Ishida T (2011) The distinct element analysis for hydraulic fracturing in hard rock considering fluid viscosity and particle size distribution, Int J Rock Mech Min Sci, 48:712–727

Stephansson O, Zang A (2012) ISRM suggested methods for rock stress estimation – Part 5: Establishing a model for the in-situ stress at a given site. Rock Mechanics and Rock Engineering 45, 955-969

Yoon JS, Zang A, Stephansson O (2014) Numerical investigation on optimized stimulation of intact and naturally fractured deep geothermal reservoirs using hydro–mechanical coupled discrete particles joints model, Geothermics 52:165–184

Yoon JS, Zang A, Stephansson O, Hofmann H, Zimmermann G (2017) Discrete element modelling of hydraulic fracture propagation and dynamic interaction with natural fractures in hard rock, Procedia Engineering, 191: 1023–1031

Zang A, Berckhemer H (1993) Classification of crystalline drill cores from the KTB deep well based on strain, velocity and fracture experiments, Int J Rock Mech Min Sci, 30(4): 331–342

Zang A, Stephansson O (2010) Stress field of the Earth's crust. Dordrecht, Springer

Zang A, Stephansson O, Heidbach O, Janouschkowetz S (2012) World stress map data base as a resource for rock mechanics and rock engineering, Geotechnical and Geological Engineering, 30(3): 625–646.

Zhou J., Zhang L, Braun A, Han Z (2016) Numerical modeling and investigation of fluid-driven fracture propagation in reservoirs based on a modified fluid-mechanically coupled model in two-dimensional Particle Flow Code, Energies, 9(9), 699

Zhou L, Ding L, Guo Q (2016) Indoor experiments on the effect of the slurry on the in–situ stress measurement results, in: Johansson E, Raasakka V (Eds.), Symposium Proceedings, 7th International Symposium on In–Situ Stress, Tampere, Finland, May 10–12, 2016, 235–246

Zoback MD (2010) Reservoir Geomechanics. Cambridge, Cambridge University Press

Chapter 5 Macroscale publication 3: Reservoir scale EGS study

Hydromechanical analysis of second hydraulic stimulation at well PX-1 in Pohang fractured geothermal reservoir, South Korea

Farkas, M. P., Hofmann, H., Zimmermann, G., Zang, A., Bethmann, F., Meier, P., Cottrell, M., Josephson, N.

Published in Geothermics 89, 101990
https://doi.org/10.1016/j.geothermics.2020.101990.

Hydromechanical analysis of the second hydraulic stimulation in well PX-1 at the Pohang fractured geothermal reservoir, South Korea

Márton Pál Farkas[a,b], Hannes Hofmann[a], Günter Zimmermann[a], Arno Zang[b,c], Falko Bethmann[d], Peter Meier[d], Mark Cottrell[e], Neal Josephson[e]

[a] Section 4.8 Geoenergy, GFZ - German Research Centre for Geosciences, Telegrafenberg, Potsdam 14473, Germany

[b] Institute for Geosciences, University of Potsdam, Karl-Liebknecht-Straße 24/25, Potsdam 14476, Germany

[c] Section 2.6 Seismic Hazard and Risk Dynamics, GFZ - German Research Centre for Geosciences, Telegrafenberg, Potsdam 14473, Germany

[d] Geo-Energie Suisse AG, Reitergasse 11, Zürich 8004, Switzerland

[e] Golder Associates (UK) Ltd., Bourne End Business Park, Bourne End SL8 5AS, United Kingdom

Abstract

In this study, we investigate numerically the hydro-mechanical behavior of fractured crystalline rock due to one of the five hydraulic stimulations at the Pohang Enhanced Geothermal site in South Korea. We use the commercial code FracMan (Golder Associates) that enables studying hydro-mechanical coupled processes in fractured media in three dimensions combining the finite element method with a discrete fracture network. The software is used to simulate fluid pressure perturbation at fractures during hydraulic stimulation. Our numerical simulation shows that pressure history matching can be obtained by partitioning the treatment into separate phases. This results in adjusted stress-aperture relationships. The evolution of aperture adjustment implies that the stimulation mechanism could be a combination of hydraulic fracturing and shearing. The simulated extent of the 0.01 MPa overpressure contour at the end of the treatment equals to ~180 m around the injection point.

Keywords: Enhanced Geothermal System, Pohang geothermal reservoir, hydraulic stimulation, PX-1, FracMan

Highlights

• Coupled hydro-mechanical simulation and characterization of the cyclic soft stimulation in August 2017 at the Pohang EGS reservoir (second stimulation in well PX-1) is performed.

• Pressure history match was achieved by splitting the simulated treatment into phases.

• The permeability is increased through opening of existing fault.

• The modeled extent of direct overpressure of 0.01 MPa at the end of the stimulation is approx. 180 m from the injection point.

5.1 Introduction

The Enhanced Geothermal System (EGS) technology is in the focus of geothermal energy research due to its large economic growth potential (e.g. Rybach, 2014). The target is the heat stored in the deeper Earth's crust at several km depth, which may be utilized for heat and/or electrical power provision. Under petrothermal conditions, i.e. rock with low intrinsic permeability, hydraulic stimulation may be applied to increase productivity. However, induced seismicity associated with such operations poses a potential risk that must be controlled to advance the EGS technology (Zang et al., 2013). Therefore, the goal is to create a permeable fracture network for an efficient heat exchanger by injecting fluid with induced seismicity below a fixed threshold.

The concept of cyclic injection with the aim to enhance permeability and to reduce the magnitude of large induced seismic events was introduced by Zang et al. (2013). The concept has been tested experimentally in recent years at different scales (Hofmann et al., 2018a): at laboratory scale by Zhuang et al. (2018) on granitic rock samples and at mine scale by Zang et al. (2017) in crystalline rock mass. At field scale, a demonstration is reported by Hofmann et al. (2019) at the Pohang EGS site in South Korea.

The underlying physical mechanism of induced seismicity due to injection of large fluid volumes at high pressure, is not yet fully understood. Zang et al. (2014) and Kang et al. (2019) show that the key mechanisms behind injection induced earthquakes are pore pressure increase, stress change as well as change in coefficient of friction from a view of rock mechanics. The interplay between these processes is referred to as hydro-mechanical (HM) coupling. It must be noted that change in coefficient of friction may imply the application of Mohr-Coulomb friction model from the view of rock mechanics, although other friction models are proposed, such as the rate-and-state friction model by Dieterich (1992). Cornet (2016) defines four levels of HM coupling depending on the level of injection pressure increase and possible stimulation mechanism. At the first level fluid pressure remains small enough that Terzaghi's effective stresses in the material are compatible with an elastic behavior of the rock mass. Therefore, stability criteria are satisfied at all points in the rock mass which may be modeled by linear poro-elastic response following Darcy-type fluid flow. At the second level, fracture shear strength is reached, i.e. slip on large pre-existing fractures may result in significant micro-earthquakes, which is referred to as slip on pre-existing fractures. Hydraulic diffusion is controlled by flow through stimulated (reactivated) fractures. For the third level, injection pressures are large enough for effective stresses in the rock mass to reach failure conditions for shearing, i.e. hydro-shearing of fresh shear fractures. Fluid flow is dominated by flow through newly sheared zone. At the fourth level, the elevated fluid pressure in the injection well induces tangential stresses that reach the tensile strength of the rock, i.e. a hydraulic fracture is generated (referred to as hydraulic fracturing).

One may improve the concept of cyclic soft stimulation by using hydro-mechanical coupled numerical codes that provide better understanding of the interrelations between stress field, fluid

diffusion and fracturing processes (e.g. Yoon et al., 2014). In this study, we use the software FracMan 7.8 (Golder Associates, 2019) to investigate the relevant coupled processes in detail. The code uses the Discrete Fracture Network (DFN) approach that combines continuum and discontinuum geomechanics. We study coupled processes during the cyclic soft stimulation treatment performed in August 2017 at the Pohang EGS site (reported by Hofmann et al., 2019) to characterize the proposed stimulation mechanism of hydro-shearing. The paper first introduces and characterizes the Pohang EGS site. This includes a summary of all hydraulic stimulations and a brief description of the magnitude 5.5 M_w earthquake in Pohang on 15th November 2017. This is followed by presenting the numerical approach. Simulation results are analyzed and discussed, and finally, conclusions are drawn.

5.2 Pohang EGS project overview

5.2.1 Background and geology

The EGS pilot site is located six kilometers north from the centre of Pohang city, in the SE part of South Korea (Figure 1). The motivation for site selection was the geothermal gradient in basement rock of at least 30 °C/km (Lee et al., 2015). The project was supposed to deliver 1 MW of electrical power by creating artificial fluid circulation between two wells (Song et al., 2015).

Figure 1: Aerial satellite image showing the location of the Pohang EGS site in South Korea and the location of the M_w 5.5 earthquake on 15 November 2017.

The local geological model is summarized by Lee et al. (2015) and Park et al. (2020). According to these, the reservoir is located in the Pohang Basin, which is a sedimentary sub-basin of the Heunghae Basin. The Pohang Basin has an extensional structural origin due to oceanic spreading of the Sea of

Japan. The basin is bounded on the west by the Yangsan fault which is characterized by post-Eocene dextral strike–slip movement (Chough et al., 2000). This regional fault strikes NNE-SSW, passing approx. 10 km west of the Pohang site.

The reservoir rock is fractured Permian granodiorite and granitic gneiss that form the bedrock of the Heunghae Basin below 2200 m depth (Figure 3). The basement rock is covered by Cretaceous sedimentary rock (sandstones and mudstones) mixed with sequences of tuff and andesite layers, with a thickness of 1000 m. The uppermost Tertiary semi-consolidated mudstone shows a varying thickness of 200 m in the northern part, which increases up to 400 m to the south. The study area is intersected by two sets of mapped surface lineaments (Park et al., 2017). One set is oriented NNE-SSW (pink lineaments in Figure 1) and is described as a steeply dipping, right-lateral strike-slip branch of the regional Yangsan fault (i.e. subparallel to that). The second fault zone, the Heunghae zone, is oriented approx. E-W and intersects the other set perpendicularly. The fault set consists of normal faults. There is no evidence that these faults extend towards the basement.

5.2.2 Stress Field

Several stress models are reported for the Pohang EGS site that are summarized in Table 1, which lists the stress magnitudes and the orientation of maximum horizontal stress (S_{Hmax}) as well as the ratio of maximum horizontal stress to vertical stress (S_v) and stress regime.

*Table 1: Reported stress models for the Pohang EGS reservoir at 4.2 km depth. The stress model used in this study is the one reported by Bethmann et al. (2019) (in **bold**). *: Kim et al., 2017 model is extrapolated to 4.2 km depth.*

Reference	**S_{HMax} orientation (°)**	**S_{HMax} magnitude (MPa)**	**S_v magnitude (MPa)**	**S_{hmin} magnitude (MPa)**	***S_{Hmax}/S_v* ratio (-)**	**Stress Regime**
Bethmann et al. (2019), *"Most Likely Stress Tensor"*	***N100E***	***133-153***	***107***	***98-119***	***1.2-1.4***	***Strike-slip/Reverse (Transpressional)***
Kim et al. (2017), "Integrated Stress Model" *	N130-136E	138	107	86	1.3	Strike-slip
Lee et al. (2019), "Preferred Stress Model"	N77±23E	243	106	120	2.3	Reverse
Lee et al. (2019), "Regional Stress Model"	N74E	203	106	93	1.9	Strike-slip
Park et al. (2017)	N65-130E	115-138	110	81-105	1.0-1.3	Strike-slip
Westaway and Burnside (2019)	N111E	200	110	120	1.8	Reverse

The integrated stress model presented by Kim et al. (2017) is derived from hydraulic fracturing and borehole breakout data of well EXP-1, which is located approx. 4 km from the Pohang EGS site. The integrated in-situ stress measurements at approx. 0.5-1 km depth indicate a S_{Hmax} orientation between N122 °E and N138 °E in a strike-slip stress regime. It should be noted that comparing deep and shallow stress field measurements, significant variations in stress field directions in SE Korea can be observed, possibly due to local geological structures (Hofmann et al., 2019). Another stress model proposed by Park et al., 2017 is derived from the model reported by Kim et al. (2017), with additional support by slip-tendency analyses. The proposed S_{Hmax} orientation varies between N65 °E and N130 °E in a strike-slip regime. Lee (2019) propose two alternative stress models. The "regional stress model" defines strike-slip faulting regime with a S_{Hmax} orientation of N74 °E. The other, "preferred stress model", suggests a reverse fault model with the orientation of S_{Hmax} N77 ± 23 °E. These models consider the previous models, include microseismic locations from hydraulic stimulations (Section 5.2.3) and seismicity data (including foreshock and mainshock events) of the 15th November 2017 earthquake event in Pohang as well as geodetic analysis. The ratio of maximum horizontal stress to vertical stress (S_v) is higher in these models compared to that in Kim et al. (2017) and Park et al. (2017), i.e. 1.9-2.3 to 1.0 to 1.3.

The stress model published by Westaway and Burnside (2019) modifies the in-situ stress stresses suggested by Lee (2019) using slip-tendency analysis. They conclude a reverse faulting stress regime with an orientation of S_{Hmax} N111 °E and S_{Hmax}/S_v ratio of 1.8.

The latest stress model is reported by Bethmann et al. (2019), the "most likely stress tensor" for the Pohang EGS site. Their analysis includes all previous studies as well, in addition to hydraulic stimulation records (see Section 5.2.3) and associated microseismicity locations. They propose a transpressional stress regime with an orientation of S_{Hmax} N100 °E and S_{Hmax}/S_v ratio of 1.2 to 1.4. Given the most up-to-date status of the suggested model, we consider the stress field proposed by Bethmann et al. (2019) for this numerical study.

5.2.3 Wells and hydraulic stimulation programs

The project timeline since launch in December 2010 is illustrated in Figure 2. Two wells were drilled for an anticipated doublet system (Figure 3). First, well PX-1 was drilled in 2012 and 2013. This was side-tracked in 2016 to a measured depth of 4 362 m and a true vertical depth of 4 215 m, with an 8 ½" diameter openhole section of 313 m length at its bottom. This well is completed with a 9 5/8" casing to 2,400 m depth and a 7" casing from 2,400 m to 3,920 m TVD (4,049 m MD), the remainder being left openhole (Figure 3). The well is deviated by 22° towards an azimuth of N71 °W. The vertical well PX-2 was drilled and completed in 2015 down to 4348 m, with a 7" casing down to 4208 m and a 140 m long 8 1/2" openhole section. On the surface the wells are 6 m apart; the distance between the bottoms is 616 m.

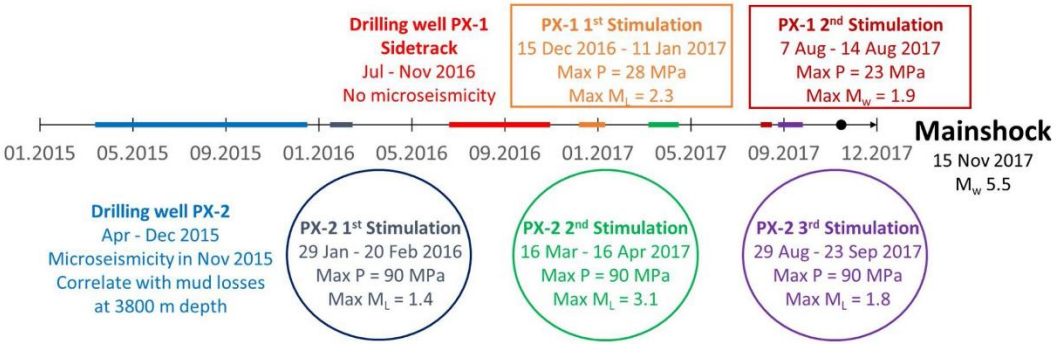

Figure 2: Timeline of the Pohang EGS Project (after Lee et al., 2019).

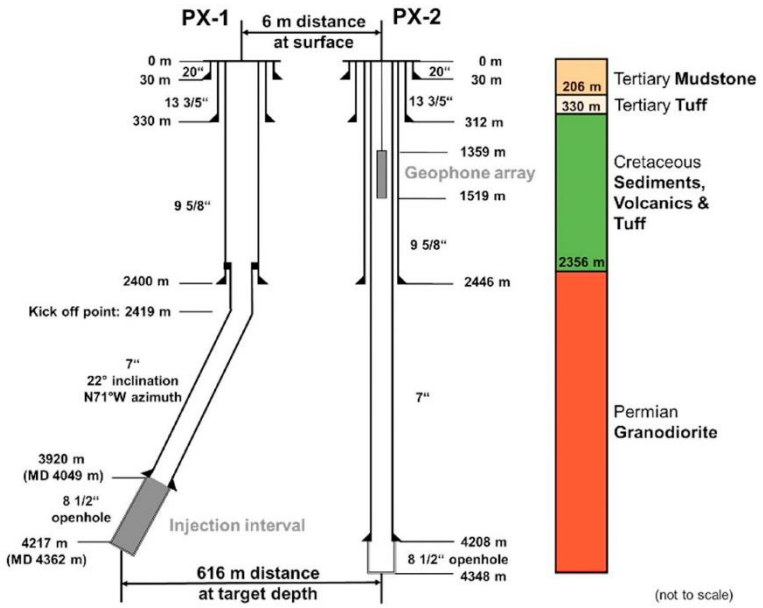

Figure 3: Well completions including injection location (PX-1, 313 m long openhole section from 4,049 m to 4,362 m MD) and 17-instrument geophone chain (installed in well PX-2, at 1,359 m – 1,519 m MD, to monitor the August 2017 stimulation in well PX-1). Depth reference is the rig floor, 26.3 m above sea-level and ~9 m above surface (modified from Hofmann et al., 2019).

Several hydraulic stimulations were conducted to improve the hydraulic performance of the system (Lee, 2019, Figure 2). Well PX-2 was stimulated first in January–February 2016 (PX-2 1st, Park et al., 2020), later in March–April 2017 (PX-2 2nd) as well as in August-September 2017 (PX-2 3rd). Well PX-1 was first stimulated in December 2016 – January 2017 (PX-1 1st, Park et al., 2020) and thereafter in August 2017 (PX-1 2nd, Hofmann et al., 2019).

The fourth stimulation at the Pohang site has been the second in the PX-1 well. The main purpose of this stimulation is twofold. One goal was to test the cyclic soft stimulation (CSS) concept in the field for the first time described in Hofmann et al. (2018b) with a restricted amount of injected water (Hofmann et al., 2019). The second goal was to monitor the reservoir with low magnitude seismic events in more detail. The basic idea behind was the option to drill a side track from PX-2 into the activated zone documented by the seismic cloud, and to be able to connect both wells for water circulation. To

reach this goal, additional equipment like a 17-instrument three component borehole geophones array was installed in the PX-2 well between 1350 and 1510 m measured depth (Hofmann et al., 2019).

The main characteristics of PX-1 2nd stimulation, on which we focus in this study, such as wellhead pressure, injection flow rates as well as net volume and seismicity are shown in Figure 4. In well PX-2 the maximum wellhead pressure reached 90 MPa during all three stimulations (Lee, 2019). Based on slip-tendency analysis reported by Park et al. (2017) and Park et al. (2020) the stimulation mechanism is tensile hydraulic fracturing. The stimulations in PX-1, on the other hand, show a lower peak wellhead pressure up to 28 MPa, and higher injectivity compared to that in PX-2. The main stimulation mechanism is inferred as hydro shearing (slip on pre-existing fracture or fresh shearing) with characteristic change in pressure at relatively low wellhead pressures of approx. 16-18 MPa, (Hofmann et al., 2019; Park et al., 2020). The local magnitudes of the largest induced seismic events during these stimulation treatments in both wells were $M_L = 2.3$ for PX-1 and $M_L = 3.1$ for PX-2 (Lee, 2019).

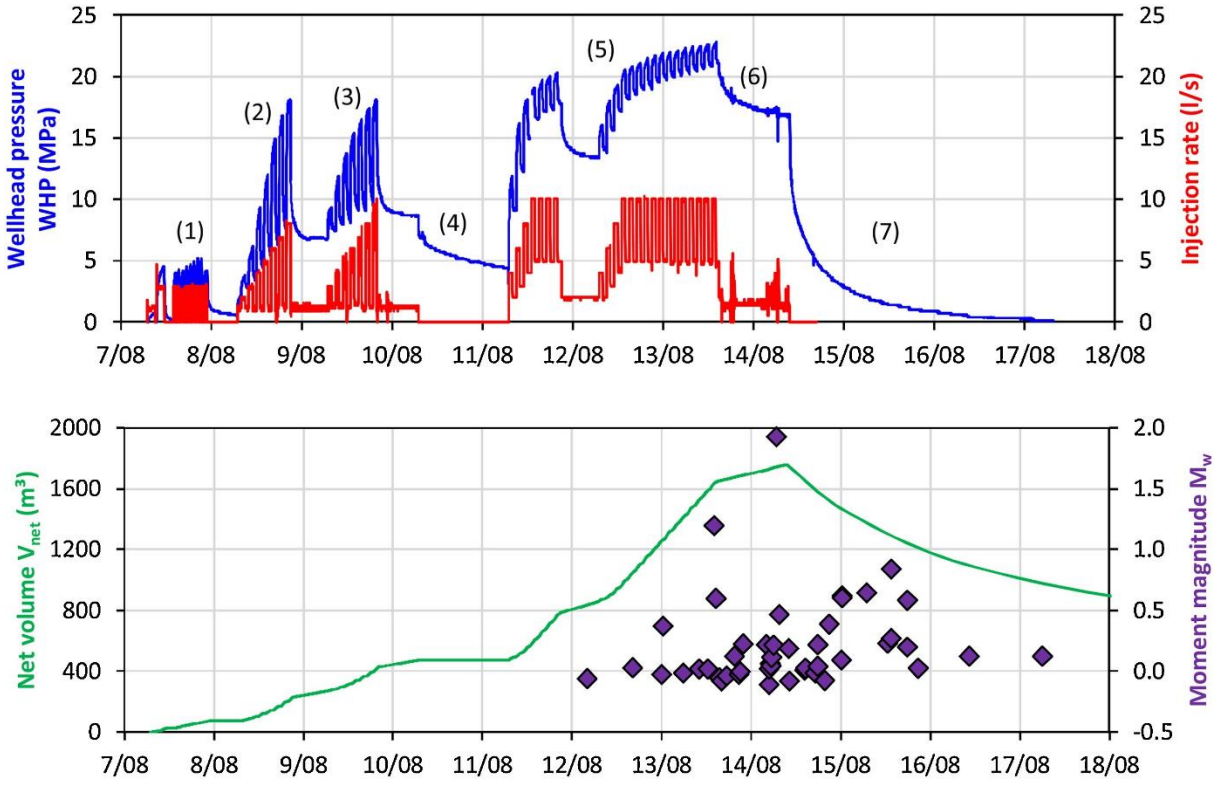

Figure 4: Overview of well head pressure (WHP), injection rate (Q), injected net volume (V_{net}), and moment magnitude M_w of induced seismic events during the August 2017 CSS treatment in well PX-1. This treatment can be divided into seven phases: (1) Day 1: initial injectivity determination, (2) Day 2: fracture opening pressure determination, (3) Day 3: hydraulic pulse tests, (4) Day 4: shut-in, (5) Days 5 through 7: main cyclic soft stimulation treatment, (6) Days 7 through 8: pressure reduction due to orange traffic light alert, and (7) complete flow back due to red traffic light alert (modified from Hofmann et al., 2019).

The EGS project was suspended because of a $M_w = 5.5$ earthquake that occurred close to the EGS site on 15th November 2017 (Ellsworth et al., 2019). Possible causal connections between EGS site activities and this event are hypothesized. Lee, 2019 argue that the possible relation is a combination of induced and triggering mechanism (fluid-injection induced poroelastic stress transfer) along a previously unmapped fault. Westaway and Burnside (2019) propose the concept of hydrochemical fault

corrosion, which is induced by injection of surface water with different chemical composition compared to the reservoir fluid.

For more information on the Pohang EGS pilot project and the hydraulic stimulation treatments, the reader is referred to Hofmann et al. (2019) and Lee (2019).

5.2.4 Structural interpretation of hydraulic stimulation programs and Mw 5.5 Pohang earthquake shocks

Joint interpretation of well test and microseismic data of the hydraulic stimulations is reported by Bethmann et al. (2019), who conclude two fault structures (Figure 5). In this paper, the joint interpretation includes microseismic locations during hydraulic stimulations and the M_w 5.5 Pohang earthquake published in Lee (2019) as well as the interpretation of seismicity during PX-1 2nd stimulation in Hofmann et al. (2019). One fault, which is referred to as plane P1, intersects the openhole section of well PX-1 at 4068 m measured depth (MD). It is assumed to be the main conductive structure as well as the plane for hydro-shearing. The other structure, plane P2, intersects the cased part of well PX-2 at approx. 3800 m MD. Characteristic for P1 is that early microseismicity is distributed along or close to the plane for both PX-1 stimulations. These events cluster around the injection point in all three studies cited above. We note that the 52 events from PX-1 2nd stimulation are not included in Figure 5, since these contain large horizontal errors, however their reported clustering feature is unambiguous. Furthermore, no PX-1 seismicity is observed SE from the intersection of the two planes or along structure P2 (see vertical view from South in Figure 5). The best fit plane P2 based on the PX-2 stimulations lies between the two wells. In contrast to PX-1 seismicity, PX-2 seismic events are also located NW from plane P2 (see top view in Figure 5). The structure contains the hypocenter of the M_w 5.5 Pohang earthquake.

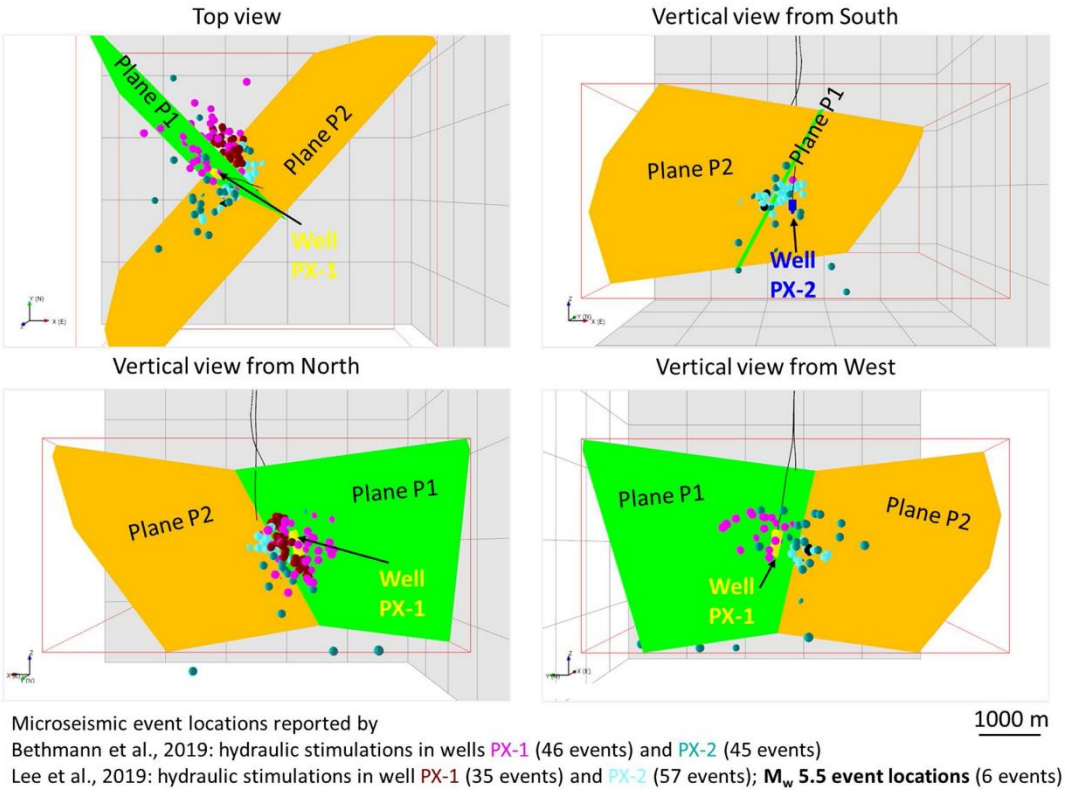

Figure 5: Joint structural interpretation of hydraulic data and microseismic clouds of PX-1 and PX-2 hydraulic stimulations. Microseismic locations are color-coded according to hydraulic treatments of respective well and source. Plane P2 contains the hypocenter of the M_w 5.5 earthquake on 15th November 2017 (based on Bethmann et al., 2019).

5.3 Numerical methodology

5.3.1 Numerical code

The hydro-mechanical behavior of the stimulated fractures is simulated through an explicit, iterative process described below. The coupling concerns the description of stress-aperture relationships according to Barton et al. (1985). The empirical equation for estimating the initial mechanical aperture, E_0, at low stress levels is based on the measured values of joint roughness coefficient (*JRC*), joint wall compressive strength (*JCS)*, and the uniaxial compressive strength of rock (*UCS*):

$$E_0 = \frac{JRC}{5}\left(0.2\,\frac{UCS}{JCS} - 0.1\right) \quad (1)$$

Note that the units are important: E_0 must be in mm, *UCS* and *JCS* must both be in same units. JRC is dimensionless. The change in mechanical aperture (ΔE) with effective normal stress (difference between the total normal stress and the pore pressure), σ_n, is calculated as

$$\Delta E = \frac{\sigma_n \kappa}{\kappa K_n + \sigma_n} \quad (2)$$

where κ is the maximum aperture closure and K_n is the fracture normal stiffness. The residual mechanical aperture, E, is provided by the equation:

$$E = E_0 - \Delta E \quad (3)$$

Hydraulic or fluid conducting aperture, e, can be estimated from mechanical aperture E and *JRC* as

$$e = \frac{JRC^{2.5}}{\left(\frac{E}{e}\right)^2} \quad (4)$$

It must be noted that E and e here are in μm unit. The strength of a fracture or fault is provided by the Mohr-Coulomb failure criterion:

$$\tau = C_0 + \mu\sigma_n \quad (5)$$

where τ is the shear strength acting in the plane of fracture surface, C_0 is the cohesion of the fracture and μ is the coefficient of (internal) friction.

Rock stress and strain are calculated in rectangular cuboid grid cells. These are calculated using Golder's FracStress package. This code uses a finite element model (FEM) with tetrahedral elements with nodes corresponding to the vertices of the grid cells. Each grid cell has material properties that are shared by all the tetrahedral elements that make up the cell. FracStress calculates stresses in the grid based on (far-field) boundary conditions, material properties, and an induced grid cell strain field.
The grid cell rock strain (ε) induced by the incremental change of fracture aperture is based on Hooke's one-dimensional elastic stress versus strain relationship:

$$\varepsilon = \frac{\Delta E}{L}\frac{A_f}{A_{max}} \quad (6)$$

Where A_f represents fracture element area inside a grid cell volume, A_{max} is the area of a plane parallel to the intersecting fracture and placed at cell center. L is strain depth, which is computed as the maximum distance between furthest cell vertex and a plane parallel to the intersecting fracture. This implementation is founded within the Oda (1986) geomechanical upscaling framework such that the one-dimensional change of a fracture aperture can be evaluated in terms of a full-3D incremental strain tensor.

The hydraulic part of the simulation is modelled by Golder's Matrix/Fracture Interaction (MAFIC) code (Golder Associates, 2001). The program models fracture flow through a network of interconnecting fracture element plates and matrix flow through a three-dimensional volume. Flow in fractures is simulated in two-dimensional triangular finite elements, assuming incompressible fluid, using the equation of Bear (1972):

$$S_{frac}\frac{\partial P}{\partial t} - T_{frac}\nabla^2 P = q \quad (7)$$

Where S_{frac} is fracture storativity, P is fluid pressure, t is time, T_{frac} is fracture transmissivity, q is source or sink term and ∇^2 is Laplace operator.

Flow in the matrix is simulated by a generic matrix block scheme. The matrix block approach here defines a single, rectangular slab block geometry. This represents all matrix blocks in a network of surrounding fractures. The slabs have a surface area of the drainage face, which is set equal to the fracture element area.

Flow through each matrix block, i.e. between fracture facelets, is treated as a one-dimensional pipe flow coupled to the pressure in the associated bounding fracture element:

$$S_m\frac{\partial P}{\partial t} - K\nabla^2 P = q_S \quad (8)$$

Where S_m is rock specific (matrix) storage, P is fluid pressure, t is time, K is hydraulic conductivity, q_S is specific source or sink term and ∇^2 is Laplace operator. The one-dimensional pipe flow approach is employed to reduce numerical costs since we focus on matrix storage in the numerical model.

It must be acknowledged that the HM coupling is not complete as the variation of fracture aperture is lumped in storativity. This is generally employed for relatively low pressures where both fractures and matrix exhibit small deformation (see e.g. discussion in Marck et al., 2015 regarding such uncoupling). As soon as shear induced plastic deformation is activated on the fault, this approach may lead to misleading results. Therefore, in the Barton-Bandis implementation (Barton et al., 1985) we follow the shear-induced modification to the stress-aperture relationship via the frictional input properties, e.g. JRC, which is slip dependent.

FracMan relates the hydraulic parameters transmissivity and storativity with aperture and compressibility for fracture/fault element and matrix using the following relationship:

$$T_{frac} = \frac{\rho_{fluid} g e^3}{12 \eta_{fluid}} \tag{9}$$

Where ρ_{fluid} and η_{fluid} are fluid density and viscosity, respectively, e is fracture element hydraulic aperture and g is acceleration of gravity.

Conversion between fracture storativity (S_{frac}) and compressibility is calculated as:

$$S_{frac} = (C_{frac} + C_{fluid}) \rho_{fluid} e \tag{10}$$

Where C_{frac}, and C_{fluid} are fracture and fluid compressibility, respectively.

Conversion between matrix storativity (S_m) and compressibility is considered as:

$$S_m = (C_m + C_{fluid}) \rho_{fluid} g \varphi \tag{11}$$

Where, C_m is matrix compressibility and φ is matrix (rock) porosity.

The hydro-mechanical coupling during simulation of fluid injection into a borehole with a given flow rate are realized with the looping in Figure 6:

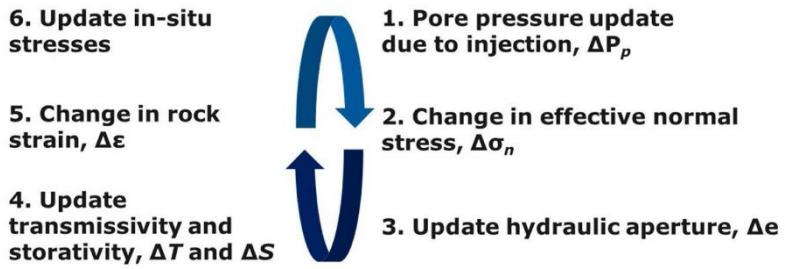

Figure 6: Cycle of hydro-mechanical coupling in FracMan.

For more details on the numerical method the reader is referred to Cottrell et al. (2016).

5.3.2 Numerical model setup

The FracMan code allows considering faults (fractures) and intact rock matrix explicitly. Faults are the dominant fluid flow paths transmitting pressure changes while the rock matrix properties and stress state

governs poro-elastic stress transfer. The 3D volume of interest, which contains the faults and the intact rock, is centered at the PX-1 open borehole section which is illustrated in Figure 7. The size of the modelling domain is 4 km x 4 km x 2 km, which ensures avoiding numerical boundary effect.

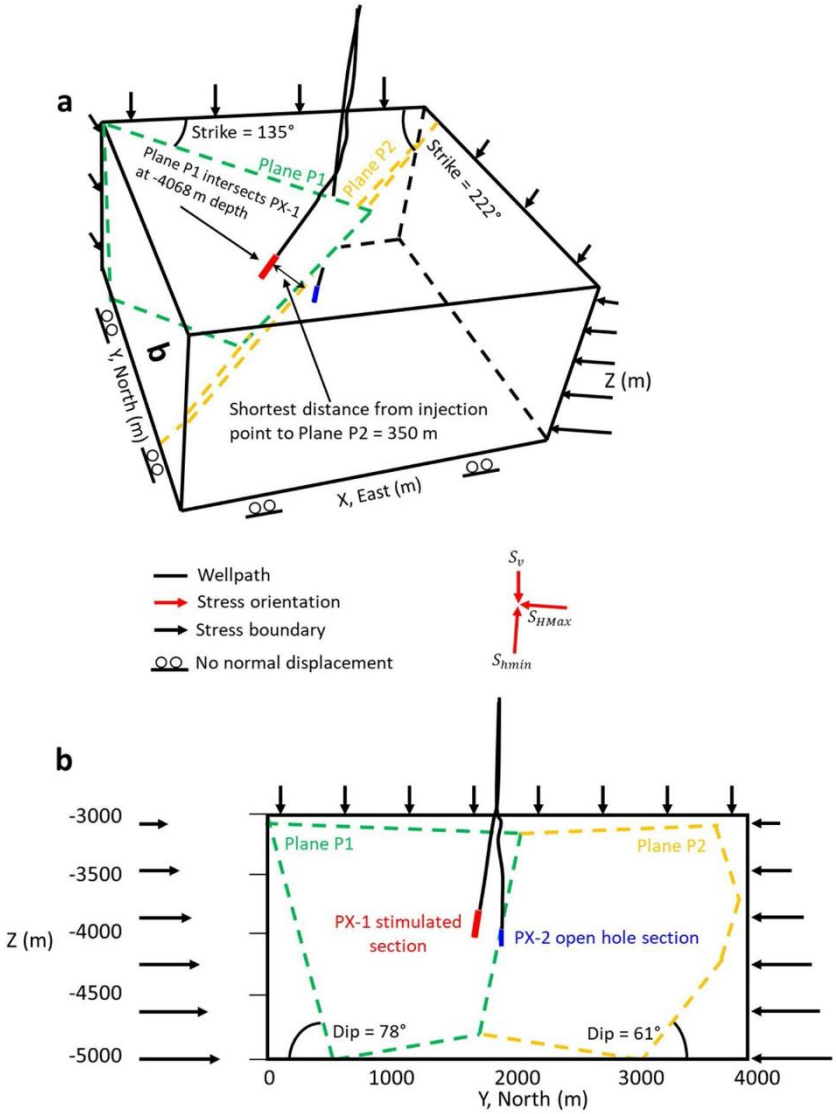

*Figure 7: Oblique view looking down from SW (**a**) and vertical view from W (**b**) illustrating the fault structures and boundary conditions of the numerical model.*

The geometries of the fault planes, P1 and P2, are based on joint interpretation of hydraulic and microseismic information described in Section 5.2.4. Plane P1 strikes NW-SE (N135 °E) and dips at 78°. The plane intersects the openhole section of well PX-1 at 4068 m MD, i.e. at the top of the interval. Plane P2 shows strike of SW-NE (N222 °E) and dip angle of 61° (Bethmann et al., 2019). According to the fault configuration, the shortest possible distance from the injection point in structure P1 to plane P2 equals 350 m.

The grid representing the intact rock considers the crystalline rock strength and the input for defining the in-situ stress field as spatially varying grid properties (Figure 8). The size of the grid

elements is set to 100 m x 100 m x 100 m, and 32000 grid cells are generated in total. We note that the size of grid cells may appear large - especially with regards to the distance between the injection point and the intersection line between fault planes P1 and P2 (350 m). However, these represent matrix blocks, and the fluid conducting faults are meshed much finer (Section 5.3.2). Consequently, the grid cells ensure considering matrix effect in fluid flow modelling and numerical stability, as well as acceptable computational costs at the same time.

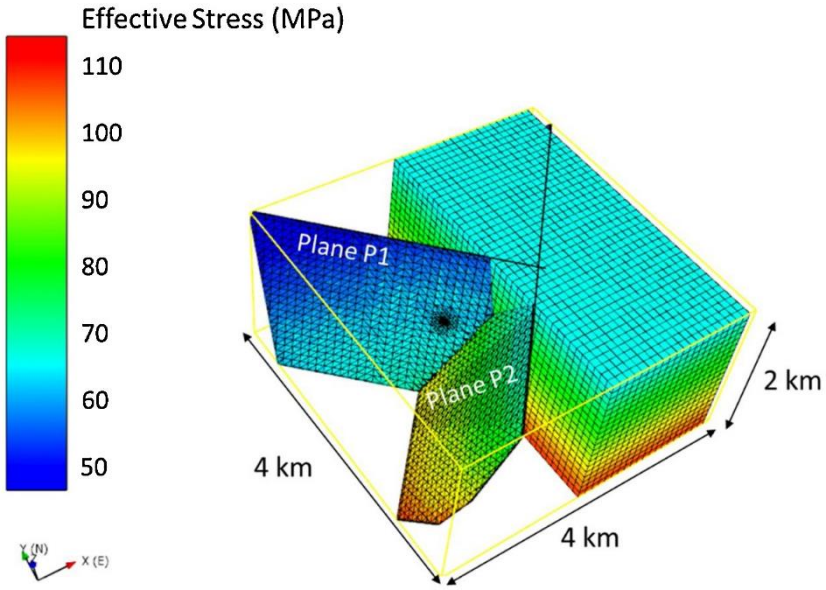

Figure 8: Oblique view looking down from SW illustrating the spatial distribution of effective maximum horizontal stress acting in the grid and that acting on the fault planes, P1 and P2. The modelling box dimensions are 4 km x 4 km x 2 km. Grid element dimensions are 100 m x 100 m x 100 m. Fault element size varies between 0.1 m and 75 m.

Constant gradient stresses are applied at the boundaries of the model. The bottom of the model is fixed (no normal displacement). The geomechanical model properties are summarized in Table 2 and Table 3.

Table 2: Granodiorite geomechanical parameters derived from laboratory tests on rock cores from PX-2 from 4.2 km depth (Kwon et al., 2019).

Geomechanical Property of Intact Rock	Mean Value	Standard deviation	Number of tests
Bulk Density (kg/m^3)	2630	5	11
Porosity (%)	0.5	0.07	11
Uniaxial Compressive Strength, *UCS* (MPa)	106.7	22.3	7
Tensile Strength (MPa)	9.2	0.4	2
Young's Modulus (GPa)	33.5	6.8	4
Poisson's Ratio	0.21	0.05	4
Mohr-Coulomb Cohesion (MPa)	15.2	-	12

Table 3: Geomechanical properties of fractures derived from laboratory tests (Kwon et al., 2019).

Geomechanical Property of Fracture	Mean Value	Standard deviation	Number of tests
Joint Wall Compressive Strength, *JCS* (MPa)	169.2	87.2	5
Joint Roughness Coefficient, *JRC* (-)	13.1	2.8	7
Fracture Coefficient of Friction, μ (-)	0.5	0.01	2

We conducted critical stress assessment based on Mohr-Coulomb friction model to establish the stress field boundary conditions for the numerical simulation using the approach described in Blöcher et al., 2018 and Zoback, 2010. The methods are applied for planes P1 and P2 at 4 km depth using the principal stress magnitudes and orientations of Bethmann et al., 2019 in Table 1 and Biot's poro-elastic

coefficient, $\alpha = 0.79$ (Chang et al., 2020). Figure 9 illustrates the effective normal stress and shear stress acting on P1 and P2. Based on the critical stress analysis, none of the planes is critically stressed at the depth of investigation prior to any hydraulic stimulation. Furthermore, the required pressure for slippage is higher for P2 than for P1. The pressure for hydro-shearing P1 is about 36 MPa and that for P2 equal 53 MPa for the laboratory fracture coefficient of friction, $\mu = 0.50$. The hydro-shearing pressure for P1 is higher than that discussed in Section 5.2.3, i.e. 16–18 MPa. Thus, the coefficient of friction must be as low as 0.23 in order to model fault slip at an injection pressure of 16–18 MPa for the given stress state. The lower μ may be explained with the clayey infilling material of the fracture (Lee, 2019) and the relatively large variability of fracture strength parameters in Table 3. Furthermore, Zang and Stephansson (2010) point out that estimated μ for field scale applications can be lower than that anticipated from laboratory tests.

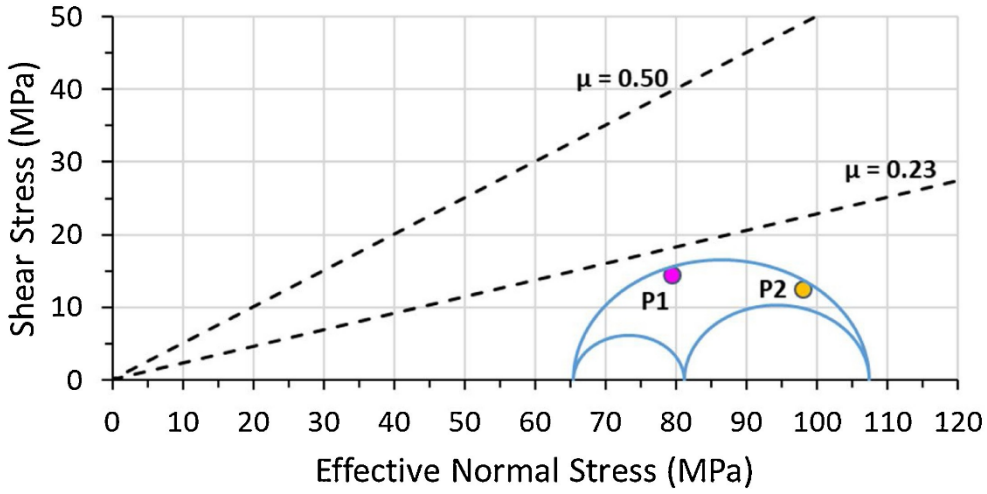

Figure 9: Critical stress analysis (Mohr-Coulomb failure plot) for planes P1 (magenta dot) and P2 (yellow dot) at 4 km depth for establishing the stress field for the numerical simulation based on the strike-slip model of Bethmann et al. (2019) (Table 1). Two coefficients of frictions are assumed for the analysis: μ = 0.50 is reported for fractures present in cored samples and μ = 0.23, which is used in the numerical model and required for observing hydro-shearing at injection pressure 16-18 MPa. Further input for Mohr-Coulomb failure plot: pore pressure =39 MPa, Biot's poro-elastic coefficient = 0.79 and cohesion=0 MPa.

Table 4 specifies the strike-slip stress field parameters with the gradients for minimum horizontal stress (S_{hmin}), vertical stress (S_v) and maximum horizontal stress (S_{Hmax}) as well as pore pressure, assuming a fluid density of 1000 kg/m³ and a gravitational acceleration of 9.81 m/s².

Table 4: Rock Stress Parameters used for the numerical study.

Parameter	Value
Maximum Horizontal Stress Gradient, S_{Hmax} (MPa/m)	0.0317
Vertical Stress Gradient, S_v (MPa/m)	0.0258
Minimum Horizontal Stress Gradient, S_{hmin} (MPa/m)	0.0227
S_{Hmax} Direction (°)	N100E
Fluid Pore Pressure Gradient (MPa/m)	0.00981

5.3.3 Simulation of high pressure fluid injection

In the model, fluid is injected into the P1 fault plane over eight days with varying flow rates following the injection protocol in Hofmann et al. (2019). Prior to simulation, the fault planes are meshed into

triangular elements with a minimum edge length of 0.1 m and maximum edge lengths of 75 m, 40 m, 30 m, 25 m and 20 m to avoid mesh-dependency. The minimum length is similar to the radius of well PX-1; and the maximum size is similar to that of matrix grid elements. The mesh is refined close to the node representing the borehole area and consists of 25650, 48367, 78679, 107894 and 153522 nodes for meshes with maximum edge length of 75 m, 40 m, 30 m, 25 m and 20 m, respectively. The injection into the plane is simulated using a source term (node) at the intersection of the open borehole section of well PX-1 and P1. An initial unperturbed hydrostatic pore pressure conditions is specified. Pressure increase from static level due to fluid injection is referred to as overpressure.

The simulated overpressure history is matched against observed wellhead pressure during the entire injection period. Frictional pressure losses in the well are negligible due to the large well diameter and the low flow rates. The history matching period begins at the onset of injection and lasts until the onset of the flowback phase. The simulated injection flow rates are identical to those recorded in the field. The matching procedure requires adjusting the input parameters governing the hydro-mechanical coupling sequentially, i.e. geomechanical properties. These are referred to as split-points dividing the simulation into sequences. At these split-points, the pressure output of the last time step is taken as input for the subsequent phase of the simulation. The parameters remain valid for a period until the next split-point is defined. In total, 6 split-points, i.e. sequences are defined in the simulation. The parameters are changed at the beginning of each stimulation sequence.

The input parameters are kept in a range that agrees with measured rock mechanical (Table 2 and Table 3) and reported hydrogeological parameters by Park et al. (2020) and Hofmann et al. (2019). Properties that are assumed to be constant include well radius, fluid and matrix properties, wellbore compressibility, fault compressibility as well as geomechanical properties except for UCS are summarized in Table 5.

Table 5: Constant fluid injection (well effect and fluid), hydrogeological (matrix and fault) and geomechanical properties of the numerical simulation of cyclic soft stimulation (CSS) treatment in well PX-1 in August 2017.

Well Effect		Reference/Remark
Well radius, r_{well} (m)	0.108	Hofmann et al. (2019)
Well storage coefficient (m^3/Pa)	$6\ 10^{-8}$	Product of borehole volume and fluid compressibility
Fluid properties		
Fluid viscosity, η_{fluid} (mPa s)	0.3	Hofmann et al. (2019)
Fluid compressibility, C_{fluid} (1/Pa)	$4.5\ 10^{-10}$	
Fluid density, ρ_{fluid} (kg/m^3)	1000	
Matrix properties		
Matrix permeability, k_m (m^2)	$1.8\ 10^{-16}$	Hofmann et al. (2019)
Porosity, φ (%)	0.5	Kwon et al. (2019)
Matrix compressibility, C_m (1/Pa)	$4.5\ 10^{-10}$	
Numerical block radius, r (m)	15	
Fault hydrogeological properties		
Fault compressibility, C_{frac} (1/Pa)	$4.5\ 10^{-10}$	
Fault geomechanical properties		
Normal stiffness, K_n (GPa/m)	200	Yoon et al. (2014)
Coefficient of friction, μ (-)	0.23	Critical stress analysis in Section 5.3.2
JRC (°)	12	Kwon et al. (2019)
JCS (MPa)	105	Kwon et al. (2019)
Maximum closure, V_m (mm)	1	

5.4 Results

Results of the numerical simulation of PX-1 2nd hydraulic stimulation are presented as follows. First, the purpose and protocol of each stimulation phase are summarized. Then, the simulated wellhead pressure is compared against field record and the parameters governing the history matching are discussed (Figure 10). The adjusted numerical parameters are summarized in Table 6. Based on the achieved history match, we characterize the resulting hydro-mechanical parameters, such as hydraulic aperture and transmissivity. The evolution of stress-aperture relationship as well as hydraulic aperture and transmissivity are shown in Figure 11 and Figure 12, respectively.

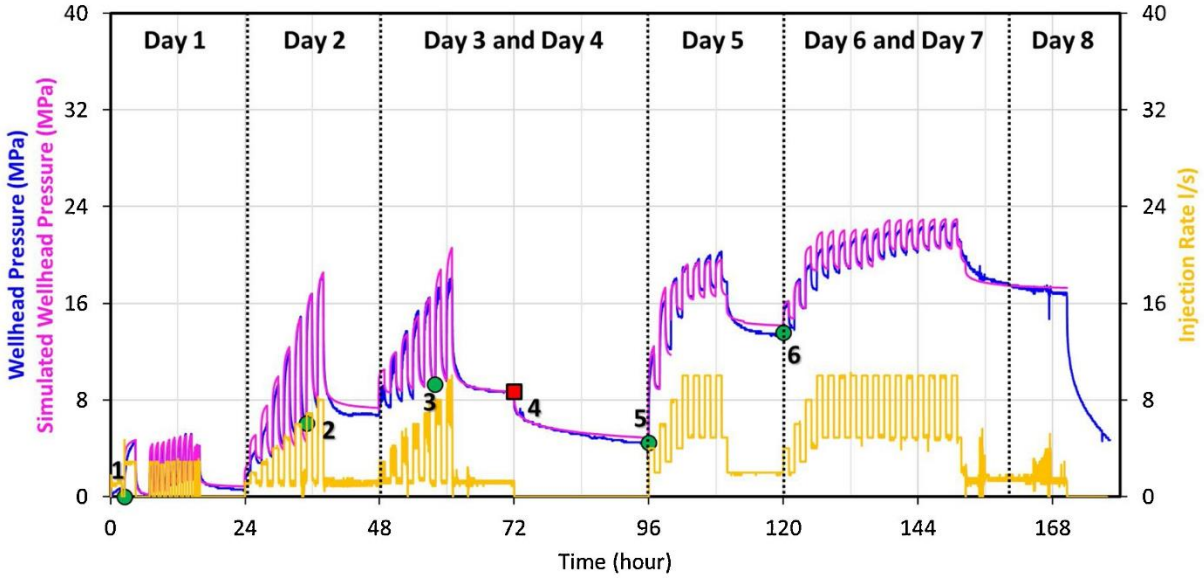

Figure 10: Comparison of recorded (blue) and modelled (violet) wellhead pressure data for cyclic soft stimulation (CSS) treatment in well PX-1 of August 2017. Numerical injection flow rates are equal to that recorded on field (yellow). Numbers of 1 to 6 of the numerical simulation represent sequential changes in the input parameters referred to as split-points (Table 6). Green circles represent increase in hydraulic aperture. Red square represents decrease in hydraulic aperture.

Table 6: Adjusted fault geomechanical property of the numerical simulation of cyclic soft stimulation (CSS) treatment in well PX-1 in August 2017.

	Day 1	Day 2	Day 3 – Day 4		Day 5	Day 6 – Day 8
Split-point ID	1	2	3	4	5	6
UCS (MPa)	103	108	113	109	110	115

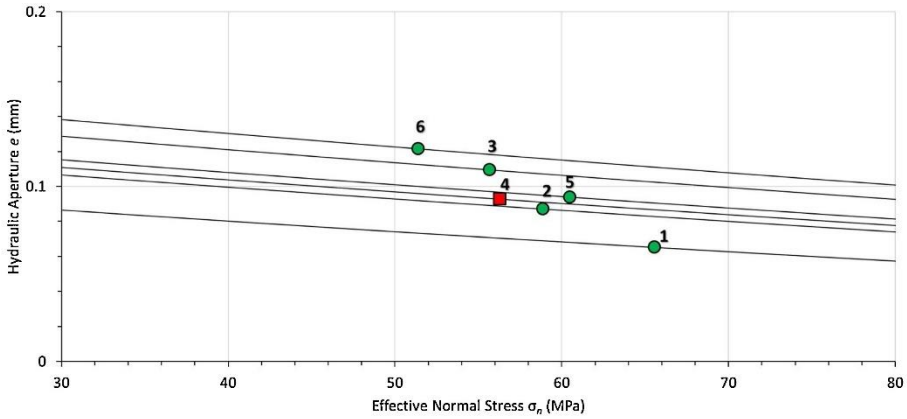

Figure 11: Evolution of stress-aperture relationships as well as hydraulic aperture at injection point. The IDs 1 through 6 represent split-points, i.e. change in input parameters, as shown in Table 6. The order of IDs increases with stimulation time. Circles represent increase in hydraulic aperture, square represents decrease in hydraulic aperture at the injection point.

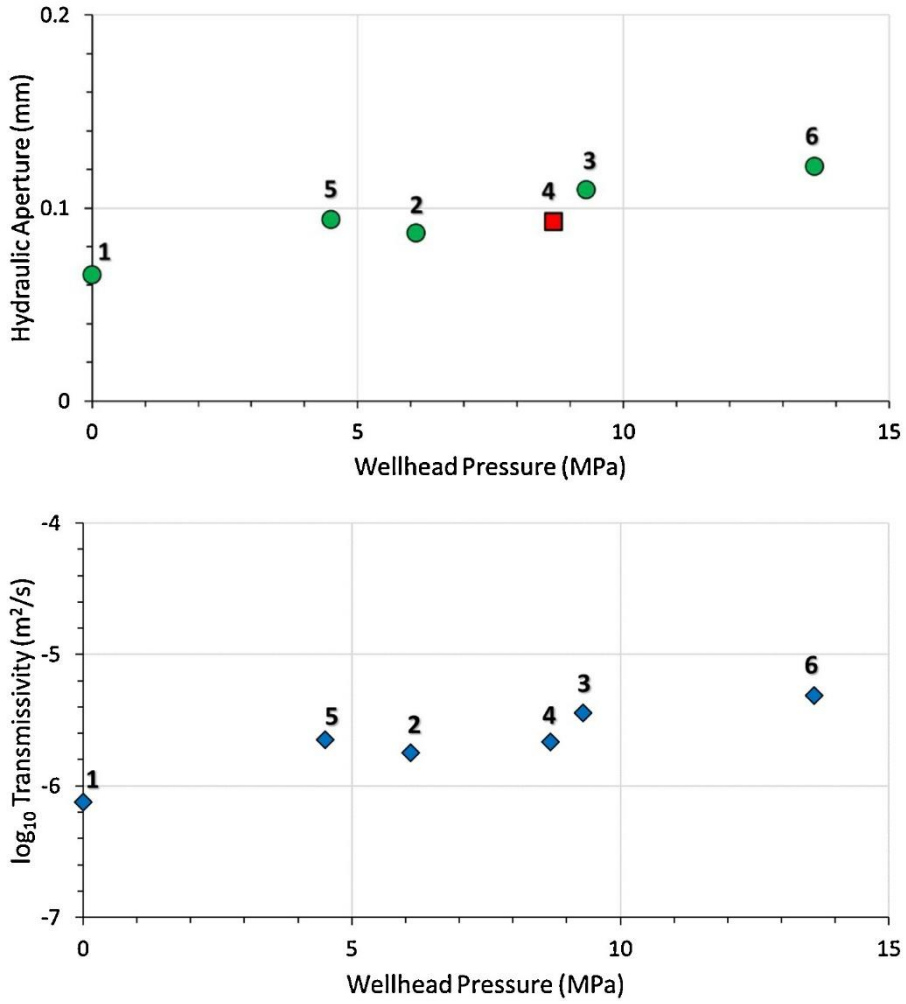

Figure 12: Top: simulated hydraulic aperture development with wellhead pressure. Bottom: simulated transmissivity (blue diamond) development with wellhead pressure. The IDs 1 through 6 represent split-points, i.e. change in input parameters, as shown in Table 6 and Figure 10. The order of IDs increases with stimulation time.

5.4.1 Day 1: Initial injectivity determination

The first day of the treatment focused on determination of the initial reservoir conditions. The stimulation program included a 2 -h-long injection with constant flow rate of 3 l/s, followed by a 2 -h shut-in phase. Afterwards, cyclic test with eight 1 -h cycles with periods of 30 minutes of 3 l/s injection and 30 minutes of shut-in were performed. At the end of the day, ten 6-minute cycles with the same flow rates were conducted. The maximum WHP reached 4 MPa at the end of the last test.

The simulated WHP response shows good match with the recorded one. At static pore pressure, marked as split-point ID 1, the hydraulic aperture is 0.06 mm at the wellbore corresponding to transmissivity of 7.5 10^{-7} m^2/s.

5.4.2 Day 2: Fracture opening pressure determination

The second day of the treatment aimed at determining the fracture opening pressure by a progressive cyclic injection test. This was realized by seven 2 -h cycles with 1 l/s base injection rate. The injection rate was progressively increased from 2 l/s to 8 l/s with 1 l/s steps. The maximum WHP reaches 18 MPa. At the end of the day, the WHP reduces to 7 MPa due to return to base flow rate.

To achieve a reasonable match of the pressure curves, an additional split-point ID 2 is inserted. The split-point is set before the pressure curve reaches the critical pressure range for deformation, i.e. 16-18 MPa as presented in Section 5.3.2, interpreted as hydro-shearing at increased flow rates (Hofmann et al. 2019). This is captured by modifying the stress-aperture relationship by increasing the UCS within the range shown in Figure 11. The hydraulic aperture, therefore, increases from 0.06 mm to 0.08 mm. Transmissivity increases from 7.5 10^{-7} m^2/s to 1.8 10^{-6} m^2/s.

5.4.3 Day 3 and day 4: Hydraulic pulse tests and shut-in

On the third day harmonic pulse tests were performed by adding pulses on top of the high rate injections. The flow rates are chosen to ensure the same injected volume and average injection rate during all cycles in both progressive cyclic injection test and hydraulic pulse tests. Injection was continued at the 1 l/s base rate until day 4 with a similar length as the previous test. On day 4, the well was kept shut-in for 24 hours. This allowed observing the hydraulic and seismic behavior of the system. The wellhead pressure reached 18 MPa on day 3 and dropped from 9 MPa to 4.5 MPa during the subsequent shut-in phase on day 4.

The simulated WHP can be matched against field record if an additional split-point is inserted during the phase of increasing flow rates. This split-point ID 3 is defined at WHP of 9.30 MPa, just before the critical pressure for hydro-shearing is reached at the following higher injection rate. At this split-point the UCS is further increased corresponding to hydraulic aperture increase to 0.11 mm and transmissivity increase to 3.6 10^{-6} m^2/s.

The simulated wellhead pressure matches with the field record using the latest hydro-mechanical parameters until the onset of the shut-in period. The simulation phase starting at ID 4 is defined at the beginning of the shut-in phase. At this point, the UCS is reduced which results in decreased hydraulic aperture and transmissivity at the injection point, 0.08 mm and 2 10^{-6} m^2/s, respectively. This can be explained with pressure drop well below the range for hydro-shearing. This simulation period lasts until the end of day 4. The variations in parameters at split-points ID 3 and 4 mimic fracture opening and closure for this period.

5.4.4 Day 5: Main cyclic soft stimulation phase

The main cyclic soft stimulation treatment began on day 5. Injection lasted for 14 hours with cycles of 2 hours length. The high injection rate during the cycling equals to 10 l/s and the low one is 5 l/s. This was followed by 10 hours of base rate injection of 2 l/s overnight. The highest observed WHP is 20 MPa. The simulation of injection begins with defining split-point ID 5 at WHP 4.5 MPa before the phase of increasing flow rates resulting in WHP larger than the pressure for hydro-shearing. The split-point is required in order to achieve an acceptable match between observed and simulated pressure record. At the end of Day 5, the WHP decreases below hydro-shearing pressure. At split-point ID 5, the UCS is increased again. The resulting hydraulic aperture is 0.095 mm and the transmissivity is 2.3 10^{-6} m^2/s.

5.4.5 Day 6 and day 7: Continuation of main cyclic soft stimulation phase. Flow rate and pressure reduction due to traffic light system alert

The main cyclic soft stimulation phase continued for days 6 and 7. In this period, the injection schedule was the same as on the previous day, except for seven more repetitions of the cycle of 5-10 l/s (Salina Borello et al., 2019). The maximum WHP reached 22.8 MPa, which equals to the absolute maximum WHP for the treatment.

Due to occurrence of M_w 1.2 microseismic event (which was first analyzed as an event with M_w 1.4), the injection rate was decreased stepwise to 2 l/s, then to 1 l/s. This action was taken according to the traffic light system (Hofmann et al., 2019). In this period, 15 microseismic events with magnitude below M_w 1.0 were observed (Figure 4).

The history matching of the pressure curve requires inserting a split-point at the beginning of day 6. At time point ID 6, where the WHP is 13.6 MPa, the UCS is increased to mimic increase in hydraulic aperture and transmissivity. The calculated hydraulic aperture and transmissivity equal 0.12 mm and 5 10^{-6} m^2/s. The split-point is inserted just before the critical pressure for hydro-shearing is reached again at the subsequent higher injection rate.

5.4.6 Day 8: Continuation of flow rate and pressure reduction. Complete flowback

On the last day of main cyclic soft stimulation phase, the injection with 1 l/s went on until the detection of event M_w 1.9. After analyzing the microseismic event, the injection was stopped, and the well was opened for flowback. Several events were detected during, and after this period with M_w around or less than 1.0. The maximum WHP was 18 MPa.

The history matching of wellhead pressure is achieved via continuing the simulation with the parameters defined at split-point ID 6. This might be related to the evolution of WHP which is above the pressure for hydro-shearing until the flowback period.

In Figure 13, the extent of pressurized subsurface area is plotted at WHP of 17.1 MPa, just before complete flowback at last time step. The pressurized area, i.e. direct pore pressure change that may be linked to induced microseismic events within fault P1 shows that the extent of overpressure of 0.01 MPa, threshold defined by Lee, 2019, in the direction of the shortest possible distance to the plane P2 is approx. 180 m. The hydraulic diffusion reaches as far as 450 m, i.e. the overpressure goes beyond the intersection between P1 and P2. However, the magnitude of overpressure on P2 is below 0.01 MPa.

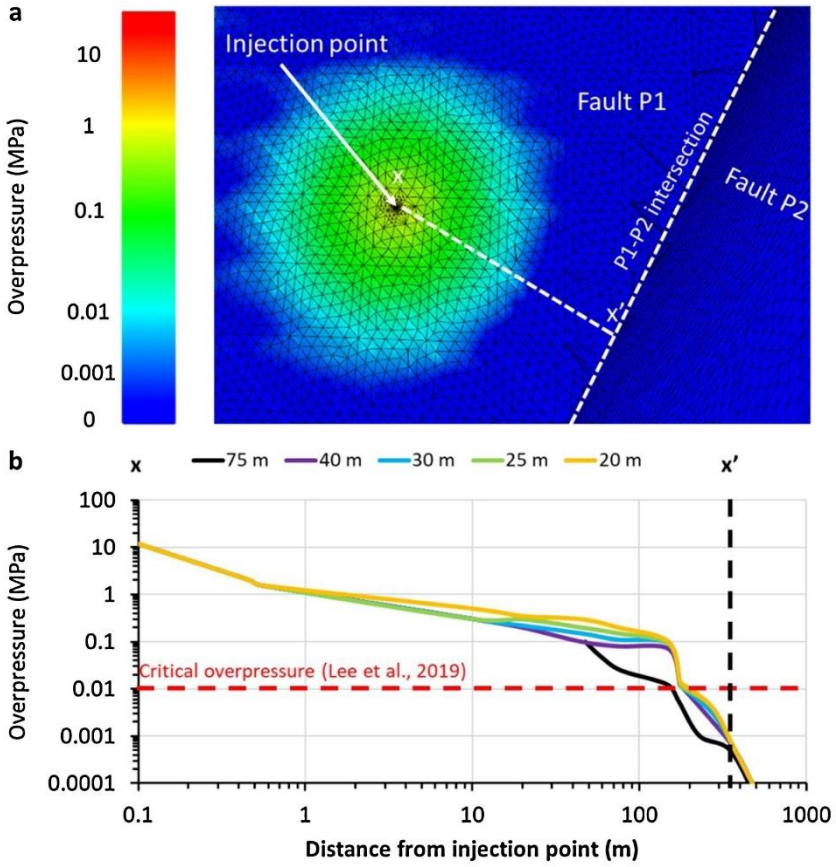

*Figure 13: The extent of pressurized subsurface area (investigation radius) at the end of the August 2017 stimulation in well PX-1 before flowback. (**a**): View is looking obliquely down from the NE. The largest edge length is 75 m. The smallest edge length is 0.1 m. (**b**): overpressure profile along section x-x'. The red dashed line denotes the critical overpressure level of 0.01 MPa defined by Lee et al., 2019 for potential induced seismic event. In order to eliminate bias due to mesh-dependence, the extent of overpressure is shown for different maximum mesh edge lengths, i.e. 75 m, 40 m, 30 m, 25 m as well as 20 m.*

The simulated extent of overpressurized area may be compared with that defined in a homogeneous and isotropic medium. In that case, the interference radius of a constant-rate well test (R) is defined analogously to the wavelength of a poroelastic wavefield as

$$\mathrm{R} = \sqrt{4\pi \frac{k_{eq}}{C_{total}\,\eta_{fluid}} t} = \sqrt{4\pi D t} \tag{12}$$

where k_{eq} is the equivalent permeability of the medium, C_{total} is the total compressibility and D is the system diffusivity (Shapiro, 2015). Conservatively assuming an 8-day-long injection test using the highest equivalent permeability reported by Hofmann et al. (2019) lies at 2.71 10^{-15} m^2, as well as fluid viscosity and total compressibility as the sum of matrix and fluid compressibility in Table 4 scaled with

porosity, the calculated radius is approx. 350 m. Thus, the upper limit of triggering front of induced seismic events agrees with the maximum extent of overpressurized area.

5.5 Discussion

5.5.1 Hydraulic aperture and transmissivity evolution

The simulation of August 2017 stimulation in well PX-1 shows that the fluid diffusion due to hydraulic stimulation is governed by several parameters. Hydro-mechanical coupling (stress versus hydraulic aperture relationship) has strong effect on the simulated wellhead pressure. The split history match shows that split-points are required to obtain good agreement between recorded and simulated pressures. Split-points are inserted when different pressure levels of hydro-mechanical coupling are reached as defined by Cornet (2016). Here, this refers to transition from linear poro-elastic response following Darcy-type fluid flow, i.e. below 16-18 MPa wellhead pressure, to hydro-shearing of pre-existing fault structure.

The hydraulic aperture variation is captured by modified stress-aperture relationships. This is done by adjusting UCS throughout the simulation as its variation allows slight shift of the stress-aperture curve. The adjustment is performed at 6 split-points. At split-point with IDs 1, 2, 3, 5 and 6, the hydraulic aperture is increased according to the pressure level of the treatment, i.e. whenever the wellhead pressure is about to reach hydro-shearing pressure. The only exception is split-point ID 4 where the stress-aperture law is adjusted so that the hydraulic aperture is reduced due to longer shut-in period. Consequently, the changes in fault properties are consistent.

We also investigated the evolution of the aperture-based transmissivity (Figure 12). The transmissivity shows an increase in the order of one magnitude approx. from 10^{-7} to 10^{-6} m^2/s. The simulated hydraulic aperture and transmissivity can be compared with those obtained from well test and pulse test analysis on day 1, day 4 and day 7 (Hofmann et al., 2019). Based on Table 7, the hydraulic apertures of this study are smaller than the reported ones. This may be explained by including joint roughness in this study that reduces aperture. On the other hand, apertures derived from reported permeability in Hofmann et al. (2019) consider apertures as smooth, parallel-plate structures. Finally, the permeability calculated from well tests depends on the reservoir thickness, which is not well constrained. Consequently, simulated transmissivities are also smaller than that of Hofmann et al. (2019).

Table 7: Comparison of simulated hydraulic aperture and transmissivity against reported values in Hofmann et al. (2019).

Period of Well test analysis in Hofmann et al. (2019)	Pressure drop 1 on Day 1	Pressure drop 2 on Day 1	Pulse test on Day 1	Pressure drop on Day 4	Pulse test on Day 5	Pulse test on Day 6 and Day 7
Respective split-point	1	1	1	4	5	6
Hydraulic aperture (mm) calculated in this study and reported in Hofmann et al. (2019) (*in bracelets*)	0.06 (*0.11*)	0.06 (*0.10*)	0.06 (*0.13*)	0.09 (*0.08*)	0.095 (*0.19*)	0.12 (*0.21*)
Transmissivity (10^{-6} m^2/s) calculated in this study and derived from Hofmann et al. (2019) (*in bracelets*)	0.76 (*3.8*)	0.76 (*3*)	0.76 (6.5)	2.1 (1.7)	1.32 (19.3)	5.0 (*25.8*)

It is interesting to note that both hydraulic stimulations in well PX-1 show characteristic changes in injectivity at WHPs between 15 and 17 MPa, being linked to hydro-shearing. However, it can be argued that the simulated hydraulic aperture development resembles hydraulic fracturing of existing fractures (Doe and Korbin, 1987). This is characterized by reversible, elastic aperture opening and closing with pressure below critical pressure level (Kewel et al., 2019). Furthermore, the calculated hydraulic apertures agree with that in Park et al. (2020), obtained from the previous stimulation in the well. Hence, we do not observe any additional permanent increase in hydraulic aperture in fault P1. This implies that the additional slip did not improve the hydraulic performance of this closed system. Moreover, a different slip model may be required to model this behavior, e.g. rate-and state strength model proposed by Dieterich (1992) and Dieterich (1994). Moreover, it is also possible that the fault may have slipped during the first stimulation. Further slip then does not significantly change the permeability anymore.

Therefore, future numerical models should employ different slip models that may predict this observed effect of cyclic changes in normal stress and in aperture (e.g. Boettcher and Marone, 2004).

5.5.2 Extent of pressurized area

The extent of directly pressurized fault radius of 180 m with 0.01 MPa cut-off value implies that the hydraulic diffusion for inducing seismic events is limited relatively close to near-well area during the time of injection. This is demonstrated by the pressure distribution around the injection point in Figure 13b. Given that the simulated injection point is located approx. 350 m as shortest distance from plane P2 along P1 (Figure 7), the modelling results reveal that the pore pressure, and thus, the effective stresses at fault P2 are changed only by less than 0.001 MPa during the treatment. The fluid pressure development shows good agreement with the microseismic locations from PX-1 stimulations, i.e. clustering around the injection borehole. However, the presented modeling study does not evaluate poroelastic stress transfer and pressure diffusion after the end of the treatment. Both may well lead to higher pressures on the P2 fault months after the end of injection and should be investigated in the future.

This is of importance as seismicity can be induced further away than the pressure diffusion front because of deformation-induced (poroelastic) pressure changes (e.g., De Simone et al., 2017; Goebel and Brodsky, 2018) as proposed by Ellsworth et al. (2019). Additionally, the pore pressure gradient

induced by the injection requires time to equilibrate due to the low permeability of the granodiorite rock, although the well was vented. Therefore, it is a subject of future modelling study to investigate the possibility of high pore pressure migration towards plane P2 after the injection was stopped and the well was vented, as well as the possibility of higher pore pressure on plane P2 several months after the stimulation as proposed by Ellsworth et al., 2019. Future studies should also consider full hydraulic history of the site including all five stimulation treatments and flowback/shut-in/production periods in between.

5.5.3 Numerical limitations

The FracMan modelling software has some limitations with respect to pressure matching of the hydraulic stimulation treatment, which are discussed in the following.

First, the change in stress versus hydraulic aperture relationship over time implies that this behavior during the treatment either cannot be characterized by a single law or a different equation may be utilized. For example, one may combine elastic opening and shear dilation as proposed by Rinaldi and Rutqvist (2019). However, using different relationship may be challenging due to several reasons. The widely used, Barton et al. (1985) hyperbolic relationship, which is also applied in this study, exhibits shallow aperture-stress curve at larger normal stresses. Such behavior is also reported in laboratory studies, e.g. in Kewel et al. (2019). An alternative, e.g. exponential relationship may be used, but that is proposed for shallow depths (Hökmark et al., 2010).

Second, the model does not include temperature-dependent fluid properties. Modelling of such behavior would require an independent sensitivity study since fluid density and viscosity have strong effect on fault transmissivity and storage. In order to incorporate such effects, a power-law based relationship between hydraulic aperture and normal stress could be employed. Moreover, different stress-aperture laws are required before and after fault slip. These may be combined following the approach described in Rutqvist and Tsang (2003).

Third, a more detailed investigation of induced seismicity would require incorporating different law for modelling fracture slippage, e.g. the rate-and-state friction model proposed by Dieterich (1992) and Dieterich (1994).

Finally, the model does not include the effects of the stimulations and flowback periods performed before and after the August 2017 stimulation in the two wells. These data could be included in order to evaluate the full hydraulic history of the site in a future study. Therefore, the presented model results do not allow making any statement about the pressure distribution in the reservoir at the time of the M_w 5.5 event since only a limited time is modeled.

It must be pointed out that the current (thermo-)hydro-mechanically coupled model can only produce pressure records that show general agreement with experimental data (e.g. Bhattacharya and Viesca, 2019; Bradford et al., 2017; Cheng et al., 2019; Lu and Ghassemi, 2019), and that for a limited period of the complete stimulation treatment. Due to the non-uniqueness associated to history matching

with complex HM coupled 3D numerical models the simulation result can only provide an idea about the influence of different processes, parameters and operations. Consequently, the present study can be considered as an attempt to improve and facilitate the discussion of 3D hydro-mechanically coupled simulation of field hydraulic stimulations in large-scale reservoirs and on the governing processes during the Pohang stimulations.

5.6 Conclusions

We investigated three-dimensional hydro-mechanical behavior of a fault that intersects the open borehole section of well PX-1 at the Pohang EGS site at approx. 4 kilometers depth. The August 2017 cyclic soft stimulation treatment, second stimulation in the well, was simulated in three dimensions using the FracMan code. The numerical wellhead pressure was matched against the field record. Our study draws the following conclusions:

1. With our model, a reasonable history match of the wellhead pressure could only be achieved by partitioning the treatment into separate periods. Partitioning the stimulation is beneficial computationally. Furthermore, it can capture phenomena related to fracture opening and closing, i.e. change in hydraulic aperture that are otherwise not captured by the code.
2. The hydraulic aperture evolution is typical of hydraulic fracturing. However, the fault is favorably oriented for hydro-shearing, which is generally characterized by permanent increase in aperture. This is explained by permeability increase through opening of the existing fault.
3. The influence of the treatment until flowback, i.e. the extent of direct pore pressure difference of >0.01 MPa is approx. 180 m in the direction of the shortest possible distance to the plane P2 along plane P1. This is half way between the injection and the plane of interest.

Declaration of Competing Interest

The authors declare that they have no known competing financial interests or personal relationships that could have appeared to influence the work reported in this paper.

Authorship contribution statement

Márton Pál Farkas: Conceptualization, Data curation, Formal analysis, Methodology, Visualization, Writing - original draft, Writing - review & editing. **Hannes Hofmann:** Conceptualization, Data curation, Formal analysis, Methodology, Resources, Validation, Visualization, Supervision, Writing - original draft, Writing - review & editing. **Günter Zimmermann:** Conceptualization, Methodology, Funding acquisition, Project administration, Resources, Supervision, Validation, Writing - original draft, Writing - review & editing. **Arno Zang:** Conceptualization, Methodology, Funding acquisition, Supervision, Validation, Writing - original draft, Writing - review & editing. **Falko Bethmann:** Supervision, Writing - original draft, Writing - review & editing. **Peter Meier:** Supervision, Writing -

original draft, Writing - review & editing. **Mark Cottrell:** Conceptualization, Methodology, Writing - review & editing. **Neal Josephson:** Conceptualization, Methodology, Writing - review & editing.

Acknowledgements

We highly appreciate the useful comments and discussion from anonymous reviewers. The DESTRESS project has received funding from the European Union's Horizon 2020 research and innovation program under grant agreement No 691728. First and second author are funded by this project. Furthermore, Hannes Hofmann is grateful for the financial support from the Helmholtz Association's Initiative and Networking Fund for the Helmholtz Young Investigator Group ARES (contract number VH-NG-1516).

References

Barton, N., Bandis, S., Bakhtar, K., 1985. Strength, deformation and conductivity coupling of rock joints. International Journal of Rock Mechanics and Mining Sciences & Geomechanics Abstracts 22(3), 121-140.

Bear, J., 1972. Dynamics of Fluids in Porous Media. American Elsevier Publishing Company, New York.

Bethmann, F., Ollinger, D., Tormann, T., 2019. Seismicity analysis with spatial or temporal relation to the deep geothermal project in Pohang during 2016/2017. Geo-Energie Suisse AG, Zürich, Switzerland.

Bhattacharya, P., Viesca, R. C., 2019. Fluid-induced aseismic fault slip outpaces pore-fluid migration. Science 364(6439), 464-468.

Blöcher, G., Cacace, M., Jacquey, A.B., Zang, A., Heidbach, O., Hofmann, H., Kluge, C., Zimmermann, G., 2018. Evaluating Micro-Seismic Events Triggered by Reservoir Operations at the Geothermal Site of Groß Schönebeck (Germany). Rock Mechanics and Rock Engineering, 51, pp. 3265-3279.

Boettcher, M. S., Marone, C., 2004. ffects of normal stress variation on the strength and stability of creeping faults. Journal of Geophysical Research: Solid Earth 109(B3), 148-227.

Bradford, J., McLennan, J., Moore, J., Podgorney, R., Plummer, M., Nash, G., 2017. Analysis of the Thermal and Hydraulic Stimulation Program at Raft River, Idaho. Rock Mechanics and Rock Engineering 50(5), 1279-1287.

Chang, K.W., Yoon, H., Kim, H.Y., Lee, M.Y., 2020. Operational and geological controls of coupled poroelastic stressing and pore-pressure accumulation along faults: Induced earthquakes in Pohang, South Korea. Scientific Reports, 10 (2020), p. 2073.

Cheng, Q., Wang, X., Ghassemi, A., 2019. Numerical simulation of reservoir stimulation with reference to the Newberry EGS. Geothermics 77, 327-343.

Chough, S.K., Kwon, S.T., Ree, J.H., Choi, D.K., 2000. Tectonic and sedimentary evolution of the Korean peninsula: a review and new view. Earth-Science Reviews 52(1), 175-235.

Cornet, F.H., 2016. Seismic and aseismic motions generated by fluid injections. Geomechanics for Energy and the Environment 5, 42-54.

Cottrell, M., Hosseinpour, H., Dershowitz, W., 2016. Deep Fluid Injection into Fractured Rock, 50th US Rock Mechanics / Geomechanics Symposium. American Rock Mechanics Association, Houston, Texas, USA.

De Simone, S., Carrera, J., Vilarrasa, V., 2017. Superposition approach to understand triggering mechanisms of post-injection induced seismicity. Geothermics 70, 85-97.

Dieterich, J. H., 1992. Earthquake nucleation on faults with rate-and state-dependent strength. Tectonophysics 211(1-4), 115-134.

Dieterich, J. H., 1994. A constitutive law for rate of earthquake production and its application to earthquake clustering. Journal of Geophysical Research 99(B2), 2601-2618.

Doe, T.W., Korbin, G.E., 1987. A Comparison Of Hydraulic Fracturing And Hydraulic Jacking Stress Measurements, The 28th U.S. Symposium on Rock Mechanics (USRMS). American Rock Mechanics Association, Tucson, Arizona, p. 8.

Ellsworth, W. L., Giardini, D., Townend, J., Ge, S., Shimamoto, T., 2019. Triggering of the Pohang, Korea, Earthquake (Mw 5.5) by Enhanced Geothermal System Stimulation, Seismological Research Letters 90(5): 1844-1858.

Goebel, T. H. W., Brodsky, E. E., 2018. The spatial footprint of injection wells in a global compilation of induced earthquake sequences, Science 361, 899-904.

Golder Associates, 2001. Matrix/Fracture Hydraulic Interaction Code with Solute Transport (MAFIC), User Documentation, v2.0.

Golder Associates, 2019. FracMan Interactive Discrete Feature Data Analysis, Geometric Modeling and Exploration Simulation, User Documentation, v7.8.

Hofmann, H., Zimmermann, G., Zang, A., Yoon, J.S., Stephansson, O., Kim, K.Y., Zhuang, L., Diaz, M., Min, K.-B., 2018a. Comparison of cyclic and constant fluid injection in granitic rock at different scales, 52nd US Rock Mechanics / Geomechanics Symposium. Seattle, USA.

Hofmann, H., Zimmermann, G., Zang, A., Min, K.-B., 2018b. Cyclic soft stimulation (CSS): a new fluid injection protocol and traffic light system to mitigate seismic risks of hydraulic stimulation treatments. Geothermal Energy, 6 (27).

Hofmann, H., Zimmermann, G., Farkas, M., Huenges, E., Zang, A., Leonhardt, M., Kwiatek, G., Martinez-Garzon, P., Bohnhoff, M., Min, K.-B., Fokker, P., Westaway, R., Bethmann, F., Meier, P., Yoon, K.S., Choi, J.W., Lee, T.J., Kim, K.Y., 2019. First field application of cyclic soft stimulation at the Pohang Enhanced Geothermal System site in Korea. Geophysical Journal International 217(2), 926-949.

Hökmark, H., Lönnqvist, M., Fälth, B., 2010. THM-issues in repository rock. Thermal, mechanical, thermo-mechanical and hydro-mechanical evolution of the rock at the Forsmark and Laxemar sites. SKB TR-10-23, Stockholm.

Kang, J.-Q., Zhu, J.-B., Zhao, J., 2019. A review of mechanisms of induced earthquakes: from a view of rock mechanics. Geomechanics and Geophysics for Geo-Energy and Geo-Resources 5(2), 171-196.

Kewel, M., Renner, J., Hassanzadegan, A., Tischner, T., 2019. Laboratory experiments investigating the hydro-mechanical behaviour of rocks containing a single fracture, 13th Euro-conference on rock physics and geomechanics - the Guéguen conference. 2-6 September 2019, Potsdam, Germany.

Kim, H., Xie, L., Min, K.-B., Bae, S., Stephansson, O., 2017. Integrated In Situ Stress Estimation by Hydraulic Fracturing, Borehole Observations and Numerical Analysis at the EXP-1 Borehole in Pohang, Korea. Rock Mechanics and Rock Engineering 50(12), 3141-3155.

Kwon, S., Xie, L., Park, S., Kim, K.-I., Min, K.-B., Kim, K.Y., Zhuang, L., Choi, J., Kim, H., Lee, T.J., 2019. Characterization of 4.2-km-Deep Fractured Granodiorite Cores from Pohang Geothermal Reservoir, Korea. Rock Mechanics and Rock Engineering 52(3), 771-782.

Lee, K.-K., Ge, S., Ellsworth, W.L., Giardini, D., Townend, J., Shimamoto, T., 2019. Summary report of the Korean Government Commission on relations between the 2017 Pohang earthquake and EGS project, in: Lee, K.-K. (Ed.) Geological Society of Korea. The Geological Society of Korea, p. 205.

Lee, T.J., Song, Y., Park, D.-W., Jeon, J., Yoon, W.S., 2015. 3D Geological Model of Pohang EGS Pilot Site, Korea, World Geothermal Congress. Melbourne, Australia.

Lu, J., Ghassemi, A., 2019. Coupled Thermo-Hydro-Mechanical-Seismic Modeling of Fractured Reservoir Stimulation with Application to EGS Collab, PROCEEDINGS, 44th Workshop on Geothermal Reservoir Engineering. Stanford University, Stanford, California, February 11-13, 2019.

Marck, J., Savitski, A. A., Detournay, E., 2015. Line source in a poroelastic layer bounded by an elastic space. Int. J. Numer. Anal. Meth. Geomech. 39, 1484-1505.

Oda, M., 1986. An equivalent continuum model for coupled stress and fluid flow analysis in jointed rock masses. Water Resour. Res., 22(13), 1845-1856.

Park, S., Xie, L., Kim, K.-I., Kwon, S., Min, K.-B., Choi, J., Yoon, W.-S., Song, Y., 2017. First Hydraulic Stimulation in Fractured Geothermal Reservoir in Pohang PX-2 Well. Procedia Engineering 191, 829-837.

Park, S., Kim, K.-I., Xie, L., Yoo, H., Min, K.-B., Kim, M., Yoon, B., Kim, K.Y., Zimmermann, G., Guinot, F., Meier, P., 2020. Observations and analyses of the first two hydraulic stimulations in the Pohang geothermal development site, South Korea. Geothermics 88, 101905.

Rinaldi, A. P., Rutqvist, J., 2019. Joint opening or hydroshearing? Analyzing a fracture zone stimulation at Fenton Hill. Geothermics 77, 83-98.

Rutqvist, J., Tsang, C.-F., 2003. Analysis of thermal-hydrologic-mechanical behavior near an emplacement drift at Yucca Mountain. Journal of Contaminant Hydrology 62-63,637-652.

Rybach, L., 2014. Geothermal Power Growth 1995–2013—A Comparison with Other Renewables. Energies 7(8), 4802-4812.

Salina Borello, E., Fokker, P.A., Viberti, D., Verga, F., Hofmann, H., Meier, P., Min, K.-B., Yoon, K., Zimmermann, G., 2019. Harmonic Pulse Testing for Well Monitoring: Application to a Fractured Geothermal Reservoir. Water Resources Research 55, 4727-4744.

Shapiro, S. A., 2015. Fluid-Induced Seismicity. Cambridge University Press, 276 p.

Song, Y., Lee, T.J., Jeon, J., Yoon, W.S., 2015. Background and Progress of the Korean EGS Pilot Project, Proceedings World Geothermal Congress 2015. Melbourne, Australia, 19-25 April 2015.

Westaway, R., Burnside, N.M., 2019. Fault “Corrosion” by Fluid Injection: A Potential Cause of the November 2017 5.5 Korean Earthquake. Geofluids 2019, 23.

Yoon, J.S., Zang, A., Stephansson, O., 2014. Numerical investigation on optimized stimulation of intact and naturally fractured deep geothermal reservoirs using hydro-mechanical coupled discrete particles joints model. Geothermics 52, 165-184.

Zang, A., Stephansson, O., 2010. Stress Field of the Earth's Crust. Springer Netherlands.

Zang, A., Yoon, J.S., Stephansson, O., Heidbach, O., 2013. Fatigue hydraulic fracturing by cyclic reservoir treatment enhances permeability and reduces induced seismicity. Geophysical Journal International 195(2), 1282-1287.

Zang, A., Oye, V., Jousset, P., Deichmann, N., Gritto, R., McGarr, A., Majer, E., Bruhn, D., 2014. Analysis of induced seismicity in geothermal reservoirs – An overview. Geothermics 52, 6-21.

Zang, A., Stephansson, O., Stenberg, L., Plenkers, K., Specht, S., Milkereit, C., Schill, E., Kwiatek, G., Dresen, G., Zimmermann, G., Dahm, T., Weber, M., 2017. Hydraulic fracture monitoring in hard rock at 410 m depth with an advanced fluid-injection protocol and extensive sensor array. Geophysical Journal International 208(2), 790-813.

Zhuang, L., Kim, K.Y., Jung, S.G., Diaz, M., Min, K.-B., Park, S., Zang, A., Stephansson, O., Zimmermann, G., Yoon, J.S., 2018. Cyclic hydraulic fracturing of cubic granite samples under triaxial stress state with acoustic emission, injectivity and fracture measurements. 52nd US Rock Mechanics / Geomechanics Symposium, Seattle, USA.

Zoback, M.D., 2010. Reservoir Geomechanics. Cambridge University Press.

Chapter 6 Discussion

In this chapter, the overarching research questions proposed in Chapter 2 and the integration of major findings of the main publications are discussed. First, hydraulic fracture growth in hard rock are discussed based on the microscale (Chapter 3) and mesoscale studies (0) in Chapter 6.1. This is followed by the discussion of the parameters controlling hydro-mechanical coupling (Chapter 6.2) and the multiple scales effects (Chapter 6.3). In the last part of the chapter (Chapter 6.4), the challenges of simulating hydraulic fracturing in hard rock are discussed.

6.1 Hydraulic fracture growth in hard rock at various scales

The numerical modelling of the laboratory microscale hydraulic fracturing experiments in quasi-isotropic Pocheon granite samples and the mesoscale minifrac tests in highly anisotropic mica schist in Hungary provide insights into the micromechanics of fracture growth due to constant-rate fluid injection. In the grain-scale study, sub-millimetre-long microcracks are generated that may link with each other to form a several-cm-long fracture in the granite sample. In the borehole-scale study, the microcracks have a length on the order of magnitude of mm to cm that may form meter-long hydraulic fractures. We note that microcracks at a given scale refer to crack elements with a length (sub-REV) that are smaller than the domain of investigation (super-REV).

These two studies share several aspects in common. First, fracture initiation and propagation are simulated in homogeneous and heterogeneous rock masses in two-dimensions. Second, heterogeneous rock bodies are simulated using pre-existing defects that are implemented using the concept of discrete fracture network or smooth joints (Mas Ivars et al., 2008). This allows assigning different mechanical and hydraulic parameters to the defects and the intact rock mass. Third, hydraulic fracture growth is monitored directly via the evolution of cumulative length or number of microcracks, and their spatial distribution across the sample as well as indirectly via fluid pressure monitoring at the injection point and in the sample. Last, although flow-back is part of hydraulic fracturing tests, these are not simulated given that this operation was either interrupted at field (Section 4.6.1 in 0), or its simulation is computationally too expensive (Section 3.5.4 in Chapter 3).

Based on Zang and Stephansson (2010), given that fluid pressure inside the injection interval exceeds the *FBP*, hydraulic fractures are expected to open as tensile (mode I) cracks perpendicular to the orientation of minimum principal stress and rapidly grow in the plane of intermediate and maximum principal stress. Both numerical studies show that hydraulic fracture growth direction is in line with maximum principal stress direction in homogeneous rock mass. However, in the case of heterogeneous models, complex fracture geometries are observed. The induced hydraulic microcracks of mode I are aligned parallel to the maximum principal stress until they interact with pre-existing or natural fractures. Due to the pressurization of the pre-existing defects, those demonstrate sliding (hydraulically generated mode II deformation or hydro-shearing) at a pressure depending on their orientation with respect to the

direction of maximum principal stress. Thus, reactivated natural fractures show varying orientations. As soon as hydraulic pressurization reaches the tip of hydro-sheared natural fractures, new mode I fractures are generated. These make the hydraulic fracture re-orientate parallel to maximum principal stress until it reaches another natural defect. This makes the hydraulic fracture process in anisotropic and heterogeneous material a mixed-mode fracturing phenomenon. This is in good agreement with Guglielmi et al. (2021) who have recently reported that water injection experiments in foliated metamorphic rock at the Sanford Underground Research Facility (USA) at a depth of approx. 1500 m, hydraulic fracture is initiated at an orientation different from expectation based on the regional stress regime due to the foliation of crystalline rock. They report that foliation at the borehole wall provides the hydraulic fracture initiation point, but then the fracture reorients away from the well driven by the far-field stress.

Induced mode II cracks in intact rock or mode I failure of pre-existing defects are not observed in any of the simulations. The lack of newly formed mode II fractures can be explained by the generally higher K_{IIC} compared to K_{IC} in granite and mica schist, i.e. higher hydraulic energy is required for initiating mode II fractures compared to mode I cracks (Backers, 2005). The lack of mode I failure of natural fractures is related to their very low tensile strength implying that these cannot sustain tensile stresses (AbuAisha et al., 2019).

Another expectation from classical theory of hydraulic fracturing is the symmetrical growth of hydraulic fractures from the injection interval (Figure 2; Zang and Stephansson, 2010). However, asymmetric hydraulic fracture growth is observed in homogeneous models A1 and A2 in Sections 3.4.2 in Chapter 3, respectively, and in model A in Section 4.5.1 in 0. Since no locations are available based on acoustic emission and microseismic data from these experiments, only possible explanations can be hypothesised. From a numerical point of view, this is an effect of discrete element topology (Potyondy and Cundall, 2004; Lisjak et al., 2017). The element boundaries are potential locations of microcrack elements that may have varying orientations, hence, localised stress heterogeneities. Thus, the side on which the first microcracks are generated will determine the location of further crack elements since less energy is required to critically pressurise the microcrack tip than to form a new microcrack in the intact rock mass on the opposite side.

The asymmetric hydraulic fracture growth is also observed in heterogeneous models B1 and B2 in Sections 3.4.3 Chapter 3, respectively, and in models B and C in Section 4.5.2 and 4.5.3 in 0. However, the asymmetric hydraulic fracture growth may not be necessarily linked to numerical element topology effects. Wright et al. (1999) show that localised stress perturbations nearby fractures may influence the direction of fracture propagation. Furthermore, several mine-scale (mesoscale) hydraulic fracturing experiments in crystalline (Zang et al., 2017) and in sandstone rock (Fischer et al., 2009) demonstrate that asymmetric hydraulic fracture growth is associated with local stress field perturbations due to man-made openings, such as drilling holes and tunnels.

6.2 Properties governing hydro-mechanical coupling and processes

The interaction of hydraulic and mechanical processes in the three main publications is treated via two-way coupled simulations, i.e. hydraulic injection results in mechanical deformation of rock mass and vice versa. The main difference in realising coupling between the numerical simulators discussed lies in the calculation of change in hydraulic aperture due to change in effective stress as a result of pore pressure perturbation. The hydraulic aperture vs effective normal stress relationship is linear in Irazu (Figure 5b in Chapter 3), exponential in Particle Flow Code (Figure 9 in 0) and hyperbolic in FracMan (eq. 2 in Chapter 5). Linear relationship can be computationally beneficial, however, laboratory experiments imply either hyperbolic or exponential relationship (Barton et al., 1985; Hökmark et al., 2010). For example, recent modelling study on the simulation of hydraulic stimulations at the Pohang EGS reservoir by Yoo et al. (2021) suggest using exponential relationship in hard rock at reservoir scale.

Apart from coupling equation, hydro-mechanical processes during hydraulic fracturing are controlled by natural, i.e. rock and hydraulic parameters as well as engineering factors. In the main publications, the effect of these parameters is studied on the simulated pressure response at the injection well. In Chapter 3, rock fabric and injection rates are varied, in 0, rock fabric and injection fluid viscosity are changed, and in Chapter 5, rock strength and injection rates are adjusted. Since all main publications focus on the verification of the simulated *FBP* against experimental data, therefore, these studies are analysed jointly with this respect. Although not all experiments are simulated in this thesis, given that the most representative tests are analysed, implications can be made on the cross-scale dependence of *FBP* on natural factors such as far-field minimum horizontal stress and depth as well as engineering factor such as injection rate.

Figure 8 illustrates the *FBP* on the surface in the function of minimum horizontal stress, depth and injection rate based on the experimental results. The depths refer to the true vertical depth of the centre of the tested open hole intervals. Figure 8a shows that at the micro- and mesoscale, the *FBP* varies approximately between 10 and 20 MPa, while minimum stress varies between 3 and 20 MPa. The corresponding depths are between 500 and 1400 m for the borehole scale experiments, and approx. 4070 and 4280 m for the reservoir scale stimulation data (Figure 8b). Injection rate varies over several orders of magnitude, i.e. from 6×10^{-4} to 4 l/min (Figure 8c). Based on the simulation results, the variance of *FBP* at laboratory and borehole scale can be attributed to the presence of natural defects in the rock mass since far-field stresses are fixed at laboratory conditions, and these are relatively well constrained at the borehole scale experiments as well. Furthermore, the variance of injection rate is much higher than that of *FBP*s across these two scales.

Interestingly, in the case of reservoir scale data associated with hydraulic stimulations at the Pohang EGS site, different dependence of the *FBP* on minimum horizontal stress, depth and injection rate is observed. During the first hydraulic stimulation in well PX-1 at the depth of 4068 m and an injection rate of between 300 and 1000 l/min, *FBP* is observed at 16 MPa wellhead pressure. This is

explained by hydro-shearing of a fault structure intersecting the open-hole interval of the well as shown in Chapter 5. On the other hand, at the depth of 4278 m and at flow rates between 1000 and 2800 l/min, *FBP* at 67 MPa wellhead pressure is observed during the first hydraulic stimulation in well PX-2. This is interpreted as a result of induced hydraulic fracture. However, caution must be given to the magnitude of minimum horizontal stress since it is constrained with relatively large error, i.e. between 86 and 120 MPa (Table 1 in Chapter 5). We note that Yoo et al. (2021) recently demonstrated that by using the numerical tool TOUGH-FLAC, the induction of hydraulic fracture at an FBP of 90 MPa for a minimum horizontal stress of 86 MPa can be verified against field pressure history of the hydraulic stimulations in well PX-2. Consequently, at reservoir scale, *FBP* strongly depends on natural factors such as the existence of pre-existing faults and in-situ minimum horizontal stress at the same time, as well as on injection rate. Moreover, Figure 8a shows that in general, the higher the minimum horizontal stress the higher the *FBP* becomes. This observation agrees with that reported by Langbauer et al. (2021) who reviewed several hydraulic fracturing stimulation tests at several scales in various rock types for energy technologies. Furthermore, Figure 8b shows that greater depth does not necessarily result in larger *FBP* on the surface. This shows that other factors discussed above affect the *FBP* stronger.

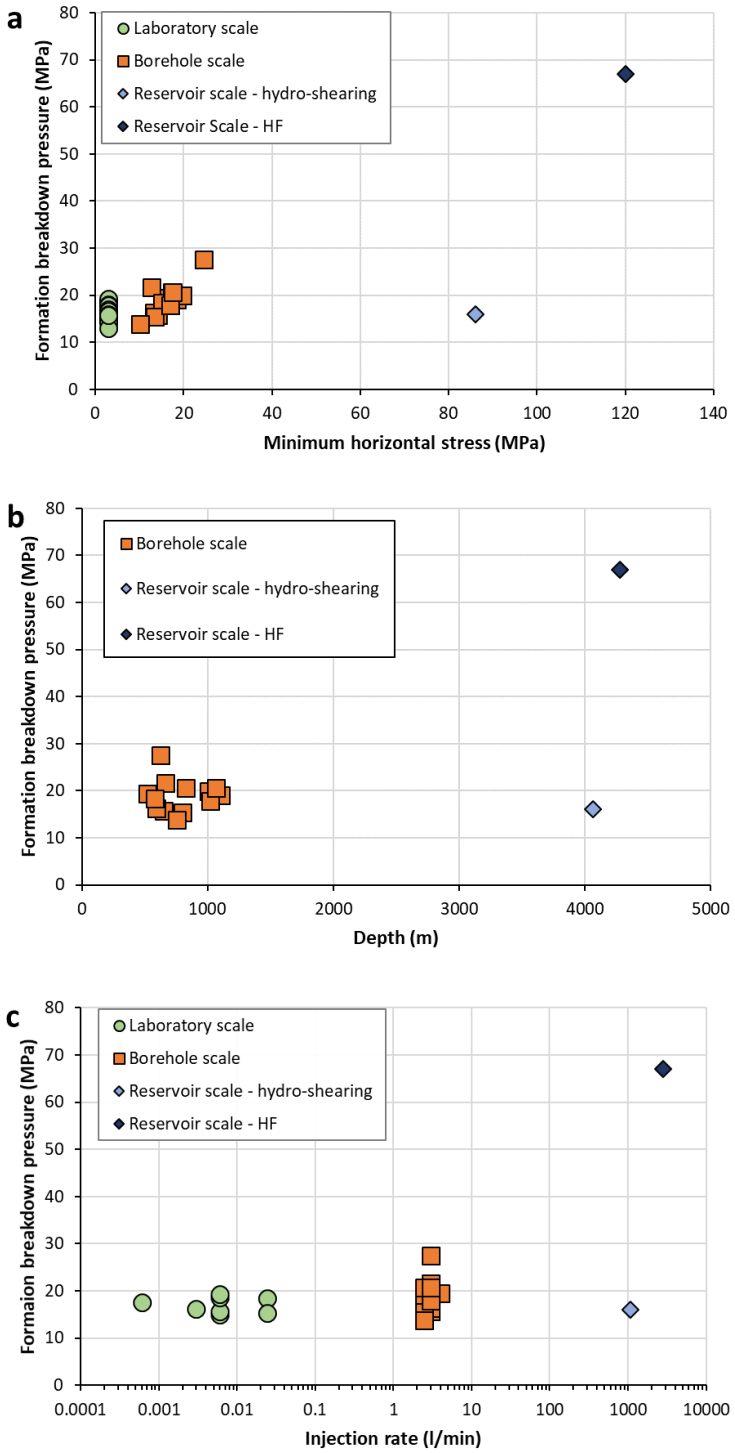

*Figure 8: Formation breakdown pressure (FBP) on the surface in the function of minimum horizontal stress (**a**), injection rate (**b**) and depth (**c**) based on the experimental results of hydraulic fracturing into crystalline rock reported in the publications included as chapters of this thesis. The tested rock types at each scale are Pocheon granite from South Korea (laboratory scale), mica schist of Variscan basement rock in Hungary (borehole scale) and Permian granodiorite at Pohang EGS site in South Korea (reservoir scale). The depths refer to the true vertical depth of the centre of tested open hole intervals. The minimum horizontal stresses at reservoir scale are best estimates that vary between 86 and 120 MPa (see Table 1 in Chapter 5). The stimulation mechanisms at reservoir scale are either hydro-shearing or hydraulic fracturing (HF). At the other scales, the stimulation mechanism is HF.*

6.3 Scale dependencies of hydraulic fracturing

In order to transfer the experimental and simulation results between different scales, special scaling-laws must be applied as described in Chapter 1.3. These determine the required parameters for studying hydraulic fracturing across scales such as apparatus and device requirements, rock geomechanical parameters, principal stresses, sample size, fluid viscosity, injection rate as well as expected time frame of the experiment, i.e. containment of the hydraulic fracture within block boundaries.

Table 5 shows the scaling analysis of the experiments studied in this thesis based on equations 9-10 in Chapter 1.3.2 and eq. 19 in Chapter 3 with respect to the duration of experiment, t_{exp}. The scale analysis of laboratory scale test "CCI1" presented therein demonstrates that the induced hydraulic fracture should reach sample boundaries within two seconds beginning from reaching the *FBP*, i.e. t_{exp}= 2 s, and it propagates dominantly in the toughness-dominated regime with large fluid lag (*OK*-edge), since $t_{exp} \sim t_{om}$ and $t_{exp} >> t_{mk}$. The simulation study with the Irazu model, which is verified against this kind of propagation regime, confirms the duration of the fracturing experiment. However, modifications of laboratory setup would have enabled observing hydraulic fracturing experiments in viscosity dominated regime without fluid lag effect, i.e. $t_{exp} >> t_{om}$ and $t_{exp} << t_{mk}$, by using a more viscous fluid, e.g. glycerine with a viscosity of 1 Pa s. Given that Irazu is capable of simulating viscosity-driven hydraulic fracture propagation and calculation time is proportional to fluid viscosity (eq. 18 in Chapter 3), future study should investigate this alternative experimental option. The alternative option would also enable the direct comparison of governing parameters of hydraulic fracturing experiments against reservoir scale experiments where viscosity-dominated dissipation mechanisms are generally expected (Detournay, 2016).

Regarding the time scale analysis of borehole scale experiments, the numerical model base case setup with water as fracturing fluid shows that hydraulic fracture propagation is toughness-dominated with neglectable fluid lag (Table 5, mesoscale, base case). In the alternative case setup, where fracturing fluid is drilling mud with higher viscosity, it is valid to assume hydraulic fracturing propagation in the viscous regime on the order of few minutes in these models since $t_{exp} << t_{mk}$.

In the case of hydraulic stimulations in the Pohang EGS reservoir (Chapter 5), the scaling analysis is only possible for the hydraulic stimulations in well PX-2 where the induction of new hydraulic fracture is hypothesised. Assuming an average flow rate of 30 l/s (3×10^{-2} m^3/s) and a minimum stress of 86 MPa for the first hydraulic stimulation in this well based on Park et al. (2020), time required for transition from viscosity-dominated to toughness-dominated hydraulic fracture propagation, t_{mk}, is about 15 minutes (830 s). Thus, hydraulic fracturing experiments in well PX-2 are governed by both viscosity and rock toughness effect (*MK*-edge) depending on the length of the water injection steps. Fluid lag can be neglected since $t_{exp} >> t_{om}$. However, the applicability of the time scale analysis is limited by several factors, such as the presence of highly permeable pre-existing fractures and the possible presence of stress barrier between the wells PX-1 and PX-2. Given that no explicit hydraulic fracture

growth is simulated either in this thesis or in studies focusing at the same site, such as Wassing et al. (2021) and Yoo et al. (2021), the calculated time scale serves as an estimation for the identification of key parameters affecting fracture growth for future studies.

Table 5: Time scale analysis of the experiments simulated in the thesis based on the similarity solutions for penny-shaped hydraulic fracture propagating in an impermeable elastic medium described in Chapter 1.3.2 (OMK-triangle). t_{exp}: characteristic experimental time length; t_{om}: characteristic time length along the OM-edge, t_{mk}: characteristic time length along the MK-edge.

Scale	σ_0 **(MPa)**	Q_0 **(m^3/s)**	E **(GPa)**	ν **(-)**	K_{Ic} **(MPa $m^{-1/2}$)**	μ **(Pa s)**	t_{exp} **(s)**	t_{om} **(s)**	t_{mk} **(s)**	**Dominant regime**
Micro	3	10^{-7}	57.5	0.25	1	0.001	2	1.7	10^{-4}	Fluid lag-Toughness (*OK*)
Micro*	3	10^{-7}	57.5	0.25	1	1	2	1670	6053	Viscosity (*M*)
Meso, base case	16.5	5.8×10^{-5}	52	0.24	1	0.001	120	0.01	1.35	Toughness (*K*)
Meso, viscous fluid case	16.5	5.8×10^{-5}	52	0.24	1	0.01	120	0.1	430	Viscosity (*M*)
Macro**	86	3×10^{-2}	33.5	0.21	1	0.001	100-1800	2.3×10^{-5}	830	Viscosity-Toughness (*MK*)

*: Parameter suggestion for studying viscosity-dominated fracturing experiment.

**: average injection rate of first hydraulic stimulation in well PX-2 is assumed based on Park et al. (2020). Experimental time length is varied during the hydraulic stimulation

6.4 Challenges in numerical modelling of hydraulic fracturing in hard rock

The numerical studies constituting this thesis demonstrate that several numerical approaches are required to study various aspects of hydraulic fracturing at different scales. However, the verification of the applied general-purpose models is challenging.

First of all, these studies show that workflow for verifying the hydro-mechanical (H-M) models against experimental data have to be tailored for the specified problems. This includes establishing a methodology for generating a synthetic material that resembles the various mechanical properties observed in the laboratory and agrees with the recorded injection fluid pressure response at the same time; i.e. it allows history matching. On one hand, the mechanical and hydraulic verification of modern numerical models using explicit time stepping approach are only possible via time-consuming trial-and-error approach. On the other hand, commercial hydraulic fracturing treatment simulators such as FracPro and Mfrac have built-in automated history matching algorithms based on Monte Carlo method. However, these numerical models use classic hydraulic fracturing models that cannot capture complex hydraulic fracturing processes (Chapter 1.4).

Second, in the case of DEM- and FDEM-based simulators, the small hydraulic time step size using realistic parameters can lead to computationally expensive simulations. Thus, these simulators are limited to testing few hydraulic fracturing treatment scenarios.

Third, due to inherent dependencies in coupled simulations described below, large number of sensitivity tests must be carried out to increase confidence in the numerical models. Therefore, a trade-off must be made between the number of numerical models and computational time. Alternatively, in the case of laboratory scale models, the number of parametric sensitivity scenarios can be decreased by the time scaling approach proposed by Bunger et al. (2005), since the number of parameters in that mathematical model are reduced.

Regarding history matching in the applied numerical tools, in the case of homogeneous isotropic rock model, these are controlled by several numerical, mechanical and hydraulic parameters. Dominant numerical parameter is the element size, which affects both the peak pressure and the slope of fluid pressure increment. Furthermore, the numerical geometry setup, i.e. borehole model affects the simulated pressure curve through injection into either a single cavity (Chapter 3 and Chapter 5) or a line source (0). Among the mechanical parameters, element tensile strength controls the magnitude of the *FBP* and element contact stiffness controls the slope of the fluid pressure increase. If hydro-shearing is simulated (Chapter 5), uniaxial compressive strength (UCS) of the FracMan model affects the simulated peak pressure. As for the hydraulic parameters, fluid bulk modulus and fluid density control the slope of the pressure increment, while hydraulic aperture controls the magnitude of *FBP*. In the case of heterogeneous models, the geometrical, mechanical and hydraulic parameters of the joint elements or faults further complicate the effects on simulated pressure response.

It must be pointed out that in the case of the macroscale study, H-M simulator FracMan should be extended by thermal coupling since the reservoir rock formation is thermally stressed in terms of cold-water injection into hot rock formation (thermal-mechanical coupling, T-M). Furthermore, this would result in temperature-dependent fluid properties such as viscosity and density (thermal-hydraulic coupling, T-H). Thus, the extended coupling would significantly affect the modelling results, e.g. the permeability of the reservoir rock. Based on the recent modelling study using the simulator TOUGH-FLAC reported by Figueiredo et al. (2020), it can be speculated that implementing temperature effects additionally can result both in decrease and increase of the permeability of host formation depending on the implementation of couplings, e.g. one-way or two-way coupling between THM processes.

Chapter 7 Conclusions and outlook

In this cumulative doctoral thesis, hydraulic fracturing in hard rock is simulated for energy technologies at micro (laboratory), meso (borehole) and macro (reservoir) scales using different numerical methods, such as finite element method (FEM) + DFN (discrete fracture network), discrete element method (DEM) as well as hybrid finite-discrete element method (FDEM). The simulations aim at gaining insights into fracture growth, understanding parameters controlling the hydro-mechanically coupled processes as well as pointing out methodological challenges in simulating various fluid injection experiments. Below conclusions are made for the research questions proposed in this thesis.

Hydraulic fracture growth in hard rock

The numerical simulations show that during hydraulic fracturing into heterogeneous crystalline rock, new cracks in tension are induced in intact rock (mode I cracks in rock mass) and natural fractures are hydro-sheared (mode II failure of smooth joints). The induced cracks are generated at a fluid pressure required to overcome the tensile strength of the rock mass, and they are aligned approx. parallel to the maximum principal stress. The hydro-sheared pre-existing fractures have various orientations with a dominant direction according to the Mohr-Coulomb failure criterion. Since at an investigation length scale, fractures are dominantly present at REV (representative elementary volume) and sub-REV domain (Chapter 1.3.1), thus, the resulting hydraulic fracturing geometry will depend "locally", i.e. at sub-REV and REV domain volume, on the geometry and strength of natural fractures, and "globally", i.e. at super-REV domain volume, on far-field stresses.

In this context, the following concluding remarks can be made on the direction of hydraulic fracture growth, the magnitude of *FBP* as well as the relationship between the location of forming microcracks and stress magnitudes, i.e. the shape of the process zone, in homogeneous (intact) rock, and in heterogeneous rock with single isotropic population of natural cracks. Regarding such pre-existing crack set, a distinction is made between that aligned parallel to and that inclined with the direction of maximum principal stress.

- In intact rock, the direction of hydraulic fracture growth is controlled by the orientation of grain boundaries (or grains) and the orientation of maximum principal stress. In any grain assembly, first tensile microcracks will be generated at those boundaries that are aligned closest to maximum principal stress direction with the lowest tensile strength. The magnitude of *FBP* is determined by the microscopic strength of the grain boundaries, pressurization rate, fluid viscosity as well as the magnitude of minimum principal stress. The elevated tensile stresses and microcrack nucleation ahead of the tips of propagating hydraulic fracture suggest that the shape of the process zone is enlarged parallel to minimum principal stress orientation (perpendicular to hydraulic fracture axis) resulting in "kidney" geometry.

- In heterogeneous rock with single isotropic fracture set aligned parallel to the maximum principal stress, if natural fractures intersect the injection interval, first hydro-sheared microcracks are generated along those. The hydraulic fracture grows further until it reaches an area with different stress orientation due to stress contrast induced by the randomly oriented rock grains and the joint set. As a result, tensile wing cracks are generated at the tip of the partly pressurised shear cracks. The tensile microcracks are oriented en echelon, i.e. in a direction different from the maximum principal stress, because of the shear component on the main fracture locally imposed by the new orientation of minimum principal stress. Eventually, the hydraulic fracture grows further from a wing crack with a path following in principle the maximum principal stress direction. Regarding the *FBP*, due to hydro-shearing of the intersecting natural fractures, it is always lower compared to homogeneous rock case. Stress magnitudes are elevated compared to confining/far-field stresses parallel to the hydraulic fracture and these are non-altered away from the process zone. Perpendicular to the hydraulic fracture, the minimum stress magnitude is slightly elevated and the maximum stress magnitude is unaffected. Consequently, the shape of the process zone is elongated across the hydraulic fracture.
- In heterogeneous rock with a single joint set aligned inclined with the maximum principal stress direction, the hydraulic fracture growth pattern is characterised by more en echelon oriented tensile wing cracks, which control the path of the hydraulic fracture. Once the hydraulic fracture leaves the wing crack, it reorientates parallel to the direction of maximum principal stress. The magnitude of FBP can be larger since the area of tilted natural structures to be fractured might be higher. Thus, the tilted structure can have larger volume for fluid storage. The shape of the process zone is elongated parallel to the hydraulic fracture.

Hydro-mechanical coupling during hydraulic fracturing in hard rock

In the numerical studies, the coupling between mechanical and hydraulic processes are analysed in terms of hydraulic aperture versus effective normal stress as well as the cross-scale dependence of *FBP* on minimum horizontal stress and injection rate. The former controls the matching procedure of simulated pressure response at the borehole against field recording. It is concluded that first, it is suggested to define separate coupling relationship for intact rock mass and natural fractures. Furthermore, both coupling relationships should be exponential. Third, verified simulation of hydro-shearing of natural fractures may require incorporating the effect of shear dilation (mode II) and jacking (mode I reopening), i.e. mixed-mode stimulation, as shown in the Pohang EGS reservoir simulations.

Regarding the variance of *FBP* in the function of minimum horizontal stress, although no clear cross-scale relationship can be defined between the two variables, it is shown that the larger the minimum horizontal stress the larger the *FBP* becomes as expected based on Kirsch relationship (Zang and Stephansson, 2010). The lack of clear relationship can be explained by the manifold influence of

natural fractures, i.e. strength and geometry, on the *FBP*. On the other hand, the variance of *FBP* over cross-scale injection rate shows an exponential relationship.

Based on the effect of studied parameters across scales, the relative importance of the factors influencing the magnitude of *FBP* in hard rock is as follows:

1) Rock volume (length scale). The larger the rock volume, the higher the probability becomes observing lower *FBP* than expected in apparently homogeneous rock mass due to hydro-shearing of pre-existing fractures.
2) Intrinsic rock parameters, such as structural anisotropy (e.g. foliation, joints) and rock permeability. Microscopic properties of elements in heterogeneous models representing structural elements may trigger stress concentrations at the fracture tip and these may have higher permeability compared to homogeneous models.
3) Fluid injection rate. Higher injection rates may result in higher FBP. This can be attributed to the strong effect of microscopic properties around the fracture tip. From a numerical point of view, microscopic elements in the studied homogeneous rock models have larger strength compared to those in heterogeneous models although the macroscopic parameters of both rock models are the same. Thus, the *FBP* in case of using a homogeneous model can became remarkably high.
4) Fluid viscosity. Higher fluid viscosity may lead to higher *FBP*. In the borehole scale study, it is shown that low-viscosity fluid infiltrates into natural structure, e.g. foliation plane immediately and pressurises its entire surface. On the other hand, when high-viscosity fluid is used, fluid infiltrates slowly through the foliation plane, pressurises parts of its surface, thus, it makes the partly opened fracture tight. As a result, higher *FBP* is observed.
5) In-situ stresses, static pore pressure, intact rock tensile strength as well as Biot's coefficient according to the poroelastic hydraulic fracture criterion. Consequently, the classical poroelastic hydraulic fracture criterion may be used as a first attempt to estimate the magnitude of *FBP* prior to hydraulic fracturing treatment. Due to factors 1-4, it is suggested to conduct rock sample- or site-specific numerical modelling study in order to get a more realistic assessment for the *FBP*.

Methodological challenges in the simulation of hydraulic fracturing in hard rock

The application of various numerical models at different length and time scales for the simulation of hydraulic fracturing in impermeable crystalline rock allows identifying numerical challenges. It can be concluded that there is a clear gap between the capacity of simulation software and the complexity of studied problems. This is related to the nature of solvers in a way that the hydro-mechanically (H-M) coupled problem is either solved by simulating complex fracture geometry using a simplified physical model, i.e. the microscale study using Irazu and mesoscale study using PFC or solved using analytical solutions with a simplified fracture geometry, i.e. the macroscale study using FracMan. Furthermore, at

reservoir scale, due to the relatively high uncertainty of input data including precise structural geology information, fluid flow and fracture interaction mechanisms operating in situ as well as stress field, several model variants must be tested. Thus, computational costs can be very high for simulating complex hydraulic fracture networks. Furthermore, the many vagaries discussed above make the decision about the optimum code for modelling hydraulic fracture growth difficult.

Consequently, the computational time of the simulation of complex hydraulic fracture geometries must be reduced while maintaining high fidelity simulation results. This can be achieved either by extending the computational resources via parallelization techniques (either locally or using cloud services) or running simulations using time scaling techniques proposed by Bunger et al. (2005) and Detournay (2016). The latter has the advantage that the number of independent variables is reduced, significant parameters or parameter groups can be identified and simulation results over scales can be compared directly. Alternatively, time scaling analysis can precede numerical simulations for reducing the number of sensitivity tests in the physical domain.

Outlook

The simulation studies reveal several aspects of hydro-mechanically (H-M) numerical models that can be the subject of future research.

Regarding failure criteria, recent geomechanical studies, e.g. Dieterich et al. (2015) and Andrés et al. (2019), test the application of the state-and-rate friction law proposed by Dieterich (1992) and Dieterich (1994) for analysing fault slippage and associated induced seismicity. Since this criterion for fault slippage has been widely used in recent laboratory experiments (e.g. Xing et al., 2019), commercial code verified against this failure criterion may be released in the future. This criterion may enable the verified simulation of recorded hydro-mechanical-seismic (H-M-S) activity during fracturing treatments in geothermal reservoirs where various stimulation mechanisms are expected.

In energy technologies, hydraulic fracturing often requires the consideration of extending the couplings by thermal and chemical processes as well (T-H-M-C coupling). However, the extension of couplings poses further challenges for numerical modelling. First, the significance of two-way coupling can be asymmetrical (Ahusborde et al., 2021). For example, on the time scale of a stimulation treatment, the effect of temperature change on mechanical properties (T→M: thermal stressing), that on hydraulic parameters (T→H: temperature-dependent fluid density and viscosity) and that on chemical processes (T→C: temperature-dependent reactions) can be different than the opposite way. These include the effect of mechanical changes on temperature (M→T: frictional heating), the effect of chemical processes on temperature (C→T: reactive heat) as well as the effect of hydraulic transport on temperature (H→T: advective heat transport). Second, from a methodological point of view, increasing the number of parameters results in higher computational costs which hinders filling the gap between the capacity of the H-M-coupled simulation software and the complexity of the studied problems mentioned above.

Therefore, it is suggested to weight the two-way couplings between the respective processes to maintain reasonable computational resources.

The ongoing development of used and reviewed numerical tools focuses on tackling the challenges discussed above. For example, explicit borehole model and T-H-M coupling have been recently implemented in Irazu 2D in order to consider the compressibility of the total pumping system, and temperature effects, respectively (Geomechanica, 2020).

Bibliography

AbuAisha, M., D. Eaton, J. Priest, R. Wong, B. Loret, Kent, A. H., 2019. Fully coupled hydro–mechanical controls on non-diffusive seismicity triggering front driven by hydraulic fracturing. Journal of Seismology, 23(1), 109–121.

Ahmed, U., Meehan, D. N., 2016. Unconventional oil and gas resources exploitation and development. In: Emerging trends and technologies in petroleum engineering (ed. by Dandekar, A. Y.). CRC Press, Boca Raton, 862 p.

Ahusborde, E., Amaziane, B., Baksay, A., Bátor, G., Becker, D., Bednár, A., Béreš, M., Blaheta, R., Bőthi, Z., Bracke, G. , Brazda, L., Brendler, V., Brenner, K., Březina, J., Cancès, C., Chainais-Hillairet, C., Chave, F., Claret, F., Domesová, S., Havlova, V., Hokr, M., Horák, D., Jacques, D., Jankovsky, F. Kazymyrenko, C., Kolditz, O., Koudelka, T., Kovács, T., Krejci, T., Kruis, J., Laloy, E., Landa, J., Lipping, T., Lukin, D., Mašín, D., Masson, R., Meeussen, J.C.L, Mollaali, M., Mon, A., Montenegro, L., Montoya, V., Pepin, G., Poonoosamy, J., Prasianakis, N., Saâdi, Z., Samper, J., Scaringi,G., Sochala, P., Tournassat, C., Yoshioka, K., Yuankai, Y., 2021. State of the Art Report in the fields of numerical analysis and scientific computing. Final version as of 16/02/2020 of deliverable D4.1 of the HORIZON 2020 project EURAD (European Joint Programme on Radioactive Waste Management).

Amadei, B., Stephansson, O., 1997. Rock stress and its measurement. Chapman & Hall, London, 490 p.

Andrés, S., Santillán, D., Mosquera, J. C., Cueto-Felgueroso, L., 2019. Delayed Weakening and Reactivation of Rate-and-State Faults Driven by Pressure Changes Due to Fluid Injection. Journal of Geophysical Research: Solid Earth, 124, 11917–11937.

Asahina, D., Houseworth, J., Birkholzer, J., Rutqvist, J., Bolander, J., 2014. Hydro-mechanical model for wetting/drying and fracture development in geomaterials. Computers & Geosciences, 65, 13–23.

Backers, T., 2005. Fracture toughness determination and micromechanics of rock under Mode I and Mode II loading. Doctoral thesis, University of Potsdam and scientific technical report 05/05, GFZ - German Research Centre for Geosciences, Potsdam.

Bai, Q., Konietzky, H., Zhang, C., Xia, B., 2021. Directional hydraulic fracturing (DHF) using oriented perforations: The role of micro-crack heterogeneity. Computers and Geotechnics, 140, 104471.

Barboza, B. R., Chen, B., Li, C., 2021. A review on proppant transport modelling. Journal of Petroleum Science and Engineering, 204, 108753.

Barton, N., Bandis, S., Bakhtar, K., 1985. Strength, deformation and conductivity coupling of rock joints. International Journal of Rock Mechanics and Mining Sciences & Geomechanics Abstracts, 22(3), 121–140.

Bear, J., Verruijt, A., 1987. Modeling Groundwater Flow and Pollution. In: Theory and Applications of Transport in Porous Media (ed. by Bear, J.), Reidel, Dordrecht, 425 p.

Biot, M. A., 1941. General theory of three-dimensional consolidation. Journal of Applied Physics, 12(2), 155–164.

Blöcher, G., Reinsch, T., Henninges, J., Milsch, H., Regensprug, S., Kummerow, J., Francke, H., Kranz, S., Saadat, A., Zimmermann, G., Huenges, E., 2016. Hydraulic history and current state of the deep geothermal reservoir Groß Schönebeck. Geothermics, 63, 27–43.

Breede, K., Dzebisashvili, K., Liu, X., Falcone, G., 2013. A systematic review of enhanced (or engineered) geothermal systems: past, present and future. Geothermal Energy, 1, article ID: 4.

Bruhn, D., López-Hernández, A., and the GEMex consortium, 2021. GEMex – Cooperation in Geothermal energy research Europe-Mexico for development of Enhanced Geothermal Systems and Superhot Geothermal Systems. Proceedings of the World Geothermal Congress 2020+1, March-October, 2021.

Bunger, A. P., Detournay, E., 2007. Early-time solution for a radial hydraulic fracture. Journal of Engineering Mechanics, 133(5), 534–540.

Bunger, A. P., Jeffrey, R. G., Detournay, E., 2005. Application of Scaling Laws to Laboratory-Scale Hydraulic Fractures. Proceedings of Alaska Rocks 2005, The 40th U.S. Symposium on Rock Mechanics (USRMS): Rock Mechanics for Energy, Mineral and Infrastructure Development in the Northern Regions, held in Anchorage, Alaska, June 25-29, 2005.

Carbonell, R., Desroches, J., Detournay, E., 1999. A comparison between a semi-analytical and a numerical solution of a two-dimensional hydraulic fracture. International Journal of Solids and Structures, 36(31–32), 4869–4888.

Chen, B., Barboza, B. R., Sun, Y., Bai, J., Thomas, H. R., Dutko, M., Cottrell, M., Li, C., 2021. A Review of Hydraulic Fracturing Simulation. Archives of Computational Methods in Engineering.

Cleary, M. P., 1980. Comprehensive design formulae for hydraulic fracturing. Paper presented at the SPE Annual Technical Conference and Exhibition, Dallas, Texas.

Cleary, M. P., Fonseca, A. J., 1992. Proppant convection and encapsulation in hydraulic fracturing: practical implications of computer and laboratory simulations. Paper presented at the SPE Annual Technical Conference and Exhibition, Washington, D.C.

Cleary, M. P., Keck, R. G., Mear, M. E., 1983. Microcomputer models for the design of hydraulic fractures. Paper presented at the SPE/DOE Low Permeability Gas Reservoirs Symposium, Denver, Colorado.

Clifton, R. J., Abou-Sayed, A. S., 1979. On the computation of the three-dimensional geometry of hydraulic fractures. Paper presented at the Symposium on Low Permeability Gas Reservoirs, Denver, Colorado.

Clifton, R. J., Abou-Sayed, A. S., 1981. A variational approach to the prediction of the three-dimensional geometry of hydraulic fractures. Paper presented at the SPE/DOE Low Permeability Gas Reservoirs Symposium, Denver, Colorado, vol SPE-9879-MS.

Cottrell, M., Hosseinpour, H., Derschowitz, W., 2013. Rapid Discrete Fracture Analysis of Hydraulic Fracture Development in Naturally Fractured Reservoirs. Paper presented at the Unconventional Resources Technology Conference held in Denver, Colorado, USA.

Cottrell, M., Hosseinpour, H., Derschowitz, W., 2016. Deep Fluid Injection into Fractured Rock. Paper presented at the 50th US Rock Mechanics / Geomechanics Symposium held in Houston, Texas, USA.

Damjanac, B., Cundall, P., 2016. Application of distinct element methods to simulation of hydraulic fracturing in naturally fractured reservoirs. Computers and Geotechnics, 71, 283–294.

Detournay, E., 2004. Propagation Regimes of Fluid-Driven Fractures in Impermeable Rocks. International Journal of Geomechanics, 4(1), 1–11.

Detournay, E., 2016. Mechanics of Hydraulic Fractures. Annual Review of Fluid Mechanics, 48, 311–339.

Detournay, E., Cheng, A. H. D., McLennan, J. D., 1990. A poroelastic PKN hydraulic fracture model based on an explicit moving mesh algorithm. Journal of Energy Resources Technology, 112(4), 224–230.

Dieterich, J.H., 1992. Earthquake nucleation on faults with rate-and state-dependent strength. Tectonophysics 211(1-4), 115–134.

Dieterich, J.H., 1994. A constitutive law for rate of earthquake production and its application to earthquake clustering. Journal of Geophysical Research, 99(B2), 2601–2618.

Dieterich, J. H., Richards-Dinger, K. B., Kroll, K. A., 2015, Modeling Injection-Induced Seismicity with the Physics-Based Earthquake Simulator RSQSim, Seismological Research Letters, 86(4), 1–8

Eberhardt, E., Amini, A., 2018. Hydraulic Fracturing. In: Bobrowsky, P.T., Marker, B. (eds), Encyclopedia of Engineering Geology. Encyclopedia of Earth Sciences Series. Springer, Cham, Switzerland, 489–495.

Economides, M. J., Nolte, K. G., 2000. Reservoir stimulation. Wiley-VCH, Weinheim, 824 p.

Farkas, M. P., Yoon, J., Zang, A., Zimmermann, G., Stephansson, O., Lemon, M., Dankó, G., 2019. Effect of Foliation and Fluid Viscosity on Hydraulic Fracturing Tests in Mica Schists Investigated Using Distinct Element Modeling and Field Data. Rock Mechanics and Rock Engineering, 52(2), 555–574.

Farkas, M. P., Hofmann, H., Zimmermann, G., Zang, A., Bethmann, F., Meier, P., Cottrell, M., Josephson, N., 2021. Hydromechanical analysis of second hydraulic stimulation at well PX-1 in Pohang fractured geothermal reservoir, South Korea, Geothermics, 89, 101990.

Farkas, M. P., Hofmann, H., Zimmermann, G., Zang, A., Zhuang, L., Kim, K. Y., 2022. Numerical investigation of laboratory hydraulic fracturing tests in Pocheon granite. Under review at Acta Geotechnica.

Figueiredo, B., Tsang, C.-F., Niemi, A., 2020. The Influence of coupled thermomechanical processes on the pressure and temperature due to cold water injection into multiple fracture zones in deep rock formation. Geofluids, 8947258.

Fischer, T., Hainzl, S., Dahm, T., 2009. The creation of an asymmetric hydraulic fracture as a result of driving stress gradients. Geophysical Journal International, 179(1), 634–639.

Garagash, D. I., 2006. Propagation of plane-strain hydraulic fracture with a fluid lag: early-time solution. International Journal of Solids and Structures, 43(18–19), 5811–5835.

Gaucher, E., Schoenball, M., Heidbach, O., Zang, A., Fokker, P. A., van Wees, J.-D., Kohl, T., 2015. Induced seismicity in geothermal reservoirs: A review of forecasting approaches. Renewable and Sustainable Energy Reviews, 52, 1473–1490.

Geertsma J., De Klerk, F., 1969. A rapid method of predicting width and extent of hydraulically induced fractures. Journal of Petroleum Technology, 21(12), 1571–1581.

Geomechanica Inc., 2020. Irazu 2D Geomechanical Simulation Software version 4.0. Theory Manual.

Goodman, R. E., 1989. Introduction to Rock Mechanics. Wiley, New York, 563 p.

Guglielmi, Y., Cook, P., Soom, F., Schoenball, M., Dobson, P., Kneafsey, T., 2021. In situ continuous monitoring of borehole displacements induced by stimulated hydrofracture growth. Geophysical Research Letters, 48(4), e2020GL090782.

Grünthal, G., 2014. Induced seismicity related to geothermal projects versus natural tectonic earthquakes and other types of induced seismic events in Central Europe. Geothermics, 52, 22–35.

Haimson, B. C., Cornet, F. H., 2003. ISRM Suggested Methods for rock stress estimation—Part 3: hydraulic fracturing (HF) and/or hydraulic testing of pre-existing fractures (HTPF). International Journal of Rock Mechanics and Mining Sciences, 40(7–8), 1011–1020.

Haimson, B. C., Fairhurst, C., 1967. Initiation and Extension of Hydraulic Fractures in Rocks. Society of Petroleum Engineers Journal, 7(3), 310–318.

Hofmann, H., Zimmermann, G., Farkas, M., Huenges, E., Zang, A., Leonhardt, M., Kwiatek, G., Martinez-Garzon, P., Bohnhoff, M., Min, K.-B., Fokker, P., Westaway, R., Bethmann, F., Meier, P., Yoon, K.S., Choi, J.W., Lee, T.J., Kim, K.Y., 2019. First field application of cyclic soft stimulation at the Pohang Enhanced Geothermal System site in Korea. Geophysical Journal International, 217(2), 926–949.

Hökmark, H., Lönnqvist, M., Fälth, B., 2010. THM-issues in repository rock. Thermal, mechanical, thermo-mechanical and hydro-mechanical evolution of the rock at the Forsmark and Laxemar sites. SKB TR-10-23, Stockholm.

Hudson, J., Harrison, J., 2000. Engineering rock mechanics. An introduction to the principles. Elsevier Science Ltd, Kidlington, 524 p.

Huenges, E., 2010. Geothermal Energy Systems. Exploration, Development and Utilization. Wiley-VCH, Weinheim, 487 p.

Huenges, E., Ellis, J., Welter, S., Westaway, R., Min, K.-B., Genter, A., Meier, P., Wassing, B., Marti, M., 2021. Demonstration of Soft Stimulation Treatments in Geothermal Reservoirs. Proceedings of the World Geothermal Congress 2020+1, March-October, 2021.

Hyman, J. D., Jiménez-Martínez, J., Viswanathan, H. S., Carey, J. W., Porter, M. L., Rougier, E., Karra, S., Kang, Q., Frash, L., Chen, L., Lei, Z., O'Malley, D., Makedonska, N., 2016. Understanding hydraulic fracturing: a multi-scale problem. Philosophical transaction of the Royal Society A, 374, 20150426.

Khristianovic, S., Zheltov, Y., 1955. Formation of vertical fractures by means of highly viscous liquid. World Petroleum Congress, Rome, Italy.

Kolawole, O., Ispas, I., 2020. Interaction between hydraulic fractures and natural fractures: current status and prospective directions. Journal of Petroleum Exploration and Production Technology, 10, 1613–1634.

Konietzky, H., Wasantha, P. L. P., Weber, F., 2017. Simulating the Single- and Multi-Stage Hydraulic Fracturing: Some Insights Gleaned from Discontinuum and Continuum Modelling. Procedia Engineering, 191, 1096–1103.

Jaeger, J. C., Cook, N. G. W., Zimmerman, R. W., 2007. Fundamentals of Rock Mechanics. Blackwell Publishing, Oxford, 489 p.

Jing, L., 2003. A review of techniques, advances and outstanding issues in numerical modelling for rock mechanics and rock engineering. International Journal of Rock Mechanics and Mining Sciences, 40(3), 283–353.

Langbauer, C., Fazeli Tehrani, F., Mastobaev, B., 2021. A holistic review on hydraulic fracturing stimulation laboratory experiments and their transition to enhanced geothermal system field research and operations. Liquid and Gaseous Energy Resources, 1(1), 30–63.

Lavrov, A., Larsen, I., Bauer, A., 2016. Numerical Modelling of Extended Leak-Off Test with a Pre-Existing Fracture. Rock Mechanics and Rock Engineering, 49, 1359–1368.

Lecampion, B., Detournay, E., 2007. An implicit algorithm for the propagation of a hydraulic fracture with a fluid lag. Computer Methods in Applied Mechanics and Engineering, 196(49–52), 4863–4880.

Lepillier, B., Yoshioka, K., Parisio, F., Bakker, R., Bruhn, D., 2020. Variational Phase-Field Modeling of Hydraulic Fracture Interaction with Natural Fractures and Application to Enhanced Geothermal Systems. Journal of Geophysical Research: Solid Earth, 125(7), e2020JB019856.

Lisjak, A., Grasselli, G., 2014. A review of discrete modeling techniques for fracturing processes in discontinuous rock masses. Journal of Rock Mechanics and Geotechnical Engineering, 6, 301–314.

Lisjak, A., Kaifosh, P., He, L., Tatone, B. S. A., Mahabadi, O. K., Grasselli, G., 2017. A 2D, fully-coupled, hydro-mechanical, FDEM formulation for modelling fracturing processes in discontinuous, porous rock masses. Computers and Geotechnics, 81, 1–18.

Lu, S.-M., 2017. A global review of enhanced geothermal system (EGS). Renewable and Sustainable Energy Reviews, 81(2), 2902–2921.

Mas Ivars, D., Potyondy, D. O., Pierce, M., Cundall, P.A., 2008. The smootjoint contact model. In: Proceedings of the 8th World Congress on computational mechanics—5th European Congress on computation mechanics and applied science and engineering, Venice, Italy.

Meyer, B. R., 1989. Three-dimensional hydraulic fracturing simulation on personal computers: Theory and comparison studies. Paper presented at the SPE Eastern Regional Meeting, Morgantown, West Virginia.

Miehe, C., Mauthe, S., 2016. Phase field modeling of fracture in multi-physics problems. Part III: crack driving forces in hydro-poro-elasticity and hydraulic fracturing of fluid-saturated porous media. Computer Methods in Applied Mechanics and Engineering, 304, 619–655.

Moska, R., Labus, K., Kasza, P., 2021. Hydraulic Fracturing in Enhanced Geothermal Systems—Field, Tectonic and Rock Mechanics Conditions—A Review. Energies, 14, 5725.

Nordgren, R.P., 1972. Propagation of a vertical hydraulic fracture. Society of Petroleum Engineers Journal, 12(4), 306–314.

Nur, A., Byerlee. J. D., 1971. An exact effective stress law for elastic deformation of rocks with fluids. Journal of Geophysical Research, 76(26), 6414–6419.

Ouyang, S., Carey, G. F., Yew, C. H., 1997. An adaptive finite element scheme for hydraulic fracturing with proppant transport. International Journal for Numerical Methods in Fluids, 24(7),645–670.

Park, S., Kim, K.-I., Xie, L., Yoo, H., Min, K.-B., Kim, M., Yoon, B., Kim, K.Y., Zimmermann, G., Guinot, F., Meier, P., 2020. Observations and analyses of the first two hydraulic stimulations in the Pohang geothermal development site, South Korea. Geothermics 88, 101905.

Perkins, T. K., Kern, L. R., 1961. Widths of hydraulic fractures. Journal of Petroleum Technology, 13(9), 937–949.

Potyondy, D. O., Cundall, P. A., 2004. A bonded-particle model for rock. International Journal of Rock Mechanics and Mining Sciences, 41(8), 1329–1364.

Profit, M., Dutko, M., Yu, J., Cole, S., Angus, D., Baird, A., 2016. Complementary hydro-mechanical coupled finite/discrete element and microseismic modelling to predict hydraulic fracture propagation in tight shale reservoirs. Computational Particle Mechanics, 3(2), 229–248.

Savitski, A. A., Detournay, E., 2002. Propagation of a penny-shaped fluid-driven fracture in an impermeable rock: Asymptotic solutions. International Journal of Solids and Structures, 39(26), 6311–6337.

Shahid, A. S. A., Fokker, P. A., Rocca, V., 2016. A Review of Numerical Simulation Strategies for Hydraulic Fracturing, Natural Fracture Reactivation and Induced Microseismicity Prediction. The Open Petroleum Engineering Journal, 9 (Suppl–1:M5), 72–91.

Shen, B., Stephansson, O., Rinne, M., 2020. Modelling Rock Fracturing Processes. Theories, Methods and Applications. Springer Switzerland, Cham, 579 p.

Siebrits, E., Peirce, A. P., 2002. An efficient multi-layer planar 3d fracture growth algorithm using a fixed mesh approach. International Journal for Numerical Methods in Engineering, 53(3), 691–717.

Tester, J. W., 2006. The Future of Geothermal Energy. Impact of Enhanced Geothermal Systems (EGS) on the United States in the 21st Century. Report prepared for the U.S. Department of Energy.

Wangen, M., 2011. Finite element modeling of hydraulic fracturing on a reservoir scale in 2D. Journal of Petroleum Science and Engineering, 77(3–4),274–285.

Wangen, M., 2013. Finite element modeling of hydraulic fracturing in 3D. Computers & Geosciences, 17(4), 647–659.

Wong, J. K. W., 2018. Three-dimensional multi-scale hydraulic fracturing simulation in heterogeneous material using Dual Lattice Model. PhD thesis submitted to the Department of Engineering at the University of Cambridge, 337 p.

Xing, T., Zhu, W., French, M., Belzer, B., 2019. Stabilizing Effect of High Pore Fluid Pressure on Slip Behaviors of Gouge-bearing Faults. Journal of Geophysical Research: Solid Earth, 124, 9526–9545.

Yoo, H., Park, S., Xie, L., Kim, K.-I., Min, K.-B., Rutqvist, J., Rinaldi, A. P., Hydro-mechanical modeling of the first and second hydraulic stimulations in a fractured geothermal reservoir in Pohang, South Korea. Geothermics, 89, 101982.

Yoon, J. S., Zang, A., Stephansson, O., 2014. Numerical investigation on optimized stimulation of intact and naturally fractured deep geothermal reservoirs using hydro-mechanical coupled discrete particles joints model. Geothermics, 52, 165–184.

Wassing, B. B. T., Gan, Q., Candela, T., Fokker, P. A., 2021. Effects of fault transmissivity on the potential of fault reactivation and induced seismicity: Implications for understanding induced seismicity at Pohang EGS. Geothermics, 91, 101976.

Wright, C. A., Weijers, L., Davis, E. J., & Mayerhofer, M., 1999. Understanding Hydraulic Fracture Growth: Tricky but Not Hopeless. Paper presented at the SPE Annual Technical Conference and Exhibition, Houston, Texas, USA.

Zang, A., Oye, V., Jousset, P., Deichmann, N., Gritto, R., McGarr, A., Majer, E., Bruhn, D., 2014. Analysis of induced seismicity in geothermal reservoirs – An overview. Geothermics, 52, 6–21.

Zang, A., Stephansson, O., 2010. Stress field of the Earth's crust. Springer, Dordrecht, 326 p.

Zang, A., Stephansson, O., Stenberg, L., Plenkers, K., Specht, S., Milkereit, C., Schill, E., Kwiatek, G., Dresen, G., Zimmermann, G., Dahm, T., Weber, M., 2017. Hydraulic fracture monitoring in hard rock at 410 m depth with an advanced fluid-injection protocol and extensive sensor array. Geophysical Journal International, 208(2), 790–813.

Zimmermann, G., Reinicke, A., 2010. Hydraulic stimulation of a deep sandstone reservoir to develop an enhanced geothermal system: laboratory and field experiments. Geothermics 39,70–77.

Zhou, L., Hou, M. Z., 2013. A new numerical 3D-model for simulation of hydraulic fracturing in consideration of hydro-mechanical coupling effects. International Journal of Rock Mechanics and Mining Sciences, 60, 370–380.

Zhuang, L., Zang, A., 2021. Laboratory hydraulic fracturing experiments on crystalline rock for geothermal purposes. Earth-Science Reviews, 216, 103580.

Zoback, M. D., 2007. Reservoir Geomechanics. Cambridge University Press, Cambridge, 505 p.

Acknowledgments

First of all, I would like to thank to several funders of the PhD research. This includes Golder Associates Hungary for financing the borehole scale study including field experiments. Furthermore, I would like to thank the European Union's Horizon 2020 research and innovation program under grant agreement No 691728, i.e. the DESTRESS project, for supporting this work. I am also grateful to section leaders at GFZ Potsdam, Ernst Huenges (4.8 - Geoenergy) and Fabrice Cotton (2.6 - Seismic Hazard and Risk Dynamics) for financing the numerical tools and providing bridge funding to finalise the thesis.

I would like to thank my supervisors Arno Zang and Günter Zimmermann who gave me the opportunity to pursue a PhD research on this fantastic topic, shared their immense knowledge with me and who supported me in many aspects. I would like to thank to Hannes Hofmann for the many amusing and fruitful discussions, the personal motivation and the advises to the publications. A big thank goes to Gyula Dankó and the Golder Associates team in Budapest who introduced me to the world of in-situ stress measurements and safety assessment for nuclear waste repositories. They introduced me to the little but enthusiastic Hungarian rock mechanics community, including Ákos Török and Balázs Vásárhelyi at the Budapest University of Technology and Economics. I also thank Ove Stephansson and Jeoung Seok Yoon who strongly supported my early PhD career and made a huge contribution to the borehole scale study. Ove, I hope you have enough rock samples to test up there. In general, I am more than grateful for the section Geoenergy at GFZ Potsdam for the excellent working conditions and the great social atmosphere. The support of my PhD student colleagues helped a lot to get through the valleys. I wish all PhD students good luck to finish their projects. A big thank goes to János Kovács at the University of Pécs and the local geoscience cluster for promoting geothermal research.

Lastly, and most importantly, I would like to thank my family for supporting and motivating me to realise my dissertation. Dorka, thank you for giving me the time and motivation to work on my thesis, and accepting all the unexpected struggles that this project brought along. Luca, thank you for being such a sweet girl. I thank mom and dad for supporting me all the way up, from a challenging child to a doctoral degree.